

Modelling and characterization of Quantum Dots as QLED devices for automotive lighting systems

Abstract

This work reports the design, manufacturing and numerical simulation approach of an electroluminescent quantum dot light emitting device (QLED) based on quantum dots as an active layer. In addition, the electrical I-V curve was measured, observing how the fabrication process and layer thickness have an influence in the shape of the plot.

This experimental device enabled us to create a computational model for the QLED based on the Transfer Hamiltonian approach to calculate the current density $J(\text{mA}/\text{cm}^2)$, the band diagram of the system and the accumulated charge distribution. Thanks to the QLED simulator developed, it would be possible to model the device and anticipate the electrical performance in a theoretical design step before going to QLED manufacturing at the laboratory.

Eventually, particular automotive lighting system demonstrators were designed to integrate the theoretical and experimental research carried out in an industrial automotive product.

ISSUED by

Juan J Santaella Hernández

SUPERVISOR

Dr. Francisco M Gómez Campos



UNIVERSIDAD
DE GRANADA

DATE: 24/03/2021

Editor: Universidad de Granada. Tesis Doctorales
Autor: Juan José Santaella Hernández
ISBN: 978-84-1117-579-1
URI: <https://hdl.handle.net/10481/77699>

CONTENTS

ACKNOWLEDGEMENTS.....	7
I. LIST OF FIGURES.....	8
II. LIST OF TABLES.....	14
INTRODUCTION.....	16
1 BL1 – STATE-OF-THE-ART	24
1.1 Scope	24
1.1.1 Research Plan.....	24
1.2 QDs Lighting Physical Mechanism.....	25
1.2.1 Electroluminescence	25
1.2.2 Photoluminescence.....	26
1.3 Definitions	27
1.3.1 Quantum Yield (QY)	27
1.3.2 Full width at half maximum (FWHM).....	27
1.3.3 Stokes Shift.....	28
1.4 RoHS & GADSL Compliance:.....	28
1.5 QDs Cd-Free	29
1.5.1 Indium phosphide (InP).....	30
1.5.2 Copper indium sulfide (CIS).....	31
1.5.3 Silver indium sulfide (AgInS ₂)	32
1.5.4 ZAlSe (Zn–Ag–In–Se)	33
1.5.5 Doped Zn chalcogenides (Mn:ZnS).....	34
1.5.6 Graphene	35
1.5.7 Silicon	36
1.5.8 Indium arsenide (InAs)	37
1.6 Final QD Selection	40
1.7 InP-based QLED	42
1.7.1 InP/ZnSe/ZnS.....	42
1.7.2 InP/ZnSeS	44
1.7.3 InP/ZnSeS/ZnS.....	45
1.8 CIS-based QLED	49
1.8.1 CuInS ₂ /ZnS.....	49

1.8.2	Cu-Zn-In-S/ZnS	50
1.9	Conclusions	53
2	BL2 – QUANTUM DOTS	56
2.1	Scope	56
2.1.1	Research Plan	56
2.2	QD Characterization	57
2.2.1	Goals	57
2.2.2	Experimental Units	57
2.2.3	Supplier datasheet	58
2.2.4	Laboratory Instrumentation	62
2.2.5	Experimental Design 1: QD characterization	65
2.2.6	Summary	76
2.3	QD Synthesis	77
2.3.1	Goals	77
2.3.2	Laboratory Instrumentation	77
2.3.3	Experimental Design 2: QD synthesis	79
2.3.4	Summary	84
2.4	Conclusions	84
3	BL3 – QLED DEVICE	86
3.1	Scope	86
3.1.1	Research Plan	86
3.2	Photoluminescence vs Electroluminescence	87
3.3	QDF Proof of Concept (photoluminescence)	88
3.4	QLED Design (electroluminescence)	89
3.4.1	QLED energy levels	89
3.4.2	Layer device selection	90
3.4.3	QLED Architecture	94
3.4.4	Device Physical Implementation	94
3.4.5	Summary	97
3.5	QLED Manufacturing	98
3.5.1	Goals	98
3.5.2	Laboratory Instrumentation	98

3.5.3	Experimental Design 3: QLED physical implementation	101
3.5.4	Summary	107
3.6	QLED Characterization	108
3.6.1	Experimental Units.....	108
3.6.2	Goals	109
3.6.3	Laboratory Instrumentation.....	109
3.6.4	Experimental Design 4: QLED electrical characterization	110
3.6.5	Summary	111
3.7	Conclusions	112
4	BL4 – QLED MODELLING	114
4.1	Scope	114
4.1.1	Research Plan	114
4.2	QLED simulator.....	115
4.2.1	Literature research.....	115
4.3	Transfer Hamiltonian approach	117
4.3.1	Definition	117
4.3.2	Computational algorithm proposal: QLEDsim	135
4.4	Simulation results.....	136
4.4.1	Current density J	137
4.4.2	Approximation to 3D device (I-V curve).....	137
4.4.3	Theoretical vs Experimental.....	138
4.4.4	Band Diagram.....	139
4.4.5	Accumulated charge distribution.....	143
4.5	Validity of Simulation Model.....	145
4.5.1	Radiative recombination	145
4.5.2	Density of States (DOS)	145
4.5.3	Thermal Dissipation	146
4.5.4	Electrode Interface Capacitance	146
4.5.5	Quantum Dot size	147
4.5.6	Fitting parameters.....	148
4.5.7	Future research with QLEDsim simulator	148
4.6	Conclusions	149

5	BL5 – AUTOMOTIVE INTEGRATION.....	150
5.1	Scope	150
5.1.1	Research Plan	150
5.2	VALEO - Smart Technology for Smarter Mobility	151
5.2.1	Visibility Systems	153
5.3	Lighting Systems Definitions	154
5.3.1	The human eye.....	154
5.3.2	Light color.....	155
5.3.3	Photometric basis	157
5.4	Automotive Lighting Systems: to see and to be seen	161
5.4.1	Front Lighting Functions – HEADLAMPS Beams.....	162
5.4.2	Signaling Functions – REAR and HEADLAMPS	162
5.4.3	Photometry in signaling functions	163
5.4.4	Materials used in automotive lighting systems	165
5.5	Electroluminescence or Photoluminescence	166
5.6	Demonstrators	167
5.6.1	Quantum Dot Demonstrator.....	167
5.6.2	QLED Automotive Lighting Application	168
5.7	QLED Automotive Application Characterization	174
5.7.1	Goals	174
5.7.2	Experimental Units.....	174
5.7.3	Laboratory Instrumentation.....	174
5.7.4	Experimental Design 5: QLED demonstrator characterization	176
5.7.5	Summary	193
5.8	Conclusions	194
6	CONCLUSIONS.....	196
6.1	Future Research	197
6.1.1	Photoluminescence.....	197
6.1.2	Electroluminescence	197
6.1.3	Synergies	197
7	PUBLICATIONS.....	198
7.1	Journal Articles.....	198

7.2	Patents	198
7.3	Oral presentations.....	199
7.4	Poster presentations	199
8	REFERENCES	200

ACKNOWLEDGEMENTS

A María, por creer en mí y apoyarme desde el principio, por soportar incontables horas de soledad, por animarme en los momentos más difíciles, que no han sido pocos, y encontrar siempre esas palabras para seguir adelante. Por TODO, gracias. Sin ti no lo hubiera conseguido.

A mis padres, por haber sido tan importantes durante todo este tiempo. Sin ellos no hubiera podido llegar finalmente hasta aquí. A mi hermana, por saber que siempre puedo contar con ella.

A mi Director Francisco, por su enorme dedicación y orientación en estos años, sin la cual no hubiéramos completado ni la mitad de lo propuesto. A Salvador Rodríguez Bolívar, por su inestimable ayuda desde el inicio y concepción de este proyecto de investigación.

A Madi, por su ayuda en lengua extranjera. A Sergio Illera, por su gran soporte en el modelado computacional.

A la Universidad de Leeds y, en especial, a Kevin Critchley y Marco Califano, por su acogida y supervisión.

A la Universidad de Granada en general y en particular a Araceli González y Juan M. Cuerva, por hacer uso de los laboratorios de Química Orgánica.

A VALEO y en particular a M^a Ángeles, Jesús Romo, Manuel Rubio y Fernando Dinis, por apoyar desde el principio esta idea. A mis compañeros Lucía y Alberto, por su ayuda en la última parte del desarrollo.

A todos, GRACIAS.

“Cuando quieras emprender algo, habrá mucha gente que te dirá que no lo hagas; cuando vean que no pueden detenerte, te dirán cómo tienes que hacerlo; y cuando finalmente vean que lo has logrado, dirán que siempre creyeron en ti”

-John C. Maxwell

“Sólo sé que no sé nada”

-Sócrates

I. LIST OF FIGURES

FIGURE 1: CUSTOMIZATION OF AN AUTOMOTIVE LIGHTING SYSTEM. LIGHTING IS KEY IN THE CURRENT AUTOMOTIVE INDUSTRY REVOLUTIONS. DESIGNED BY VALEO® FOR THIS WORK.	16
FIGURE 2: AUTOMOTIVE LIGHTING SYSTEM DESIGN INTEGRATION. HEADLAMPS WITH LARGE AND CURVED LIGHT BLUE SURFACE FOR DAYTIME RUNNING LIGHT (DRL). DESIGNED BY VALEO® FOR THIS WORK.	17
FIGURE 3: VEHICLE INTEGRATING LARGE AND HOMOGENEOUS LIGHTING SURFACES. DESIGNED BY VALEO® FOR THIS WORK.	17
FIGURE 4: POSSIBLE OLED DESIGN FOR SIGNALLING BACK LIGHTING. DESIGNED BY VALEO® FOR THIS WORK.	18
FIGURE 5: STYLE AND AESTHETICS ARE KEY IN AUTOMOTIVE R&D DEVELOPMENTS. DESIGNED BY VALEO® FOR THIS WORK.	18
FIGURE 6: REARLAMP INTEGRATION OF TURN INDICATOR (TI) FUNCTION (IN YELLOW). DESIGNED BY VALEO® FOR THIS WORK.	19
FIGURE 7: HEADLAMP DRL FUNCTION (IN WHITE) FOR CAR-TO-X COMMUNICATION. DESIGNED BY VALEO® FOR THIS WORK.	19
FIGURE 8: THE QUANTUM CONFINEMENT ALLOWS ADJUSTING THE EMISSION WAVELENGTH BY CONTROLLING THE SIZE OF THE QUANTUM DOT. THE LARGER THE QUANTUM DOT, THE LONGER THE EMITTED PHOTON WAVELENGTH. THE DIAMETER OF THE BLUE QD (D_{BLUE}) IS SMALLER THAN THE GREEN AND RED ONE I.E. $D_{\text{BLUE}} < D_{\text{GREEN}} < D_{\text{RED}}$	20
FIGURE 9: WORLD RANKING OF VEHICLE PRODUCERS (IN MILLIONS OF UNITS AND MARKET SHARE) ACCORDING TO ANFAC. REPRODUCED FROM [13].	21
FIGURE 10: PHD BOTTOM-UP METHODOLOGY.	22
FIGURE 11: BLOCK BL1. BOTTOM-UP METHODOLOGY.	24
FIGURE 12: (A) QLED ARCHITECTURE DESIGNED IN THIS WORK. A) CATHODE, B) ELECTRON TRANSPORT LAYER, C) QUANTUM DOT LAYER, D) HOLE TRANSPORT LAYER, E) ANODE. (B) EXPERIMENTAL QLED FABRICATED IN THIS WORK AND ELECTRICALLY EXCITED.	25
FIGURE 13: EXPERIMENTAL QDF FABRICATED IN THIS WORK INCORPORATING RED AND GREEN QDs IN TWO DIFFERENT SUBSTRATES: TYPICAL PL MECHANISM WHEN EXCITING QDs EMBEDDED IN A SUBSTRATE WITH UV OR DEEP BLUE LIGHT.	26
FIGURE 14: FULL WIDTH AT HALF MAXIMUM (FWHM).	27
FIGURE 15: ABSORPTION AND EMISSION SPECTRA.	28
FIGURE 16: EMISSION SPECTRA OF INP, INP/ZNS, INP/ZNSE AND INP/ZNSE/ZNS QDs. DESIGNED FOR THIS WORK.	30
FIGURE 17: EMISSION SPECTRA OF CuInS ₂ , CuInS ₂ /ZNS AND Cu-In-Zn-S/ZNS QDs. DESIGNED FOR THIS WORK.	31
FIGURE 18: EMISSION SPECTRA OF AgInS ₂ AND AgInS ₂ /ZNS QDs. DESIGNED FOR THIS WORK.	32
FIGURE 19: EMISSION SPECTRUM OF Zn-Ag-In-Se QDs. DESIGNED FOR THIS WORK.	33
FIGURE 20: EMISSION SPECTRUM OF Mn:ZNS QDs. DESIGNED FOR THIS WORK.	34
FIGURE 21: EMISSION SPECTRUM OF GRAPHENE QDs. DESIGNED FOR THIS WORK.	35
FIGURE 22: EMISSION SPECTRUM OF SILICON QDs. DESIGNED FOR THIS WORK.	36
FIGURE 23: EMISSION SPECTRA OF InAs QDs. DESIGNED FOR THIS WORK.	37
FIGURE 24: EMISSION SPECTRA RANGE VS QY OF Cd-FREE QDs. DESIGNED FOR THIS WORK.	39
FIGURE 25: BLOCK BL2. BOTTOM-UP METHODOLOGY.	56
FIGURE 26: SUPPLIER1 (S1): CuInS ₂ /ZNS ABSORPTION & EMISSION SPECTRUM. ADAPTED FOR THIS WORK.	58
FIGURE 27: SUPPLIER1 (S1): INP/ZNS ABSORPTION & EMISSION SPECTRUM. ADAPTED FOR THIS WORK.	59
FIGURE 28: SUPPLIER2 (S2): CuInS ₂ /ZNS ABSORPTION & EMISSION SPECTRUM. ADAPTED FOR THIS WORK.	60
FIGURE 29: SUPPLIER2 (S2): INP/ZNS ABSORPTION & EMISSION SPECTRUM. ADAPTED FOR THIS WORK.	61
FIGURE 30: (A) TEM OPERATING PRINCIPLE DESCRIBING THE PATH OF ELECTRON BEAM. REPRODUCED FROM [66]. (B) EXAMPLE OF HRTEM IMAGES OF CuInS ₂ QDs. REPRODUCED FROM [28].	63

FIGURE 31: PREPARATION OF SAMPLES INSIDE THE FUME HOOD AT UGR-CIC (CENTRO DE INSTRUMENTACIÓN CIENTÍFICA, UNIVERSIDAD DE GRANADA). ULTRASONIC CLEANER IS SHOWN AT THE RIGHT.	65
FIGURE 32: (S/TEM) TITAN [®] LOCATED AT UGR-CIC (CENTRO DE INSTRUMENTACIÓN CIENTÍFICA, UNIVERSIDAD DE GRANADA).	66
FIGURE 33: INTERNAL ARCHITECTURE OF (S/TEM) TITAN [®] FROM UGR.	66
FIGURE 34: CuInS ₂ 620 SAMPLE. (A) HAADF PICTURE FROM (S/TEM) TITAN [®] IN SCANNING MODE. (B) IMAGE PROCESSED WITH IMAGEJ [®] TO CALCULATE THE DIAMETER OF THE QD CORES USED AT THIS STAGE OF THE RESEARCH.	67
FIGURE 35: CuInS ₂ 620 SAMPLE. HISTOGRAM + NORMAL CURVE FOR QDs CORE USED AT THIS STAGE OF THE RESEARCH.	67
FIGURE 36: CuInS ₂ 620 SAMPLE. TEM PICTURES FROM (S/TEM) TITAN [®] IN TRANSMISSION MODE TO CALCULATE THE DIAMETER OF THE QDs CORE/SHELL USED AT THIS STAGE OF THE RESEARCH. (A) 10 NM RESOLUTION. (B) 5 NM RESOLUTION.	68
FIGURE 37: CuInS ₂ 620 SAMPLE. HISTOGRAM + NORMAL CURVE FOR QDs CORE/SHELL USED AT THIS STAGE OF THE RESEARCH.	68
FIGURE 38: INP620 SAMPLE. (A) HAADF PICTURE FROM (S/TEM) TITAN [®] IN SCANNING MODE. (B) IMAGE PROCESSED WITH IMAGEJ [®] TO CALCULATE THE DIAMETER OF THE QD CORES USED AT THIS STAGE OF THE RESEARCH.	69
FIGURE 39: INP620 SAMPLE. HISTOGRAM + NORMAL CURVE FOR QD CORES USED AT THIS STAGE OF THE RESEARCH.	69
FIGURE 40: INP620 SAMPLE. TEM PICTURES FROM (S/TEM) TITAN [®] IN TRANSMISSION MODE TO CALCULATE THE DIAMETER OF THE QD CORE/SHELL USED AT THIS STAGE OF THE RESEARCH.	70
FIGURE 41: INP620 SAMPLE. HISTOGRAM + NORMAL CURVE FOR QD CORE/SHELL USED AT THIS STAGE OF THE RESEARCH.	70
FIGURE 42: DATASHEET VS MEASURED SUPPLIER1 (S1): CuInS ₂ /ZNS ABSORPTION & EMISSION SPECTRUM.	72
FIGURE 43: DATASHEET VS MEASURED SUPPLIER1 (S1): INP/ZNS ABSORPTION & EMISSION SPECTRUM.	73
FIGURE 44: DATASHEET VS MEASURED SUPPLIER2 (S2): CuInS ₂ /ZNS ABSORPTION & EMISSION SPECTRUM.	74
FIGURE 45: DATASHEET VS MEASURED SUPPLIER2 (S2): INP/ZNS ABSORPTION & EMISSION SPECTRUM.	75
FIGURE 46: ENCLOSING LAB CHEMICAL HOOD (NOTE THAT THE WORK AREA IS INSIDE THE HOOD). REPRODUCED FROM [70].	77
FIGURE 47: FUME HOOD WITH THREE-NECKED ROUND BOTTOM AND CONDENSER COLUMN SET UP USED TO SYNTHESIZE QUANTUM DOTS AT UNIVERSITY OF LEEDS (UoL).	79
FIGURE 48: COOLING PROCESS OF CuInS ₂ CORE NANOPARTICLES SYNTHESIZED AT UoL.	80
FIGURE 49: CuInS ₂ /ZNS CORE/SHELL NANOPARTICLES FORMED AND SYNTHESIZED AT UoL.	80
FIGURE 50: CuInS ₂ /ZNS CORE/SHELL NANOPARTICLES SYNTHESIZED AT UoL BEFORE INTRODUCING THEM INTO THE CENTRIFUGE.	81
FIGURE 51: CuInS ₂ /ZNS CORE/SHELL NANOPARTICLES SYNTHESIZED AT UoL ON BOTTOM OF CONTAINER AFTER CENTRIFUGATION.	81
FIGURE 52: COLLOIDAL SOLUTION OF CuInS ₂ /ZNS QUANTUM DOTS (SYNTHESIZED AT UoL) IN HEXANE UNDER UV-LIGHT AFTER PURIFICATION PROCESS.	82
FIGURE 53: ABSORPTION AND EMISSION SPECTRA MEASURED OF CuInS ₂ /ZNS QUANTUM DOTS SYNTHESIZED AT UoL.	83
FIGURE 54: BLOCK BL3. BOTTOM-UP METHODOLOGY.	86
FIGURE 55: (A) QDF CuInS ₂ /ZNS QDs-BASED SYNTHESIZED IN THIS WORK AT UoL UNDER UV LIGHT. (B) QDF FABRICATED IN THIS WORK USING CuInS ₂ /ZNS QDs-BASED FROM SUPPLIER1 (GREEN AND RED QDs OUTPUT WAVELENGTH USED) UNDER UV LIGHT. QDF HAVE A GLASS SUBSTRATE.	88
FIGURE 56: QLED LAYERS STRUCTURE PROPOSAL. DESIGNED FOR THIS WORK.	89
FIGURE 57: QLED BULK ENERGY LEVELS DIAGRAM SKETCH PROPOSAL. DESIGNED FOR THIS WORK.	89
FIGURE 58: QLED ARCHITECTURE BASED ON ENERGY LEVELS AND MATERIAL LAYERS SELECTION. DESIGNED FOR THIS WORK.	94

FIGURE 59: PRE-PATTERNED ITO GLASS SUBSTRATES FROM OSSILA. REPRODUCED FROM [76].	95
FIGURE 60: QLED ACTIVE AREA FROM OSSILA. REPRODUCED FROM [76].	95
FIGURE 61: HIL, HTL, EL, ETL LAYERS DEPOSITION. REPRODUCED FROM [76].	96
FIGURE 62: CATHODE LAYER DEPOSITION. REPRODUCED FROM [76].	96
FIGURE 63: ENCAPSULATION STEP. REPRODUCED FROM [76].	96
FIGURE 64: EXTERNAL ELECTRICAL CONTACTS. REPRODUCED FROM [76].	97
FIGURE 65: (A) 6-PIXEL QLED DEVICE DIMENSIONS. (B) QLED FINAL DEVICE. REPRODUCED FROM [76].	97
FIGURE 66: EXAMPLE OF SPIN COATING A SMALL MOLECULE IN SOLUTION USING A STATIC DISPENSE. FIRST THE SUBSTRATE IS COATED IN THE INK CONTAINING THE MOLECULES DISSOLVED IN A SOLVENT (1). THEN THE SUBSTRATE IS ROTATED AT HIGH SPEED AND THE MAJORITY OF THE INK IS FLUNG OFF THE SIDE (2). AIRFLOW THEN DRIES THE MAJORITY OF THE SOLVENT LEAVING A PLASTICISED FILM (3) BEFORE THE FILM FULLY DRIES TO JUST LEAVE THE MOLECULES ON THE SURFACE (4). REPRODUCED FROM [96].	99
FIGURE 67: GLOVEBOX CONTAINER FROM MBRAUN® TO BE USED WITH INERT ATMOSPHERES. REPRODUCED FROM [70].	99
FIGURE 68: UV OZONE CLEANER USED. REPRODUCED FROM [76].	100
FIGURE 69: QLED ARCHITECTURE CHOSEN: SUBSTRATE + THIN FILM LAYER. DESIGNED FOR THIS WORK.	102
FIGURE 70: CLEANING RACK CONTAINING THE PRE-PATTERNED ITO SUBSTRATES. REPRODUCED FROM [76].	102
FIGURE 71: SONICATION PROCESS FOR THE PRE-PATTERNED ITO SUBSTRATES AT UoL.	103
FIGURE 72: APPLYING PEDOT:PSS ON THE SUBSTRATE USING THE SPIN COATER. REPRODUCED FROM [76].	104
FIGURE 73: CATHODE AREA TO BE WIPED FREE AFTER SPIN COATING. REPRODUCED FROM [76].	104
FIGURE 74: VACUUM EVAPORATOR USED AT UoL.	105
FIGURE 75: (A) SHADOW MASK USED FOR CATHODE LAYER DEPOSITION. (B) MASK LOCATED INSIDE THE VACUUM EVAPORATOR. DESIGNED FOR THIS WORK.	106
FIGURE 76: DEVICE ENCAPSULATION PROCESS. REPRODUCED FROM [76].	106
FIGURE 77: FINAL QLED DEVICES MANUFACTURED IN THIS WORK.	107
FIGURE 78: QLED1. ELECTRICALLY EXCITED DEVICES FABRICATED IN THIS WORK.	108
FIGURE 79: QLED2. ELECTRICALLY EXCITED DEVICES FABRICATED IN THIS WORK.	108
FIGURE 80: OSSILA LIFETIME SYSTEM USED AS SMU UNIT TO MEASURE I-V CURVES. REPRODUCED FROM [76].	109
FIGURE 81: FIGURE ILLUSTRATING THE FUNDAMENTAL QLED I-V CURVE MEASURED IN THIS WORK AND TEMPTED TO MODELLING.	110
FIGURE 82: BLOCK BL4. BOTTOM-UP METHODOLOGY.	114
FIGURE 83: GENERAL GOAL OF BL4 BY CREATING THE QLED SIMULATOR: <i>QLEDsim</i> . DESIGNED FOR THIS WORK.	115
FIGURE 84: ILLUSTRATION OF THE HIERARCHY OF TRANSPORT MODELS. ADAPTED FROM [99].	116
FIGURE 85: GEOMETRY OF THE TUNNELING SYSTEM WITH TWO ELECTRODES AND THE INSULATING BARRIER: THE SYSTEM IS SHARED INTO A LEFT AND A RIGHT PART BY A BOUNDARY Σ ENTIRELY LOCATED IN THE BARRIER. ADAPTED FROM [103].	117
FIGURE 86: (A) A TUNNEL JUNCTION WITH A HOMOGENEOUS BARRIER. (B) AND (C) THE TWO ELECTRODE BARRIER SUBSYSTEMS USED IN THE TRANSFER HAMILTONIAN DESCRIPTION OF THE JUNCTION. ADAPTED FROM [104].	118
FIGURE 87: STRUCTURE OF THE QLED DEVICE PROPOSED WITH ALL LAYERS DEPICTED (ITO AS ANODE, PEDOT:PSS AS HOLE INJECTION LAYER (HIL), TFB AS HOLE TRANSPORT LAYER (HTL), CuInS ₂ /ZnS QDs AS ACTIVE OR EMISSION LAYER, ZnO NPs AS ELECTRON TRANSPORT LAYER (ETL) AND Al LAYER AS CATHODE. DESIGNED FOR THIS WORK.	120
FIGURE 88: (A) QLED MODEL PROPOSED. (B) 3D VIEW FOR QLED MODEL WITH ALL TRANSPORT LAYER OF THE EXPERIMENTAL DEVICE INTRODUCED I.E. ANODE/HIL/HTL/QDs/ETL/CATHODE. NB: THE QUANTUM DOTS	

REPRESENTED IN THE FIGURE ARE SPHERICAL. DIFFERENT SCALES WERE USED IN EACH DIRECTION FOR THE SAKE OF CLARITY. DESIGNED FOR THIS WORK.	122
FIGURE 89: DIFFERENT TUNNELING PROCESSES IDENTIFIED FOR OUR QLED SYSTEM. ADAPTED FROM [100].	125
FIGURE 90: ENERGY BAND DIAGRAM FOR A) DIRECT TUNNEL AND B) FOWLER-NORDHEIM PROCESS (TRAPEZOIDAL). ADAPTED FROM [100], [109].	126
FIGURE 91: SELF-CONSISTENT FIELD IN ORDER TO ACHIEVE A FINAL SOLUTION VALUE CONVERGENCE. DESIGNED FOR THIS WORK.	134
FIGURE 92: SELF-CONSISTENT FIELD ALGORITHM IMPLEMENTED. DESIGNED FOR THIS WORK.	135
FIGURE 93: (A) TOP VIEW OF QLED DEVICE MODELLING. (B) 3D VIEW FOR QLED MODEL WITH ALL TRANSPORT LAYERS OF THE EXPERIMENTAL DEVICE INTRODUCED I.E. ANODE/HIL/HTL/QDs/ETL/CATHODE. NB: THE QUANTUM DOTS REPRESENTED IN THE FIGURE ARE SPHERICAL. DIFFERENT SCALES WERE USED IN EACH DIRECTION FOR THE SAKE OF CLARITY. DESIGNED FOR THIS WORK.	136
FIGURE 94: SIMULATED CURRENT DENSITY J (MA/CM ²) CURVE FOR THE QLED MODELLING DEVICE EXTRACTED FROM QLEDSIM SIMULATOR.	137
FIGURE 95: SIMULATED CURVE FOR THE QLED MODELLING DEVICE EXTRACTED FROM QLEDSIM SIMULATOR.	137
FIGURE 96: EXPERIMENTAL CURVE FOR THE 6-PIXEL QLED DEVICE MANUFACTURED IN THIS WORK COMPARED TO THE SIMULATED CURVE (RED-SQUARE LINE) OBTAINED FROM QLEDSIM.	138
FIGURE 97: ENERGY LEVELS PROPOSED FROM VACUUM REFERENCE EXTRACTED FROM QLEDSIM SIMULATOR. DESIGNED FOR THIS WORK.	139
FIGURE 98: EQUILIBRIUM BAND DIAGRAM OF THE HETEROJUNCTION FROM QLEDSIM SIMULATOR.	140
FIGURE 99: QLED FORWARD BIASED (V=2V) BAND DIAGRAM OF THE HETEROJUNCTION FROM QLEDSIM SIMULATOR.	141
FIGURE 100: QLED FORWARD BIASED (V=5V) BAND DIAGRAM OF THE HETEROJUNCTION FROM QLEDSIM SIMULATOR.	141
FIGURE 101: QLED FORWARD BIASED (V=8V) BAND DIAGRAM OF THE HETEROJUNCTION FROM QLEDSIM SIMULATOR.	142
FIGURE 102: QLED FORWARD BIASED (V=10V) BAND DIAGRAM OF THE HETEROJUNCTION FROM QLEDSIM SIMULATOR.	142
FIGURE 103: QLED ACCUMULATED CHARGE FOR EACH LAYER EXTRACTED FROM QLEDSIM SIMULATOR.	143
FIGURE 104: QLED GRAPHICAL COLOR MAPPING OF ACCUMULATED CHARGE FOR EACH LAYER EXTRACTED FROM QLEDSIM.	144
FIGURE 105: I-V QLED PLOT VARYING ANODE-HIL INTERFACE CAPACITANCE. SIMULATED FOR THIS WORK.	147
FIGURE 106: BLOCK BL5. BOTTOM-UP METHODOLOGY.	150
FIGURE 107: VALEO LOGO. REPRODUCED FROM [119].	151
FIGURE 108: VALEO BUSINESS GROUPS. REPRODUCED FROM [119].	152
FIGURE 109: VALEO PRODUCT LINES. REPRODUCED FROM [119].	153
FIGURE 110: RELATIVE EYE SENSITIVITY. REPRODUCED FROM [120].	154
FIGURE 111: DAY AND NIGHT-TIME EYE SENSITIVITY. REPRODUCED FROM [120].	154
FIGURE 112: CIE CHROMATIC DIAGRAM. REPRODUCED FROM [120].	155
FIGURE 113: CIE X,Y CHROMATICITY DIAGRAM. REPRODUCED FROM [120].	156
FIGURE 114: LIGHT SOURCE EMISSION PROFILE. INTENSITY VERSUS ANGULAR VIEWING. REPRODUCED FROM [120].	157
FIGURE 115: LIGHT SOURCES. THE THEORETICAL AND IDEAL LIGHT SOURCE FOR A HUMAN EYE WOULD HAVE A SPECTRAL DECOMPOSITION FITTING PERFECTLY INTO THE RED LINE. REPRODUCED FROM [120].	158
FIGURE 116: DIAGRAM OF THE ILLUMINANCE PROJECTION OF A HEADLAMP. REPRODUCED FROM [120].	159
FIGURE 117: LIGHTING AND SIGNALING FUNCTIONS IN AUTOMOTIVE. REPRODUCED FROM [120].	161
FIGURE 118: LIGHTING HEADLAMPS BEAMS. REPRODUCED FROM [120].	162

FIGURE 119: PHOTOMETRIC CHARTS WITH VERTICAL (V) AND HORIZONTAL (H) COORDINATES IN FRONT OF THE VEHICLE. REPRODUCED FROM [120].	163
FIGURE 120: ESTIMATION OF QUANTUM DOT TECHNOLOGY INTEGRATION IN AUTOMOTIVE LIGHTING SYSTEMS APPLICATIONS IN TERMS OF PHYSICAL EXCITATION PHENOMENA. DESIGNED FOR THIS WORK.	166
FIGURE 121: DYNAMIC QUANTUM DOT DEMONSTRATOR. DESIGNED FOR THIS WORK.	167
FIGURE 122: DIFFERENT COLLOIDAL QUANTUM DOTS EXCITED WITH 450NM WAVELENGTH. DESIGNED FOR THIS WORK.	167
FIGURE 123: DYNAMIC PHOTOLUMINESCENCE QLED APPLICATION FOR AUTOMOTIVE LIGHTING SYSTEMS. DESIGNED FOR THIS WORK.	168
FIGURE 124: COMMERCIAL QDF FROM NANJING BREADY ELECTRONICS®. REPRODUCED FROM [124].	168
FIGURE 125: AUTOMOTIVE LIGHTING FUNCTIONS POSSIBILITIES FROM A QDF INCORPORATING GREEN AND RED QDs. (A) PHYSICAL IMPLEMENTATION. (B) OUTPUT OPTICAL SPECTRUM ACHIEVED. DESIGNED FOR THIS WORK.	169
FIGURE 126: CAD SOFTWARE BLENDER®.	170
FIGURE 127: EXPLODED VIEW OF THE EXPERIMENTAL QLED DEVICE ASSEMBLED. A) CASE, B) BLUE LEDs, C) OPTICAL SYSTEM, D) QDF, E) LIGHT COVER. DESIGNED FOR THIS WORK.	170
FIGURE 128: DEMONSTRATOR MECHANICAL BASE. DESIGNED FOR THIS WORK.	171
FIGURE 129: HW BLOCK DIAGRAM. DESIGNED FOR THIS WORK.	171
FIGURE 130: MECHATRONICS INTEGRATION. (A) ELECTRONICS + PCB. (B) MECHANICAL BASE WITH POWER SUPPLY. DESIGNED FOR THIS WORK.	172
FIGURE 131: DIGITAL OLED DEMONSTRATOR BY AUDI®, ISAL 2019.	173
FIGURE 132: DIGITAL QLED DEVICE DYNAMIC LIGHTING SCENARIO EXAMPLES IN THIS WORK. CAR-TO-X COMMUNICATION IN REARLAMPS. (A) COMING HOME SCENARIO 1. (B) COMING HOME SCENARIO 2. (C) WARNING MODE SCENARIO. (D) LEAVING HOME SCENARIO. DESIGNED FOR THIS WORK.	173
FIGURE 133: FEASA LED SPECTROMETER. REPRODUCED FROM FEASA® WEBSITE.	175
FIGURE 134: LMK IMAGING PHOTOMETER USED. REPRODUCED FROM TECHNOTEAM® WEBSITE.	175
FIGURE 135: BLUE LED OPTICAL SPECTRUM @ $I_F=100\text{MA}$ MEASURED IN THIS WORK.	178
FIGURE 136: CIE DIAGRAM CREATED @ $I_F=100\text{MA}$. THE CROSS-SHAPED SET-POINT SHOWS THE COLOR FROM THE BLUE LED SOURCE.	178
FIGURE 137: QDF OPTICAL SPECTRUM MEASURED @ $I_F=100\text{MA}$.	180
FIGURE 138: QDF CIE DIAGRAM CREATED @ $I_F=100\text{MA}$. SET POINT IS OUT OF AUTOMOTIVE WHITE AREA. BLUE, ORANGE AND RED HIGHLIGHTED POLYGONS INDICATE THE ALLOWED AUTOMOTIVE POINTS FOR WHITE, AMBER AND RED COLORS FROM A LEGAL ASPECT. THE CROSS-SHAPED SET-POINT SHOWS THE OUTPUT COLOR OF THE QDF, WHICH IS OUT OF AUTOMOTIVE WHITE AREA [10].	180
FIGURE 139: LUMINOUS INTENSITY VS CURRENT ON THE QDF LAYER USED IN THIS WORK. THE LINES ARE A GUIDE FOR THE EYE.	182
FIGURE 140: QDF PERFORMANCE INDICATORS CALCULATED FOR THIS WORK.	183
FIGURE 141: LUMINANCE ANALYSIS PROCEDURE OF THE QLED DEVICE (QDF@25 MA) USED IN THIS WORK.	185
FIGURE 142: L_{MIN} THRESHOLD ANALYSIS PROCEDURE OF THE QLED DEVICE (QDF@25 MA) USED IN THIS WORK.	185
FIGURE 143: EXAMPLE OF L_{MAX} AND L_{MIN} MEASUREMENTS OF 6 SEGMENTS OF THE QLED DEVICE (QDF@25 MA) USED IN THIS WORK.	186
FIGURE 144: NORMALIZED SPECTRAL CURVES BEFORE PMMA FILTER (SOURCE) AND AFTER IT (RESULTING COLOR). THE GREEN CURVE (FILTER1) IS THE PMMA TRANSFER FUNCTION FOR THE MATERIAL USED IN THIS WORK.	187

FIGURE 145: PMMA CIE DIAGRAM CREATED FOR THIS WORK. RESULTING COLOR IS OUT OF AUTOMOTIVE RED AREA. BLUE, ORANGE AND RED HIGHLIGHTED POLYGONS INDICATE THE ALLOWED AUTOMOTIVE POINTS FOR WHITE, AMBER AND RED COLORS FROM A LEGAL ASPECT [10]. THE CROSS-SHAPED SET-POINT SHOWS THE OUTPUT COLOR OF THE QDF.	188
FIGURE 146: CIE DIAGRAM CREATED FOR THIS WORK AND CENTERED ON THE LEGAL AUTOMOTIVE REGULATION AREA (RED LINE POLYGON) FOR ECE AND SAE NORMS. RED SQUARE: RESULTING OUTPUT COLOR ($x=0.654$, $y=0.297$) AFTER PMMA FILTER.	188
FIGURE 147: LUMINOUS INTENSITY VS CURRENT AFTER THE RED PMMA FILTER USED IN THIS WORK.....	189
FIGURE 148: SW-PROCESSED QLED DEVICE WITH PMMA FILTER FOR LUMINANCE ANALYSIS IN THIS WORK.	190
FIGURE 149: QLED (THIS WORK) AND OLED COMPARISON OF LUMINANCE VS UNIFORMITY VALUES. OLED VALUES ARE EXTRACTED FROM KRUPPA <i>ET AL.</i> WORK [7], [8]. TYPICAL $V_F=2.9$ V FROM TABLE 55 IS USED IN ALL CASES AS APPROXIMATION TO CALCULATE THE POWER IN THE BLUE SOURCE.....	190

II. LIST OF TABLES

TABLE 1: INP QDs PARAMETERS.	30
TABLE 2: CIS QDs PARAMETERS.	31
TABLE 3: AGINS ₂ QDs PARAMETERS.	32
TABLE 4: ZAlSe (Zn-Ag-In-Se) QDs PARAMETERS.	33
TABLE 5: ZAlSe (Zn-Ag-In-Se) QDs PARAMETERS.	34
TABLE 6: GRAPHENE QDs PARAMETERS.	35
TABLE 7: SILICON QDs PARAMETERS.	36
TABLE 8: INAs QDs PARAMETERS.	37
TABLE 9: QDs PARAMETER SUMMARY.	38
TABLE 10: GADSL INVOLVING QDs MATERIALS IDENTIFIED. EXTRACTED FROM [18].	41
TABLE 11: INP/ZnSe/ZnS BASED QLED STRUCTURES. FIRST COLUMN REFERS TO SPECIFIC (NUMBERED) QLED CONFIGURATION.	43
TABLE 12: INP/ZnSe/ZnS BASED QLED FIGURES OF MERIT. FIRST COLUMN REFERS TO SPECIFIC (NUMBERED) QLED CONFIGURATION.	44
TABLE 13: INP/ZnSeS BASED QLED STRUCTURES. FIRST COLUMN REFERS TO SPECIFIC (NUMBERED) QLED CONFIGURATION.	45
TABLE 14: INP/ZnSeS BASED QLED FIGURES OF MERIT. FIRST COLUMN REFERS TO SPECIFIC (NUMBERED) QLED CONFIGURATION.	45
TABLE 15: INP/ZnSeS/ZnS BASED QLED STRUCTURES. FIRST COLUMN REFERS TO SPECIFIC (NUMBERED) QLED CONFIGURATION.	46
TABLE 16: INP/ZnSeS/ZnS BASED QLED FIGURES OF MERIT. FIRST COLUMN REFERS TO SPECIFIC (NUMBERED) QLED CONFIGURATION.	46
TABLE 17: SUMMARY OF INP-BASED QLED STRUCTURES. FIRST COLUMN REFERS TO SPECIFIC (NUMBERED) QLED CONFIGURATION.	47
TABLE 18: SUMMARY OF INP-BASED QLED FIGURES OF MERIT. FIRST COLUMN REFERS TO SPECIFIC (NUMBERED) QLED CONFIGURATION.	48
TABLE 19: CuInS ₂ /ZnS BASED QLED STRUCTURES. FIRST COLUMN REFERS TO SPECIFIC (NUMBERED) QLED CONFIGURATION.	49
TABLE 20: CuInS ₂ /ZnS BASED QLED FIGURES OF MERIT. FIRST COLUMN REFERS TO SPECIFIC (NUMBERED) QLED CONFIGURATION.	50
TABLE 21: Cu-Zn-In-S/ZnS BASED QLED STRUCTURES. FIRST COLUMN REFERS TO SPECIFIC (NUMBERED) QLED CONFIGURATION.	50
TABLE 22: Cu-Zn-In-S/ZnS BASED QLED FIGURES OF MERIT. FIRST COLUMN REFERS TO SPECIFIC (NUMBERED) QLED CONFIGURATION.	51
TABLE 23: SUMMARY OF CIS-BASED QLED STRUCTURES. FIRST COLUMN REFERS TO SPECIFIC (NUMBERED) QLED CONFIGURATION.	51
TABLE 24: SUMMARY OF CIS-BASED QLED FIGURES OF MERIT. FIRST COLUMN REFERS TO SPECIFIC (NUMBERED) QLED CONFIGURATION.	52
TABLE 25: SUMMARY OF COMMERCIAL CuInS ₂ QDs PARAMETERS.	62
TABLE 26: SUMMARY OF COMMERCIAL INP QDs PARAMETERS.	62
TABLE 27: UV-VIS-NIR RADIATION. EXTRACTED FROM [68].	63
TABLE 28: SUMMARY OF MEASUREMENT TOOLS USED FOR QDs.	64

TABLE 29: SUMMARY OF CORE QD SIZE MEASUREMENTS VS SUPPLIER DATASHEET.	71
TABLE 30: SUMMARY OF CORE/SHELL QD SIZE MEASUREMENTS VS SUPPLIER DATASHEET.....	71
TABLE 31: SUMMARY OF QD PARAMETERS MEASUREMENTS VS SUPPLIER1 DATASHEET.	73
TABLE 32: SUMMARY OF QD PARAMETERS MEASUREMENTS VS SUPPLIER2 DATASHEET.	75
TABLE 33: SUMMARY OF MEASUREMENT TOOLS USED FOR QDS.	78
TABLE 34: SUMMARY OF MEASURED PARAMETERS OF QDS SYNTHESIZED.....	83
TABLE 35: SUMMARY OF MEASURED PARAMETERS OF QDS (COMMERCIAL AND SYNTHESIZED).....	83
TABLE 36: ITO BULK MATERIAL PROPERTIES.	90
TABLE 37: PEDOT:PSS BULK MATERIAL PROPERTIES.	91
TABLE 38: TFB BULK MATERIAL PROPERTIES.	91
TABLE 39: CUINS2/ZNS BULK MATERIAL PROPERTIES.....	92
TABLE 40: ZNO BULK MATERIAL PROPERTIES.	92
TABLE 41: ALUMINUM BULK MATERIAL PROPERTIES.	93
TABLE 42: QLED LAYERS (ANODE-HIL-HTL-EL-ETL-CATHODE) BULK MATERIAL PROPERTIES.	93
TABLE 43: SUMMARY OF INSTRUMENTATION USED FOR QLED MANUFACTURING.	100
TABLE 44: SUMMARY OF MEASUREMENT TOOLS USED FOR QLED MANUFACTURING.....	110
TABLE 45: RELATIONSHIP BETWEEN VARIOUS TRANSPORT REGIMES AND SIGNIFICANT DEVICE SCALES. ADAPTED FROM [99].	115
TABLE 46: VALEO 2019 KEY FIGURES. EXTRACTED FROM [119].	151
TABLE 47: LIGHT INTENSITY SYMBOL. EXTRACTED FROM [120].	157
TABLE 48: FLUX SYMBOL. EXTRACTED FROM [120].	158
TABLE 49: ILLUMINANCE SYMBOL. EXTRACTED FROM [120].	158
TABLE 50: LUMINANCE SYMBOL. EXTRACTED FROM [120].	159
TABLE 51: LUMINANCE SYMBOL. EXTRACTED FROM [120].	160
TABLE 52: MINIMUM LUMINOUS INTENSITY AND FLUX REQUIREMENTS BASED ON ECE AUTOMOTIVE REGULATIONS. EXTRACTED FROM [121] AND [122].	164
TABLE 53: OPTICAL SPECIFICATIONS OF QDF USED FROM NANJING BREADY ELECTRONICS®. EXTRACTED FROM [124].	169
TABLE 54: SUMMARY OF INSTRUMENTATION USED FOR QLED DEVICE CHARACTERIZATION.	176
TABLE 55: BLUE LED ELECTRICAL/OPTICAL CHARACTERISTICS FROM DATASHEET. EXTRACTED FROM [127].	176
TABLE 56: EXPERIMENTALLY CHARACTERIZATION OF BLUE LED USED AS MAIN SOURCE.	177
TABLE 57: EXPERIMENTALLY CHARACTERIZATION OF QDF LAYER.	179
TABLE 58: LUMINOUS INTENSITY IN CD AS OUTPUT FROM THE QDF LAYER.	181
TABLE 59: QDF LAYER PERFORMANCE INDICATORS.....	182
TABLE 60: LUMINANCE VS UNIFORMITY CALCULATION OF THE QLED DEVICE FOR THE QDF LAYER USED IN THIS WORK.	186
TABLE 61: EXPERIMENTAL VALUES OF LUMINOUS INTENSITY IN CD AS OUTPUT OF THE PMMA FILTER.....	189
TABLE 62: EXPERIMENTAL VALUES OF MEAN LUMINANCE AND UNIFORMITY AT THE OUTPUT OF THE PMMA FILTER.	190

INTRODUCTION

Nowadays, the automotive industry is undergoing some technological and social revolutions that are shaping the greatest ever upheaval in transportation [1]. For the automotive sector, these forces are giving rise to three disruptive technological trends: electrification, autonomous vehicles, and digital mobility [2], [3]. As well as being simultaneous, all three revolutions are extremely fast-paced [1].

Therefore, with the increase of electric motors to the detriment of diesel engines, the vehicles of the future will be much more environmentally friendly thanks to electrification. Likewise, with the autonomous revolution, vehicles will be connected and the driver will delegate more tasks for the car to handle complex traffic situations [1], [3], [4]. Finally, the digital revolution is paving the way for new forms of mobility, implying the vehicle integration of new functions of communication with other vehicles and road environment [1]–[4]. Thus, as reported by Aschenbroich [1] the revolutions currently taking place in the automotive industry are going to disrupt usage patterns in such a way that it is difficult to know exactly how people will be using cars tomorrow.

In the frame of these revolutions, automotive lighting systems play an important role. Indeed, lighting in the automotive world has undergone a radical change in recent years thanks to Light Emitting Devices (LEDs). Thus, LEDs are replacing the use of halogen lamps in rear and headlamps [5], [6]. Those solid-state devices offer a low energy consumption and a long useful life, which is key in the eventual integration in the electric vehicle, contributing therefore to the carbon footprint reduction.

Moreover, as indicated by Kruppa *et al.* [7], [8], customization and Car-to-X communication i.e. real-time information exchange between the vehicle and its surroundings, is a desirable feature in lighting systems since digital information can be shared and transmitted to other vehicles and road users, which is vital for the final autonomous vehicle implementation and the desired digital mobility introduced above.

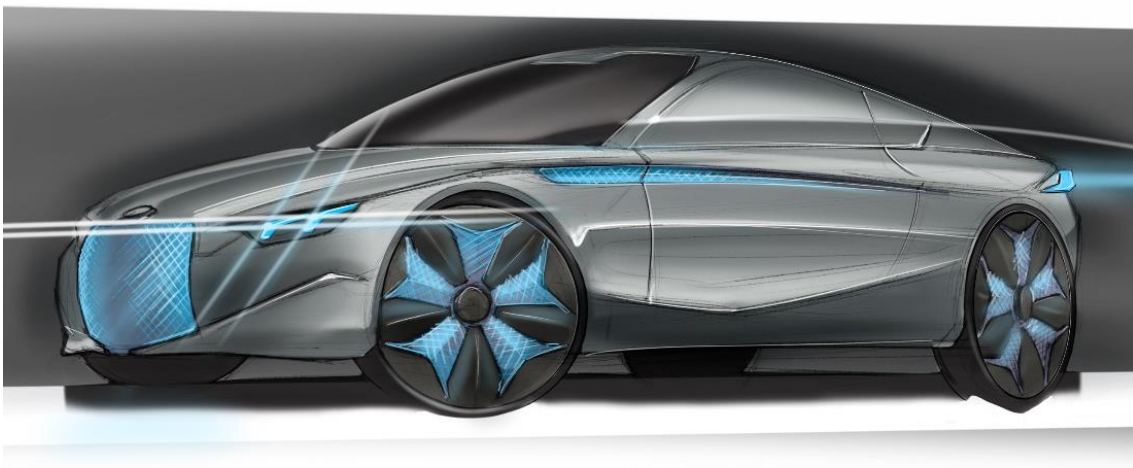


Figure 1: Customization of an automotive lighting system. Lighting is key in the current automotive industry revolutions. Designed by Valeo® for this work.

Nevertheless, apart from the consumption and the long useful life that LEDs can offer to automotive lighting systems, style is also imperative in vehicle designs and particularly in lighting products. The current and future trend in the automotive world is to achieve even greater lighting surfaces with flexible features and shapes in three dimensions (3D) as shown in Figure 2.

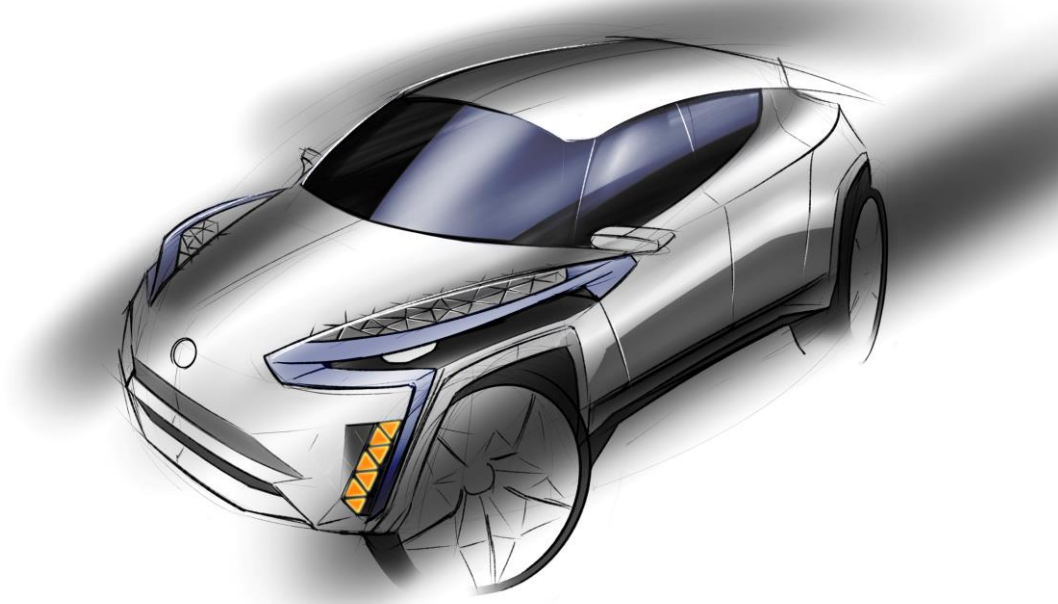


Figure 2: Automotive lighting system design integration. Headlamps with large and curved light blue surface for Daytime Running Light (DRL). Designed by Valeo® for this work.

As already highlighted, style is a fundamental parameter for automotive lighting systems. In fact, the homogeneity aspect of the lighting functions and the surfaces that conform the rear and headlamps is one of the highly desired factors [7], [8] and a main objective that carmakers are pursuing from an aesthetic point of view as shown in Figure 2 and Figure 3.

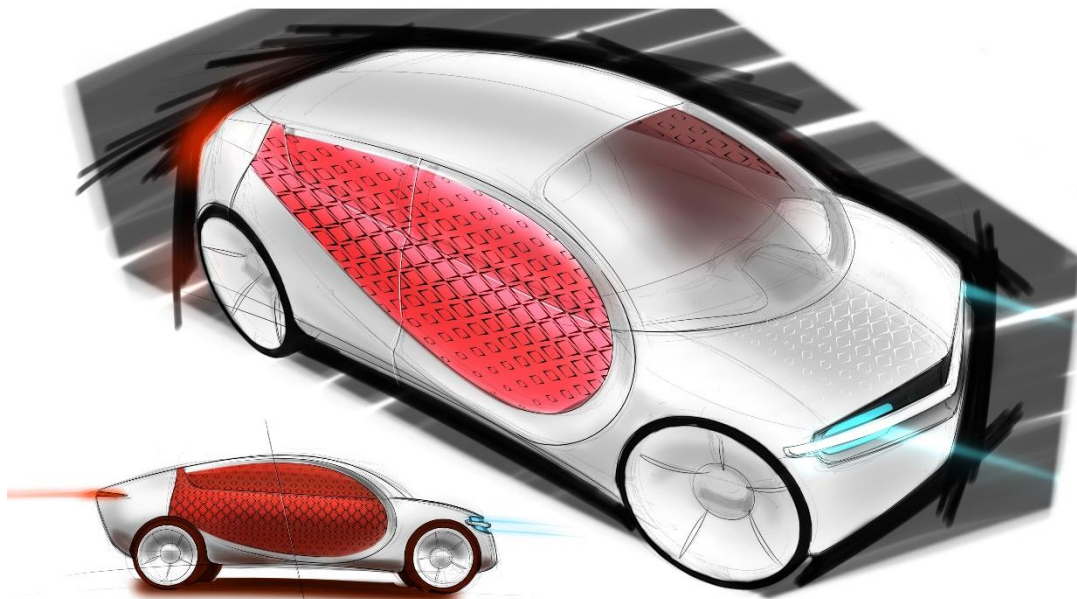


Figure 3: Vehicle integrating large and homogeneous lighting surfaces. Designed by Valeo® for this work.

However, the current LED technology formed by discrete devices of point light sources makes this task very complex and expensive. Following this high-homogeneous lighting surface strategy, and to achieve endless ways of designs and styles, a real and validated alternative to cover these technological needs described above is based on the use of Organic Light Emitting Devices (OLEDs) [6] as shown in Figure 4.

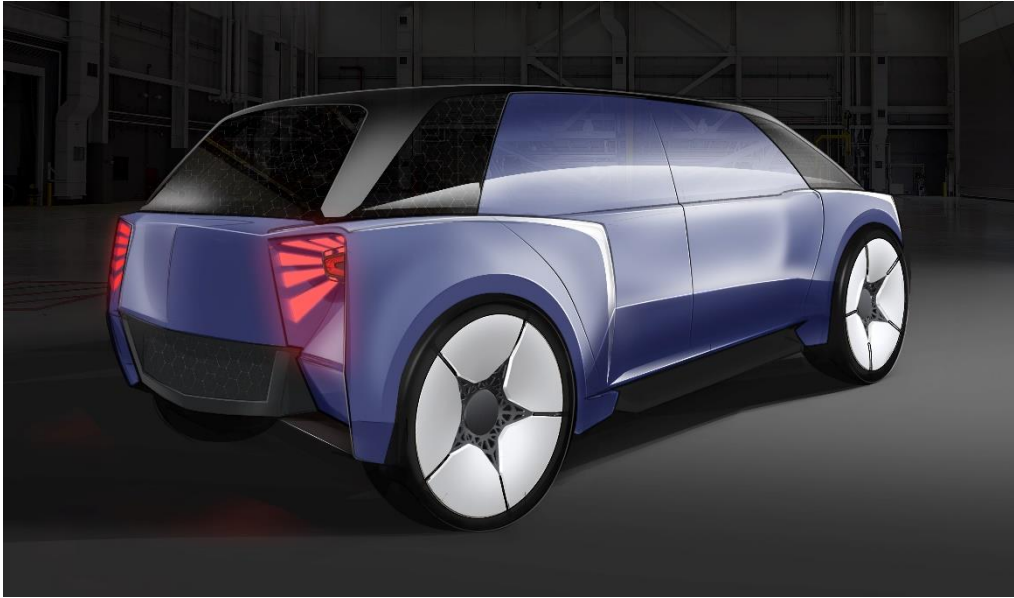


Figure 4: Possible OLED design for signalling back lighting. Designed by Valeo® for this work.

Nevertheless, although the current automotive OLED complies with the car manufacturer requirements, the intrinsic instability of those optoelectronic devices, due to their organic nature, makes them unreliable when subjected to large temperature differences such as those in the automotive industry with ranges from -40°C to 105°C . Thus, the degradation that might occur due to the organic character of the OLEDs makes their life time drastically reduced [9] when compared with other consumer electronic OLED devices, where environmental conditions are more friendly than in the automotive field. In addition, the alteration of the electrical parameters such as the forward voltage V_F of the device, which might significantly vary its value, influences the electronic control circuits used to control the OLEDs, making them difficult to design. Therefore, to tackle that degradation issues for OLED, complex manufacturing processes must be put in place, increasing the final cost of the OLED to be used in the automotive environment.

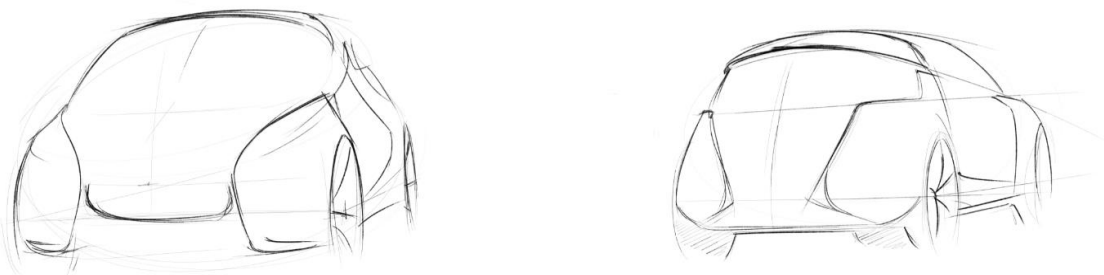


Figure 5: Style and aesthetics are key in automotive R&D developments. Designed by Valeo® for this work.

In addition, nowadays only taillighting (TAIL) can be performed using OLEDs due to the higher luminance optical requirements requested for the rest of automotive lighting functions (STOP, TURN INDICATOR, DRL ...). Then, nowadays, optical diffusers to scatter the light in combination with single-color emitting LEDs (red LEDs for TAIL or STOP lighting functions; amber or yellow for TURN INDICATOR for example) are mandatory to comply with automotive regulation norms [10] in terms of minimum luminance values. In this manner, in order to improve the homogeneity, it is necessary to increase the diffuser material thickness [7], [8], which leads to a low-efficiency optical systems as a whole.

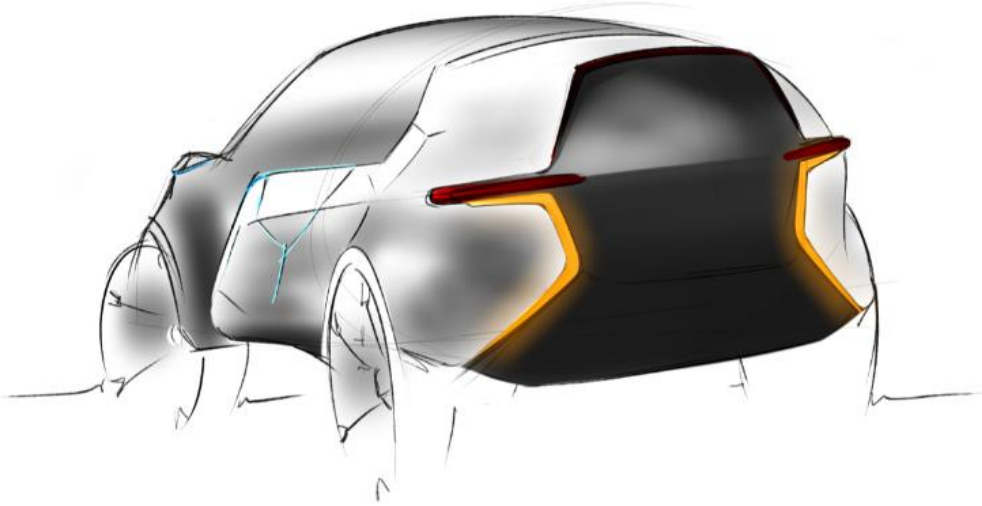


Figure 6: Rearlamp integration of Turn Indicator (TI) function (in yellow). Designed by Valeo® for this work.

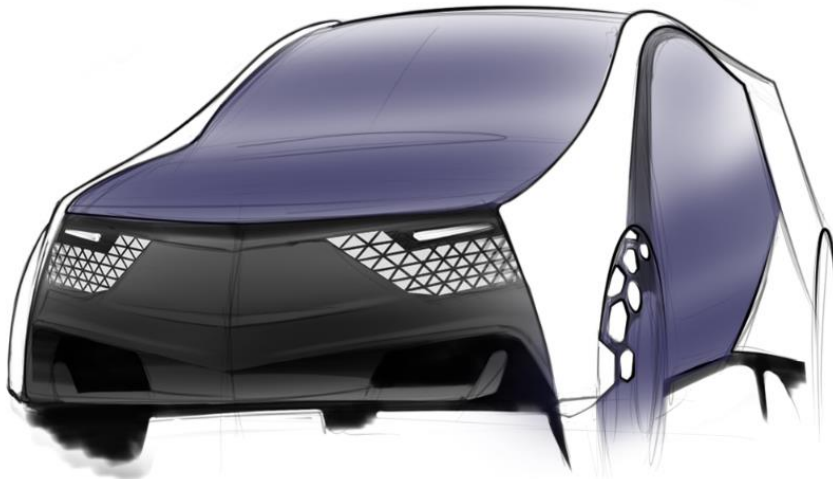


Figure 7: Headlamp DRL function (in white) for Car-to-X communication. Designed by Valeo® for this work.

Hence, the possibility to find new potential lighting alternatives for the automotive industry to support and complement the use of the already validated OLED technology shapes the motivation of this work.

Nowadays, a nanomaterial called quantum dots (QDs) could solve the issues described above effectively in the automotive field. QDs are nanocrystal semiconductors where electrons are confined in a region of space of nanometric dimensions. This implies the existence of a quantum confinement in the three dimensions of space. A particular kind of QDs, the colloidal quantum dots (CQD), are of interest for our purposes. The main characteristics exhibited by these nanostructures due to the confinement are [11]:

1. Diameters between [2-50]nm.
2. The density of states (DOS) becomes abrupt behaving therefore as "artificial atoms" or superatoms.
3. The energy spectrum of both absorption and emission becomes discrete.
4. The optical and electronic properties can be adjusted by controlling the size of the nanocrystals.

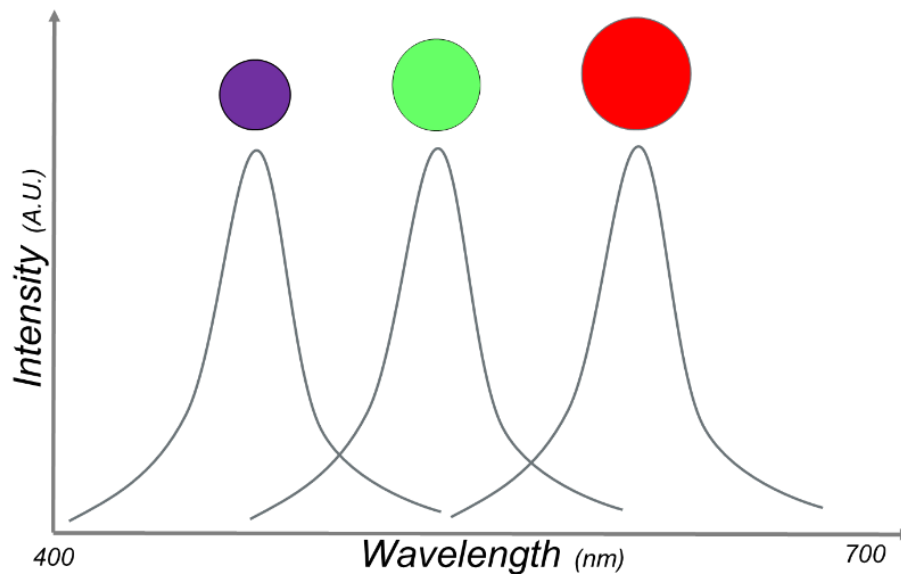


Figure 8: The quantum confinement allows adjusting the emission wavelength by controlling the size of the quantum dot. The larger the quantum dot, the longer the emitted photon wavelength. The diameter of the blue QD (d_{blue}) is smaller than the green and red one i.e. $d_{\text{blue}} < d_{\text{green}} < d_{\text{red}}$.

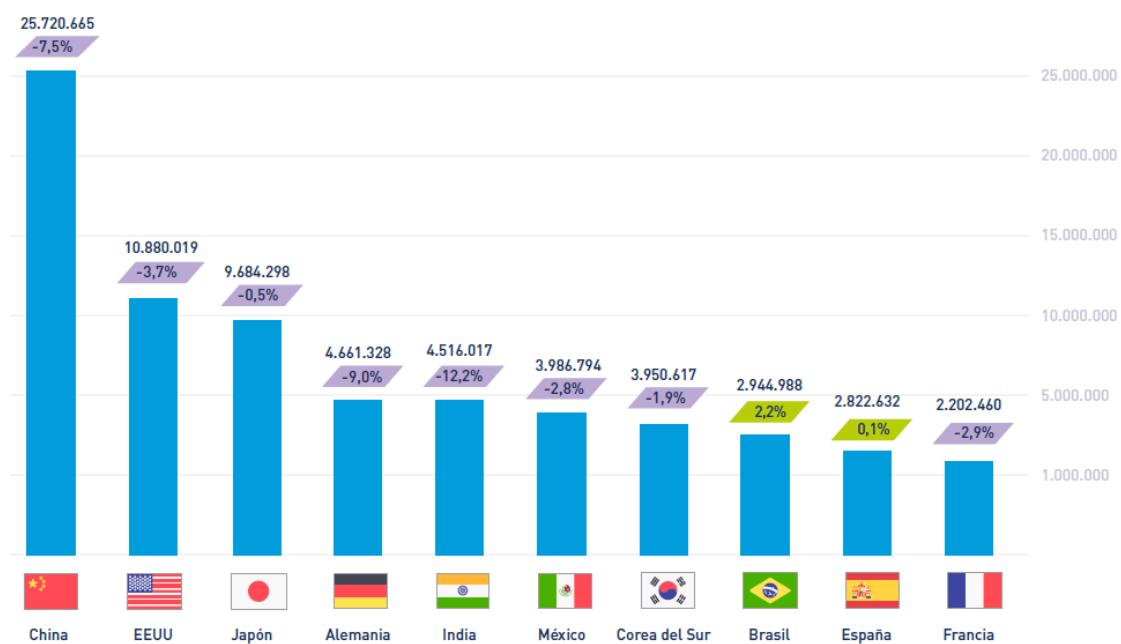
Optoelectronics is among the multiple applications that these groups of atoms can offer us. Specifically, LED lighting devices based on quantum dots (quantum dot LEDs), known by their acronym QLED, offer a promising future as a new generation of lighting devices due mainly to three factors [12]:

- a) **Purity of color.** Narrow emission bands that can be spectrally positioned by controlling the size of the nanocrystal during its synthesis.
- b) **Processability.** Methods of synthesis through colloidal solutions that allow the use of low cost deposition techniques on large surfaces, both rigid and flexible.
- c) **Stability.** Composed of inorganic materials, the quantum dot LEDs can be designed to withstand wide temperature ranges and environmental profiles.

As exposed above, the possibility to integrate new emerging technologies as potential lighting systems in the automotive field is one of the stimulus behind this PhD. In this manner, Research and Development (R&D) and Research and Innovation (R&I) are vital to achieve the levels of lighting designs shown from an aesthetic and functional point of view. Therefore, this work is framed in an industrial PhD, which tries to explore all steps of some particular nanotechnology optoelectronic devices from the state-of-the-art to the real and final integration in automotive lighting products. Thus, a compromise has been reached between pure scientific research at academic level and R&D - R&I activities from an industrial standpoint during the development of this PhD.

It is worth highlighting also the importance behind this research due to the actual social and economic impact that the automotive field has in society. The automotive industry is one of the most valuable sector from an economic standpoint worldwide and especially in some countries like Spain as shown in Figure 9, which shows that Spain was the ninth vehicle producing country in the world in 2019, and the second in Europe only behind Germany [13]. It generates a great number of jobs yearly and highly contributes to economy stability of the country. In fact it represents 10% of the Gross National Product (GNP) and it implies 9% of the employment over the active population in Spain [14].

To the best of our knowledge, this is the first study made to introduce this nanotechnology in automotive lighting products, particularly in exterior lighting systems. This assumption is based on the scientific articles released and the patents filed created in this work in that respect. Therefore, we believe that this first research could set the basis to further investigations and applications on the topic to the final integration and validation on automotive systems, contributing therefore to the increase of innovation and expertise of the scientific and technological knowledge in the following years from both an academic and industrial point of view.



FUENTE: OICA

Figure 9: World ranking of vehicle producers (in millions of units and market share) according to ANFAC. Reproduced from [13].

In this way, this work is divided into five parts or blocks (BL) as described in the research plan defined and approved at the beginning of the PhD. In the first block (BL1) the state-of-the-art of QDs has been assessed. A literature research was performed by targeting the suitable nanoparticles from an automotive viewpoint. Once the QDs were identified in BL1, a thorough study on those QDs is carried out in BL2 on the synthesization and characterization of the nanoparticles selected, which will be integrated in an experimental QLED device designed, fabricated and characterized in BL3. This QLED device from BL3 is then electrically modelled in BL4. That computational model allowed us to correlate the experimental QLED electrical behavior to make some proposals relating to the manufacturing process. Eventually, a real QLED demonstrator, based on the current automotive lighting trends, was designed, fabricated and characterized in BL5.

Figure 10 shows the bottom-up methodology followed to successfully achieve all the steps described above. It is worth noting that, although the scope of the PhD was large and ambitious in some extent since experimental and theoretical activities were mixed at once, we successfully achieved to complete all the objectives defined in the original research plan approved.

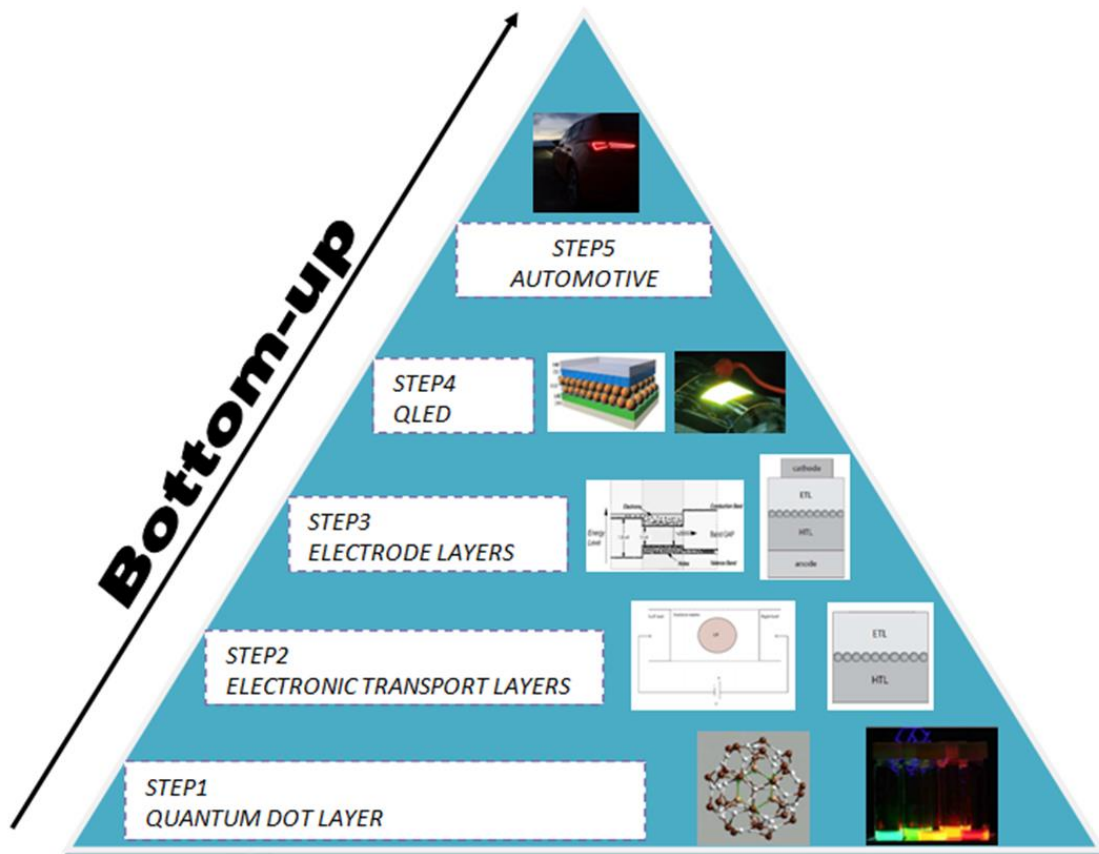


Figure 10: PhD BOTTOM-UP methodology.

1 BL1 – STATE-OF-THE-ART

1.1 SCOPE

One of the main objectives of this project is the modelling and experimental construction of a QLED electrically driven for the automotive field. In order to achieve this goal successfully, different steps have been defined in the frame of this industrial PhD work, until reaching the last automotive integration step.

Therefore, in this first move a thorough literature study on diverse material options to reach the correct emission wavelength along with the QDs size needed and the quantum yield (QY) given has been analyzed. Thus, a research on the optimal QDs, which comply with the automotive international requirements, has been carried out to develop an experimental QLED. This point is quite important since the automotive field has very restrictive norms relating to the allowed materials to be introduced in automotive products.

Then, depending on these results obtained, several materials will be selected as candidates to create the active layer of the experimental QLED to be designed, composed by multiple layers of those quantum dots.

1.1.1 Research Plan

Having a look into the research plan defined at the beginning of the PhD project, it is possible to depict graphically the location level of this block inside the bottom-up methodology presented.

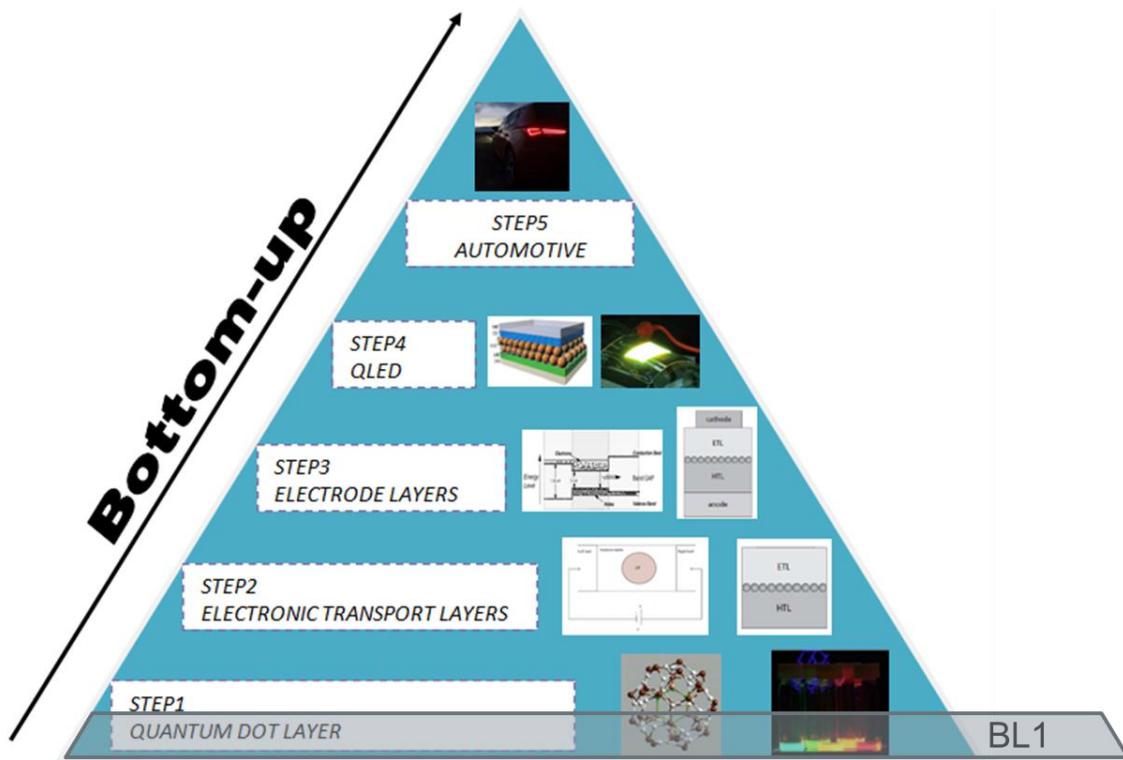


Figure 11: Block BL1. BOTTOM-UP methodology.

1.2 QDs LIGHTING PHYSICAL MECHANISM

There are two physical mechanisms from which it is possible to take advantage of when it comes to lighting-emitting devices. First, when an electrical current is used to excite QDs, electroluminescence (EL) devices are obtained. Secondly, if that QD excitation comes from a higher energy radiation than the one defined by the QD layer to be excited, photoluminescence (PL) phenomenon is considered.

After the literature research made in the following chapters, there is no standard nomenclature defined for QDs devices depending on the physical phenomena described previously. Therefore, Quantum Dot LED (QLED) will be referred in this work for both electroluminescence and/or photoluminescence lighting devices made out of quantum dots. Besides, the term Quantum Dot Film (QDF) will be used to particular devices where QDs are embedded in isolated substrate films (rigid or flexible) as shown in Figure 13.

1.2.1 Electroluminescence

One of the luminescence mechanisms used in a QLED is electroluminescence (EL). In this case, the emission of light is caused by the injection of an electric current through the device. Taking into account the previous mechanism, the internal structure of a QLED (electrically controlled) can be divided into five clearly differentiated layers [9]. Thus, this optoelectronic device is composed of a layer of quantum dots ("QD layer" in Figure 12) located between a layer of transport of holes (HTL) and an electron transport layer (ETL). Finally, an anode and a cathode make up the electrical contacts that enable the flow of electrical current and therefore the recombination of holes and electrons in the quantum dot layer producing the emission of photons.

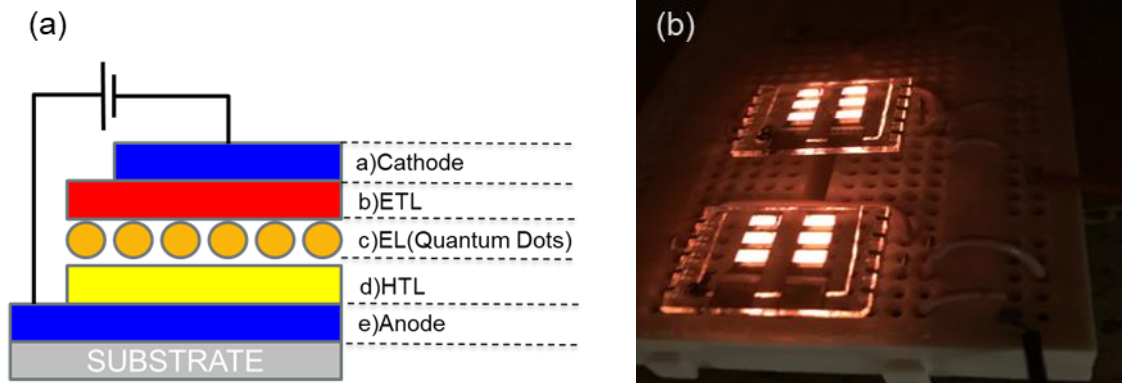


Figure 12: (a) QLED architecture designed in this work. a) cathode, b) electron transport layer, c) quantum dot layer, d) hole transport layer, e) anode. (b) Experimental QLED fabricated in this work and electrically excited.

These photons will be emitted at a predetermined wavelength or frequency within the electromagnetic spectrum and depending on the size of the QDs, which will determine the final color within the visible area. For this, it is necessary to take into account both the type of material used to form the quantum dot layer and the size thereof.

1.2.2 *Photoluminescence*

On the other hand, photoluminescence (PL) is another mechanism used in a QLED. In this case the device acts as a wavelength converter. This phenomenon is initiated by photoexcitation (i.e. photons that excite electrons to a higher energy level in an atom). Following excitation, various relaxation processes in which other photons are radiated again but with less energy typically occur. Thus, the output wavelength from the QD is larger than the input one. Using a UV or deep blue source to excite QDs it is possible to convert the light into the desired color (depending on the QD size).

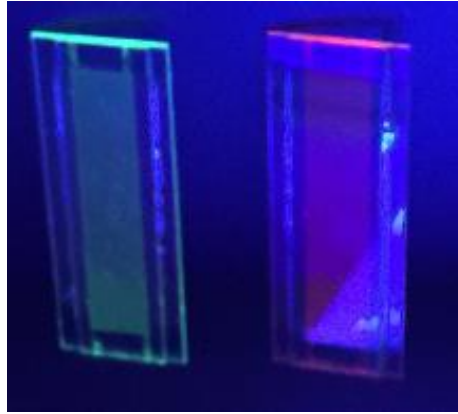


Figure 13: Experimental QDF fabricated in this work incorporating red and green QDs in two different substrates: typical PL mechanism when exciting QDs embedded in a substrate with UV or deep blue light.

1.3 DEFINITIONS

Some specific parameters, which characterize quantum dots are introduced below.

1.3.1 *Quantum Yield (QY)*

The optoelectronic behavior of quantum dots is strongly size-dependent. The ratio between the photons absorbed and the photons emitted is known as the quantum yield. This parameter defines the efficiency of the emission conversion process in QDs and has a maximum value of $QY=1$ i.e. every single absorbed photon is emitted by the material. Due to the non-radiative processes within QDs, this value of 100% is almost impossible to achieve in reality [15].

1.3.2 *Full width at half maximum (FWHM)*

Full width at half maximum (FWHM) is an expression of the extent of function given by the difference between the two extreme values of the independent variable at which the dependent variable is equal to half of its maximum value. In QDs, it is the width of the emission spectrum curve measured between those points on the y-axis, which are half the maximum amplitude. It indicates the purity of the color that can be achieved.

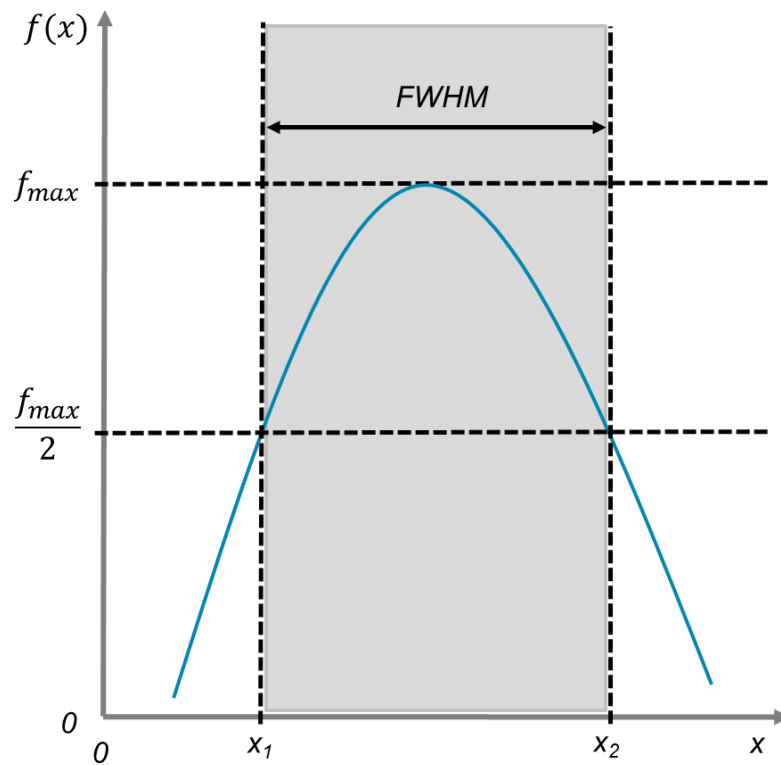


Figure 14: Full width at half maximum (FWHM).

1.3.3 Stokes Shift

Stokes shift is the difference (in energy, wavenumber or frequency units) between positions of the band maxima of the absorption and emission spectra

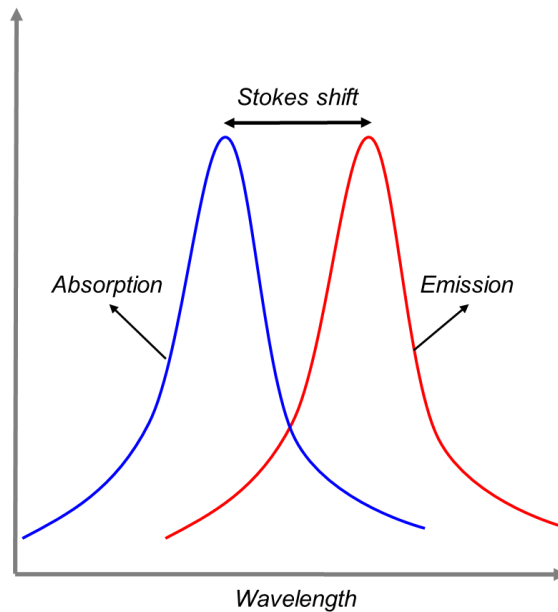


Figure 15: Absorption and emission spectra.

1.4 RoHS & GADSL COMPLIANCE:

By looking in the literature, cadmium chalcogenide based materials were the first nanocrystals studied due to the emissions wavelength found in the visible spectrum with high quality optical properties [16]. However the use of toxic heavy metals such as Cd and Pb is restricted in some countries and the technology trend should avoid them [16]. Indeed Cd is considered a cancer-inducing element [17] being considered one element inside Restriction of Hazardous Substances (RoHS) norm. Therefore, while the percentage of cadmium in a QLED is small, demonstration of high-performing Cd-free QLEDs will likely be crucial to securing widespread industry and government support for QLEDs. Thus alternative emitters may offer the potential to overcome these concerns [9].

Moreover, since the scope of the project is to define a device to be used in the automotive field it is necessary to look inside specific norms. In this way, Global Automotive Declarable Substance List (GADSL) has the objective to facilitate communication and exchange of information regarding the use of particular substances in automotive products by listing individual declarable substances and describing how they have to be used [18]. Thus, GADSL forms the basis for the declaration in the International Material Data System (IMDS) and it is a great support to improve products of the automotive industry relating to quality and safety by minimizing the harmful effects on the health and environment [19].

Likewise, this first step taken will involve the search of Cd-Free quantum dots focused on automotive application. To do so, GADSL will be the reference to follow for the state-of-the-art (SoA) study on candidate elements for QLEDs in the active layer of the optoelectronic device.

1.5 QDs CD-FREE

Nowadays the main challenge of Cd-free QDs is to achieve at least a performance comparable to Cd-based QDs. Thus, many research groups are looking for new nanochemistry methods to design and fabricate Cd-free quantum dots [20].

Over the last few years a diversity of Cd-free QDs have been synthesized from materials including indium phosphide (InP) [16], [20], [21], copper indium sulfide (CuInS₂) [22]–[29], silver indium sulfide (AgInS₂) [30]–[34], ZAlSe(Zn–Ag–In–Se) [35] doped Zn chalcogenides [36], [37], graphene [38], silicon [39], indium arsenide (InAs) [40]–[43], Zinc selenide (ZnSe) [44] and Gallium arsenide (GaAs) [45].

Therefore, the materials presented above, which offer the possibility to be used as the active layer of the QLED, will be briefly analyzed. Thereby four key parameters are identified to enable us to select the best candidates for the QLED: i) synthesis method, ii) size (diameter) range of the nanocrystals, iii) range of spectral emission achieved and iv) quantum yield (QY).

1.5.1 Indium phosphide (InP)

Indium phosphide (InP) nanocrystals are QDs of group III-V semiconductors which offer a higher robustness and stability than those QDs of II-VI materials such as CdSe due to the fact that the bonding is less ionic and more covalent [20]. Nonetheless, the PL intensity and the QY of InP QDs is lower because of less effective passivation of dangling bonds and surface defects [20]. In order to overcome this issue, InP QDs can be built up in a core/shell structure with ZnS or ZnSe wider band gap semiconductors as a shell. Table 1 shows the main key features of these QDs.

QD	Synthesis Method	Max diameter (nm)	Emission λ (nm)	Max QY(%)	REF
InP	hot colloidal	2,8	480-750	30	[46]
InP/ZnS	hot colloidal	6	480-735	80	[16][46]
InP/ZnSe	hot colloidal	No data	510-630	50	[16]
InP/ZnSe/ZnS	heating-up	3,6	450-550	50-70	[21]
InP/ZnSeS	heating-up	4	500-540	81	[47][48]
InP/ZnSeS/ZnS	heating-up	7,4	525-607	70-82	[49][50]

Table 1: InP QDs parameters.

DEFINITIONS:

- QD: kind of structure and material of the quantum dot under evaluation.
- Synthesis method: chemical method followed to fabricate the QD.
- Max diameter: maximum diameter of the quantum dot from the references used.
- Emission: range of spectral emission achieved with the QD selected.
- Max QY: maximum quantum yield measured.

And Figure 16 shows the emission spectra that can be achieved versus the QY parameter.

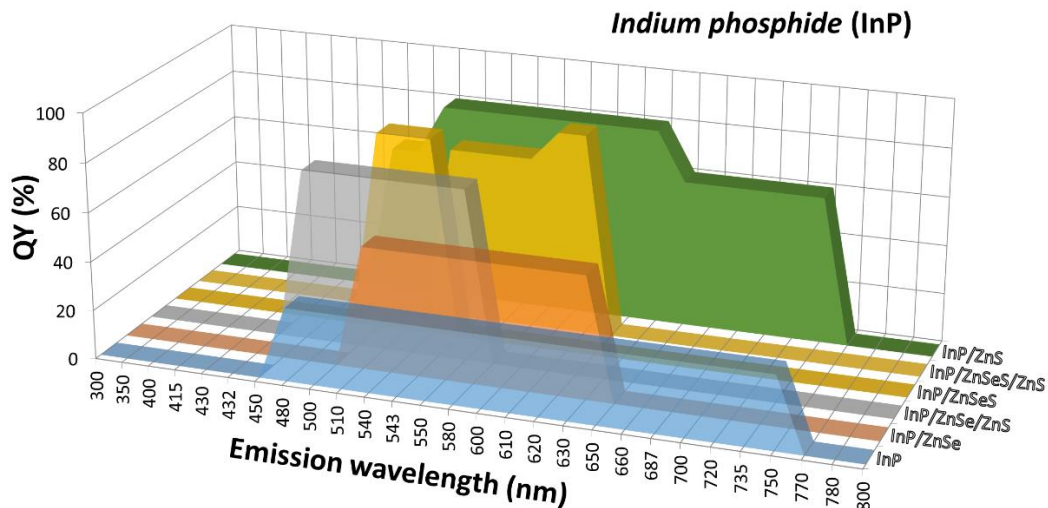


Figure 16: Emission spectra of InP, InP/ZnS, InP/ZnSe and InP/ZnSe/ZnS QDs. Designed for this work.

1.5.2 Copper indium sulfide (CIS)

Quantum confinement effects of copper indium sulfide (CIS) can be observed when its diameter is below 8 nm since Bohr exciton radius is set at 4.1 nm [28]. However, the low PL QY shown for bare CIS QDs is due to their instability in air or water. Therefore, to improve this parameter it is needed to coat CIS QDs with ZnS shell. This signal boost is attributed to the passivation of defects at the core QD surface [20]. Table 2 shows the main key features of these QDs. And Figure 17 shows the emission spectra that can be achieved versus the QY parameter.

QD	Synthesis Method	Max diameter (nm)	Emission λ (nm)	Max QY(%)	REF
CuInS ₂	hot colloidal	4	620-870	18	[22]–[24]
CuInS ₂ /ZnS	hot colloidal aqueous solution	7,1	540-815	89	[23][25][27]–[29]
Cu–In–Zn–S/ZnS	continuous flow	3,5	432-615	40	[26]

Table 2: CIS QDs parameters.

NB: Cu–In–Zn–S quaternary nanocrystals can be synthesized by alloying ZnS and CuInS₂. These alloyed (ZnS)_x(CuInS₂)_{1-x} QDs have a wide tunable band gap by changing the ratio of ZnS to CuInS₂ [26].

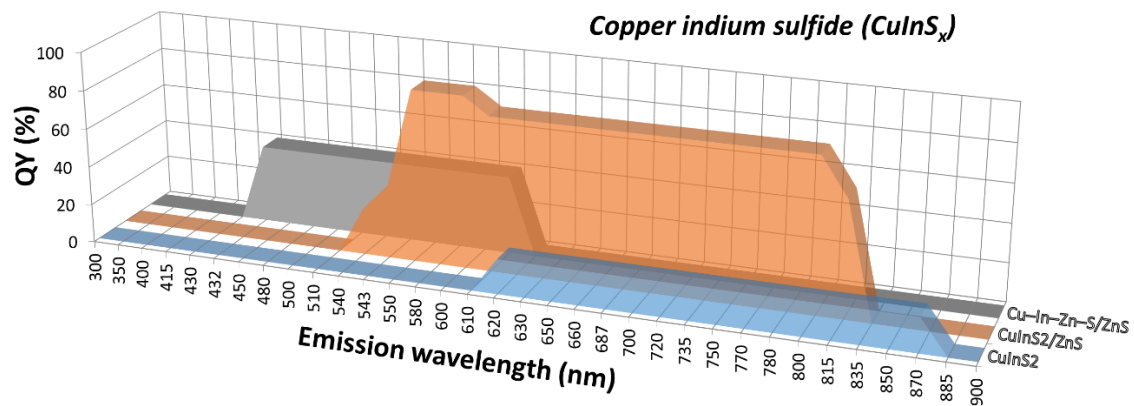


Figure 17: Emission spectra of CuInS₂, CuInS₂/ZnS and Cu–In–Zn–S/ZnS QDs. Designed for this work.

1.5.3 Silver indium sulfide (AgInS_2)

Ternary AgInS_2 QDs, which can exist in two crystal phases chalcopyrite and orthorhombic [20], and their alloys are suitable alternatives to Cd-, Hg-, and Pb-based binary ones due to their similar optoelectronic properties along with the low toxicity exhibited [35] and the possibility to be synthesized at very low temperatures [32]. Furthermore AgInS_2 QDs are candidates to be used for near-infrared (NIR) applications with the chance to improve the PL efficiency by increasing the stability through the use of semiconductor coating materials like ZnS (although making the alloy with a wide-band gap may result in a blue shift of the PL that needs to be taken into account) [32]. Table 3 shows the main key features of these QDs. And Figure 18 shows the emission spectra that can be achieved versus the QY parameter.

QD	Synthesis Method	Max diameter (nm)	Emission λ (nm)	Max QY(%)	REF
AgInS_2	hot colloidal	4,3	770-885	63	[30][31]
$\text{AgInS}_2/\text{ZnS}$	hot colloidal, thermal, decomposition, sonochemical	12	480-815	57,6	[32]–[34]

Table 3: AgInS_2 QDs parameters.

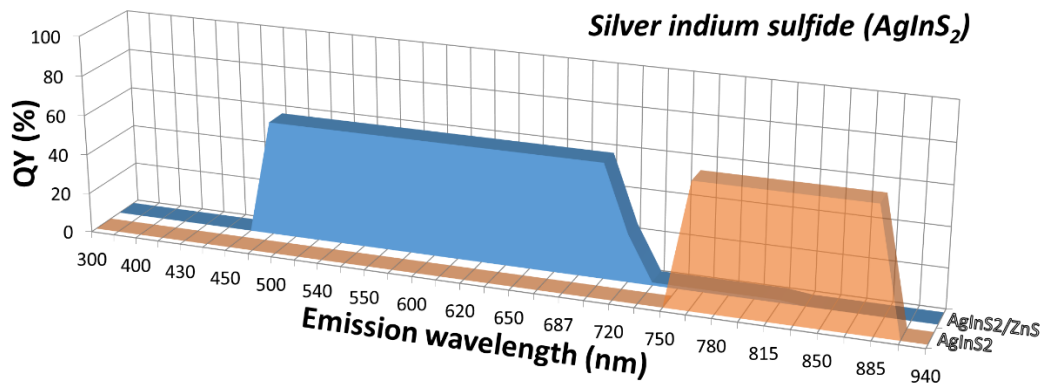


Figure 18: Emission spectra of AgInS_2 and $\text{AgInS}_2/\text{ZnS}$ QDs. Designed for this work.

1.5.4 *ZAlSe (Zn-Ag-In-Se)*

Another novel strategy is to fabricate quaternary Zn-I-III-VI QDs, particularly Zn-Ag-In-Se (ZAlSe) nanostructures whose QY can reach a value of 50% [35]. Therefore, Table 4 shows the main key features of these QDs.

QD	Synthesis Method	Max diameter (nm)	Emission λ (nm)	Max QY(%)	REF
Zn-Ag-In-Se	hot colloidal	5	660-800	50	[35]

Table 4: ZAlSe (Zn-Ag-In-Se) QDs parameters.

And Figure 19 shows the emission spectrum that can be achieved versus the QY parameter.

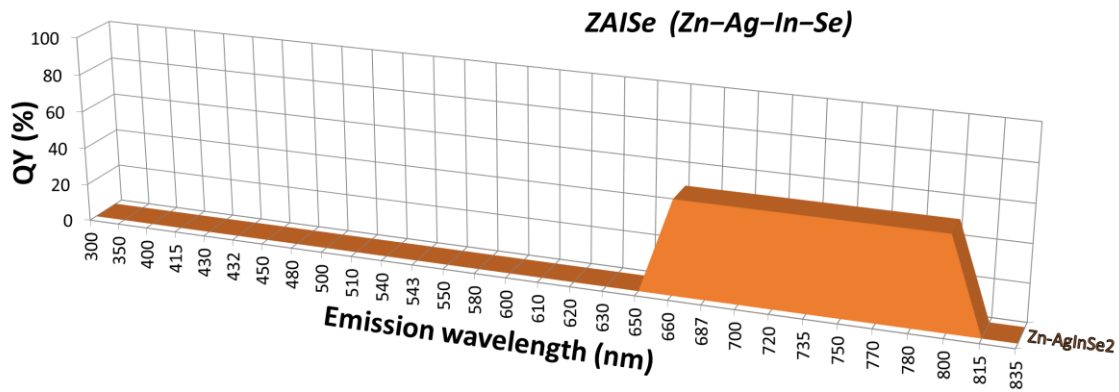


Figure 19: Emission spectrum of Zn-Ag-In-Se QDs. Designed for this work.

1.5.5 Doped Zn chalcogenides (Mn:ZnS)

Doped semiconductor QDs (d-dots) with low intrinsic toxicity are mostly based on zinc chalcogenides doped with Mn^{2+} , Eu^{2+} , Cu^{2+} , or Ga^{2+} [20], [37]. Among these QDs, Mn-doped semiconductor is one of the most studied. In this sense, when a semiconductor is doped by Mn ions, the exciton generated by photoexcitation of the host nanocrystal recombines via the lower lying states of the Mn^{2+} ion leading to an optical emission pattern relatively independent of the nanocrystal size [36]. Therefore, the PL emission peaks of these doped QDs can be tuned by changing the dopant concentration [20].

Thus, these kinds of QDs are the ideal emissive materials for applications requiring significant power, such as light emitting diode (LED) and solid-state lighting due to their efficiency, stability and tunable dopant emission [37]. Therefore, Table 5 shows the main key features of these QDs. In addition, Figure 20 shows the emission spectrum that can be achieved versus the QY parameter.

QD	Synthesis Method	Max diameter (nm)	Emission λ (nm)	Max QY(%)	REF
Mn:ZnS	hot colloidal	3,8	550-600	51,3	[36][37]

Table 5: ZAlSe (Zn-Ag-In-Se) QDs parameters.

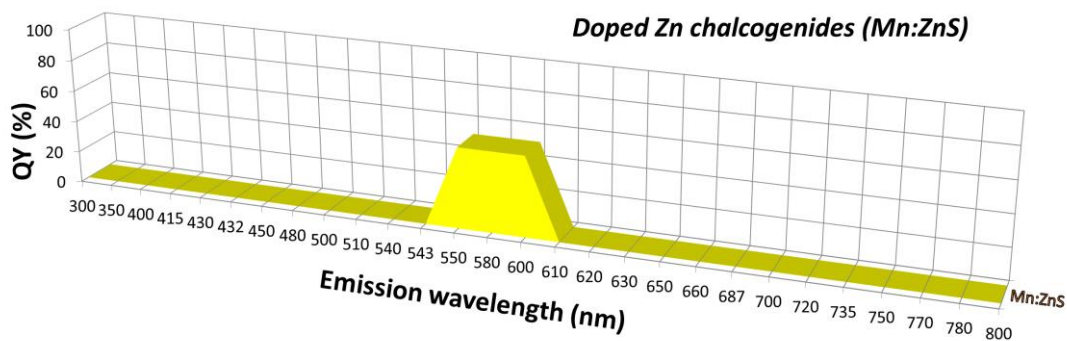


Figure 20: Emission spectrum of Mn:ZnS QDs. Designed for this work.

1.5.6 Graphene

Graphene has attracted remarkable attention due to its extraordinary optical and electronic properties and biocompatibility, in fact graphene quantum dots (GQDs) are chemically inert [38].

Nonetheless, applications of graphene in optoelectronics are limited because graphene is a zero bandgap semiconductor. Thus to create the bandgap in this material, GQDs have been developed [38].

Pristine graphene consists of a single layer of carbon atoms arranged in a hexagonal lattice. In such GQDs, PL emission can be tuned by varying the size in the two lateral dimensions, having a shift to longer wavelengths of the emission peaks when increasing the size. According to density functional theory (DFT) calculations, the emission peak of pristine GQD with an average diameter of 2nm should be in the red region [20]. Therefore, Table 6 shows the main key features of these QDs. In addition, Figure 21 shows the emission spectrum that can be achieved versus the QY parameter.

QD	Synthesis Method	Max diameter (nm)	Emission λ (nm)	Max QY(%)	REF
Graphene	pyrolysis	4,6	415-580 800-850	54,5	[38]

Table 6: graphene QDs parameters.

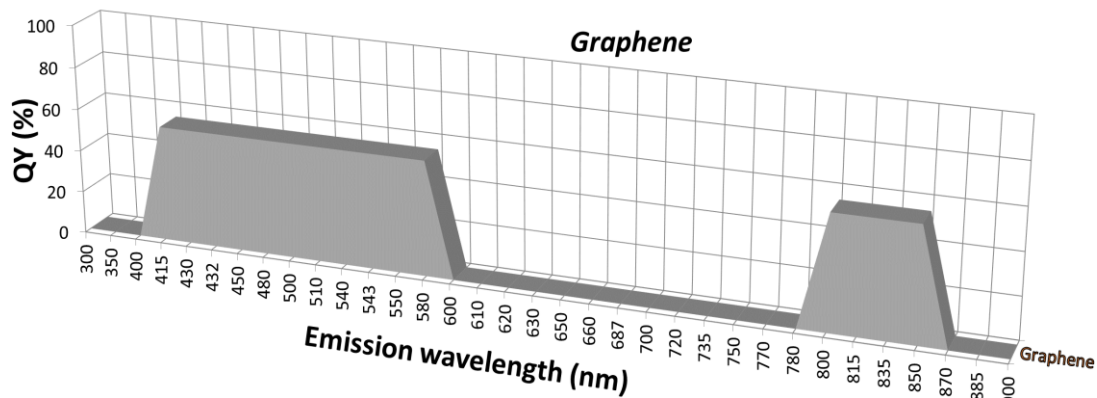


Figure 21: Emission spectrum of Graphene QDs. Designed for this work.

1.5.7 *Silicon*

As it is well known silicon bulk has an indirect band gap, which produces a restricted radiative recombination of electron and holes due to the mismatch between k-vectors at the minimum of the conduction band and the valence band maximum.

However, quantum confinement effects on Si QDs relaxes the wave vector matching requirement since the valence and conduction bands become discrete states. Moreover if the QD surface is well passivated avoiding any other recombination routes, silicon quantum dots can exhibit efficient size-tunable photoluminescence (PL) emission [20] with a wavelength window in the range of [700-1000] nm [39].

Relating to the synthesis method and due to the strong covalent bonding in silicon, high temperature gas-phase methods have to be applied [20] producing Si QDs that can be hydrophilic and be dispersed in water in a wide pH range [39]. Thus, Table 7 shows the main key features of these QDs. In addition, Figure 22 shows the emission spectrum that can be achieved versus the QY parameter.

<i>QD</i>	<i>Synthesis Method</i>	<i>Max diameter (nm)</i>	<i>Emission λ(nm)</i>	<i>Max QY(%)</i>	<i>REF</i>
Silicon	gas phase	5,2	700-1000	10,2	[39]

Table 7: silicon QDs parameters.

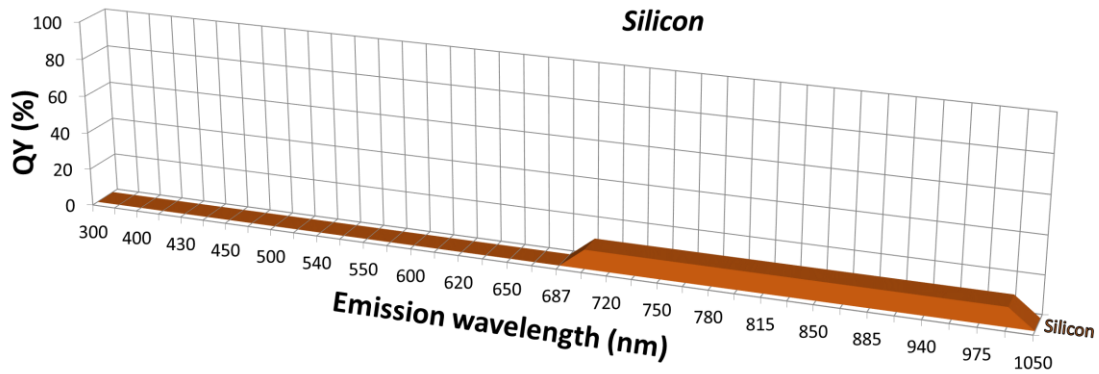


Figure 22: Emission spectrum of silicon QDs. Designed for this work.

1.5.8 Indium arsenide (InAs)

III–V QDs have historically struggled to match the high-quality optical properties of II–VI QDs [43]. Furthermore, these III–V semiconductors are widely used as light-emitting or absorbing materials in optoelectronic applications like LEDs, lasers, IR photodetectors or multijunction solar cells [42].

Relating to the synthesis method, colloidal nanocrystals are used in those applications because of their size-tunable optoelectronic properties and solution-based processing [42]. Furthermore, colloidal synthesis of III–V QDs is mainly restricted to InP and InAs. Whereas the first is widely considered as the most promising alternative to Cd-based QDs for light-emitting devices, InAs QDs cover the short-wave IR with possible applications in infrared photodetectors, photovoltaics or *in vivo* imaging [42]. Thus with the need of applications on short-wavelength infrared (SWIR), InAs quantum dots are optimal candidates to cover these wavelength range [43]. Thus, Table 8 shows the main key features of these QDs.

QD	Synthesis Method	Max diameter (nm)	Emission λ (nm)	Max QY(%)	REF
InAs	hot colloidal	3,4	700-1200	-	[42][43]
InAs/ZnS	hot colloidal	No data	900-1100	10	[43]
InAs/ZnSe	hot colloidal	No data	900-1100	10	[43]

Table 8: InAs QDs parameters.

And Figure 23 shows the emission spectra that can be achieved versus the QY parameter.

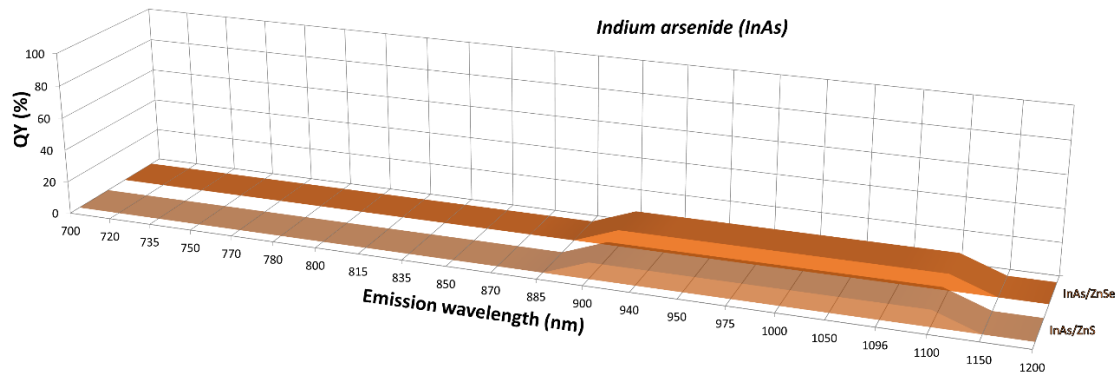


Figure 23: Emission spectra of InAs QDs. Designed for this work.

To sum up the results found previously are shown in Table 9 and Figure 24.

<i>QD</i>	<i>Synthesis Method</i>	<i>Max diameter (nm)</i>	<i>Emission λ(nm)</i>	<i>Max QY(%)</i>	<i>REF</i>
InP	hot colloidal	2,8	480-750	30	[46]
InP/ZnS	hot colloidal	6	480-735	80	[16][46]
InP/ZnSe	hot colloidal	*	510-630	50	[16]
InP/ZnSe/ZnS	heating-up	3,6	450-550	50-70	[21]
InP/ZnSeS	heating-up	4	500-540	81	[47][48]
InP/ZnSeS/ZnS	heating-up	7,4	525-607	70-82	[49][50]
CuInS ₂	hot colloidal	4	620-870	18	[22]–[24]
CuInS ₂ /ZnS	hot colloidal aqueous solution	7,1	540-815	89	[23][25][27]–[29]
Cu-In-Zn-S/ZnS	continuous flow	3,5	432-615	40	[26]
AgInS ₂	hot colloidal	4,3	770-885	63	[30][31]
AgInS ₂ /ZnS	hot colloidal, thermal, decomposition, sonochemical	12	480-815	57,6	[32]–[34]
Zn-Ag-In-Se	hot colloidal	5	660-800	50	[35]
Mn:ZnS	hot colloidal	3,8	550-600	51,3	[36][37]
Graphene	pyrolysis	4,6	415-580 800-850	54,5	[38]
Silicon	gas phase	5,2	700-1000	10,2	[39]
InAs	hot colloidal	3,4	700-1200	-	[42][43]
InAs/ZnS	hot colloidal	*	900-1100	10	[43]
InAs/ZnSe	hot colloidal	*	900-1100	10	[43]

Table 9: QDs parameter summary.

* No data

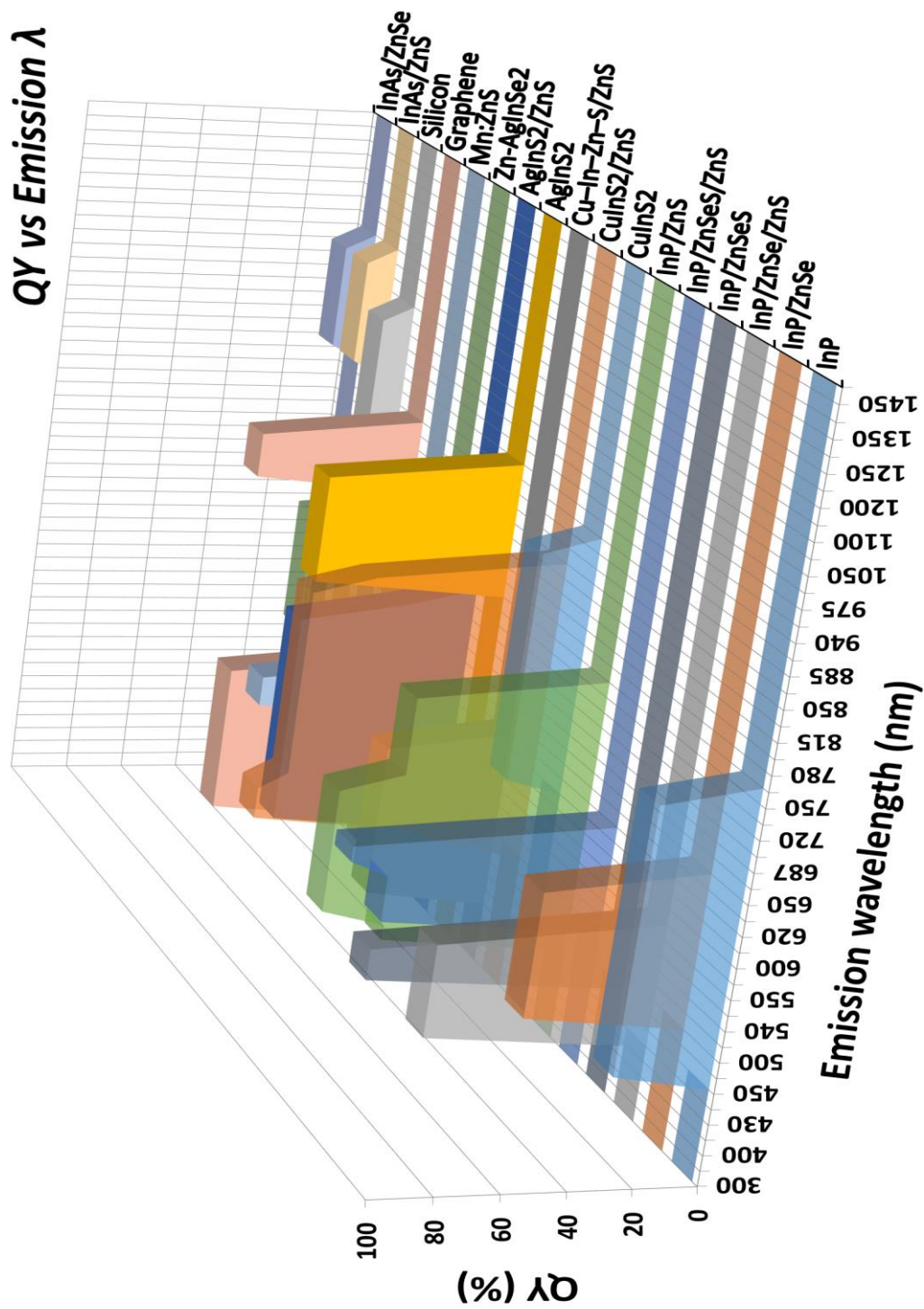


Figure 24: Emission spectra range vs QY of Cd-free QDs. Designed for this work.

1.6 FINAL QD SELECTION

Once a thoroughly study on the Cd-free materials for building the active layer of the QLED has been carried out, it is necessary to decide which ones will be the best candidates to take so as to follow the next step of this project. This decision is based on the key parameters identified, particularly on the PL QY and the range of spectral emission achievable, which is related to the size of the nanocrystal.

Firstly, it could be stated that materials like InAs and Si present a low PL QY (5%-10%) and emission wavelengths centered in the infrared. Thus, the main applications are focused on short-wavelength infrared (SWIR). Moreover, the synthesis method for SiQDs based on gas phase process is different from colloidal one, which could be a drawback to prepare this kind of QDs for mass production purposes. Besides relating to InAs synthesis methods like molecular beam epitaxy (MBE) or metal-organic vapor-phase epitaxy (MOVPE) give way to large QDs (height=5-10 nm y diameter=15-45 nm) [40], [41], [51]–[53].

On the other hand, silver indium sulfide (AgInS_2), ZnSe , Mn:ZnS and graphene could be interesting materials to take into account since the emission wavelength achieved is inside the visible spectrum. However the PL QY is lower than in other compounds like InP or CuInS_2 .

Therefore, taking into account desired key parameters like high PL QY, specific emission wavelength along with the size of the nanocrystals and the final applications from the literature, it is concluded that indium phosphide (InP) and copper indium sulfide (CuInS_2) together with their alloys in the different core/shell structures are the best candidates to form the active layer of the QLED.

Finally, the last step to take deals with the validation of the materials selected i.e. InP and CuInS_2 and their alloys to be used as qualified in the automotive field. As mentioned, GADSL will be the reference list to make the crosscheck and it is represented in Table 10. In addition, definitions from [18] are given.

The GADSL document and the reference list use two main classifications to identify regulatory status, declarable (D) and prohibited (P).

There has been some confusion in the user community over the use of the "declarable" classification.

When a substance is classified D three reason codes are possible:

D/LR: reporting is required by a regulation;

D/FA: it is being assessed by a regulatory agency for possible but not necessarily probable restriction or;

D/FI: information is being collected for a non-regulatory purpose.

In the latter two cases the substance may be removed from the list after the evaluation has been completed as is the case with several substances that were evaluated under the Canadian Chemical Challenge because it was determined that no action or restriction on use was necessary to protect human health or the environment.

Elem	CAS number	Status/Cod		Regulations	Example	Comment	Automotive compliant
InP	22398-80-7	-	-	-	-	Nil*	YES
CuInS ₂	12018-94-9	-	-	-	-	Nil	YES
CuInS	177715-14-9	-	-	-	-	Nil	YES
ZnS	1314-98-3	D/P	LR	P: Forbidden use as biocide in product-type:7 Authorisation as biocide needed for product-type:8 P: Forbidden use as biocide in product-type:9	-	-Reporting required -No biocide use	YES
ZnSe	1315-09-9	D	FI	-	-	-	YES
Cu	7440-50-8	D	FI	No current regulations but substance of concern in dispersive friction material applications due to environmental impact potential; could be subject to future regulation	Dispersive applications (Brake and Friction linings)	-No friction material use	YES
			LR	Authorisation as biocide needed for product-type 7 D: Allowed use as biocide in product-type 8 Authorisation as biocide needed for product-type 9	-	-Reporting required -No biocide use	
In	7440-74-6	-	-	-	-	Nil	YES
Zn	7440-66-6	-	-	-	-	Nil	YES
S	7704-34-9	-	-	-	-	Nil	YES

Table 10: GADSL involving QDs materials identified. Extracted from [18].

*Nil(Not in List)

Therefore it can be concluded that InP and CIS alloys can be used in the automotive field.

1.7 INP-BASED QLED

Once the two QDs candidates i.e. InP and CuInS₂ have been identified to form the active layer of the QLED, a research will be made focused on the SoA of devices (electroluminescence) which use those semiconductor materials to build the whole lighting system.

Additionally, this research will study the structure chosen (QDs and QLED layers), the solvent used, the layer deposition methods and the measurement instrumentations needed to analyze the main physical parameters from the QLED. Besides, specific figures of merit achieved like maximum brightness (cd/m²), current efficiency (cd/A), turn-on voltage (V) and external quantum efficiency (EQE) among others will be highlighted.

Back to InP based QLED three core/shell structures have been identified due to their experimental feasibility to obtain green to red emission wavelengths (similar spectrum range to Cd-based QDs) as shown below.

1.7.1 InP/ZnSe/ZnS

As seen in Table 9 the use of multishell structures around the core semiconductor material becomes essential to achieve highly-efficient photoluminescent QLEDs by improving the QY values. In this sense, cadmium-free InP/ZnSe/ZnS multishell QDs can be employed to achieve real electroluminescent (EL) devices with luminance up to 2751 cd/m² [54], [55] and current efficiency from 1 to 5.1 cd/A [56]–[58].

The passivation of InP QDs with a ZnSe/ZnS multishell assembly results in an improved recombination efficiency due to the lattice mismatch reduction between the shells and the core. Thus the ZnSe shell acts as a buffer layer between InP (core) and ZnS (external shell) to provide a smoother interface with fewer defects and thus less non-radiative recombination pathways since the ZnSe lattice constant of 5.67Å is just in between the lattice constants of InP with 5.87Å and ZnS with 5.41 Å [56].

Moreover, by having a thicker ZnS outer shell from QDs, two of the main issues of QLED like the luminescence quenching as well as QD charging can be suppressed due to the strong confinement produced which implies an improvement of the lighting device performance [59].

Therefore, Table 11 and Table 12 below show different numbered experimental constructions of InP/ZnSe/ZnS based QLEDs presenting both the structure chosen for the device and the figures of merit which give the performance of the lighting system.

InP/ZnSe/ZnS												
	Solvent*	Structure**	Layers									R E F
			Substrate	Anode	HIL	HTL	EBL	QD	HL	ETL	Cathode	
1	Toluene Chloroform or Alkanes	N	Glass	ITO	PEDOT:PSS	Poly-TPD	-	InP/ZnSe/ZnS	-	TPBI	Ca/Ag	[56]
2	Nonane	I	Glass	Ag	MoO ₃	TCTA	-		PEI	Al:ZnO NPs	ITO	[60]
3	Nonane or Hexane	N	Glass	ITO	PEDOT:PSS	Poly-TPD	-		-	TPBi	LiF/Al	[59]
4	Nonane	N	PEN	ITO	PEDOT:PSS	Poly-TPD	-		-	TPBi	LiF/Al	[57]
5	Nonane	I	Glass	Al	MoO ₃	CBP	-		-	ZnO	ITO	[54] [55]
6	Nonane	I	Glass	Al or IZO	MoO ₃	CBP or TAPC	-		-	ZrO ₂ NPs	ITO	[58]

Table 11: InP/ZnSe/ZnS based QLED structures. First column refers to specific (numbered) QLED configuration.

*Final solvent for QDs before depositing and building the QLED

**N=normal structure. I= inverted structure (inverted device structure is useful for directly applying QD-LEDs to the well-developed large size active-matrix (AM) OLED technology [60].

DEFINITIONS:

- PEN: polyethylene naphthalate. It is used to achieve flexible substrates.
- Ag: Silver
- ITO: Indium tin oxide
- IZO: Indium zinc oxide. It is used to achieve transparent electrodes.
- PEDOT:PSS: poly(3,4-ethylenedioxythiophene) polystyrene sulfonate
- MoO₃: molybdenum oxide
- Poly-TPD: Poly(4-butylphenyl-diphenyl-amine)
- TCTA: 4,4',4'-Tris(carbazol-9-yl)triphenylamine
- CBP: 4,4A-N,NA-dicarbazole-biphenyl
- TAPC: 4,4'-cyclohexylidenebis[N,N-bis(4-methylphenyl) benzenamine]
- PEI: polyethylenimine. It is used as an interfacial dipole layer.
- TPBi: 2,2',2''-(1,3,5-Benzinetriyl)-tris(1-phenyl-1-H-benzimidazole)
- Al:ZnO NPs: aluminum doped ZnO Nanoparticles
- ZnO: Zinc oxide
- ZrO₂ NPs: Zirconium dioxide Nanoparticles:
- Ca/Ag: Calcium and silver
- LiF/Al: Lithium fluoride and Aluminium

The layer deposition methods used are spin coating and thermal evaporation. These kinds of techniques are described in detail in block BL3.

The figures of merit for InP/ZnSe/ZnS-based QLED which give the yield and performance of the lighting system are shown in Table 12.

InP/ZnSe/ZnS											
	Max brightness (cd/m ²)	Current Efficiency (cd/A)	Turn-on voltage (V)	EQE (%)	Max QY (%)	Emission λ (nm)		FWHM (nm)		Size (nm)	REF
						PL	EL	PL	EL		
1	448(G)	1,5	3,7	-	44	507	521	46	53	2,0	[56]
	1806(Y)	5,1			42	560	573	55	58	4,4	
	1710(R)	1,8			65	618	625	77	76	6,9	
2	466(G)	3,17	2,5	-	50	554	565	62	-	-	[60]
3	1960(G)	3,32	2,4	-	40	540	555	52	56	2,5	[59]
	2430(G)	4,65	3,3					54		2,9	
4	640(G)	1	-	-	45	545	555	50	-	-	[57]
5	2751(G)	1,89	2,5	-	-	-	555	-	-	-	[54]
											[55]
6	530(G)	1	9	-	-	586	600	74	74	5,5	[58]
	200(G)*	0,47*	10								

Table 12: InP/ZnSe/ZnS based QLED figures of merit. First column refers to specific (numbered) QLED configuration.

*With transparent electrode

DEFINITIONS:

- G, Y, R: Green, Yellow, Red.
- EQE: External quantum efficiency.
- SIZE: the diameter of the whole QD (multishell) i.e. core/shell is measured. Thus depending on the experimental implementation the size of the shells can differ from one implementation to the other.

The measurement instrumentation used to obtain those figures of merit are thoroughly described in chapters BL2, BL3 and BL5.

1.7.2 InP/ZnSeS

Following the same core/shell structure of QDs it is possible to achieve high efficient QLEDs showing EQE of 3.46% and brightness up to 3900 cd/m² by using InP/ZnSeS as active layer [48].

This efficient exciton recombination is due, among other effects, to ZnSeS composition-gradient shells, which give values of PL QY of 81% using monolayers of ZnSeS alloy layers. The thickness of ZnSeS shells provides a potential barrier from the defect states, which results in a tuned device structure along with the protection of excitons from quenching by surface defect states enhancing, therefore, the radiative recombination of electrically generated excitons [48]. Moreover it is important to state that the inverted device structure with hybrid (organic and inorganic) charge-transport layers is known to be particularly useful to optimize the carrier transport in QLEDs [48].

Thus, as done previously, Table 13 and Table 14 show different experimental constructions of InP/ZnSeS based QLEDs presenting both the structure and the figures of merit of the system.

InP/ZnSeS												
	Solvent	Structure	Layers									REF
			Substrate	Anode	HIL	HTL	EBL	QD	HBL	ETL	Cathode	
7	-	N	Glass	ITO	-	Poly-TPD	-	InP/ZnSeS	-	TPBi	LiF/Al	[47]
8	Hexane	I	Glass	Al	MoO ₃	TCTA			-	ZnO+PFN	ITO	[48]

Table 13: InP/ZnSeS based QLED structures. First column refers to specific (numbered) QLED configuration.

DEFINITIONS:

- PFN: poly-[(9,9-bis(30-(N,N-dimethylamino)propyl)-2,7-fluorene)-alt-2,7-(9,9- ioctylfluorene)]. It is used at the interface of ZnO with InP@ZnSeS QDs to reduce the electron injection barrier. The PFN, conjugated polyelectrolyte, serves as an interfacial dipole layer and it is known to achieve a vacuum level shift over 0.5 eV [48].

The figures of merit for InP/ZnSeS-based QLED are presented in Table 14

InP/ZnSeS											
	Max brightness (cd/m ²)	Current Efficiency (cd/A)	Turn-on voltage (V)	EQE (%)	Max QY (%)	Emission λ (nm)		FWHM (nm)		Size (nm)	REF
						PL	EL	PL	EL		
7	700(G)	-	4,5	0,26	-	-	550	-	55	4,0	[47]
8	3900(G)	10,9	2,2	3,46	81	500	520	50	65	2,8	[48]

Table 14: InP/ZnSeS based QLED figures of merit. First column refers to specific (numbered) QLED configuration.

1.7.3 InP/ZnSeS/ZnS

The multishell structure of InP/ZnSeS/ZnS is introduced. As shown in Table 9 it is possible to achieve a QY of 80% for QDs made of core/shell structure of InP/ZnS [16], [46]. However when the thickness of the ZnS shell is gradually increased, the strong lattice strain of the ZnS shell on the InP core crystal causes lattice defects and low PL [49]. Thus it is possible to decrease that lattice mismatch between InP and Zns by introducing a buffer layer of ZnSeS resulting in a multishell QDs formed by InP/ZnSeS/ZnS with an enhanced stability [49].

Likewise it is remarkable to say that the use of inorganic nanoparticles as electron transport layer like (ZnMgO or ZnO) can reduce the electron injection barrier between the electron transport layer and the QD-emitting layer [49], [50] giving way to an efficient QLED. Thus, Table 15 shows the different experimental constructions.

InP/ZnSeS/ZnS												
	Solvent	Structure	Layers									R E F
			Substrate	Anode	HIL	HTL	EBL	QD	HBL	ETL	Cathode	
9	Octane	I	Glass	Al	HATCN	NPB	TcTa	InP/ZnSeS/ZnS	-	ZnMgO NPs	ITO	[49]
10	Hexane	N	Glass	ITO	PEDOT	PVK or TFB	-	InP/ZnSeS/ZnS	-	ZnO NPs	Al	[50]

Table 15: InP/ZnSeS/ZnS based QLED structures. First column refers to specific (numbered) QLED configuration.

DEFINITIONS:

- HATCN: Dipyrazino[2,3-f:2',3'-h]quinoxaline-2,3,6,7,10,11-hexacarbonitrile
- NPB: N,N'-di(1-naphthyl)-N,N'-diphenyl-(1,1'-biphenyl)-4,4'-diamine
- TcTa: Tris(4-carbazoyl-9-ylphenyl) amine
- PVK: poly(9-vinylcarbazole)
- TFB: poly[(9; 9-dioctylfluorenyl-2; 7-diyl)-co-(4; 4'-(N-(4-sec-butylphenyl))diphenyl-amine)

The figures of merit for InP/ZnSeS/ZnS-based QLED are presented in Table 16.

InP/ZnSeS/ZnS											
	Max brightness (cd/m ²)	Current Efficiency (cd/A)	Turn-on voltage (V)	EQE (%)	Max QY (%)	Emission λ (nm)		FWHM (nm)		Size (nm)	REF
						PL	EL	PL	EL		
9	10490(G)	4,4	2,2	1,5	70	525	545	65	-	7,4	[49]
10	2849(R)	4,2	-	2,5	82	607	614	63	-	7,2	[50]

Table 16: InP/ZnSeS/ZnS based QLED figures of merit. First column refers to specific (numbered) QLED configuration.

Finally, all QLED structures and the figures of merit are summarized in Table 17 and Table 18.

InP/ZnSe/ZnS												
	Solvent	Structure	Layers									R E F
			Substrate	Anode	HIL	HTL	EBL	QD	HBL	ETL	Cathode	
1	Toluene Chloroform or Alkanes	N	Glass	ITO	PEDOT:PSS	Poly-TPD	-	InP/ZnSe/ZnS	-	TPBI	Ca/ Ag	[56]
2	Nonane	I	Glass	Ag	MoO ₃	TCTA			PEI	Al:ZnO NPs	ITO	[60]
3	Nonane or Hexane	N	Glass	ITO	PEDOT:PSS	Poly-TPD	-		-	TPBi	LiF/ Al	[59]
4	Nonane	N	PEN	ITO	PEDOT:PSS	Poly-TPD	-		-	TPBi	LiF/ Al	[57]
5	Nonane	I	Glass	Al	MoO ₃	CBP	-		-	ZnO	ITO	[54] [55]
6	Nonane	I	Glass	Al or IZO	MoO ₃	CBP or TAPC	-		-	ZrO ₂ NPs	ITO	[58]
InP/ZnSeS												
	Solvent	Structure	Layers									R E F
			Substrate	Anode	HIL	HTL	EBL	QD	HBL	ETL	Cathode	
7	-	N	Glass	ITO	-	Poly-TPD	-	InP/ZnSeS	-	TPBi	LiF/Al	[47]
8	Hexane	I	Glass	Al	MoO ₃	TCTA	-		-	ZnO+PFN	ITO	[48]
InP/ZnSeS/ZnS												
	Solvent	Structure	Layers									R E F
			Substrate	Anode	HIL	HTL	EBL	QD	HBL	ETL	Cathode	
9	Octane	I	Glass	Al	HATCN	NPB	TcTa	InP/ZnSeS/ZnS	-	ZnMgO NPs	ITO	[49]
10	Hexane	N	Glass	ITO	PEDOT	PVK or TFB	-		-	ZnO NPs	Al	[50]

Table 17: Summary of InP-based QLED structures. First column refers to specific (numbered) QLED configuration.

InP/ZnSe/ZnS											
	Max brightness (cd/m ²)	Current Efficiency (cd/A)	Turn-on voltage (V)	EQE (%)	Max QY (%)	Emission λ (nm)		FWHM (nm)		Size (nm)	REF
						PL	EL	PL	EL		
1	448(G) 1806(Y) 1710(R)	1,5 5,1 1,8	3,7	-	44 42 65	507 560 618	521 573 625	46 55 77	53 58 76	2,0 4,4 6,9	[56]
2	466(G)	3,17	2,5	-	50	554	565	62	-	-	[60]
3	1960(G) 2430(G)	3,32 4,65	2,4 3,3	-	40	540	555	52 54	56	2,5 2,9	[59]
4	640(G)	1	-	-	45	545	555	50	-	-	[57]
5	2751(G)	1,89	2,5	-	-	-	555	-	-	-	[54] [55]
6	530(G) 200(G)*	1 0,47*	9 10	-	-	586	600	74	74	5,5	[58]
InP/ZnSeS											
	Max brightness (cd/m ²)	Current Efficiency (cd/A)	Turn-on voltage (V)	EQE (%)	Max QY (%)	Emission λ (nm)		FWHM (nm)		Size (nm)	REF
						PL	EL	PL	EL		
7	700(G)	-	4,5	0,26	-	-	550	-	55	4,0	[47]
8	3900(G)	10,9	2,2	3,46	81	500	520	50	65	2,8	[48]
InP/ZnSeS/ZnS											
	Max brightness (cd/m ²)	Current Efficiency (cd/A)	Turn-on voltage (V)	EQE (%)	Max QY (%)	Emission λ (nm)		FWHM (nm)		Size (nm)	REF
						PL	EL	PL	EL		
9	10490(G)	4,4	2,2	1,5	70	525	545	65	-	7,4	[49]
10	2849(R)	4,2	-	2,5	82	607	614	63	-	7,2	[50]

Table 18: Summary of InP-based QLED figures of merit. First column refers to specific (numbered) QLED configuration.

NB: SIZE: The diameter of the whole QD (multishell) i.e. core/shell is measured. Thus depending on the experimental implementation the size of the shells can differ from one implementation to the other.

1.8 CIS-BASED QLED

Once InP-based QLEDs have been studied, the project is focused now on the second material candidate taken from the literature i.e. CuInS₂ to build the lighting device. Following the same procedure as it has been adopted for InP, two QLED core/shell structures have been identified: CuInS₂/ZnS and Cu-In-Zn-S/ZnS.

As seen in Table 9, the use of CuInS₂ QDs gives an opportunity for lighting device manufacturing due to the fact that they can cover the spectral wavelength of [432-870] nm with high quantum yields up to 89%.

1.8.1 CuInS₂/ZnS

Furthermore, the use of core/shell structure becomes vital to achieve high QY values which give a final figure of merit of the QLED brightness of 8735 cd/m² [61] and a current efficiency from 2.53 to 9.43 cd/A [61], [62] for CuInS₂/ZnS-based QLEDs.

Besides, some issues like the thickness of the QD emission layer [62] or the low efficiency of charge injection from charge transport layers to the QD emitting layer [61] are determinant in the electroluminescent (EL) performance.

Therefore, Table 19 shows two experimental constructions of CuInS₂/ZnS-based QLEDs presenting the structure chosen for the device.

CuInS ₂ /ZnS												
	Solvent*	Structure**	Layers									R E F
			Substrate	Anode	HIL	HTL	EBL	QD	HBL	ETL	Cathode	
11	Hexane	N	Glass	ITO	PEDOT:PSS	PVK	-	CuInS ₂ /ZnS	-	ZnO NPs	Al	[62]
12	Ethanol	I	Glass	Al	MoO ₃	TCTA	CBP	CuInS ₂ /ZnS	-	ZnO	ITO	[61]

Table 19: CuInS₂/ZnS based QLED structures. First column refers to specific (numbered) QLED configuration.

*Final solvent for QDs before depositing and building the QLED

**N=normal structure. I= inverted structure (inverted device structure is useful for directly applying QD-LEDs to the well-developed large size active-matrix (AM) OLED technology.

The figures of merit for CuInS₂/ZnS-based QLED which give the yield and performance of the lighting system are presented in Table 20.

CuInS ₂ /ZnS											
	Max brightness (cd/m ²)	Current Efficiency (cd/A)	Turn-on voltage (V)	EQE (%)	Max QY (%)	Emission λ (nm)		FWHM (nm)		Size (nm)	REF
						PL	EL	PL	EL		
11	1564(Y)	2,52	5	1,1	65	580	603	114	114	3,2	[62]
12	8735(Y)	9,43	3,75	3,2	70	560	580	100	100	3,1	[61]

Table 20: CuInS₂/ZnS based QLED figures of merit. First column refers to specific (numbered) QLED configuration.

1.8.2 Cu-Zn-In-S/ZnS

The second core/shell structure of Cu-Zn-In-S/ZnS is analyzed. As shown in Table 9 it is possible to achieve a QY of 40% for Cu-In-Zn-S/ZnS QDs with a PL emission that ranges from 432 nm to 615 nm [26]. In the following particular QLED maximum values of brightness of 3071 cd/m² for yellow color with 7.71 cd/A of current efficiency are achieved [63].

One particular Cu-Zn-In-S/ZnS based QLED found in the literature [63] has been analyzed and presented in Table 21.

Cu-Zn-In-S/ZnS											
	Solvent	Structure	Layers								
			Substrate	Anode	HIL	HTL	EBL	QD	HBL	ETL	Cathode
13	Toluene Ethanol	N	Glass	ITO	PEDOT:PSS	TFB	-	Cu-In-Zn-S/ZnS	-	ZnO	Al

Table 21: Cu-Zn-In-S/ZnS based QLED structures. First column refers to specific (numbered) QLED configuration.

*Final solvent for QDs before depositing and building the QLED

**N=normal structure. I= inverted structure (inverted device structure is useful for directly applying QD-LEDs to the well-developed large size active-matrix (AM) OLED technology.

The figures of merit for Cu–Zn–In–S/ZnS-based QLED, which give the yield and performance of the lighting system are presented in Table 22.

Cu–Zn–In–S/ZnS											
13	Max brightness (cd/m ²)	Current Efficiency (cd/A)	Turn-on voltage (V)	EQE (%)	Max QY (%)	Emission λ (nm)		FWHM (nm)		Size (nm)	REF
						PL	EL	PL	EL		
						520	540	80	-		
	1100(G)	0.84	2,0	0,25	-	-	552	-	-	-	[63]
	3061(Y)	7.71	1,8	2,42	-	-	552	-	-	-	[63]
	1247(R)	1.16	2,0	0,91	-	640	642	120	-	-	[63]

Table 22: Cu–Zn–In–S/ZnS based QLED figures of merit. First column refers to specific (numbered) QLED configuration.

Finally all QLED structures and the figures of merit are summarized in Table 23 and Table 24.

CuInS ₂ /ZnS												
11	Solvent	Structure	Layers									R E F
			Substrate	Anode	HIL	HTL	EBL	QD	HBL	ETL	Cathode	
			Glass	ITO	PEDOT:PSS	PVK	-	CuInS ₂ /ZnS	-	ZnO NPs	Al	
12	Ethanol	I	Glass	Al	MoO ₃	TCTA	CBP	CuInS ₂ /ZnS	-	ZnO	ITO	[61]
Cu–Zn–In–S/ZnS												
13	Solvent	Structure	Layers									R E F
			Substrate	Anode	HIL	HTL	EBL	QD	HBL	ETL	Cathode	
			Glass	ITO	PEDOT:PSS	TFB	-	Cu–Zn–In–S/ZnS	-	ZnO	Al	

Table 23: Summary of CIS-based QLED structures. First column refers to specific (numbered) QLED configuration.

CuInS ₂ /ZnS											
	Max brightness (cd/m ²)	Current Efficiency (cd/A)	Turn-on voltage (V)	EQE (%)	Max QY (%)	Emission λ (nm)		FWHM (nm)		Size (nm)	REF
						PL	EL	PL	EL		
11	1564(Y)	2,52	5	1,1	65	580	603	114	114	3,2	[62]
12	8735(Y)	9,43	3,75	3,2	70	560	580	100	100	3,1	[61]
Cu–Zn–In–S/ZnS											
	Max brightness (cd/m ²)	Current Efficiency (cd/A)	Turn-on voltage (V)	EQE (%)	Max QY (%)	Emission λ (nm)		FWHM (nm)		Size (nm)	REF
						PL	EL	PL	EL		
13	1100(G)	0.84	2,0	0,25	-	520	540	80	-	-	[63]
	3061(Y)	7.71	1,8	2,42	-	-	552	-	-	-	
	1247(R)	1.16	2,0	0,91	-	640	642	120	-	-	

Table 24: Summary of CIS-based QLED figures of merit. First column refers to specific (numbered) QLED configuration.

1.9 CONCLUSIONS

Relating to InP-based QLED, it can be stated that the QD configuration n°:9 of InP/ZnSeS/ZnS from Table 15 and Table 16 seems to be the most suitable to manufacture a QLED. The choice is based on the maximum brightness achieved of 10490 cd/m² due mainly to the better quantum confinement, along with the good recombination in the core, thanks to the low mismatch between InP and ZnS when ZnSeS is used as a buffer layer [49]. However other configurations could give good brightness values of 3900 cd/m² [48] for InP/ZnSeS or 2751 cd/m² [54], [55] for InP/ZnSe/ZnS. These values are in line with the higher efficient Cd-based QLEDs and also the current market OLEDs. It is worth saying that all these brightness values are achieved for green color with a current efficiency range from 0.47 to 10.9 cd/A.

Moreover turn-on voltage can vary from 2.2 to 10 volts depending on the layer structure of the final device which is in line with current LEDs and OLEDs. Moreover the narrow bandwidth shown and the possibility to tune the emission spectra from green to red color make the device quite attractive for different fields like the automotive one.

On the other hand CIS-based QLED configuration n°:12 (CuInS₂/ZnS) from Table 19 and Table 20, seems to be the best choice among the QDs structures introduced. A brightness of 8735 cd/m² with a current efficiency of 9.43 cd/A and a EQE of 3.2% [61] offers a good choice to manufacture a QLED.

However, it is true that not many configurations have been found in the literature compared to InP-based QLED. It makes us think that more efforts in Cd-free lighting devices are put on InP as base material for the emitting layer instead of CIS in spite of the good performance that CIS-based QLEDs can achieve. When comparing figures of merit between both materials it is possible to obtain the conclusion that one of the reasons is the large FWHM values that CIS QLEDs (~100nm) exhibit, probably because of the radiative transitions in donor-acceptor levels and/or the emission from surface defects sites [40]. In fact, it can be twice the InP(~50nm) FWHM what experimentally implies that InP shows a purer color than CIS-based QLEDs. Therefore at a first glance it can be concluded that InP material is more suitable than CIS to build displays and therefore, efforts were made to achieve InP-based QLEDs instead of CIS ones [58].

Indeed, as extracted from [61] some issues still hinder the development of CIS-based QDs for electroluminescence (EL) devices:

- (i) low efficiency of charge injection from charge transport layers to the QD emitting layer.
- (ii) exciton quenching caused by accumulated space charges near the interface between the charge transport layer and QDs.
- (iii) layer intermixing of neighboring layers during the solution process.

Nevertheless, according to Table 23 and Table 24 it seems that it is easier to achieve deeper red color with CIS QDs, which can result in a good advantage for the design of state-of-the-art automotive lighting systems, particularly taillight applications [7], [64]. Moreover, the purity of the color in this automotive field (exterior and interior lighting) relating to FWHM values might not be so critical comparing to electronic consumer displays and therefore great attention should be drawn to CIS QDs as emitting layer to form the QLED.

Relating to the QLED structure, the good selection of the material to conform the different layers of the device for both InP and CIS materials becomes essential. The objective is to obtain the best heterojunction band diagram to enable the highest recombination rate at the core of the QD active layer and the balance charge injected from cathode and anode [58].

According to the Schottky-Mott rule [65] the injection efficiency of the diodes is mainly determined by the potential barrier height i.e. the difference of the lowest unoccupied molecular orbital (LUMO) (for electron injection) or the highest occupied molecular orbital (HOMO) (for hole injection) between the adjacent semiconductor layers [61]. Therefore, the selection of electron and holes injection and transport layers like ZnMgO or ZnO materials along with the blocking electron and hole film are vital to the performance of the whole system.

Moreover, most of QDs are presented in alkane solvent like nonane or hexane or another chemical component like toluene or ethanol due to the compatibility with the other layers when conforming in the deposition method process the lighting device.

Furthermore, the inverted structure of the QLED, in which the cathode is placed on the substrate and may be connected to the drain of an n-channel, offers the possibility to make it compatible with the well-known large size active-matrix (AM) OLED technology [60].

Likewise, the substrate normally chosen is glass although flexible applications can be built by using polyethylene naphthalate (PEN). In addition, transparent electrodes can be made by using indium zinc oxide (IZO).

Finally, since a lighting application for the automotive field is pursued, it would be highly recommended to make an inorganic approach for all layers of the QLED (not only the active layer) due to the harsh environmental conditions and extreme temperature profiles found. In this sense the stability and the lifetime of the lighting device would be enhanced by using inorganic layers in the QLED.

Generally, we could state that an extensive study on the optimal Cd-free QDs to be used in the automotive field has been carried out, identifying InP and CuInS₂ together with their alloys in the different core/shell structures as qualified materials to form the active layer of the automotive QLED device. As already highlighted, this point is essential as the automotive field has restrictive international norms like RoHS & GADSL relating to the allowed materials to be introduced in automotive products.

2 BL2 – QUANTUM DOTS

2.1 SCOPE

Quantum dots are the key elements behind the whole project developed. Additionally, as it can be extracted from block BL1 after a literature research, two main core QDs materials have been identified i.e. **InP** and **CuInS₂** as suitable materials which could be used for lighting devices.

Therefore, the next step to be taken is to deeply study these kinds of QDs. In order to carry out this task, several samples of both InP and CuInS₂ commercial quantum dots have been acquired to experimentally measure the main parameters and confirm what is expected from both literature (BL1) and QD datasheet. The objective is to select the suitable one, along with the configuration core/shell to be used, for integrating in the automotive QLED device.

Finally, once the latter selection is made, the experimental synthesization of those identified colloidal QDs is also performed to compare, after a nanoparticles characterization, both synthesization processes relating to key QDs parameters like QY or emission spectrum.

2.1.1 Research Plan

Having a look into the research plan defined at the beginning of the PhD project, it is possible to depict graphically the location level of this block inside the bottom-up methodology presented.

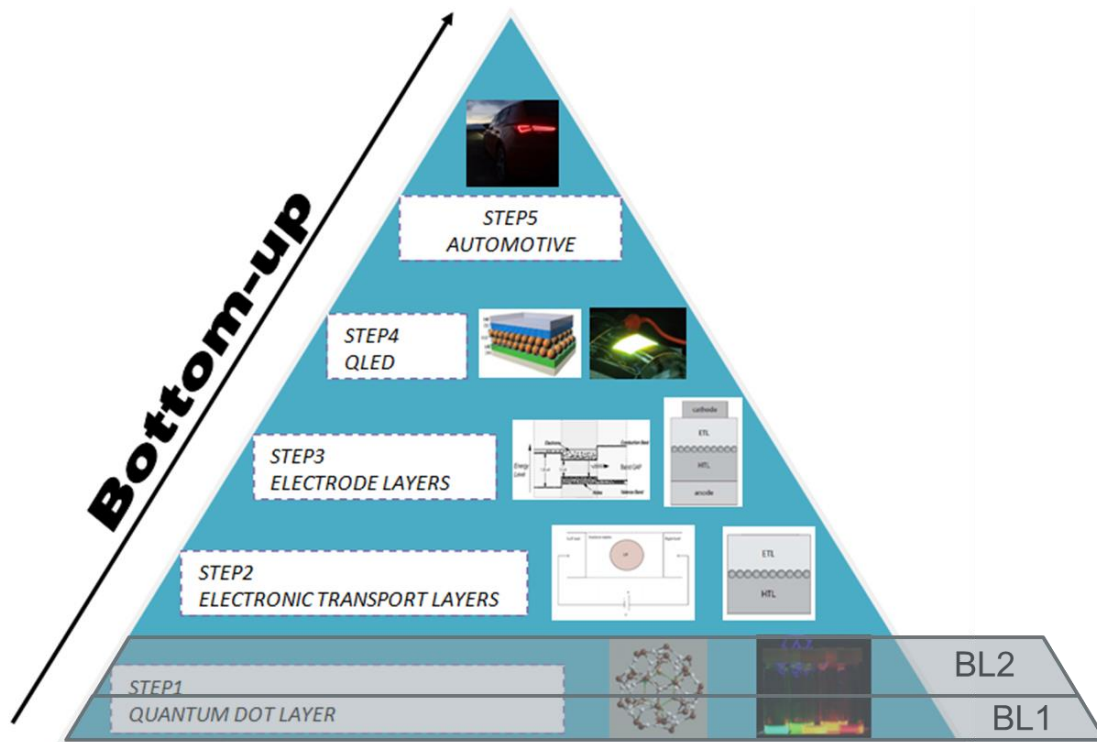


Figure 25: Block BL2. BOTTOM-UP methodology.

2.2 QD CHARACTERIZATION

As it has been explained in the scope of chapter 2.1, once the two candidates to conform the active layer of the QLEDs i.e. InP and CuInS₂ have been selected, some experimental measurements will be performed to confirm the QD features relating to its applicability to the lighting field (size, absorption/emission spectrum, quantum yield and FWHM). Thus, different commercial quantum dots samples have been requested from a nanotech supplier. The same shell structure has been selected i.e. ZnS so that it can be compared to **InP/ZnS** and **CuInS₂/ZnS** samples at the same emission peak wavelength. At the end of this experiment, it will be possible to assess both elements (InP and CuInS₂) from an experimental point of view and compare the data provided by the nanotech supplier.

2.2.1 Goals

By performing this experiment, the following data from QDs in colloidal solutions want to be extracted:

- a) QDs size
- b) Absorption spectrum
- c) Emission spectrum
- d) FWHM
- e) PL quantum yield

This experiment has been carried out at Universidad de Granada (UGR), particularly in the laboratories of the Centro de Instrumentación Científica (CIC), Facultad de Ciencias in the organic chemistry laboratory and in the Molecular and Nanoscale Physics Department at the University of Leeds (UoL).

2.2.2 Experimental Units

Quantum dots in colloidal solutions (CQD) will be the experimental units to be analyzed. Three samples of InP/ZnS QDs core/shell structure in toluene solvent and three samples of CuInS₂/ZnS QDs core/shell structure in toluene solvent were provided. Each sample is formed by 10 mg of QDs with a concentration of 5 mg/ml of toluene solvent, which is equal to a total volume of 2 ml. These samples have been commercially acquired from Mesolight® and NN-Crystal®, two nanotechnology companies specialized in producing nanomaterials.

Likewise, the difference of each three samples, formed by the same material, is based on the emission peak wavelength. The objective is to build up a QD-demonstrator as it will be shown in BL5. However, although three main colors i.e. green, yellow and red were available, output emission centered on red color of the visible spectrum will be analyzed. The justification of that choice is based on chapter 1.9 as a conclusion of the use of CuInS₂ as core material to achieve deep red wavelength in the automotive field and BL5 where the particular automotive application is deeply assessed.

2.2.3 Supplier datasheet

Furthermore, the data provided by the two suppliers presented in 2.2.2 in the product datasheet for red color are shown in Figure 26, Figure 27, Figure 28 and Figure 29.

SUPPLIER1 (S1): Mesolight®

- QD material: **CuInS₂/ZnS**
- Emission photoluminescence peak (PL): 611 nm
- Full Width at Half Maximum (FWHM): 107 nm
- Quantum Yield (QY): 43%
- QD size: not given by supplier
- Absorption & Emission spectrum:

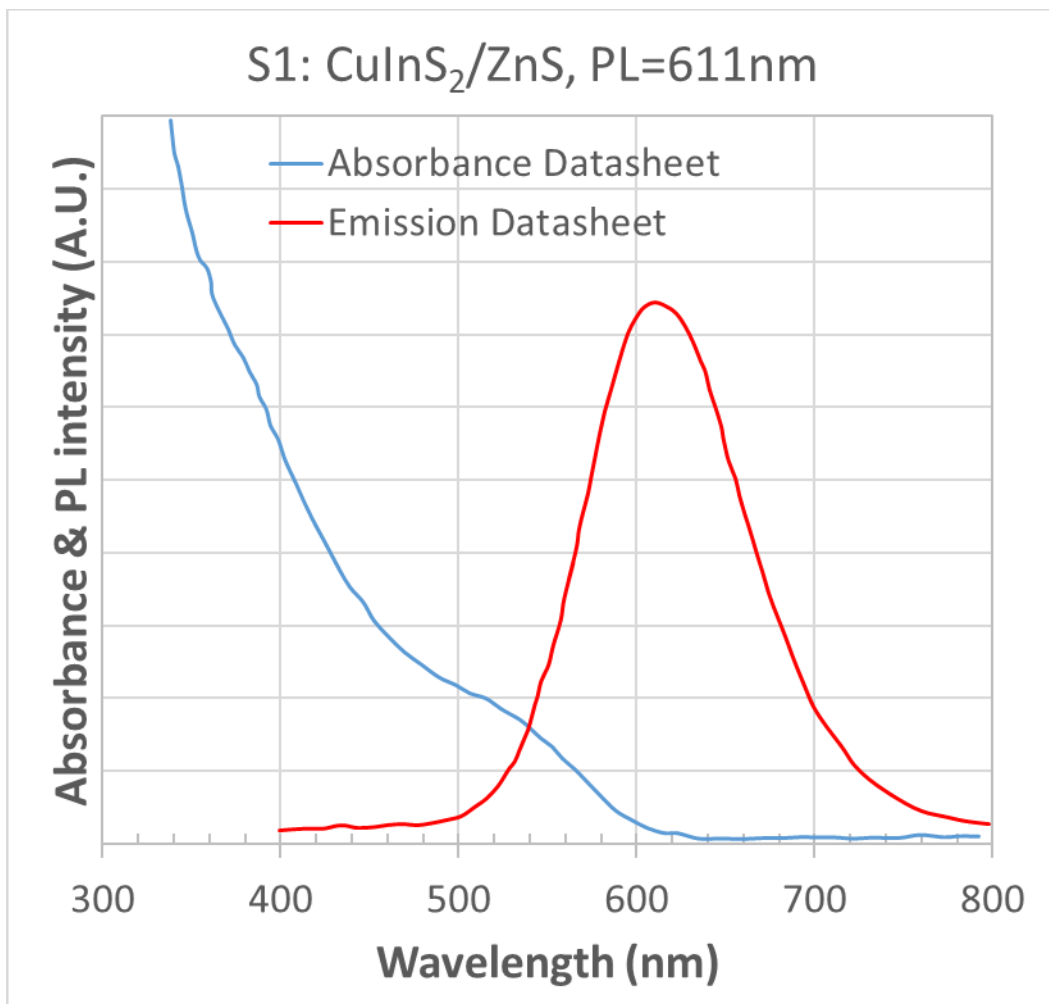


Figure 26: Supplier1 (S1): CuInS₂/ZnS absorption & emission spectrum. Adapted for this work.

SUPPLIER1: Mesolight®

-QD material: **InP/ZnS**

-Emission photoluminescence peak (PL): 617 nm

-Full Width at Half Maximum (FWHM): 49 nm

-Quantum Yield (QY): 55%

-QD size: not given by supplier.

-Absorption & Emission spectrum:

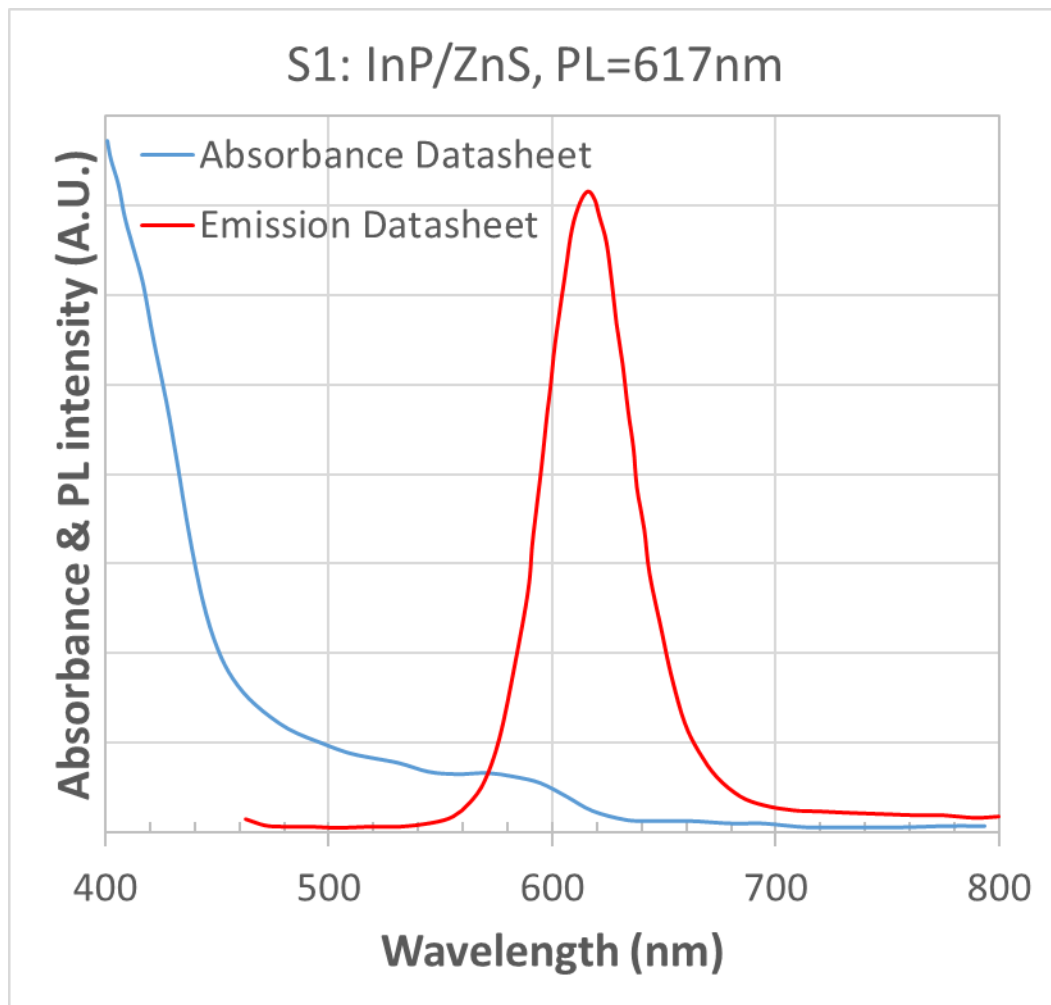


Figure 27: Supplier1 (S1): InP/ZnS absorption & emission spectrum. Adapted for this work.

SUPPLIER2 (S2): NN-Crystal®

-QD material: **CuInS₂/ZnS**

-Emission photoluminescence peak (PL): (620±15) nm

-Full Width at Half Maximum (FWHM): 99 nm

-Quantum Yield (QY): 20%

-QD size:

Core diameter=(3.3±0.5) nm

Shell thickness=(2.3±0.5) nm (Thickness of shell is expressed as total diameter added to core)

Total diameter=(5.5±0.5) nm

-Absorption & Emission spectrum:

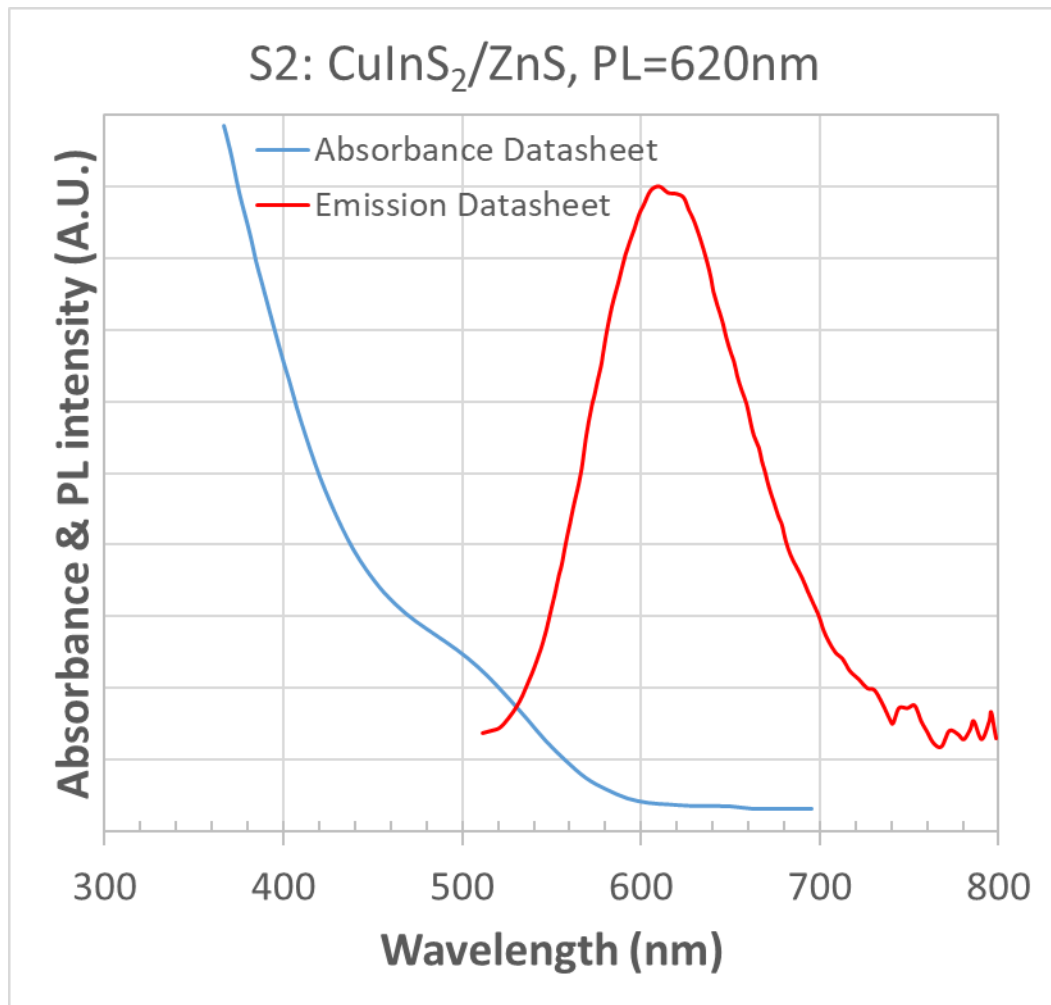


Figure 28: Supplier2 (S2): CuInS₂/ZnS absorption & emission spectrum. Adapted for this work.

SUPPLIER2: NN-Crystal®

-QD material: **InP/ZnS**

-Emission photoluminescence peak (PL): (620 ± 15) nm

-Full Width at Half Maximum (FWHM): $(58-70)$ nm

-Quantum Yield (QY): $>20\%$

-QD size:

Core diameter= (3.9 ± 0.5) nm

Shell thickness= (1 ± 0.5) nm (Thickness of shell is expressed as total diameter added to core)

Total diameter= (5.0 ± 0.5) nm

-Absorption & Emission spectrum:

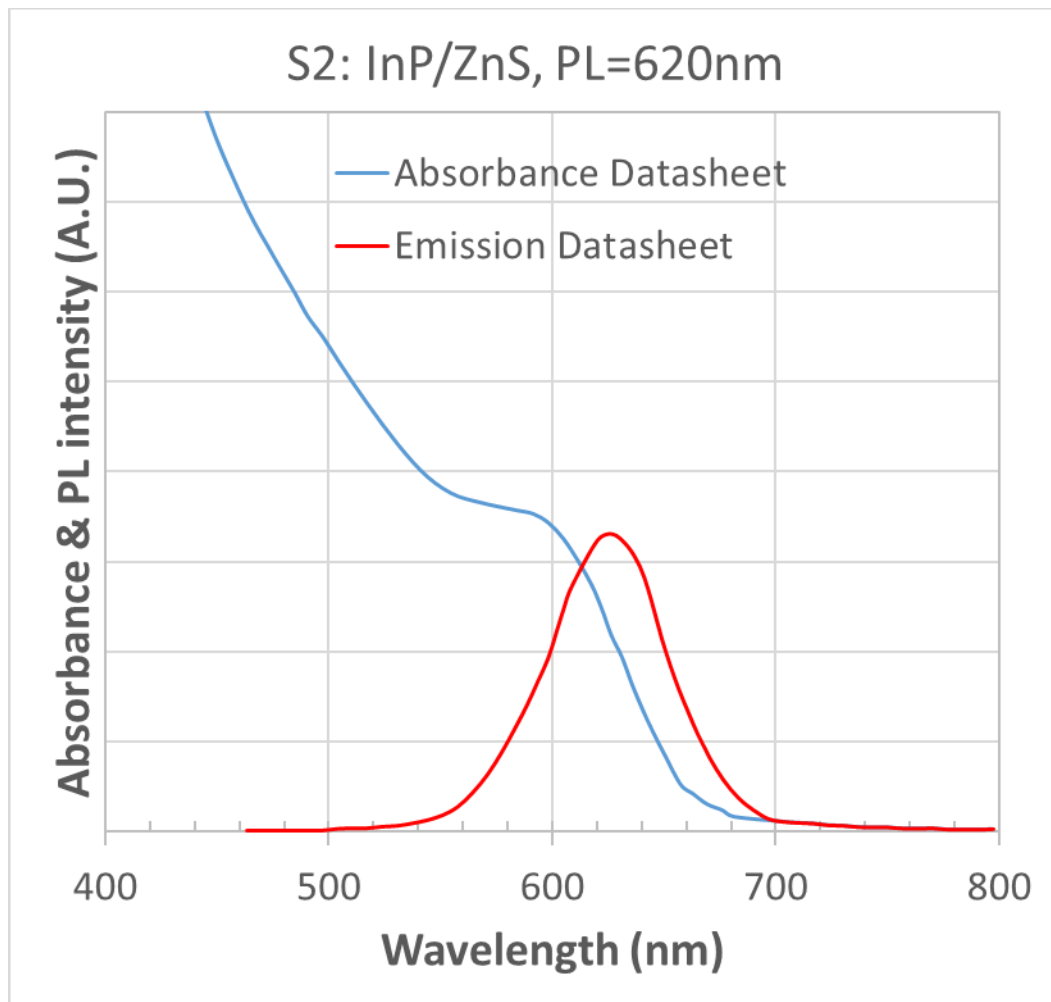


Figure 29: Supplier2 (S2): InP/ZnS absorption & emission spectrum. Adapted for this work.

Summary

<i>CuInS₂/ZnS QDs</i>	<i>PL peak(nm)</i>	<i>FWHM(nm)</i>	<i>QY(%)</i>	<i>Size(nm)</i>
<i>Supplier1</i>	611	107	43	*
<i>Supplier2</i>	620	99	20	5.5±0.5

Table 25: Summary of commercial CuInS₂ QDs parameters.

<i>InP/ZnS QDs</i>	<i>PL peak(nm)</i>	<i>FWHM(nm)</i>	<i>QY(%)</i>	<i>Size(nm)</i>
<i>Supplier1</i>	617	49	55	*
<i>Supplier2</i>	620	62	>20	5.0±0.5

Table 26: Summary of commercial InP QDs parameters.

*Size is not given by supplier. The size of QD from supplier1 can be estimated and approximated to the value given by supplier2 due to similar emission spectrum.

2.2.4 Laboratory Instrumentation

To carry out the experiment the following scientific devices and tools described below were used:

- QD size → High-Resolution Transmission Electron Microscope (HRTEM)
- Absorption spectrum, emission spectrum, FWHM → UV·VIS·NIR [UVNIR] spectrophotometer
- Quantum Yield (QY) → PL - QY spectrometer

Those laboratory instrumentations used are briefly described as follows.

2.2.4.1 TEM/HRTEM

A Transmission Electron Microscope (TEM) or High-Resolution Transmission Electron Microscope (HRTEM) uses a beam of electrons instead of light [66]. Due to the wavelength of electrons is much smaller than that of light, the optimal resolution achievable for TEM images is many orders of magnitude better than that from a light microscope. Thus, TEM can reveal the details of the internal structure of materials [67].

TEM consists of an electron emission source, electromagnetic lenses and an electron detector. A very thin sample is positioned along the electron beam. The electron beam is produced, accelerated and then focused on the sample by the lenses. The beam passes through the sample which modifies it and imprints its image [66].

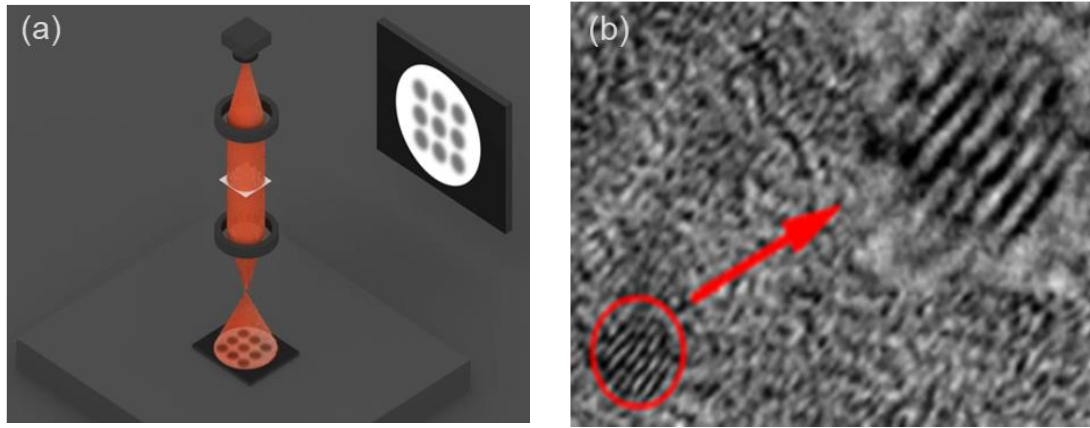


Figure 30: (a) TEM operating principle describing the path of electron beam. Reproduced from [66]. (b) Example of HRTEM images of CuInS₂ QDs. Reproduced from [28].

SCOPE: The use of TEM will be focused on determining the quantum dots size (diameter) to analyse its influence relating to photoluminescence features in the emission spectrum. Moreover, this size can be used as reference input for simulation steps.

2.2.4.2 UV·VIS·NIR [UVNIR] spectrophotometer

A UV-visible-NIR spectrophotometer is an instrument which records the UV, visible of NIR spectrum by measuring the reflection or absorbance characteristics of a sample. Accordingly, the predetermined electromagnetic radiation wavelengths for ultraviolet (uv), visible (vis) and near infrared (nir) radiation are defined as follows [68].

Radiation	Wavelength(nm)
UV	300 to 400
VIS	400 to 765
NIR	765 to 3200

Table 27: UV-VIS-NIR radiation. Extracted from [68].

SCOPE: UV·VIS·NIR [UVNIR] spectrometer will be used to extract the optical absorption and emission spectrum of quantum dots. This analysis will give us information about the excitation peak of the QDs.

2.2.4.3 PL quantum yield spectrometer

Photoluminescence (PL) is the spontaneous emission of light from a material following optical excitation. It is a technique to probe discrete energy levels and to obtain information about semiconductor sample composition or quantum dot sample monodispersity [69].

SCOPE: PL quantum yield spectrometer will provide information of QD emission spectrum and QY parameter. The results will allow the comparison and correlation with the theoretical/simulation outcomes.

Table 28 makes a short summary of the techniques and tools used for these measurements.

<i>QDs</i>	<i>Technique</i>	<i>Tool</i>	<i>*Brand</i>	<i>*Site</i>
<i>Size</i>	Electron microscopy	S/TEM	Titan (FEI®)	<i>UGR - CIC</i>
<i>-Abs/Em</i> <i>-FWHM</i>	Spectrophotometry	UV·VIS·NIR [UVNIR] spectrophotometer	Agilent	<i>UGR</i> <i>UoL</i>
<i>QY</i>	PL spectroscopy and QY analysis	PL - QY spectrometer	Edinburgh Instruments	<i>UoL</i>

Table 28: Summary of measurement tools used for QDs.

NB1: CIC (Centro de Instrumentación Científica) at UGR (Universidad de Granada)

NB2: UoL (University of Leeds)

2.2.5 Experimental Design 1: QD characterization

After having identified the main parameters from commercial QDs acquired for both InP and CuInS₂, some experimental measurements were performed to confirm the QDs features relating to their applicability to lighting field. Thus, the main goals behind this characterization experiment are

- a) Familiarization with experimental techniques to extract QDs parameters
- b) Confirmation of the data reflected in the datasheet presented in 2.2.3

Therefore, at the end of this experiment, it will be possible to assess both elements (InP and CuInS₂) from an experimental point of view and compare the data provided by the nanotech supplier to eventually select the best candidates for the lighting device design and modelling in BL3 and BL4.

2.2.5.1 QD SIZE

As explained in chapter 2.2.4, HRTEM (Titan TEM from FEI®) was used. Sample preparation is highly important to obtain the best possible quality images. Thus, firstly around 1 ml of samples were extracted from its original packaging from NN-Crystal® supplier and placed in small containers. Secondly, these containers were located in an ultrasonic cleaner to disperse the nanoparticles to avoid agglomeration. Once the ultrasonic process had finished, TEM samples were prepared for imaging in a fume hood by drying nanoparticles on a copper grid that is coated with a thin layer of carbon. This grid was introduced 25 times (optimal number of times to visualize the sample correctly throughout the microscopy) into the 2 ml colloidal quantum dots samples. Eventually the grids were left for 10 minutes so that the solvent could be evaporated completely.



Figure 31: Preparation of samples inside the fume hood at UGR-CIC (Centro de Instrumentación Científica, Universidad de Granada). Ultrasonic cleaner is shown at the right.

Titan® microscope is a powerful tool, able to perform two different techniques i.e. scanning and transmission (S/TEM). Both techniques were used to analyze the samples. Particularly, the core size of the quantum dot was characterized using SEM tool application, collecting the data by a High Angle Annular Dark Field (HAADF) detector. On the other hand, core/shell size of the QDs was measured using TEM tool application.

Before introducing the grid into the microscope a plasma cleaning process is carried out for 10 seconds to remove any organic substances to improve the visualization of the nanostructures. Finally, the sample is introduced in the HRTEM from Figure 32 and Figure 33 after making a void process in the system to analyze the QD sample.



Figure 32: (S/TEM) Titan® located at UGR-CIC (Centro de Instrumentación Científica, Universidad de Granada).



Figure 33: Internal architecture of (S/TEM) Titan® from UGR.

SUPPLIER2: NN-Crystal®-QD material: **CuInS₂/ZnS**-Emission photoluminescence peak (PL): **620 nm****-CORE**

Figure 34 below shows the particle measurement in SEM mode and with the High Angle Annular Dark Field (HAADF) detector. The post processing image to detect the core size of the QDs, using *ImageJ* software is also shown.

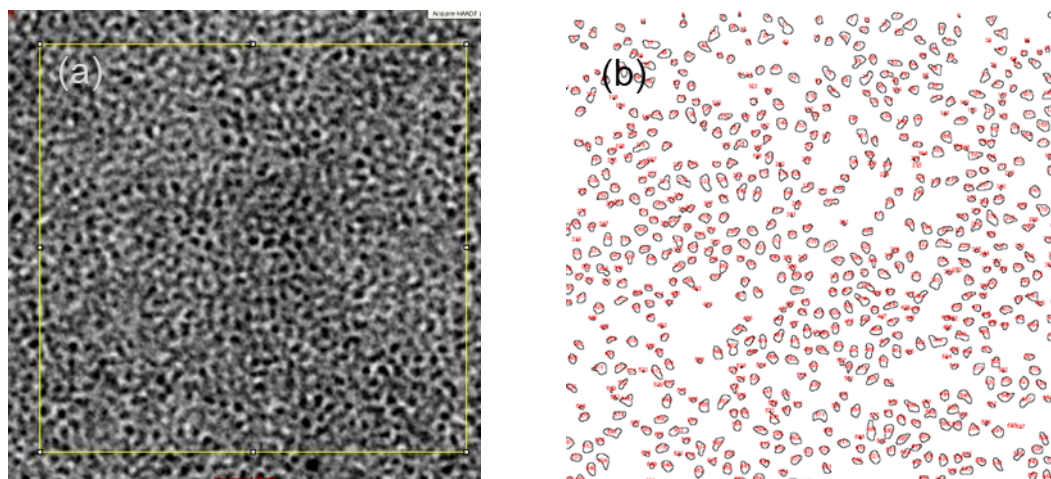


Figure 34: CuInS₂620 sample. (a) HAADF picture from (S/TEM) Titan® in scanning mode. (b) Image processed with ImageJ® to calculate the diameter of the QD cores used at this stage of the research.

After analyzing the data obtained, the histogram associated is depicted in Figure 35.

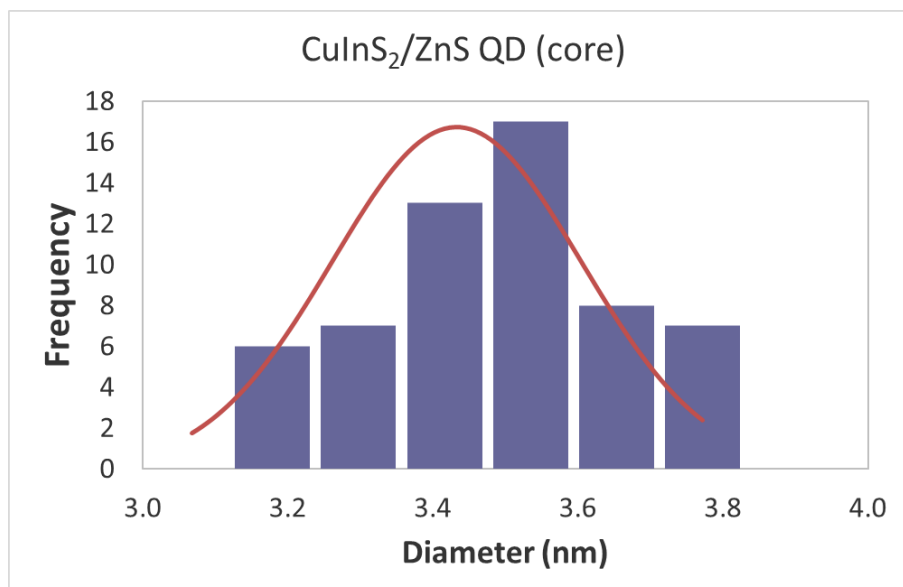


Figure 35: CuInS₂620 sample. Histogram + normal curve for QDs core used at this stage of the research.

Taking into account a normal curve to fit the results statistically, a core size of (3.4 ± 0.3) nm is obtained. Thus, it is possible to confirm the results given by the supplier datasheet relating to the quantum dot core size i.e. (3.3 ± 0.5) nm.

-CORE/SHELL

In the same way as previously done for core measurements, Figure 36 shows the particle measurement in TEM mode.

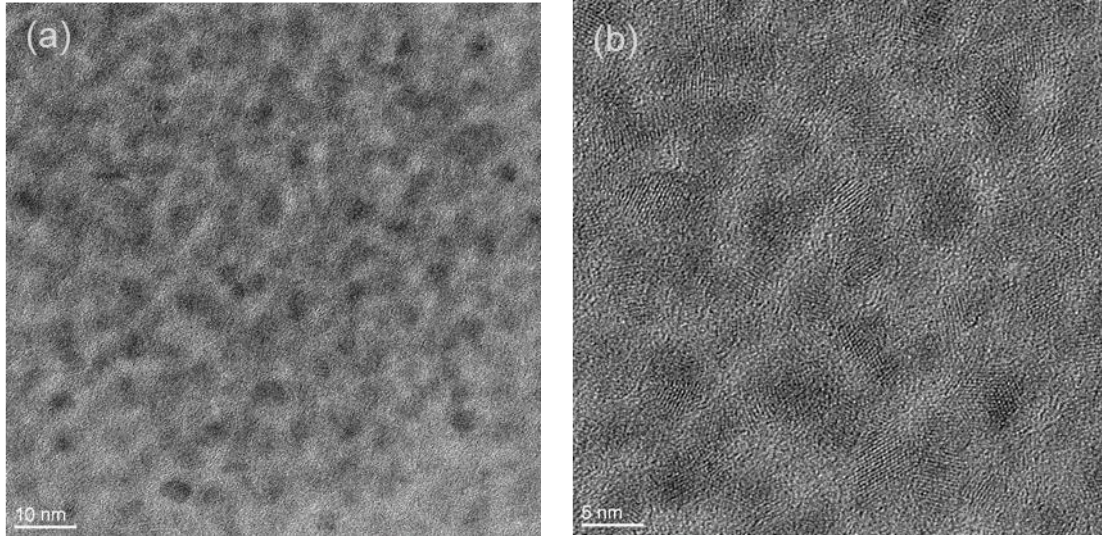


Figure 36: CuInS₂/ZnS sample. TEM pictures from (S/TEM) Titan® in transmission mode to calculate the diameter of the QDs core/shell used at this stage of the research. (a) 10 nm resolution. (b) 5 nm resolution.

After analyzing the data obtained, the histogram is depicted in Figure 37.

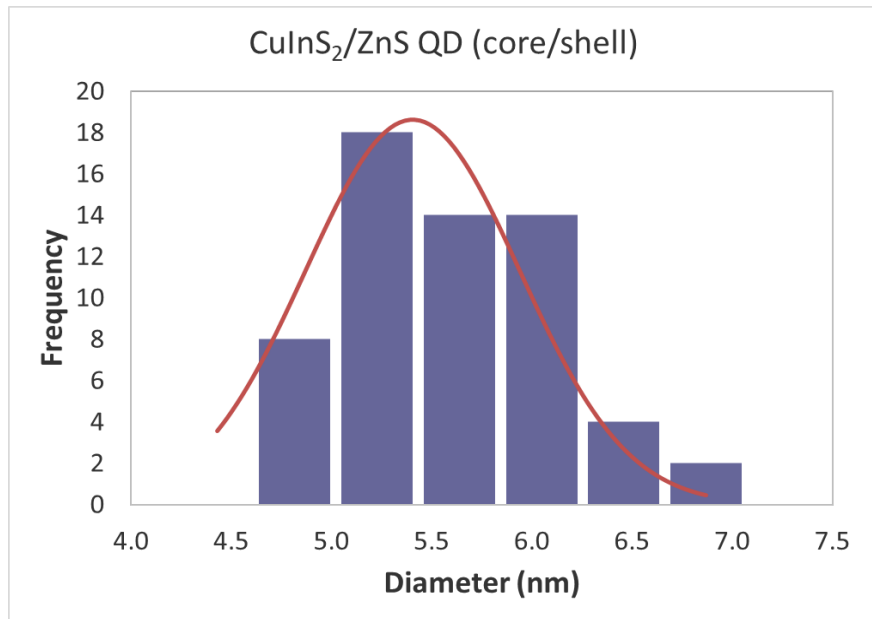


Figure 37: CuInS₂/ZnS sample. Histogram + normal curve for QDs core/shell used at this stage of the research.

Taking into account a normal curve to fit the results statistically, a core/shell size of (5.4 ± 0.5) nm is obtained. Thus, it is possible to confirm the results given by the supplier datasheet relating to the quantum dot core/shell size i.e. (5.5 ± 0.5) nm.

Now the second QDs batch formed by quantum dots made of InP/ZnS was analyzed.

-QD material: **InP/ZnS**

-Emission photoluminescence peak (PL): **620 nm**

-CORE

Figure 38 shows the particle measurement in SEM mode and with the High Angle Annular Dark Field (HAADF) detector. The post processing image to detect the core size of the QDs, using *ImageJ* software is also shown.

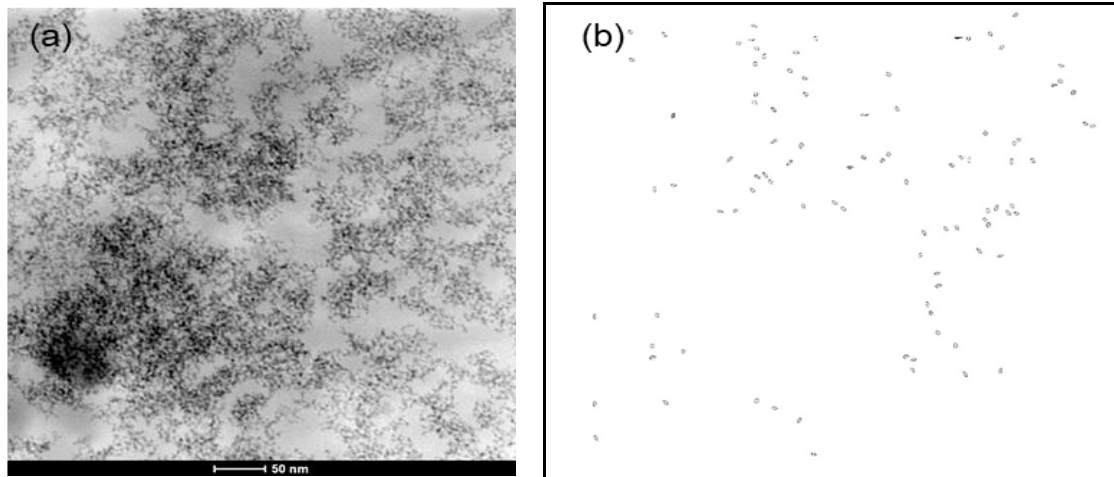


Figure 38: INP620 sample. (a) HAADF picture from (S/TEM) Titan® in scanning mode. (b) Image processed with ImageJ® to calculate the diameter of the QD cores used at this stage of the research.

After analyzing the data obtained, the histogram associated is depicted in Figure 39.

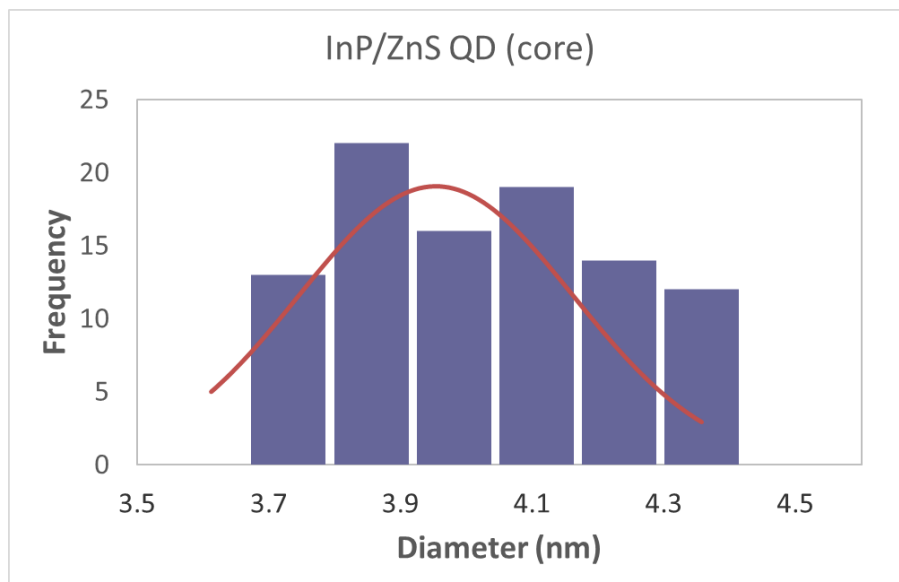


Figure 39: INP620 sample. Histogram + normal curve for QD cores used at this stage of the research.

Taking into account a normal curve to fit the results statistically, a core size of (4.0 ± 0.2) nm is obtained. Thus, it is possible to confirm the results given by the supplier datasheet relating to the quantum dot core size i.e. (3.9 ± 0.5) nm.

-CORE/SHELL

In the same way as done previously for core measurements, Figure 40 shows the particle measurement in TEM mode.

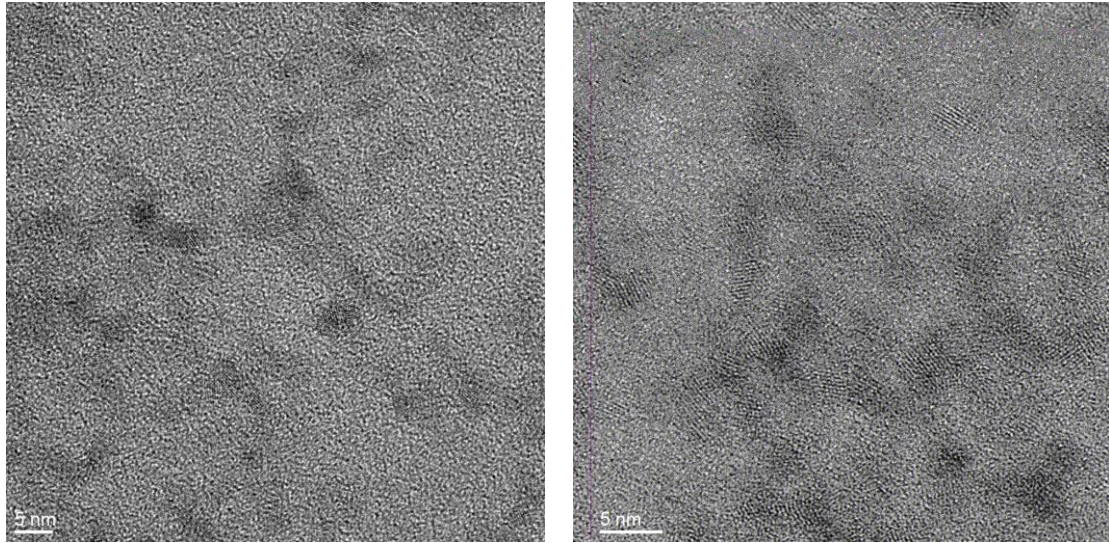


Figure 40: INP620 sample. TEM pictures from (S/TEM) Titan® in transmission mode to calculate the diameter of the QD core/shell used at this stage of the research.

After analyzing the data obtained, the histogram associated is depicted in Figure 41.

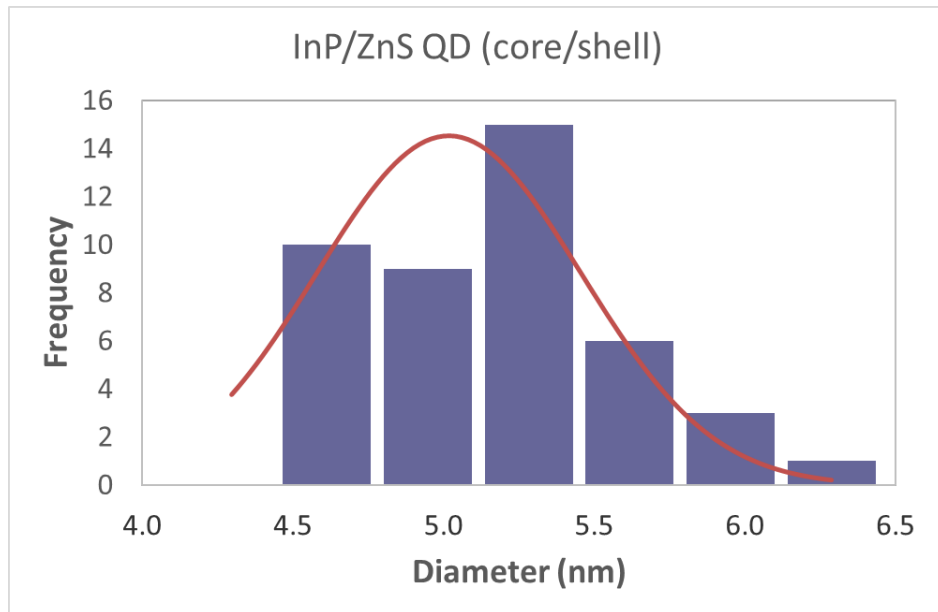


Figure 41: INP620 sample. Histogram + normal curve for QD core/shell used at this stage of the research.

Taking into account a normal curve to fit the results statistically, a core size of (5.0 ± 0.4) nm is obtained. Thus, it is possible to confirm the results given by the supplier datasheet relating to the quantum dot core/shell size i.e. (5.0 ± 0.5) nm.

Summary

<i>Supplier2</i>	<i>CORE size(nm) Datasheet</i>	<i>CORE size(nm) Measured</i>
<i>CuInS₂/ZnS QDs</i>	<i>3.3±0.5</i>	<i>3.4±0.3</i>
<i>InP/ZnS QDs</i>	<i>3.9±0.5</i>	<i>4.0±0.2</i>

Table 29: Summary of core QD size measurements vs supplier datasheet.

<i>Supplier2</i>	<i>CORE/SHELL size(nm) Datasheet</i>	<i>CORE/SHELL size(nm) Measured</i>
<i>CuInS₂/ZnS QDs</i>	<i>5.5±0.5</i>	<i>5.4±0.5</i>
<i>InP/ZnS QDs</i>	<i>5.0±0.5</i>	<i>5.0±0.4</i>

Table 30: Summary of core/shell QD size measurements vs supplier datasheet.

Then it is possible to conclude:

- Measurements made to calculate the size of the quantum dot confirm the data given by Supplier2 in its datasheet
- Top-notch nanostructure measurement techniques (S/TEM) have been used to carry out the measurements above.
- Size of QDs can be used in the modelling and simulation of block BL4.
- Since material QDs nanostructures from Supplier2 are the same as the ones from Supplier1, it is assumed that the size of QDs from Supplier1 can be approximated to the value given by Supplier2 due to similar emission spectrum.

2.2.5.2 *Absorption & Emission spectrum and FWHM*

As explained in 2.2.4, UV-VIS-NIR [UVNIR] spectrophotometer from the Organic Chemistry department at Universidad de Granada (UGR) and from the Molecular and Nanoscale Physics department at University of Leeds (UoL) have been used to perform these measurements. As explained, two main objectives are pursued for both suppliers:

- Familiarization with experimental techniques to extract QD parameters
- Confirmation the data reflected in the datasheet presented in 2.2.3

SUPPLIER1: Mesolight®

-QD material: **CuInS₂/ZnS**

-Measurement place: UoL

-Absorption & Emission spectrum (Datasheet vs Measured):

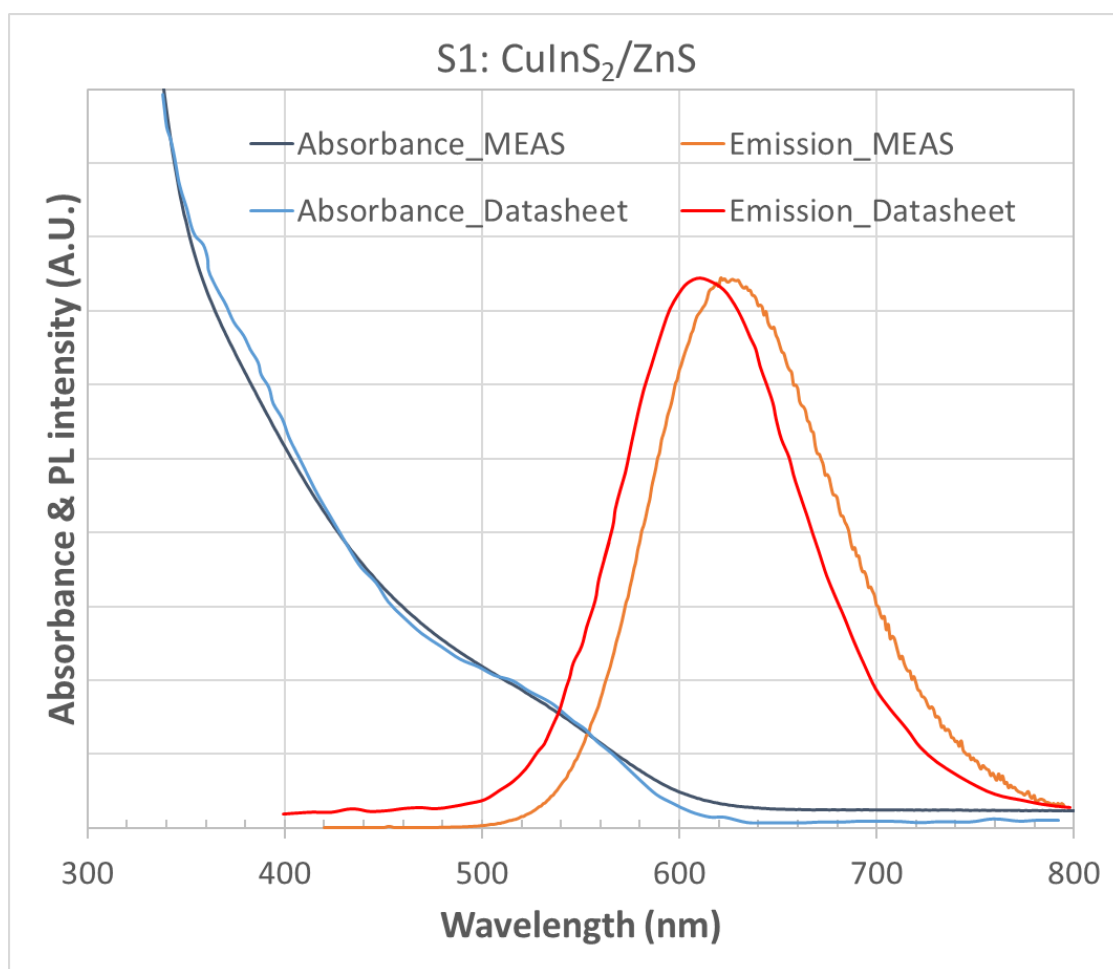


Figure 42: Datasheet vs measured Supplier1 (S1): CuInS₂/ZnS absorption & emission spectrum.

In Figure 42 above, it can be observed how absorption spectrum fits between datasheet and measurements performed. However, there is a small shift (11 nm) related to the emission spectrum when comparing datasheet with measurement results. On the other hand, FWHM parameter is

almost the same (107 nm vs 108 nm from datasheet and measurement respectively). In conclusion, it is possible to state that data from supplier are confirmed with experimental measurements.

-QD material: **InP/ZnS**

-Measurement place: UoL

-Absorption & Emission spectrum (Datasheet vs Measured):

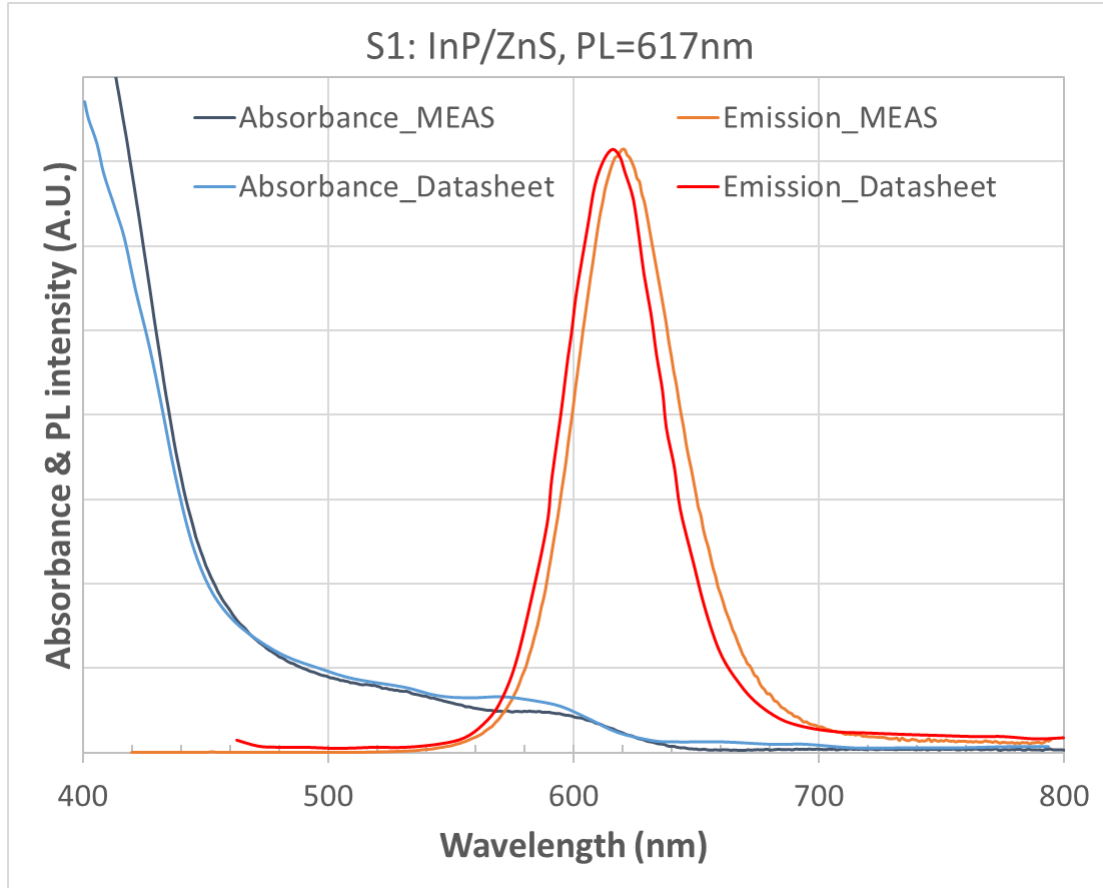


Figure 43: Datasheet vs measured Supplier1 (S1): InP/ZnS absorption & emission spectrum.

In Figure 43 above, it can be observed how absorption spectrum fits between datasheet and measurements performed. However, there is a small shift (4 nm) related to the emission spectrum when comparing datasheet with measurement results. On the other hand, FWHM parameter is almost the same (49 nm vs 53 nm from datasheet and measurement respectively). In conclusion, it is possible to state that data from supplier are confirmed with experimental measurements.

Summary

Supplier1	PL(nm) DataS	PL(nm) Meas	FWHM(nm) DataS	FWHM(nm) Meas	QY (%) DataS	QY (%) Meas
CuInS ₂ /ZnS QDs	611	622	107	108	43	41
InP/ZnS QDs	617	621	49	53	55	ND*

Table 31: Summary of QD parameters measurements vs Supplier1 datasheet.

*No Data available. The measurement was not performed.

SUPPLIER2: NN-Crystal®

-QD material: **CuInS₂/ZnS**

-Measurement place: UGR

-Absorption & Emission spectrum (Datasheet vs Measured):

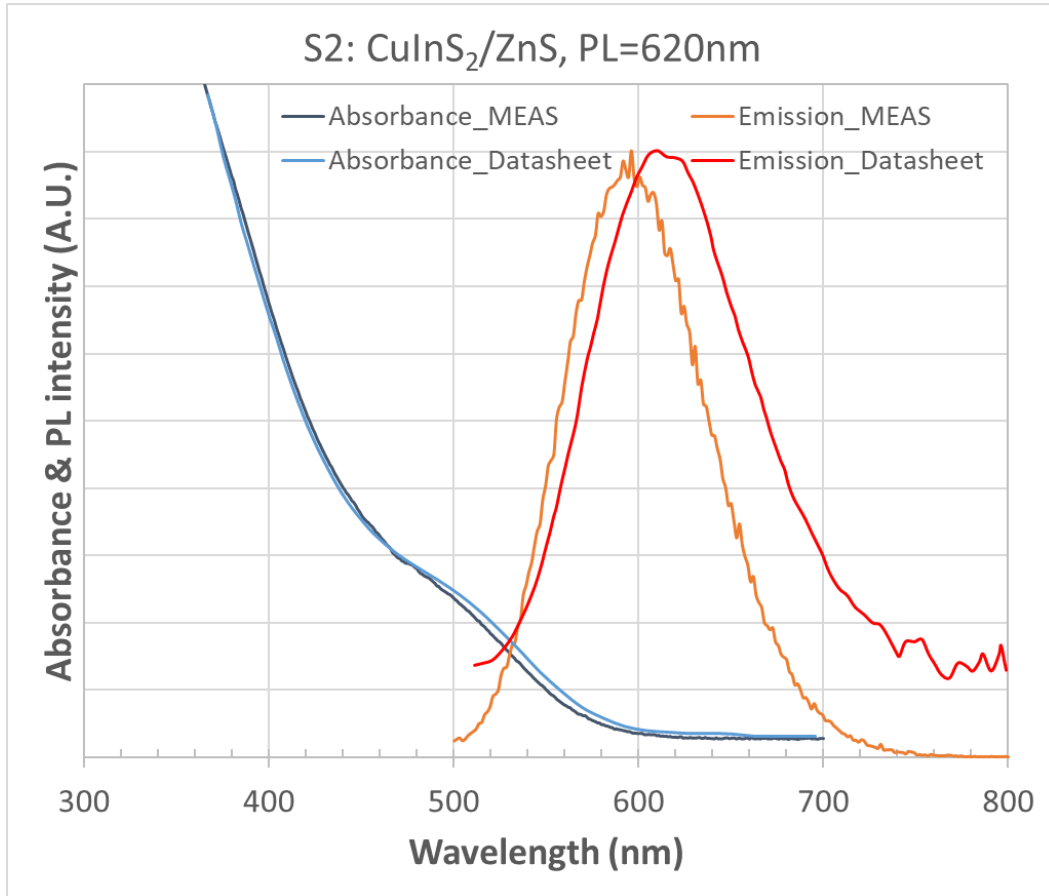


Figure 44: Datasheet vs measured Supplier2 (S2): CuInS₂/ZnS absorption & emission spectrum.

In Figure 44 above, it can be observed how absorption spectrum fits between datasheet and measurements performed. However, there is a small shift (24 nm) related to the emission spectrum when comparing datasheet with measurement results. On the other hand, FWHM parameter is almost the same (99 nm vs 98 nm from datasheet and measurement respectively). In conclusion, it is possible to state that data from supplier are confirmed with experimental measurements.

-QD material: **InP/ZnS**

-Measurement place: UGR

-Absorption & Emission spectrum (Datasheet vs Measured):

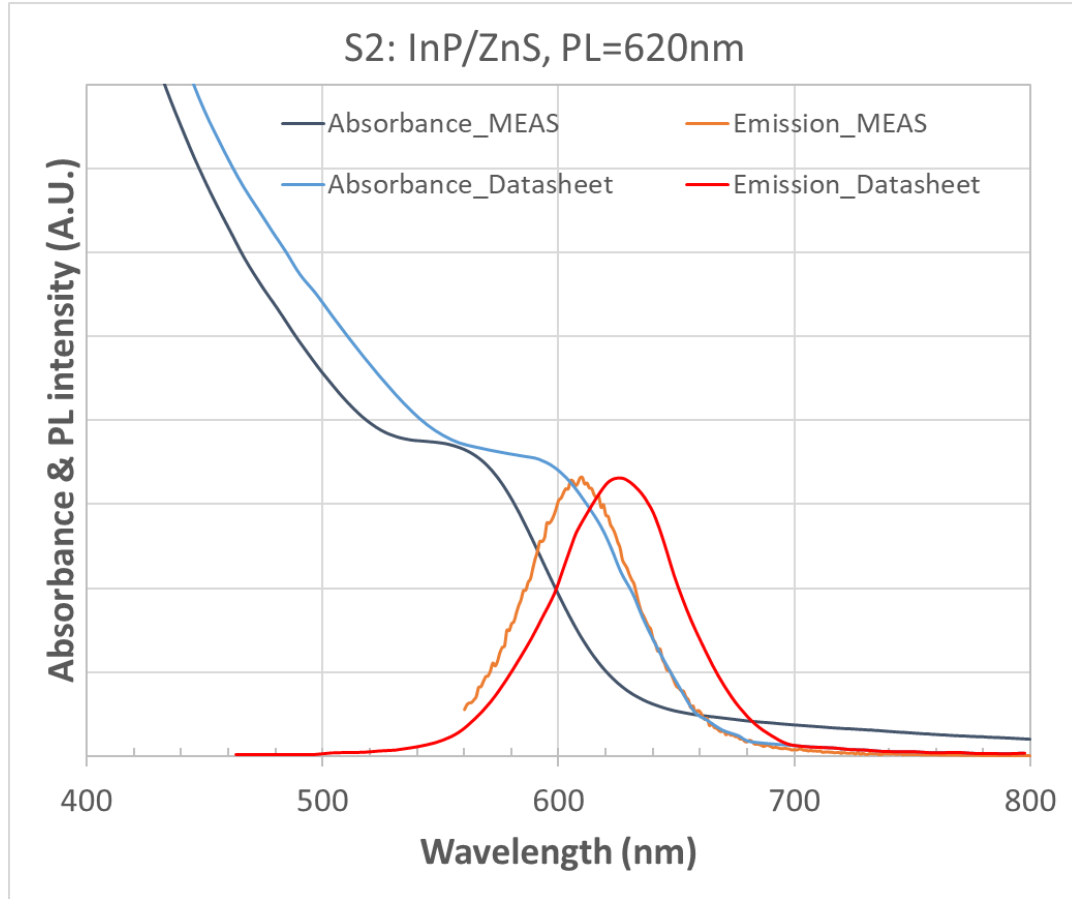


Figure 45: Datasheet vs measured Supplier2 (S2): InP/ZnS absorption & emission spectrum.

In this case, in Figure 45 above, it can be observed how both absorption and emission spectra have a shift between datasheet and measurements performed, specifically, 40 nm for absorption spectrum and 15 nm for emission one. On the other hand, FWHM parameter is almost the same (62 nm vs 58 nm from datasheet and measurement respectively). In conclusion, it is possible to state that data from supplier are valid and have been confirmed with experimental measurements.

Summary

Supplier2	PL(nm) DataS	PL(nm) Meas	FWHM(nm) DataS	FWHM(nm) Meas	QY (%) DataS	QY (%) Meas
CuInS ₂ /ZnS QDs	620	596	99	98	20	ND*
InP/ZnS QDs	620	605	62	58	>20	ND*

Table 32: Summary of QD parameters measurements vs Supplier2 datasheet.

*No Data available. The measurement was not performed

Then it is possible to conclude that measurements made to calculate the absorption and emission spectra of the quantum dot confirm the data given by Supplier1 and Supplier2 in their datasheet.

2.2.6 *Summary*

Eventually some general conclusions from this quantum dots characterization chapter 2.2 are set. As it was described at the beginning of 2.2, two main objectives were pursued. Firstly, the confirmation of data given by QD suppliers in order to proceed further to manufacture the QLED device in block BL3 and secondly, the familiarization with top-notch nanostructures measurement techniques used for quantum dots characterization. Thereby, both goals have been achieved by measuring different commercial QD parameters like size, absorption and emission spectra, FWHM and QY from two different QD suppliers focusing on red color of visible spectra as reference output photoluminescence peak emission.

Particularly, as a consequence of those measurements, it is possible to establish that datasheet fits the reality. Thus, both $\text{CuInS}_2/\text{ZnS}$ and InP/ZnS quantum dots could be good candidates for automotive lighting devices as predicted in the first literature research carried out in block BL1.

However, from now on, $\text{CuInS}_2/\text{ZnS}$ will be set as main candidate for the QLED device manufacturing and modelling due to the capability of CuInS_2 core to achieve deep red wavelength. After having a thorough look into the measurement performed, FWHM is wider for this core material as expected from BL1. Nevertheless, the purity of color could not be an issue for automotive lighting, particularly for rearlamps, since homogeneity is the key quantity to bear in mind. As highlighted in the introduction chapter, style is vital for automotive lighting systems. In fact, the homogeneity aspect of the lighting functions at rearlamp level is one of the highly desired parameters that carmakers are pursuing from an aesthetic point of view.

In this sense, a higher QY is observed from Supplier1 related to CuInS_2 (43% vs 20%). Then, those commercial quantum dots from Supplier1 will also be used in block BL3 for manufacturing the QLED device.

Finally, once $\text{CuInS}_2/\text{ZnS}$ QDs have been selected, an experimental synthesis and characterization of these quantum dots will be carried out in chapter 2.3.

2.3 QD SYNTHESIS

After having analyzed and characterized the commercial QDs in chapter 2.2, CuInS₂/ZnS QDs have been selected for the QLED device manufacturing and modelling. The decision has been taken mainly because of the capability of CuInS₂ core to achieve deep red wavelength, which is really suitable for automotive lighting applications, specifically in rearlamps.

Therefore, the next sensible step to take is to try to synthesize those kinds of QDs in the laboratory to acquire the knowledge on nanostructure chemical process in first place, and to use those hand-made QDs (along with the commercial samples selected) in order to eventually manufacture the QLED device with two different batches of QDs.

2.3.1 Goals

By performing this experiment, the following objectives are pursued

- a) CuInS₂/ZnS quantum dots synthesis focused on red color as target for output wavelength
- b) QD characterization: absorption/emission spectra, FWHM and QY parameters

This experiment has been carried out at University of Leeds (UoL), particularly in the laboratories of the School of Physics and Astronomy.

2.3.2 Laboratory Instrumentation

The laboratory techniques and instrumentation used for QD characterization have already been introduced in chapter 2.2.4. Thus, to carry out the synthesis experimental part, the following scientific devices and tools described below have been used.

2.3.2.1 CHEMICAL HOOD

Local Exhaust Ventilation (LEV) systems reduce or prevent exposure to airborne contaminants by capturing them at their source [70]. The most common LEV system used in research laboratories is the laboratory chemical hood. There are two basic types of hoods: enclosing and exterior as shown in Figure 46. The hood provides a barrier between the worker and the contaminant. Sufficient airflow must be provided through any openings in the enclosure to ensure that the contaminants do not escape the hood [70].



Figure 46: Enclosing lab chemical hood (note that the work area is inside the hood). Reproduced from [70].

SCOPE: The use of the chemical hood will be focused on the synthesis of the QDs. As it will be described in 2.3.3.1, the synthesis of QDs requires an oxygen free environment and a heating process at the same time. Thanks to the reflux process that can be carried out inside the fume hood, it is possible to heat the chemical mix at the same time using a specific hotplate to complete the whole chemical quantum dots synthesization under a N_2 atmosphere. Moreover, all chemical mixtures will be prepared by using the chemical hood in order to have a high degree of safety to avoid any contact with the chemical materials used.

2.3.2.2 CENTRIFUGE

A centrifuge is used for the separation of fluids, based on the density quantity. Separation is obtained by spinning a container at high speed and pushing heavier materials to the outside of the recipient [71].

SCOPE: The centrifuge will be used in the last QD synthesis process i.e. in the purification step which will be described in 2.3.3.1.

Table 33 gives a short summary of the techniques and tools used for these measurements.

<i>QDs</i>	<i>Technique</i>	<i>Tool</i>	<i>Site</i>
<i>Synthesis</i>	Nitrogen reflux Sample heating	Chemical Hood Hot plate	<i>UoL</i>
<i>Purification</i>	Sample Centrifuge	Centrifuge	<i>UoL</i>

Table 33: Summary of measurement tools used for QDs.

2.3.3 Experimental Design 2: QD synthesis

Once the objectives of this experiment have been set, this chapter is divided into two parts. The first one corresponds to the synthesis process to achieve $\text{CuInS}_2/\text{ZnS}$ quantum dots. On the other hand, the second part is related to the sample characterization obtained from the first part. This experiment was carried out at University of Leeds (UoL).

2.3.3.1 $\text{CuInS}_2/\text{ZnS}$ synthesis:

The synthesis process presented by M.Booth *et al.* [72], [73] has been taken as reference to create $\text{CuInS}_2/\text{ZnS}$ quantum dots and it is described as follows.

2.3.3.1.1 Chemicals

All chemical components used during the synthesis process of QDs together with their purity are listed below:

Indium acetate (99.99%), copper iodide (99.999%), dodecanethiol (DDT, >98%), zinc stearate (90%), hexane, and octadecene (ODE, 90%), high-performance liquid chromatography (HPLC)-grade methanol, chloroform, acetone, nitric acid (70%), hydrochloric acid (32%), and hexane (>97%)

NB: All chemicals were used as received.

2.3.3.1.2 CORE synthesis: CuInS_2

For the synthesis of the core CuInS_2 quantum dots, 47.5 mg of copper iodide (0.25 mmol) and 73 mg of indium acetate (0.25 mmol) were added to a three-necked round bottom flask in a mixture of 4 ml of dodecanethiol (DDT) and 6 ml of octadecene (ODE). The flask was fitted with a condenser column in a fume hood and purged with nitrogen so that the chemical mix is under a protective nitrogen atmosphere before stirring at room temperature for two hours to remove dissolved oxygen.

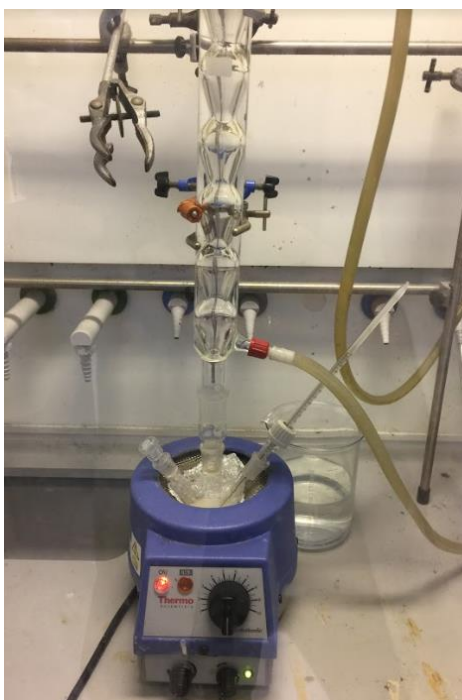


Figure 47: Fume hood with three-necked round bottom and condenser column set up used to synthesize quantum dots at University of Leeds (UoL).

The solution was then refluxed at 120 °C over 20 minutes where all solid material was seen to dissolve (a clear yellow solution was formed). Then the solution temperature was increased at 210 °C for 20 minutes, at which point it became a deep red color, indicating the formation and growth of nanoparticles. The growth was then quenched by rapidly cooling the reaction vessel by immersion in water at room temperature. Half of the reaction volume was then removed and kept.

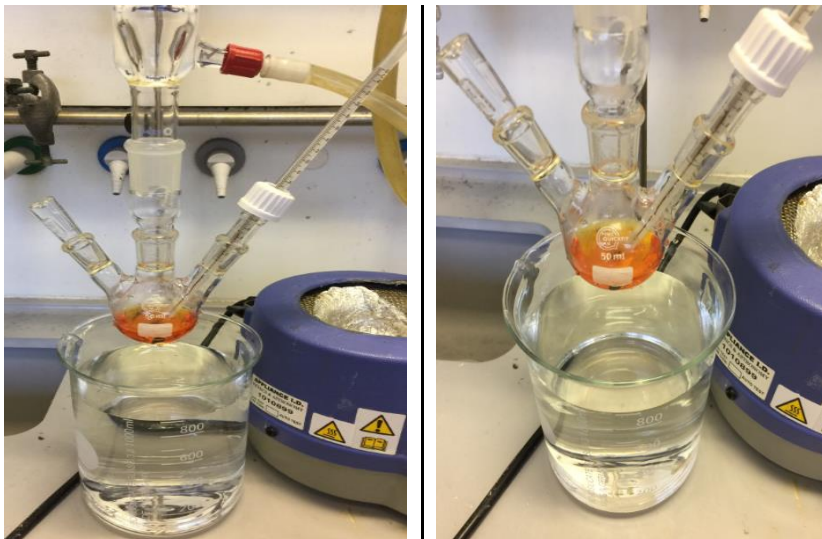


Figure 48: Cooling process of CuInS₂ core nanoparticles synthesized at UoL.

2.3.3.1.3 SHELL synthesis: CuInS₂/ZnS

Once the core or nucleus of quantum dots is created, the next step is to form the outer shell of the nanoparticles. Thereby, for the addition of a ZnS shell to form CuInS₂/ZnS core/shell QDs, 158 mg (0.25 mmol) of zinc stearate was added in 4 ml octadecene (ODE) in a flask and heated at 60 °C until a clear solution was formed. This solution was added to the cooled CuInS₂-QDs (without purification) and was subsequently heated at 220 °C and refluxed for 1 h, after which the reaction was quenched by rapidly cooling the flask in a water bath obtaining a deep red color solution as shown in Figure 49.

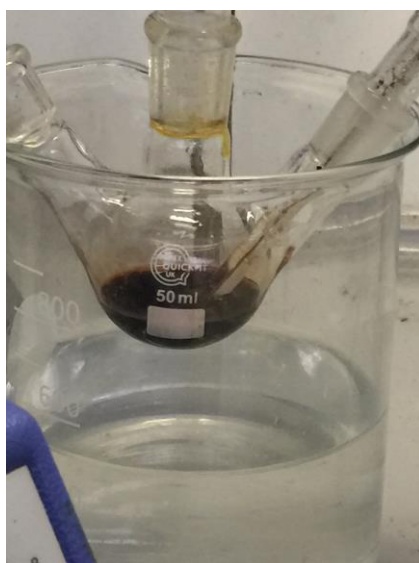


Figure 49: CuInS₂/ZnS core/shell nanoparticles formed and synthesized at UoL.

2.3.3.1.4 Purification

The resulting core/shell quantum dots were then cleaned following a centrifugation and decantation process. The QD dispersions were diluted by the addition of hexane. The solutions were added to a 1-equivalent solution of 1:1 chloroform:methanol.



Figure 50: CuInS₂/ZnS core/shell nanoparticles synthesized at UoL before introducing them into the centrifuge.

The QDs were precipitated via the addition of 10 equivalent solutions of acetone, followed by centrifugation (4000 rpm) and decantation. This process was repeated three times.

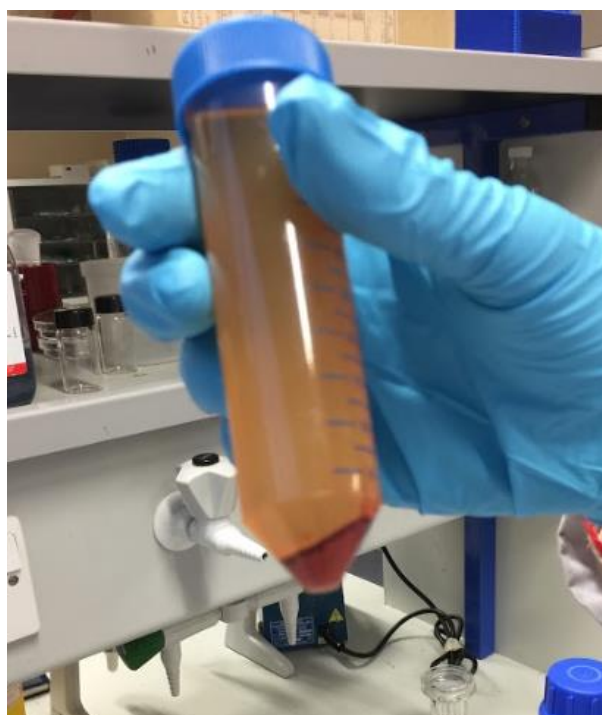


Figure 51: CuInS₂/ZnS core/shell nanoparticles synthesized at UoL on bottom of container after centrifugation.

The resulting precipitate was resuspended in hexane obtaining the final colloidal solution of $\text{CuInS}_2/\text{ZnS}$ quantum dots in hexane as shown in Figure 52.

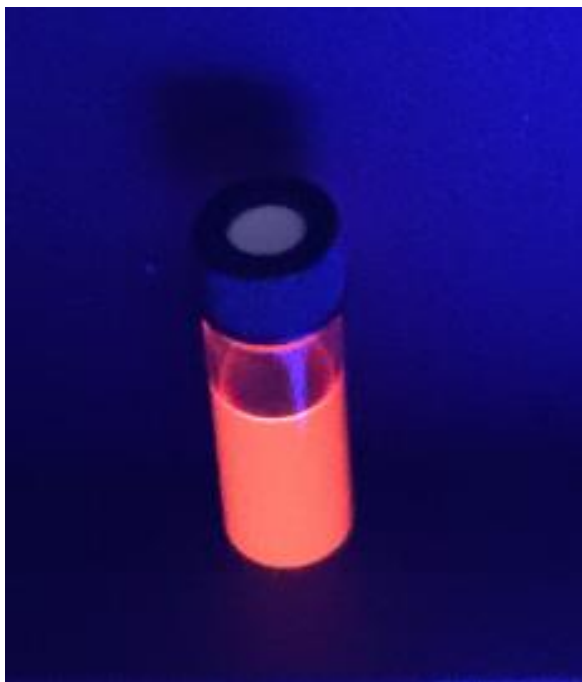


Figure 52: Colloidal solution of $\text{CuInS}_2/\text{ZnS}$ quantum dots (synthesized at UoL) in hexane under UV-light after purification process.

2.3.3.2 QDs characterization (Abs & Em spectra, FWHM and QY)

Once the quantum dots have been synthesized, the next step to take is to characterize them to obtain the absorption and emission spectra, the FWHM and QY parameters.

-QD material: **CuInS₂/ZnS**

-Measurement place: UoL

-Absorption & Emission spectra (measured):

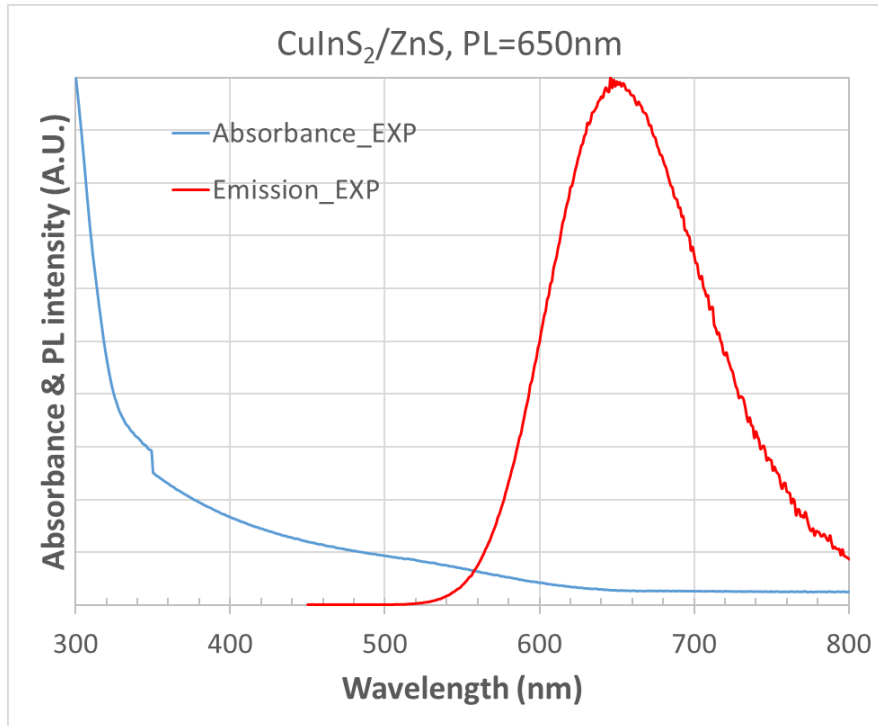


Figure 53: Absorption and emission spectra measured of CuInS₂/ZnS quantum dots synthesized at UoL.

Therefore, it is possible to calculate FWHM from Figure 53. QY was also measured and the value is summarized in Table 34.

UoL	PL(nm) Meas	FWHM(nm) Meas	QY (%) Meas
CuInS ₂ /ZnS QDs	650	118	42

Table 34: Summary of measured parameters of QDs synthesized.

Additionally, if all CuInS₂/ZnS data (commercial and synthesized) are compared it can be concluded that the parameters achieved are similar in magnitude as reflected in Table 35.

CuInS ₂ /ZnS QDs	PL(nm) Meas	FWHM(nm) Meas	QY (%) Meas
UoL	650	118	42
Supplier1	622	108	41
Supplier2	620	98	20*

Table 35: Summary of measured parameters of QDs (commercial and synthesized).

*The measurement was not performed. Data from datasheet.

Thus, the next objective of this work may be fulfilled i.e. the manufacturing of a QLED device based on the $\text{CuInS}_2/\text{ZnS}$ quantum dots presented. QDs from Supplier1 and QDs synthesized at UoL will be used based on QY values from Table 35.

2.3.4 Summary

Eventually, some general conclusions from this quantum dots synthesization chapter 2.3 are set. As it was described at the beginning of 2.3, two main objectives were pursued. Firstly, the synthesis of $\text{CuInS}_2/\text{ZnS}$ quantum dots focused on red color as output wavelength. Likewise, a familiarization with nanostructure instrumentation and techniques is achieved. The second objective was to characterize the quantum dots engineered. Thereby, both goals have been completed by synthesizing and characterizing colloidal solution of $\text{CuInS}_2/\text{ZnS}$ quantum dots in hexane solvent focusing on red color of visible spectra as reference output photoluminescence peak emission. Particularly measured parameters (abs/em spectrum, FWHM and QY) are in line with the ones extracted from the commercial quantum dots acquired.

2.4 CONCLUSIONS

Thus, $\text{CuInS}_2/\text{ZnS}$ will be set as main candidate for the QLED device manufacturing and modelling due to the capability of CuInS_2 core to achieve deep red or even the infrared wavelength (highly desired in the automotive field). Particularly in red lighting functions (aimed at rear lighting systems) where the optical requirements are lower. Thereby, once both the material and the core/shell configuration to be used have been identified, $\text{CuInS}_2/\text{ZnS}$ QDs are synthesized in colloidal solutions adapting the UoL procedure so as to compare different synthesis processes (commercial QDs and synthesized QDs) in an experimental way in the subsequent QLED device fabrication.

Based on the partial conclusions from chapters 2.2.6 and 2.3.4, it can be stated that all objectives defined at the beginning of the block and described above have been achieved.

QD CHARACTERIZATION

- a) Familiarization with experimental techniques to extract QD parameters
- b) Confirmation of data reflected in the datasheet presented in 2.2.3

QD SYNTHESIS

- c) $\text{CuInS}_2/\text{ZnS}$ quantum dots synthesis focused on red color as target for output wavelength
- d) QDs characterization: absorption/emission spectra, FWHM and QY parameters

Thereby, it is confirmed that $\text{CuInS}_2/\text{ZnS}$ might be set as a main candidate for the QLED device due to the capability of CuInS_2 core to achieve deep red wavelength, which is highly suitable for automotive lighting systems, particularly for rearlamps applications. Thus, based on the exposed above, the QLED device manufacturing and modelling step will be based on $\text{CuInS}_2/\text{ZnS}$ quantum dots from this BL2.

3 BL3 – QLED DEVICE

3.1 SCOPE

As highlighted several times, quantum dots are the base upon which all this work is developed. Thus, from block BL2, it has been concluded that **CuInS₂/ZnS QDs** are good candidates for a further QLED device manufacturing. That is based, among other properties already identified, on the possibility to achieve deeper red color [7], [64] which can result in a good advantage to design automotive lighting systems, particularly rearlamps systems.

Furthermore, CuInS₂/ZnS QDs from supplier1 and CuInS₂/ZnS QDs synthesized at UoL will be used for the quantum dot experimental device developed along this block BL3. Thus, different batches of QLEDs will be designed by mixing several fabrication procedures and adapting those to a specific common substrate with six independent pixels. The objective is to measure the electrical behaviour of each pixel over the same substrate to research in the possible differences found from an experimental point of view and to propose some improvements in the design and fabrication process once the QLED is modelled in the block BL4.

Eventually, this block BL3 deals mainly with the lighting applications that can be made out of quantum dots, particularly focused on electroluminescence physical phenomena to design, manufacture and characterize a real QLED device.

3.1.1 Research Plan

Having a look into the research plan defined at the beginning of the PhD project, it is possible to depict graphically the location level of this block inside the bottom-up methodology presented.

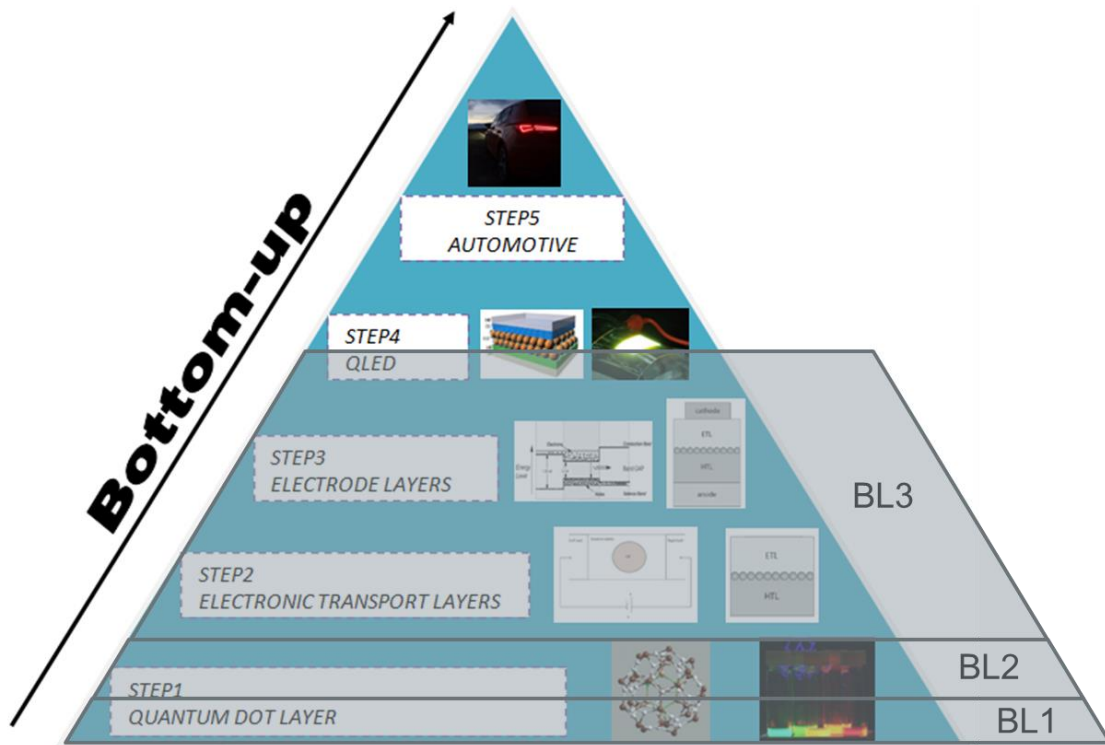


Figure 54: Block BL3. BOTTOM-UP methodology.

3.2 PHOTOLUMINESCENCE VS ELECTROLUMINESCENCE

Chapter 1.2 describes the two main physical phenomena that quantum dots can offer as lighting devices. These optoelectronic devices, which contain quantum dots, are the Quantum Dot Film (QDF) and the Quantum Dot Lighting Emitting Device (QLED).

As already defined, QDF devices are based on photoluminescence where an emission down conversion effect occurs in QDs after an absorption of photons. Those photons excite electrons to a higher energy level inside the QD which produces a re-radiation of photons, after a relaxation process, in a larger output wavelength compared to the input one.

On the other hand, QLED devices are based on electroluminescence. Here, an electrical current passes through the lighting device. Thus, a carrier transport occurs and electron-hole recombination is produced in the emissive layer i.e. QD layer, generating photons in a specific output wavelength, which depends on the band gap of the quantum dots materials used. However, the electroluminescence phenomenon is still a challenge to produce devices in mass production.

Both phenomena are interesting for automotive applications as described in block BL5, where the particular automotive QD development is carried out. Therefore, in blocks BL3 and BL4, QLED devices based on electroluminescence physical mechanisms will be researched due to the challenging and innovative perspective that can be taken from design and modelling points since the electrical QLED device behavior is critical when designing automotive electronics control modules.

Furthermore, photoluminescence phenomenon will be studied in the final automotive QD integration in BL5 since QDF for consumer electronics (not automotive tested) may be acquired. Due to the advanced maturity in the market of this physical phenomenon, research on specific automotive applications from a functional point of view, may be carried out as it will be done in the last block BL5.

3.3 QDF PROOF OF CONCEPT (PHOTOLUMINESCENCE)

Although main research of blocks BL3 and BL4 will be centered on electroluminescence devices, some work has been performed on the experimental side of QDF. In fact, a proof of concept was developed using some commercial quantum dots acquired and the ones synthesized in chapter 2.3 at University of Leeds. Those QDs were deposited on glass substrate by spin coating technique and encapsulated with UV epoxy on a glass cover slip as shown in Figure 55.

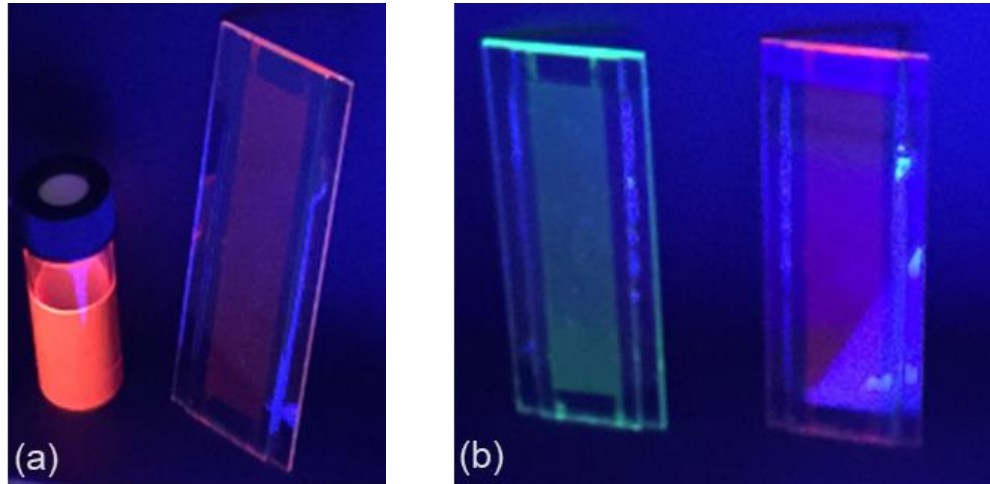


Figure 55: (a) QDF CuInS₂/ZnS QDs-based synthesized in this work at UoL under UV light. (b) QDF fabricated in this work using CuInS₂/ZnS QDs-based from Supplier1 (green and red QDs output wavelength used) under UV light. QDF have a glass substrate.

As explained, the intention of the QDF device depicted in Figure 55 is just to create a proof of concept and not a real development since, as described in chapter 3.2, QDF are already available in the market for consumer electronics application. The big challenge, developed in block BL5 consists in integrating those quantum dot films in an automotive application, as it has never been carried out so far.

Two main challenges exist when developing QDF. Firstly, the correct quantum dot alignment on the selected material is critical. This is not an easy task since a QD matrix has to be pursued in order to have a homogenous QD distribution avoiding nanoparticles agglomeration that could lead to a low efficient energy down conversion. The second challenge is related to the latter efficiency but based on the QY of the nanoparticle. In order to achieve a high quality QDF, quantum dots with high QY (100% as target) have to be pursued. In this sense, the use of environmentally friendly Cd-free quantum dots makes it more difficult in relation to QY. Thus, it is necessary to reach a compromise on both topics to make high quality QDF devices.

3.4 QLED DESIGN (ELECTROLUMINESCENCE)

As it was already stated in chapter 3.2, QLED devices based on an electroluminescence physical mechanism represent a more challenging and innovative objective than QDF (photoluminescence) devices, from design and modelling points of view. Then, a lighting emitting diode based on quantum dots, which are excited with an electrical current passing through, will be designed in this chapter.

3.4.1 QLED energy levels

After revisiting the literature research made in chapter 1.8, it is possible to identify that, from a physics point of view, correct layers selection is key to conform an efficient electroluminescent lighting device. In this way, a non-inverter structure, similar to the structure 11 found in chapter 1.8 but using different materials for specific layers, will be taken as reference as shown in Figure 56.

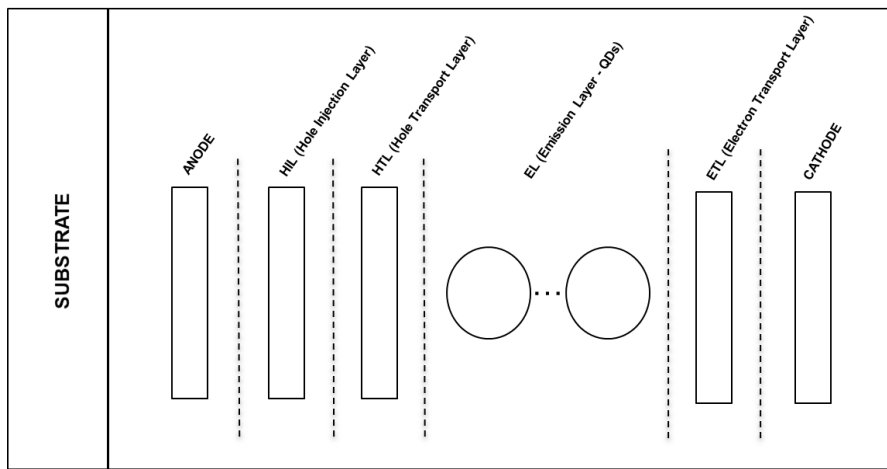


Figure 56: QLED layers structure proposal. Designed for this work.

Optimal energy levels between layers directly influence the final performance of the QLED. Therefore, based on chapter 1.8, the approximate following bulk energy levels diagram sketch is proposed in Figure 57 as target to achieve when the material layers will be selected in 3.4.2.

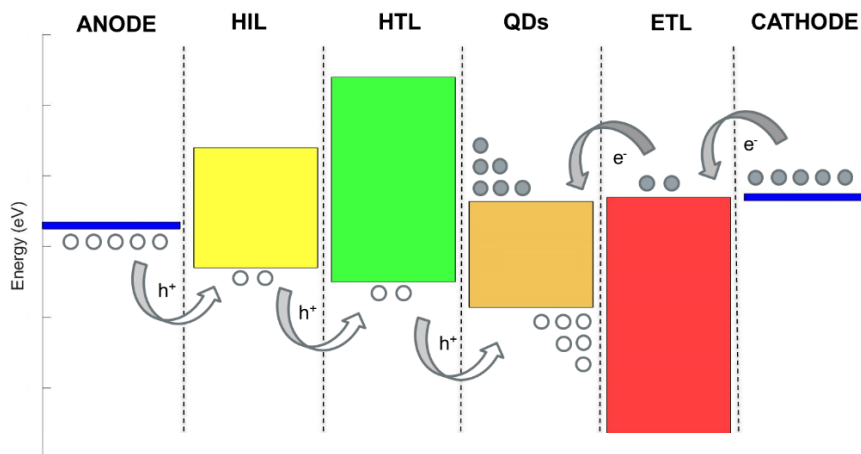


Figure 57: QLED bulk energy levels diagram sketch proposal. Designed for this work.

Furthermore, the main objective, if eventually that energy level diagram could be achieved, is that a hole-electron recombination occurs inside the quantum dot layer and therefore a photon emission, with output wavelength proportional to QD bandgap, is produced.

3.4.2 Layer device selection

Once the QLED energy levels have been chosen, it is necessary to define the materials that will be associated to each layer in the QLED structure as a whole. Thus, these materials are presented in the next section.

3.4.2.1 Substrate

Following the conclusions from chapter 1.8, particularly structure 11 from [62], a rigid substrate will be used as base where to deposit the other layers. There are other options to even create flexible QLEDs. However, since it is the first QLED prototype to manufacture, that glass substrate may provide robust protection for manual QLED handling.

3.4.2.2 Anode

ITO, or Indium Tin Oxide, will be used as anode. ITO is one of the most widely used transparent conducting oxides because of its two main properties: its electrical conductivity and optical transparency, as well as the ease with which it can be deposited as a thin film. As with all transparent conducting films, a compromise must be made between conductivity and transparency, since increasing the thickness and the concentration of charge carriers increases the material conductivity, but decreases its transparency. ITO is an optoelectronic material that is widely applied in both research and industry. ITO can be used for many applications, such as flat-panel displays, smart windows, polymer-based electronics, thin film photovoltaics, glass doors of supermarket freezers, and architectural windows. Moreover, ITO thin films for glass substrates can be helpful for glass windows to conserve energy [74].

Table 36 resumes the main properties (bulk) proposed that will be used mainly in the QLED modelling and simulation block BL4 [75].

ANODE	Relative permittivity $\epsilon_r (\epsilon_0)$	Electron Eff mass $m_e^*(m_0)$	Hole Eff mass $m_h^*(m_0)$	Electron Affinity $E_A(\text{eV})$	Ionization energy $E_i(\text{eV})$	Work function $\Phi (\text{eV})$	Bandgap BG (eV)
ITO	-	-	-	-	-	4.70	-

Table 36: ITO bulk material properties.

3.4.2.3 Hole Injection Layer - HIL

PEDOT:PSS, or Poly(3,4-ethylenedioxythiophene) polystyrene sulfonate, will be used as hole injection layer (HIL). PEDOT:PSS, is a transparent conductive polymer consisting of a mixture of the ionomers poly(3,4-ethylenedioxythiophene) and polystyrene sulfonate. Due to its unique combination of conductivity, transparency, ductility, and ease of processing, PEDOT:PSS has become a benchmark material in thin-film electronic fabrication. The PEDOT:PSS layer performs three functions [76]:

- Planarization of the ITO surface
- Matching of the ITO interface energy with the active layer
- Due to its deep work function, it acts as an interfacial layer for efficient hole injection layer.

It is worth saying that PEDOT to PSS ratio has an influence on the optical and electrical layer parameter [77]. Furthermore, the uptake of water into the PEDOT:PSS matrix has also an influence on those values, for example by increasing the film's average dielectric constant (ϵ_r) [77], [78]. Thus, there is a wide variety of parameter values in the literature. Since the chemical material used has not been characterized, different values have been assumed after a correlation done through simulation with a manufactured experimental QLED device.

Therefore, Table 37 resumes the main properties (bulk) proposed that will be used mainly in the QLED modelling and simulation block BL4.

<i>HIL</i>	<i>Relative permittivity</i> $\epsilon_r (\epsilon_0)$	<i>Electron Eff mass</i> $m_e^*(m_0)$	<i>Hole Eff mass</i> $m_h^*(m_0)$	<i>Electron Affinity</i> $E_A(\text{eV})$	<i>Ionization energy</i> $E_i(\text{eV})$	<i>Work function</i> $\Phi (\text{eV})$	<i>Bandgap</i> $BG (\text{eV})$
PEDOT:PSS	17	0.25	1.30	3.60	5.30	4.50	1.70

Table 37: PEDOT:PSS bulk material properties.

NB: Values proposed were correlated with simulations performed in BL4 for the experimental QLED device implemented.

3.4.2.4 Hole Transport Layer - HTL

TFB, or Poly(9,9-dioctylfluorene-alt-N-(4-sec-butylphenyl)-diphenylamine), will be used as hole transport layer (HTL). TFB is a triarylamine based semiconductor. Due to its low ionization potential and high hole mobility, TFB serves primarily as hole transport layer (HTL). When built into device as an interface material, TFB as an electron blocking layer will not only reduce the chance of electron leakage, but also reduce the possibility of exciton quenching between the interface of the active layer and charge transport layer [76]. Thus, TFB layer performs two main functions [79]:

- The small barrier between the highest occupied molecular orbital (HOMO) of PEDOT: PSS and TFB allows facile transport and therefore the injection of holes from ITO to the QD layer [79].

- The high lowest unoccupied molecular orbital (LUMO) of TFB can effectively block injected electrons leading to the confinement of the charges within the QD layer [79].

It is also worth saying here that layer thickness has an influence on material layer parameter[80]. Thus, there is a wide variety of parameter values in the literature. Since the chemical material used has not been characterized, different values have been assumed after a correlation done through simulation with experimental QLED device manufactured.

Table 38 resumes the main properties (bulk) proposed that will be used mainly in the QLED modelling and simulation block BL4 [76], [80], [81].

<i>HTL</i>	<i>Relative permittivity</i> $\epsilon_r (\epsilon_0)$	<i>Electron Eff mass</i> $m_e^*(m_0)$	<i>Hole Eff mass</i> $m_h^*(m_0)$	<i>Electron Affinity</i> $E_A(\text{eV})$	<i>Ionization energy</i> $E_i(\text{eV})$	<i>Work function</i> $\Phi (\text{eV})$	<i>Bandgap</i> $BG (\text{eV})$
TFB	15	0.25	1.30	2.60	5.50	4.50	2.90

Table 38: TFB bulk material properties.

3.4.2.5 Emissive layer - EL

Two different CuInS₂/ZnS quantum dot nanoparticles will be used as emissive layer. CuInS₂/ZnS commercially available from supplier1 (Mesolight) and CuInS₂/ZnS synthesized at the laboratory facilities.

Furthermore, it can be highlighted that after consulting the literature available [82]–[89], material parameters can vary with no common value found. Therefore, correlation done through simulation with experimental QLED device manufactured has been performed, always keeping the magnitude of the values found in the latter references. Thus, Table 39 resumes the main properties values proposed that will be used mainly in the QLED modelling and simulation block BL4.

EL	Relative permittivity $\epsilon_r (\epsilon_0)$	Electron Eff mass $m_e^* (m_0)$	Hole Eff mass $m_h^* (m_0)$	Electron Affinity $E_A (eV)$	Ionization energy $E_i (eV)$	Work function $\Phi (eV)$	Bandgap BG (eV)
CuInS ₂ (core)	8.7	0.16	1.30	4.36	5.86	5.36	1.50
ZnS(shell)	8.9	0.28	0.61	3.90	7.80	6.30	3.90

Table 39: CuInS₂/ZnS bulk material properties.

3.4.2.6 Electron Transpor Layer - ETL

ZnO nanoparticles (NPs) will be used as electron transport layer (ETL). Zinc oxide (ZnO) nanoparticles are inorganic nanomaterials that have a great interest for optoelectronics. In photoelectronic contexts, ZnO is described as a II-VI semiconductor. This novel group of semiconductors exhibits wide bandgaps which enable optoelectronic devices to operate at elevated temperatures, and to generate luminescence at a fraction of the energy cost of incandescent light sources [90]. Thus, ZnO NPs layer performs two main functions [90]:

- High-performance electron transport material.
- The low valence band (VB) of ZnO can effectively block injected holes, leading to the confinement of the charges within the QD layer [79].

Likewise, it can be highlighted that after consulting the literature available [91]–[94], material parameters can vary with no common value found. Therefore, correlation done through simulation with experimental QLED device manufactured has been performed, always keeping the magnitude of the values found in the latter references. Thus, Table 40 resumes the main properties values proposed that will be used mainly in the QLED modelling and simulation block BL4.

ETL	Relative permittivity $\epsilon_r (\epsilon_0)$	Electron Eff mass $m_e^* (m_0)$	Hole Eff mass $m_h^* (m_0)$	Electron Affinity $E_A (eV)$	Ionization energy $E_i (eV)$	Work function $\Phi (eV)$	Bandgap BG (eV)
ZnO	8.5	0.23	1.21	4.30	7.67	5.30	3.37

Table 40: ZnO bulk material properties.

3.4.2.7 Cathode

Aluminum (Al) will be used as cathode electrode. Aluminum has been chosen because it is an excellent thermal and electrical conductor that can be deposited easily through CVD (chemical vapor deposition techniques) and acts as reflector layer to project light out of the QLED device.

Table 41 resumes the main properties (bulk) proposed that will be used mainly in the QLED modelling and simulation block BL4 [62].

CATHODE	Relative permittivity $\epsilon_r (\epsilon_0)$	Electron Eff mass $m_e^*(m_0)$	Hole Eff mass $m_h^*(m_0)$	Electron Affinity $E_A(\text{eV})$	Ionization energy $E_i(\text{eV})$	Work function $\Phi (\text{eV})$	Bandgap BG (eV)
Al	-	-	-	-	-	4.30	-

Table 41: Aluminum bulk material properties.

3.4.2.8 Parameters sum-up

Table 42 summarizes all bulk material parameters proposed that will be used in the QLED modelling and simulation block BL4.

LAYER	Relative permittivity $\epsilon_r (\epsilon_0)$	Electron Eff mass $m_e^*(m_0)$	Hole Eff mass $m_h^*(m_0)$	Electron Affinity $E_A(\text{eV})$	Ionization energy $E_i(\text{eV})$	Work function $\Phi (\text{eV})$	Bandgap BG (eV)
ITO	-	-	-	-	-	4.70	-
PEDOT:PSS	17	0.25	1.30	3.60	5.30	4.50	1.70
TFB	15	0.25	1.30	2.60	5.50	4.50	2.90
CuInS ₂	8.7	0.16	1.30	4.36	5.86	5.36	1.50
ZnS	8.9	0.28	0.61	3.90	7.80	6.30	3.90
ZnO	8.5	0.23	1.21	4.30	7.67	5.30	3.37
Al	-	-	-	-	-	4.30	-

Table 42: QLED Layers (anode-HIL-HTL-EL-ETL-cathode) bulk material properties.

3.4.3 QLED Architecture

Eventually, following energy levels from chapter 3.4.1 and material selected for each layer in chapter 3.4.2, the final QLED architecture is depicted in Figure 58.

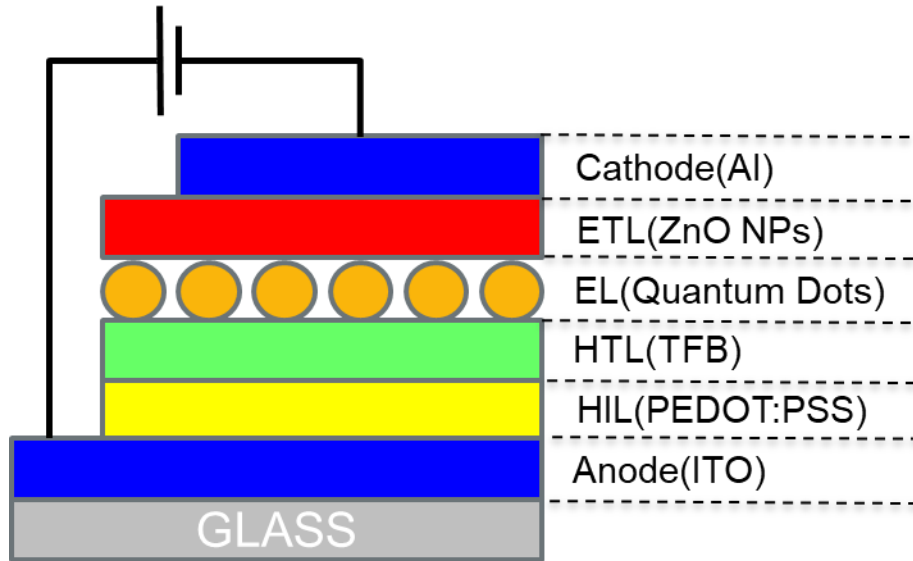


Figure 58: QLED architecture based on energy levels and material layers selection. Designed for this work.

3.4.4 Device Physical Implementation

Finally, once the theoretical structure has been designed and the material layers have been selected due to the optimal compatibility with the energy levels set as target to achieve, the physical design takes place. The mechanical design to make the QLED happen will be developed in the following lines.

Moreover, after making some research about how to implement a hardware architecture for the QLED, it was decided to adapt [76], where OLEDs were developed, as a guideline to complete the latter goal. Then in this work, all the steps followed have been adapted particularly to quantum dots and generally to the QLED device.

Therefore, as defined in layer selection in chapter 3.4.2, a rigid substrate was selected to deposit all different QLED layers. Furthermore, it was decided that ITO material would act as the first electrode (anode) and therefore, it would be the first layer over the glass substrate. On the other hand, ITO deposition is not an easy task because it implies a Chemical Vapor Deposition (CVD) process. In order to simplify the latter, pre-patterned ITO glass substrates were acquired as shown in Figure 59.

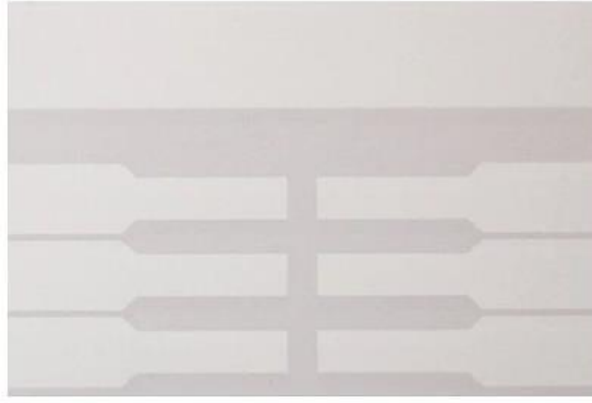


Figure 59: Pre-patterned ITO glass substrates from Ossila. Reproduced from [76].

The great advantage is that ITO is already deposited on the rigid glass substrate in a pre-defined structure. Indeed, this structure is prepared to create and manufacture a 6-pixel lighting device as it will be explained below.

Therefore, each layer defined i.e. HIL, HTL, EL, ETL and cathode will be deposited one by one using different thin-film layers techniques, allowing an active area in the device, as shown in Figure 60, where electrical process takes place.

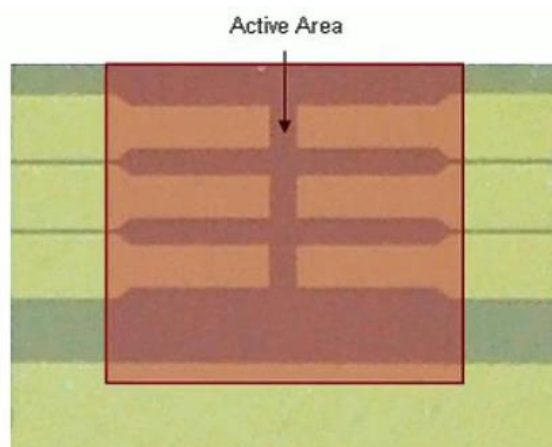


Figure 60: QLED active area from Ossila. Reproduced from [76].

This layer deposition process will be thoroughly explained in QLED manufacturing chapter 3.5. That process is briefly depicted in the following figures reproduced from [76].

3.4.4.1 HIL, HTL, EL, ETL layers deposition

Using spin coating technique, HIL, HTL, EL and ETL layers are deposited on top of each other. As said, this whole process is thoroughly described in chapter 3.5

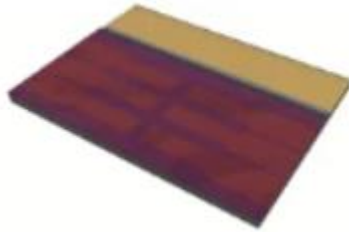


Figure 61: HIL, HTL, EL, ETL layers deposition. Reproduced from [76].

3.4.4.2 CATHODE layer deposition

Cathode (aluminum) is deposited using CVD techniques. As said, this whole process is thoroughly described in chapter 3.5.

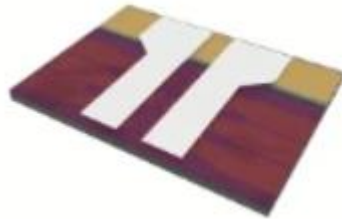


Figure 62: CATHODE layer deposition. Reproduced from [76].

3.4.4.3 Encapsulation

With the encapsulation system, devices can be stored for extended durations with minimum degradation in performance. A drop of our UV-cured epoxy is put on the device and a glass coverslip is put on top before curing in a UV light box [76].

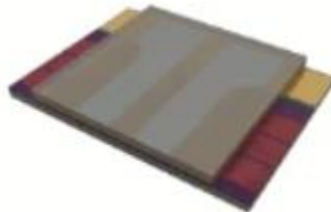


Figure 63: Encapsulation step. Reproduced from [76].

3.4.4.4 *External electrical contacts*

By adding metallic connections, devices can be inserted into most prototyping boards, allowing electrical connection to the six individual pixels [76].

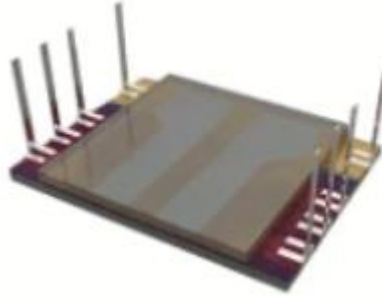


Figure 64: External electrical contacts. Reproduced from [76].

At the end of the process, the following mechanical structure shown in Figure 65 will shape the 6-pixel QLED device. Each individual pixel has a total area of 4.5 mm^2 . This parameter will be used later in the modelling and simulation block BL4.

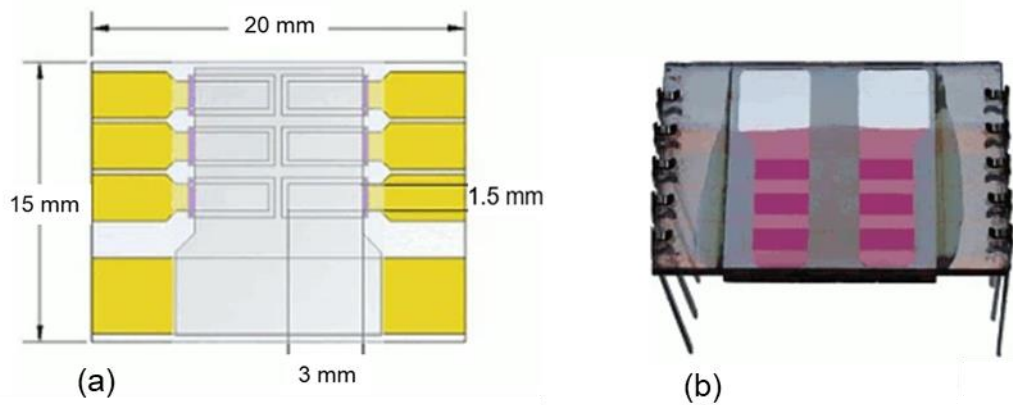


Figure 65: (a) 6-pixel QLED device dimensions. (b) QLED final device. Reproduced from [76].

3.4.5 *Summary*

Finally, it can be stated that a lighting emitting diode based on quantum dots, which are excited with an electrical current passing through, has been utterly defined and designed. Thus, the next step is to physically implement that theoretical development in an experimental QLED device, which will be manufactured in chapter 3.5.

3.5 QLED MANUFACTURING

After making the QLED theoretical design in chapter 3.4, where the whole device architecture (substrate and layer stack-up) were defined, the next step to take is to implement the lighting device physically. This experimental design will be performed following the thin-film layer deposition techniques and laboratory instrumentation, which will be explained in chapter 3.5.2.

3.5.1 *Goals*

By performing this experiment, the following objectives are pursued

- a) CuInS₂/ZnS-based QLED device manufacturing using the quantum dots selected in BL2
- b) Familiarization with nanotechnology thin-film layer deposition techniques

This experiment was carried out at University of Leeds (UoL), particularly in the laboratories of the School of Physics and Astronomy.

3.5.2 *Laboratory Instrumentation*

The specific laboratory techniques and instrumentation used for QLED manufacturing are described below.

- Surface cleaning → UV Ozone cleaner, sonicator
- Layers deposition techniques → Spin coating and thermal evaporation
- Scientific instrumentation → Fume hood, glovebox

There are two main techniques to deposit the different materials so as to build up the QLED layer by layer i.e. spin coating and thermal evaporation techniques. According to the literature and the references previously analyzed, both techniques can be applied to the same QLED building process but at different times depending on the layer to be deposited. In the following lines, both methods will be presented.

3.5.2.1 *SPIN COATING*

Spin coating is used to spread thin films [95] on substrates. The main feature of this technique is to produce uniform films, ranging from a few nanometres to a few microns in thickness [96]. The process consist in depositing a fluid resin onto the center of a substrate, which is spin at high speed [95]. That high speed rotation of the substrate pulls the liquid coating into an even covering. During the rotation, the solvent evaporates to leave the material on the substrate [96]. Final film thickness will depend on the nature of the resin and the parameters chosen for the process [95].

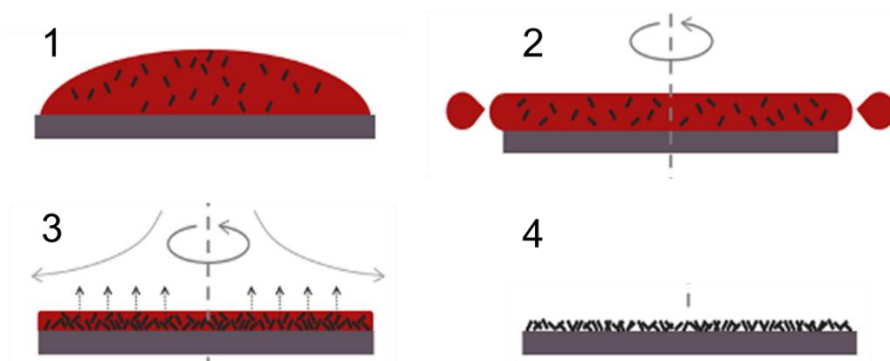


Figure 66: Example of spin coating a small molecule in solution using a static dispense. First the substrate is coated in the ink containing the molecules dissolved in a solvent (1). Then the substrate is rotated at high speed and the majority of the ink is flung off the side (2). Airflow then dries the majority of the solvent leaving a plasticised film (3) before the film fully dries to just leave the molecules on the surface (4). Reproduced from [96].

SCOPE: The use of spin-coating technique will allow the assembly of several layers to form the QLED.

3.5.2.2 THERMAL EVAPORATION

Thermal evaporation is regarded as one of the traditional Physical Vapor Deposition (PVD). This technique is used to apply coatings of materials on the surface of target samples through thin film deposition methods by evaporating materials like metal in a vacuum chamber [97].

SCOPE: The use of thermal evaporation technique will allow the deposition of final Aluminum layer of the QLED.

3.5.2.3 GLOVEBOX

A glovebox is a laboratory container designed to manipulate object in specific atmosphere conditions. It is composed of gloves arranged to perform that manipulation inside the box without breaking the sealing of the container. One type of glovebox allows the user to work with substances in a high purity inert atmosphere, such as argon or nitrogen [17].



Figure 67: Glovebox container from MBRAUN® to be used with inert atmospheres. Reproduced from [70].

SCOPE: The use of the glove box could give the chance to work in a specific inert atmosphere to build up the QLED in the optimal conditions.

3.5.2.4 UV OZONE CLEANER

UV Ozone cleaning is a technique used to remove contamination and residual organics from the surface of samples. After this cleaning process, where the surface contaminants break down into volatile compounds thanks to the ozone generated by using a UV light source, atomically clean surfaces and free from organic contaminants are achieved [76].



Figure 68: UV Ozone Cleaner used. Reproduced from [76].

SCOPE: UV ozone cleaner will be used to clean the QLED substrate before depositing the thin film layers of the optoelectronic device.

3.5.2.5 SONICATOR

Ultrasonic cleaners use the acoustic cavitation physical effect to clean objects. This technique is specifically useful for surface decontamination due to the cavitation produced in a liquid medium. In this manner, by introducing the object in the sonicator with a specific liquid and detergent, cavitation is formed due to the ultrasonic waves generated traveling through that liquid, which are used to remove dirt from the object surface. Those ultrasonic waves create cavities in the liquid and thanks to the repetitive collapse in specific areas, the cleaning action is achieved [98].

SCOPE: Sonicator will be used to remove the dirt from the QLED substrate before introducing it into the UV ozone cleaner previously described.

Table 43 makes a short summary of the techniques and tools used for the QLED device manufacturing process.

QLED	Technique	Tool	*Site
Layers depositions	Spin coating	Spin coater	UoL
	Thermal evaporation	Vacuum evaporator	UoL
	Inert atmosphere	Glovebox	UoL
Chemicals Substrate	Chemicals preparation	Fumehood	UoL
	Surface cleaning	UV Zone cleaner, sonicator	UoL

Table 43: Summary of instrumentation used for QLED manufacturing.

* University of Leeds (UoL)

3.5.3 Experimental Design 3: QLED physical implementation

This chapter is divided into five parts. The first one corresponds to the chemical materials used in the QLED device implementation. The second part is related to the substrate preparation to go on to the third part afterwards, where all layers are deposited consecutively. Finally, the last parts are devoted to the encapsulation process with the objective to embed all layers and isolate them from the external environment, along with the external metallic contacts device fitting.

The QLED manufacturing process followed can be found in many references in the literature [61]–[63]. Those have been adapted to the one described in [76], where it is possible to find a fabrication guideline focused on Organic Photovoltaics (OPV) and Organic Lighting Emitting Diodes (OLED). Therefore, the novelty is based on the fact that a mix between QLED and OLED fabrication processes have been used to finally implement our specific QLED device. Thus, different physical processes have been used to generate a 6-pixel optoelectronic device over the same substrate with the objective to compare the electrical behavior of each pixel independently and to generate a computational model (BL4) so as to support and improve the QLED fabrication process in the future.

Eventually, it is worth saying that it is recommended that the whole QLED manufacturing process should be performed inside the glovebox to achieve an inert and controlled atmosphere. However, due to some technical limitations found during the project development, the QLED was built out of the glovebox. Thus, although the optoelectronic device worked properly, a possible reduction in the global device efficiency in time was expected. Particularly, the lifetime of the QLED or the output luminous flux could have been affected and reduced due to the fabrication process.

3.5.3.1 Chemical base materials

Following the QLED architecture chosen in chapter 3.4, where the lighting device was designed, the final structure selected is depicted in Figure 69.

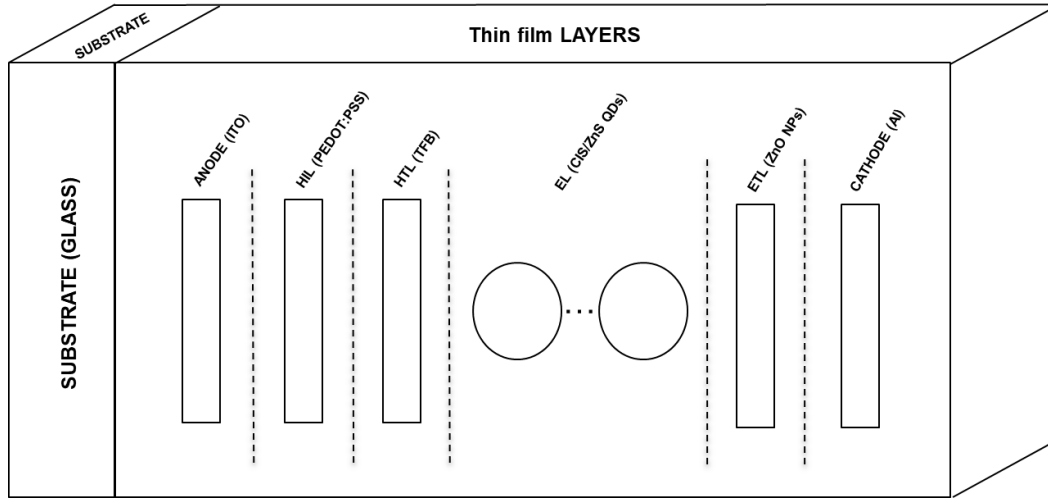


Figure 69: QLED architecture chosen: substrate + thin film layer. Designed for this work.

All chemical components and materials used during the manufacturing process of QLED are listed below:

IPA (Isopropyl alcohol), Decon™ 90, PEDOT:PSS - Al 4083 (Poly(3,4-ethylenedioxythiophene) polystyrene sulfonate), TFB (Poly(9,9-dioctylfluorene-alt-N-(4-sec-butylphenyl)-diphenylamine)) (99%), Chlorobenzene (99.8%), CuInS₂/ZnS quantum dots, ZnO NPs (Avantama N-10), Aluminum, UV curable epoxy.

NB: PEDOT:PSS and TFB materials were acquired from Ossila® and ZnO NPs were acquired from Avantama®.

3.5.3.2 Substrate cleaning

Firstly, it is necessary to clean the substrate thoroughly. That glass rigid substrate was selected when QLED was designed in chapter 3.4. Particularly, the substrates acquired were pre-patterned Indium Tin Oxide (ITO) substrates. It means that ITO material, used for the anode electrode of the QLED, was already incorporated in the substrate. Substrates require a simple pre-cleaning routine, which takes 20 minutes, to remove dirt and dust and create a pristine and hydrophilic ITO surface [76].

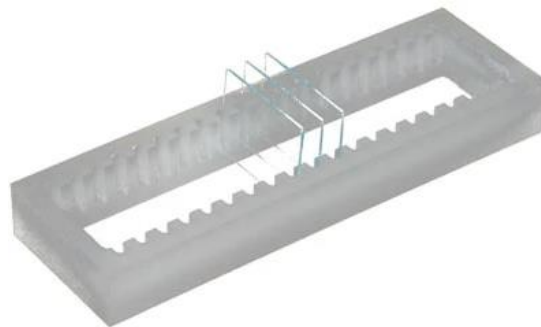


Figure 70: Cleaning rack containing the pre-patterned ITO substrates. Reproduced from [76].

The first step was to load the pre-patterned ITO substrates into a cleaning rack. Then the loaded substrate rack was submerged in a beaker filled with 10% Decon90 cleaning solution. That substrate rack was placed afterwards in a sonicator for 5 minutes and rinsed 5 times in ultrapure water after the sonication bath. This first cleaning process was repeated again but using IPA (isopropanol) instead of Decon90.



Figure 71: Sonication process for the pre-patterned ITO substrates at UoL.

Once the first cleaning process had been finished, the substrates were blow-dried with a N_2 gun and introduced into a UV Ozone cleaner for 10 minutes. That ultraviolet light and ozone atmosphere create a pristine and hydrophilic ITO surface.

3.5.3.3 Layers deposition

3.5.3.3.1 ANODE (ITO)

As it was explained in the substrate cleaning process, the substrates purchased were pre-patterned ITO (Indium Tin Oxide) substrates. Thus, there was no need to deposit that on the substrate.

3.5.3.3.2 HIL (PEDOT:PSS)

Obtaining a high quality PEDOT:PSS film is critical for effective device performance and it is often the most difficult part of device fabrication [76]. PEDOT:PSS requires a pristine, hydrophilic surface in order to coat properly. That step was achieved with the cleaning routine above.

The grade and composition of PEDOT:PSS is also very important. Heraeus Clevios™ P AI 4083 was used. Before depositing the layer, a filtering process consisting on putting 2 ml of PEDOT:PSS in a solvent safe syringe ended in a 0.45 μm PES (hydrophilic) filter was performed and stored in an amber solvent resistant vial [76].

Then, PEDOT:PSS filtered was deposited on the ITO substrates by spin coating technique at 5000 rpm for 30 seconds to produce a film thickness of ~ 20 nm.



Figure 72: Applying PEDOT:PSS on the substrate using the spin coater. Reproduced from [76].

Finally, after HIL deposition is made by spin coating technique, two more actions are needed. Firstly due to ITO-patterned design chosen, it is necessary to clean the cathode area with chlorobenzene solvent and remove PEDOT:PSS from that area to wipe free the cathode strip [76] for the last aluminium layer deposition.

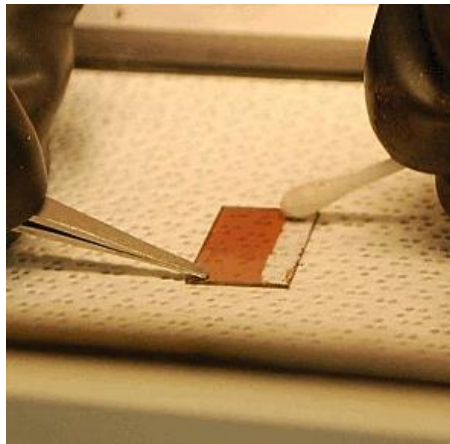


Figure 73: Cathode area to be wiped free after spin coating. Reproduced from [76].

Eventually, the substrate was placed on a hotplate at 150 °C for 30 minutes to cure and remove the water from the HIL layer, and placed to cool at room temperature.

3.5.3.3.3 HTL (TFB)

Before depositing HTL layer, it is necessary to make a solution of 80 mg of TFB with 10 ml of chlorobenzene. This mix was prepared inside the fume hood for safety reasons and put in an amber solvent resistant vial through a solvent safe syringe ended in a 0.1 μm PTFE (hydrophobic) filter.

Then, filtered TFB was deposited on the substrate, just above HIL layer, by spin coating technique at 4000 rpm for 30 seconds to produce a film thickness of ~ 30 nm.

Finally, after HTL deposition has been made by spin coating technique, we proceed in the same way as done for HIL layer. Cathode area is cleaned with chlorobenzene and the substrate is put on a hotplate at 150 °C for 30 minutes to cure, and placed to cool at room temperature.

3.5.3.3.4 EL (CuInS₂/ZnS QDs)

For emission layer deposition, two batches of samples were prepared. First batch used commercially acquired quantum dots (from supplier1: Mesolight®), already characterized on chapter 2.2. Second batch was prepared with quantum dots synthesized in the laboratory and defined on chapter 2.3.

Following the same strategy as done for the other layers, colloidal quantum dots solutions were deposited on the substrate, just above HTL layer, by spin coating technique at 2000 rpm for 20 seconds to produce a film thickness of ~20 nm.

Eventually, after EL deposition had been made by spin coating technique, we proceeded in the same way as done for HIL layer. Cathode area was cleaned with chlorobenzene and the substrate was put on a hotplate at 60 °C for 15 minutes to cure, and placed to cool at room temperature.

3.5.3.3.5 ETL (ZnO NPs)

Before depositing ETL layer, ZnO nanoparticles suspended in 2-propanol were put in an amber solvent resistant vial through a safe syringe ended in a 0.1 µm PTFE (hydrophobic) filter. Then, ZnO NPs were deposited on the substrate, just above EL layer, by spin coating technique at 1500 rpm for 60 seconds to produce a film thickness of ~35 nm.

Finally, after ETL deposition had been made by spin coating technique, we proceeded in the same way as done for all layers. Cathode area was cleaned with chlorobenzene and the substrate was put on a hotplate at 60 °C for 30 minutes to cure, and placed to cool at room temperature.

3.5.3.3.6 CATHODE (Aluminum)

The last layer to be conformed is the cathode one. The material used is aluminum, thus a different thin-layer deposition technique from spin coating was put in place. Thereby thermal evaporation technique was used to create the last metallic contact with the support of a metallic shadow mask previously cleaned with IPA.



Figure 74: Vacuum evaporator used at UoL.

Likewise, the substrates were placed face down in the vacuum thermal evaporation shadow mask with the cathode strip at the wide end of the apertures. This was the only time the substrates were placed with the active layer face down [76].

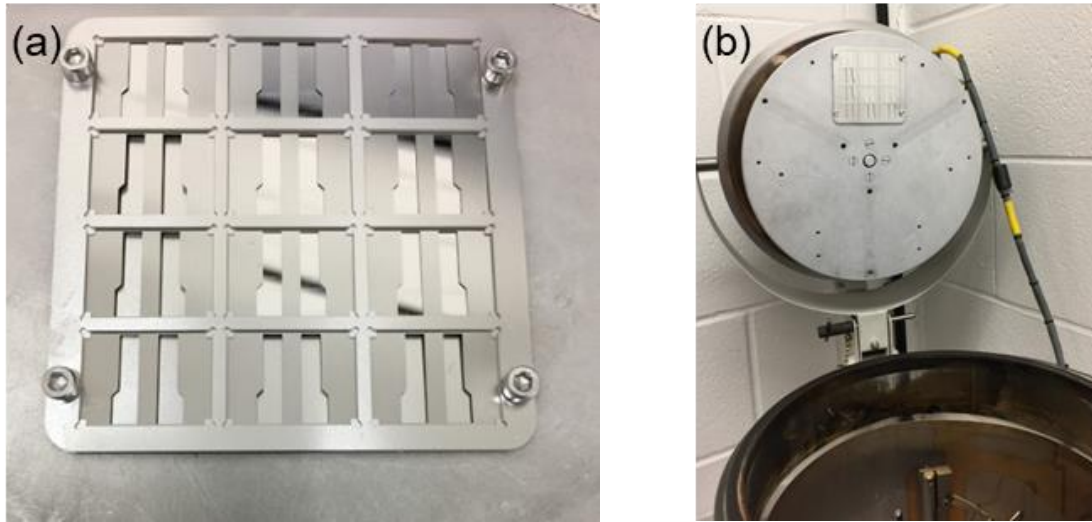


Figure 75: (a) Shadow mask used for cathode layer deposition. (b) Mask located inside the vacuum evaporator. Designed for this work.

Then, cathode mask was put inside the evaporator and ~ 100 nm of Al were deposited on ETL layer with an evaporation rate of 1.5 \AA/s . Eventually, the substrate was placed on a hotplate at 150°C for 15 minutes for annealing purposes, and placed to cool at room temperature.

3.5.3.4 Encapsulation

After cathode deposition has been implemented, an encapsulation process was performed [76]. The encapsulating goal is to protect the devices against degradation by oxygen and moisture. Thus, UV curable epoxy was placed just above the active layer and a glass coverslip on top of the substrate. After that, a curing process was carried out by using a low power UV light (of 380 nm) over the course of about 30 minutes.



Figure 76: Device encapsulation process. Reproduced from [76].

3.5.3.5 *External metallic contacts*

Finally, to complete the manufacturing of the QLED device, metallic legs were used to connect and access electrically to each independent pixels anodes and the common cathode device [76].

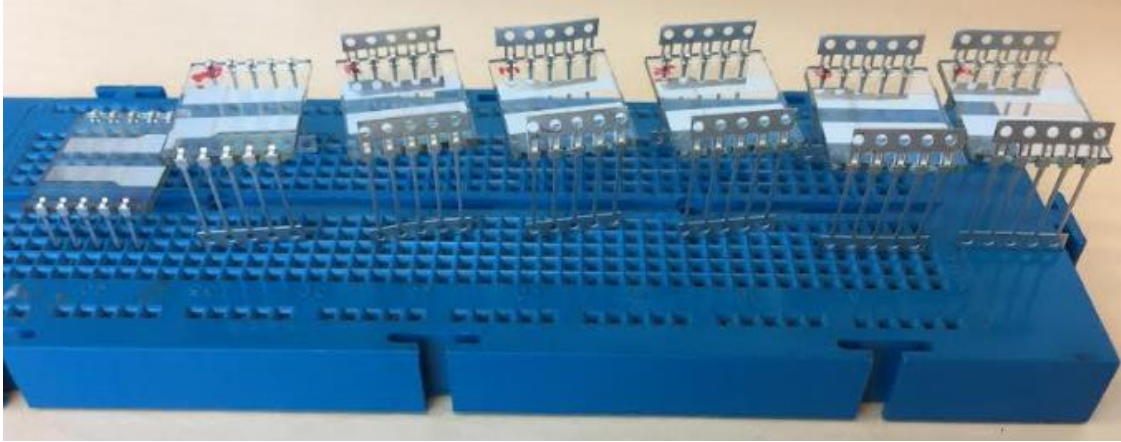


Figure 77: Final QLED devices manufactured in this work.

3.5.4 *Summary*

Eventually, some general conclusions from this QLED device manufacturing chapter 3.5 may be set. As it was described at the beginning of 3.5, two main objectives were pursued. Firstly, the manufacturing of a $\text{CuInS}_2/\text{ZnS}$ -based QLED device with independent pixels or segments over the same substrate by using the quantum dots selected in BL2. Secondly, a familiarization with nanotechnology thin-film layer deposition techniques.

Thereby, both goals have been completed by following the QLED design defined in chapter 3.4. Now the next step to take will be the electrical characterization of the device manufactured with the main objective to obtain the I-V curve behavior of the QLED for each pixel or segment.

3.6 QLED CHARACTERIZATION

Once the QLED has been manufactured in chapter 3.5, where the whole device architecture (substrate and layer stack-up) designed in chapter 3.4 has been implemented physically, the next step is to electrically characterize the lighting device. This experimental design will be performed following basic electronics techniques to finally obtain the I-V performance curve of each pixel individually.

3.6.1 *Experimental Units*

The experimental units used here are the QLEDs manufactured in chapter 3.5. These QLEDs were fabricated with two different CuInS₂/ZnS quantum dot nanoparticles. CuInS₂/ZnS commercially available from supplier1 (Mesolight®) and CuInS₂/ZnS synthesized in the laboratory facilities. Figure 78 shows the QLEDs manufactured when an electrical current is applied on both configurations.

a) QLED batch 1: CuInS₂/ZnS-based QLED from supplier1 (Mesolight)

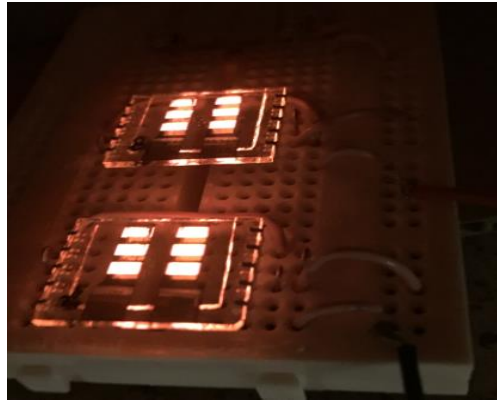


Figure 78: QLED1. Electrically excited devices fabricated in this work.

Although the electroluminescence (EL) output spectrum was not measured, red color was achieved as expected. It means the recombination of electrons and holes was taking place in the QD layer since those quantum dots had a photoluminescence (PL) output spectrum centered at 622 nm. Therefore, it is possible to conclude that QLED device was working in electroluminescent physical phenomenon as it was assumed.

b) QLED batch 2: CuInS₂/ZnS-based QLED synthesized at UoL laboratory facilities

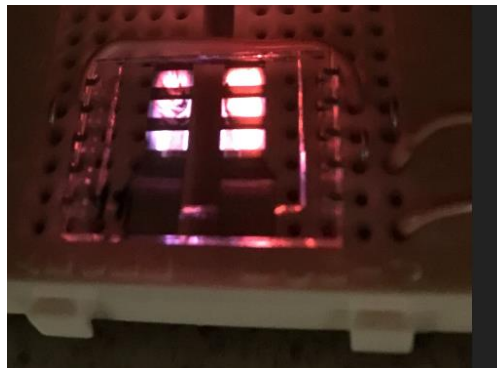


Figure 79: QLED2. Electrically excited devices fabricated in this work.

Nevertheless, although the electroluminescence (EL) output spectrum was not measured, it was color shifted related to batch1. Moreover, the homogeneity was not utterly achieved and areas inside the own pixels appeared with different levels of luminosity. The first conclusion extracted is that the electron-hole recombination was not taking place in the quantum dot layer but between the other deposited layers, probably at ETL. After some research on the possible issue, the second conclusion is stated after reviewing in detail some literature. Particularly, in [62] it is said that in QDs synthesized using DDT (1-dodecanethiol), which serves as an organic surface ligand, the charge injection and transport across the QD emission layer (EML) were rather limited, leading to low levels in current flow [62]. This is due to the fact that DDT derives into a longer (more insulating) alkyl chain when a QD surface is capped [62]. Thus, other different surface ligands, like 1-octanethiol (OTT), need to be considered if electroluminescent devices want to be manufactured. This happens when QDs are capped with DDT, which has a longer (more insulating) alkyl chain versus OTT.

In conclusion, QLED from batch 1 i.e. CuInS₂/ZnS-based QLED from supplier1 (Mesolight) will be used to characterize the I-V curve since better performance was achieved.

3.6.2 Goals

By performing this experiment, the following objective is pursued

- a) Current versus Voltage (I-V) curve from QLED batch 1: CuInS₂/ZnS-based QLED from supplier1 (Mesolight®)

3.6.3 Laboratory Instrumentation

To make it possible the following scientific devices are presented below.

-Current versus Voltage (I-V) curve → Source meter to make an I-V (current-voltage) analysis.

This experiment was carried out at Universidad de Granada. To measure the I-V performance a Source Meter Unit (SMU) instrument is needed. This electronics laboratory tool is described as follows.

3.6.3.1 SOURCE METER

A Source Meter Unit (SMU) is an instrument that outputs a voltage and measures the current that flows. Unlike power supplies, the SMU is programmable and allows us to make a sweep of the voltage over a defined range, offering a more accurate data than a regular power supply [76].



Figure 80: Ossila lifetime system used as SMU unit to measure I-V curves. Reproduced from [76].

SCOPE: The use of the source meter will allow us to perform an I-V analysis of the QLED manufactured.

Table 44 makes a short summary of the technique and tool used for these measurements.

QLED	Technique	Tool	Brand	Site
Current - Voltage	I-V analysis	Source meter	OSSILA	UGR

Table 44: Summary of measurement tools used for QLED manufacturing.

3.6.4 Experimental Design 4: QLED electrical characterization

Once the main objective of this experiment had been set, the electrical characterization of the QLED manufactured was performed. By using the SMU device, an electrical current was injected through each QLED individual pixel. At the same time the voltage drop across that pixels was measured. Figure 81 was extracted from the experiment performed.

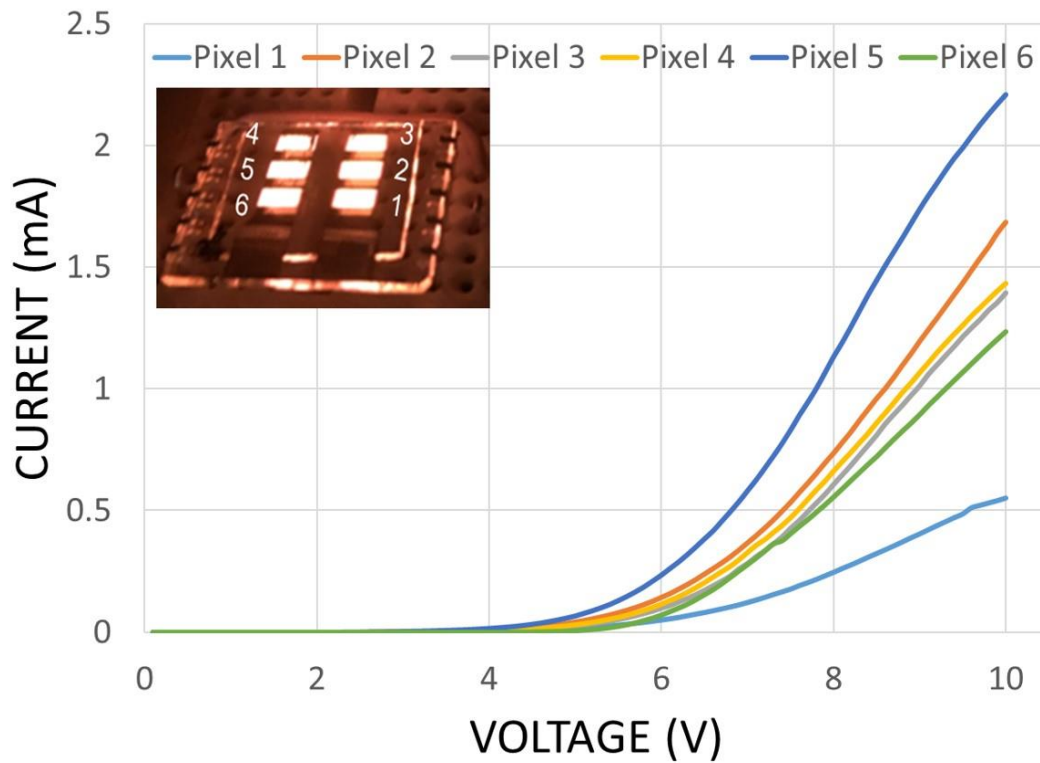


Figure 81: Figure illustrating the fundamental QLED I-V curve measured in this work and tempted to modelling.

Figure 81 shows different I-V curves depending on the pixel measured. The current difference shown is due to variability in the manufacturing process. Since it is a prototype where the main thin film deposition technique is performed by spin-coating as laboratory tool, the thicknesses of the different layers that conform the QLED are not uniform. This leads to different electrical behaviors for each pixel. These different electrical behaviors found for each individual pixel will be analyzed in BL4,

through a computational proposal that model the electrical behavior of the QLED experimentally fabricated and characterized.

3.6.5 *Summary*

Eventually, some general conclusions from this QLED device characterization chapter 3.6 may be set. As it was described at the beginning of 3.6, the main objective of current-voltage QLED curve measurement was set as target. The QLED selected was the one from batch 1 i.e. CuInS₂/ZnS-based QLED from supplier1 (Mesolight®). That decision was based on the output spectrum that was centered in red color and the best performance obtained. On the other hand, the QLED from batch 2 i.e. CuInS₂/ZnS-based QLED synthesized at UoL laboratory facilities was discarded since the output wavelength (blue shifted) was not achieved as expected. The root cause was identified in the quantum dots synthesized, where surface ligands were not correctly selected and therefore the correct working point of the electroluminescence devices was compromised.

Finally, the electrical characterization of QLED from batch1 was achieved. I-V curves for all pixels were extracted. Those measurements will be useful for the next BL4, where the modelling of the electrical behavior of the QLED is pursued in order to understand the differences between each electrically excited pixels and to propose some possible improvements to support the manufacturing QLED process.

3.7 CONCLUSIONS

In this block BL3, CuInS₂/ZnS QDs analyzed in block BL2 have been used to research two types of QDs-based lighting devices, focusing on the two possible physical phenomena that may excite those nanoparticles i.e. photoluminescence and electroluminescence. These phenomena derive into two kinds of structures, QDF and QLED respectively.

Furthermore, it had been concluded that the electroluminescence physical mechanism was going to be researched due to the more challenging and innovative angle since there are already market suppliers who offer high quality QDF for consumer electronics. Thus, a QLED device was designed, manufactured and characterized.

Therefore, different batches of QLEDs were designed and manufactured, using and combining different procedures and chemical materials (commercial QDs and laboratory-synthesized QDs) and adapting those to a specific substrate made up of six independent pixels or segments. Then, the QLED was characterized and the I-V curve was extracted for each individual pixel, something key in the investigation to be able to study the electrical behavior of each independent segment. It was concluded that the different electrical behaviors are related to parameters dependent on the manufacturing process. Thus, the next step is to propose some improvements in the design and fabrication process once the QLED is modelled in the block BL4, which will allow us to identify the root cause of those electrical differences.

Besides, it can be stated that all objectives defined at the scope of the block relating to the QLED design, manufacturing and characterization have been achieved.

QLED DESIGN

- a) QLED energy levels target has been analyzed
- b) Layers selection depending on the target above have been selected

QLED MANUFACTURING

- c) CuInS₂/ZnS-based QLED device manufacturing using the quantum dots selected in BL2
- d) Familiarization with nanotechnology thin-film layer deposition techniques

QLED CHARACTERIZATION

- e) Current versus Voltage (I-V) curve from QLED batch 1: CuInS₂/ZnS-based QLED from supplier1 (Mesolight) has been measured

Thereby, it is confirmed that a QLED device based on electroluminescence phenomenon can be manufactured and measured relating to electrical I-V parameters. Thus, based on the previously exposed, the QLED device manufactured will be modelled in next block BL4 to create a simulation tool able to reproduce the electrical behavior already obtained.

4 BL4 – QLED MODELLING

4.1 SCOPE

As it can be extracted from the initial research plan, the goal to be achieved consists in creating an electronic transport model for the whole QLED system i.e. anode-ETL-QD-HTL-cathode. The purpose behind the latter is to draw the I-V characteristic, the charge distribution and the band diagram of the QLED device.

This computational model of the QLED experimentally designed, fabricated and characterized will allow us to understand the different electrical behaviors observed for each independent QLED segment. Thus, a literature research on the possible simulation methods was performed in first place, identifying one possible computational strategy to be adapted to our experimental QLED device designed. Based on the strategy found in the literature, our upgraded model was adapted to the optoelectronic device fabricated, creating a new simulation tool able to simulate the electrical behavior and allowing us to correlate the experimental results obtained in BL3.

Once the results are analyzed and the root causes of those different electrical behaviors are identified some proposals will be made in order to improve the QLED design in the future. In addition, this new QLED simulation tool will allow us to make further research on these optoelectronic devices from a theoretical point of view, before going to the laboratory to physically implement the QLED. Moreover, thanks to that simulation tool, other design possibilities like introducing new layer materials or even different QDs could be explored.

4.1.1 Research Plan

Having a look into the research plan defined at the beginning of the PhD project, it is possible to depict graphically the location level of this block inside the bottom-up methodology presented.

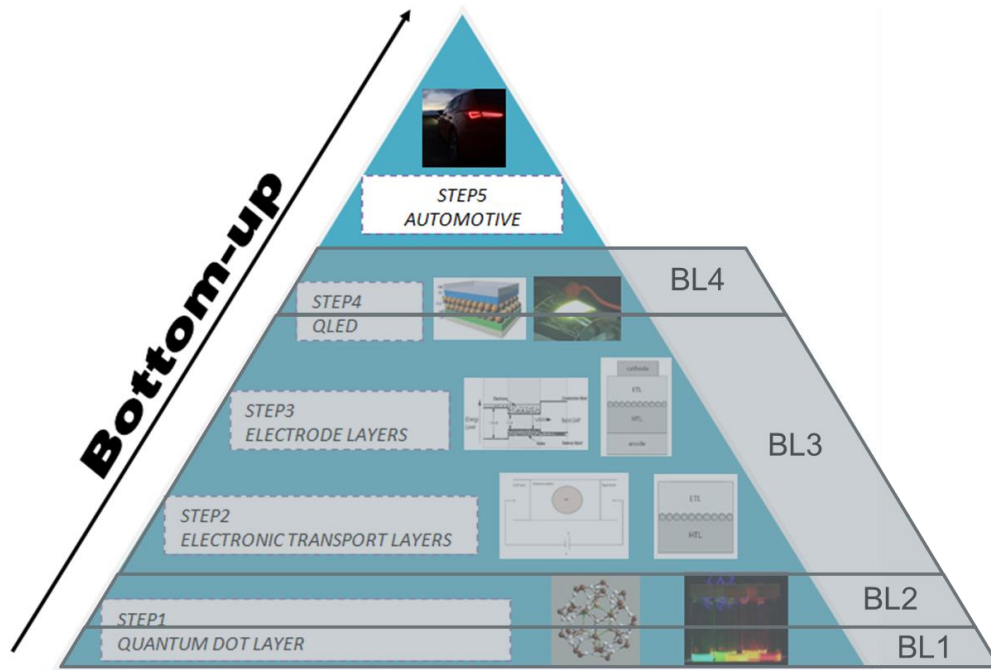


Figure 82: Block BL4. BOTTOM-UP methodology.

4.2 QLED SIMULATOR

Therefore, a QLED simulator (*QLEDsim*) has been proposed. The advantages of having a simulation tool able to perform electrical performance of a QLED system are appreciated. Additionally, this QLEDsim will enable us to

- Correlate electrical behavior from QLED designed and manufactured
- Find the optimal QLED structure (Anode/HTL/EL/ETL/Cathode)
- Design and test new materials before going to experimental manufacturing in the future

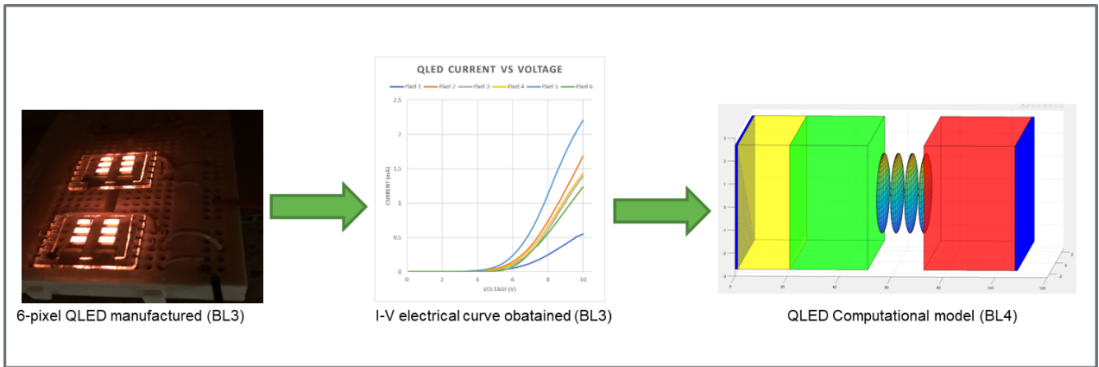


Figure 83: General goal of BL4 by creating the QLED simulator: *QLEDsim*. Designed for this work.

4.2.1 Literature research

The first step before designing the QLED simulator is to find out what kinds of numerical and computational methods could lead to the best solution in terms of

- Accuracy in the I-V curve calculation
- Correlation with experimental results
- Computational power implications

It is possible to extract a wide range of computational methods available that could fit with the purpose pursued. Some of them have been extracted from [99] and shown in Table 45 and Figure 84.

Computational model vs Applications				
COMP MODEL				
Drift-diffusion				
Hydrodynamic				
Monte Carlo				
Schrödinger equation				
Green's function				
APPLICATIONS	Nanowires, superlattices	Ballistic transistor	Present time ICs	Older ICs

Table 45: Relationship between various transport regimes and significant device scales. Adapted from [99].

Approximate					Easy, fast
Semiclassical approaches	MODEL	IMPROVEMENTS			
	Compact models	Appropriate for circuit design			
	Drift-diffusion equations	Good for devices down to 0.5μm, include μ(E)			
	Hydrodynamic equations	Velocity overshoot effect can be treated properly			
	Boltzmann transport equation Monte Carlo/CA methods	Accurate up to the classical limits			
Quantum approaches	Quantum hydrodynamics	Keep all classical hydrodynamic features + quantum corrections			
	Quantum Monte Carlo/CA methods	Keep all classical features + quantum corrections			
	Quantum-kinetic equation (Liouville, Wigner-Boltzmann)	Accurate up to single particle description			
	Green's functions method	Includes correlations in both space and time domain			
	Direct solution of the <i>n</i> -body Schrödinger equation	Can be solved only for small number of particles			
Exact					Difficult

Figure 84: Illustration of the hierarchy of transport models. Adapted from [99].

Therefore, based on the three points above i.e. accuracy, experimental results correlation and computational power used, the different possibilities found in literature were studied. Drift-diffusion method was first checked due to its simplicity in a simulator implementation. Nevertheless, the accuracy of the outcome was not at the level expected since our QLED device works in a nanometric scale. It means that drift-diffusion semiclassical approach does not fit the physical behavior of the QLED designed, where the dimensions of transport and emissive layers are below the limits for the latter computational method. Indeed, as shown in Figure 84 above, that approach is recommended for devices down to 0.5 μm .

Furthermore, other methods were considered like Non Equilibrium Green Function Formalism (NEGFF) or direct solution of the n -body problem Schrödinger equation through Density Functional Theory (DFT). However, although better accuracy could be achieved due to the possible quantum methods used, the power computational cost was very high to be considered in a final simulator implementation.

Eventually, after checking a wide range of methods and approaches that could lead to the modelling of the QLED device fabricated, it was decided to make use of the method known in literature as *Transfer Hamiltonian* approach, which is usually employed to describe the tunneling processes in different devices [100]. That theory has been thoroughly studied by many authors and treats the tunneling events as a perturbation [100], [101]. The theoretical development behind the latter and the implementation of it in a real simulation tool is introduced in the following chapters.

4.3 TRANSFER HAMILTONIAN APPROACH

4.3.1 Definition

The Transfer Hamiltonian method was first introduced by Bardeen [102], to the case of solid junctions [101], to calculate the current passing through a planar tunnel junction when a small bias V is applied between the electrodes [103]. The system, consisting in two electrodes in contact with an insulating layer, is conceptually shared in two parts, called the left and right parts, L and R, limited by a surface Σ [103] as shown in Figure 85.

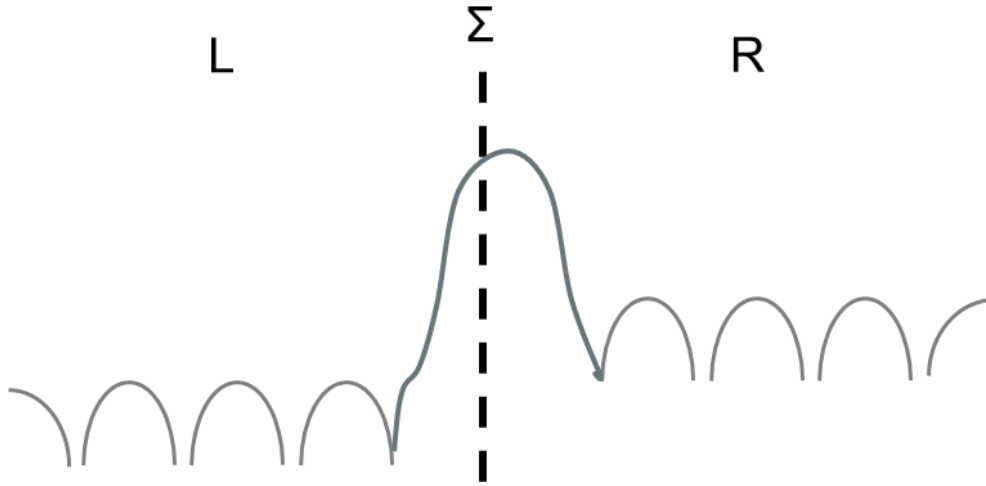


Figure 85: Geometry of the tunneling system with two electrodes and the insulating barrier: the system is shared into a left and a right part by a boundary Σ entirely located in the barrier. Adapted from [103].

Generally, to analyze the physics of tunneling in complex systems, transfer Hamiltonian formalism is available. It is derived from time dependent perturbation theory, by which, multidimensional and many body effects may be included [101]. It has been successfully applied to a number of problems including tunneling between a superconductor and a normal metal, and inelastic tunneling due to interaction between tunneling electrons and vibrational modes of molecules in the tunnel barrier [104].

As well explained in [104], the Transfer Hamiltonian technique is based on the separation of the tunnel system into subsystems. Each of them consists of a single electrode connected to a semi-infinite barrier as depicted in Figure 86, in the case of a tunnel junction containing a homogeneous potential barrier between two electrodes.

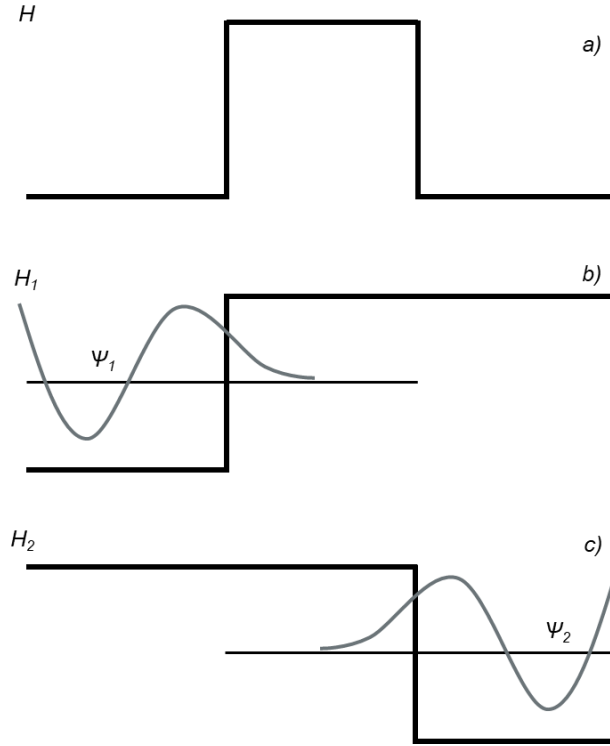


Figure 86: (a) A tunnel junction with a homogeneous barrier. (b) and (c) The two electrode barrier subsystems used in the transfer Hamiltonian description of the junction. Adapted from [104].

These subsystems are described by Hamiltonians H_1 and H_2 . The eigenstates of the subsystems Ψ_1 and Ψ_2 and their energies E_1 and E_2 are defined by

$$\begin{aligned} H_1 \Psi_1 &= E_1 \Psi_1 \\ H_2 \Psi_2 &= E_2 \Psi_2 \end{aligned} \quad (1)$$

The probability of tunneling from left to right is assumed to be the perturbative parameter [103]. The matrix element for the transition $\Psi_1 \rightarrow \Psi_2$ is given by Bardeen [102] where the integral is taken over any surface in the barrier.

$$M_{1 \rightarrow 2} = \left(\frac{\hbar^2}{2m} \right) \int_S (\Psi_1 \nabla \Psi_2^* - \Psi_2^* \nabla \Psi_1) \cdot dS \quad (2)$$

Finally, by introducing the energy distribution function in each part of the barrier, the total tunneling rate from all occupied states on the left part1 to all unoccupied states on the right part2 can be assessed [100]. The opposite tunneling rate can be calculated in a similar way. Thus, assuming symmetry in the transmission coefficient and taking the Fermi golden rule form, it is possible to write the net tunneling current [100]–[104]:

$$I_{12} = \frac{4\pi q}{\hbar} \int |M_{12}|^2 \rho_1(E) \rho_2(E) (f_2(E) - f_1(E)) dE \quad (3)$$

where $|M_{12}|^2$ is the transmission coefficients, $f_1(E)$ and $f_2(E)$ are the Fermi distribution functions and $\rho_1(E)$ and $\rho_2(E)$ are the density of states. A factor of 2 has been taken into account due to the spin. From this expression, it can be seen that only ballistic transport has been considered i.e. the electron does not undergo energy loss scattering processes when it moves through the barrier [100].

Furthermore, using that approach the whole system can be described as independent subsystems connected by a transmission probability through the dielectric media [100]. Generally, for a more complex system, it is possible to define the current flowing between two parts (i,j) of the latter. Assuming no inelastic scattering and symmetry in the transmission coefficient [105] as stated above, the net current flux between two parts of the system can be written as

$$I_{ij} = \frac{4\pi q}{h} \int T_{ij}(E) \rho_i(E) \rho_j(E) (f_j(E) - f_i(E)) dE \quad (4)$$

where $T_{ij}(E)$ is the transmission probability, $\rho_i(E)$ and $\rho_j(E)$ are the density of states and $f_i(E)$ $f_j(E)$ are the non-equilibrium energy distribution functions in each side of the barrier. These distribution functions take into account how the energy levels are filled f_j or emptied $(1 - f_j)$, as it is expected the electron transport only occurs if the initial state is filled and the final state is empty. However, the distribution function of each part of the system is unknown [100].

Although the Transfer Hamiltonian method is less general than other theories, it has some quite attractive aspects, such as its relative simplicity and transparent physical interpretation, which opens the possibility of analytical investigations [101].

4.3.1.1 *The QLED model*

Once the method to extract the I-V curve has been identified i.e. Transfer Hamiltonian approach, it is necessary to define how the latter will be applied to our QLED device system as a whole. In this way and following the same strategy proposed by Illera *et al.* [100], [105]–[109], a set of non-coherent rate equations (NCRE) to study electrical transport in the QLED layers have been applied taking into account self-charge effects. Thus and based on Transfer Hamiltonian approach described in 4.3.1, each QLED layer has been processed as an individual subsystem associating a NCRE equation for each one. That equation describes the relationship between the charge inside the layers, which depends on the tunnel probability of the barriers limited for each layer and the applied bias voltage. Furthermore, the interactions between the QDs and between the QDs and the other layers are introduced by transition rates and capacitive couplings taking into account the density of states (DOS) [109]. Eventually, so as to solve the multielectron problem, the effects of the local potential are computed within the self-consistent field (SCF) regime [100], [109].

Having a close look at the work developed by Illera *et al.* it is possible to check that there are some differences compared to the QLED device proposed in this work. As explained by Illera *et al.* [100], [105]–[109], they present a model of electron transport through a random distribution of interacting bare quantum dots (Si) embedded in a dielectric matrix (SiO_2) connected to the electrodes to simulate some particular devices.

As well described in [100], the basics of the device developed by Illera *et al.* is in essence an insulator layer sandwiched between two metallic electrodes. Inside the insulator layer, a random distribution of N quantum dots has been included. Nevertheless, our work is based on quantum dots in core/shell ($\text{CuInS}_2/\text{ZnS}$) structures (not bare QDs as in Illera *et al.* work) embedded between different transport layers (hole injection/transport layers and electron transport layers) connected to the electrodes.

Therefore, the architecture proposed in our work is different and implies a different simulation approaches (although the Transfer Hamiltonian method is used) and the theoretical framework proposed by Illera *et al.* has been followed and adapted to our specific QLED device.

Moreover, the devices that Illera *et al.* work is targeting are mainly MOS transistors and solar cells (different from the QLED we are pursuing). This is a remarkable difference, since the quantum dots are synthesized in a distinct way in reality. Thus, bare Si quantum dots insulated in a SiO_2 block are normally fabricated through epitaxial processes. However, our work is proposing colloidal quantum dots (quantum dots in core/shell, incorporated in a liquid solvent) which are depositing layer by layer using thin-film deposition techniques. This also implies different considerations when implemented in the simulator.

Likewise, as described in [100], one of the particular device pursued by Illera *et al.* is a specific confined two-dimensional structure [105] i.e. the metal-oxide-semiconductor (MOS) transistor. This device is formed by three electrodes (drain, source and gate). This third electrode only changes the local potential of the dots (i.e, moves the DOS) and injects no current [100].

As it can be concluded, Illera *et al.* use interacting Si quantum dots embedded in a SiO_2 dielectric matrix in contact with two electrodes. Then by using Transfer Hamiltonian approach described previously, they are able to figure out the I-V characteristic of the whole electronic system.

However, the particular device proposed in this work i.e. QLED, has both a different purpose as application (lighting system) and therefore a distinct working physics architecture. As generally explained below, it implies a different adaptation of the Transfer Hamiltonian method to the QLED device experimentally fabricated in this work. In this way, from the experimental part in BL3, the QLED device proposed has the following physical structure shown in Figure 87.

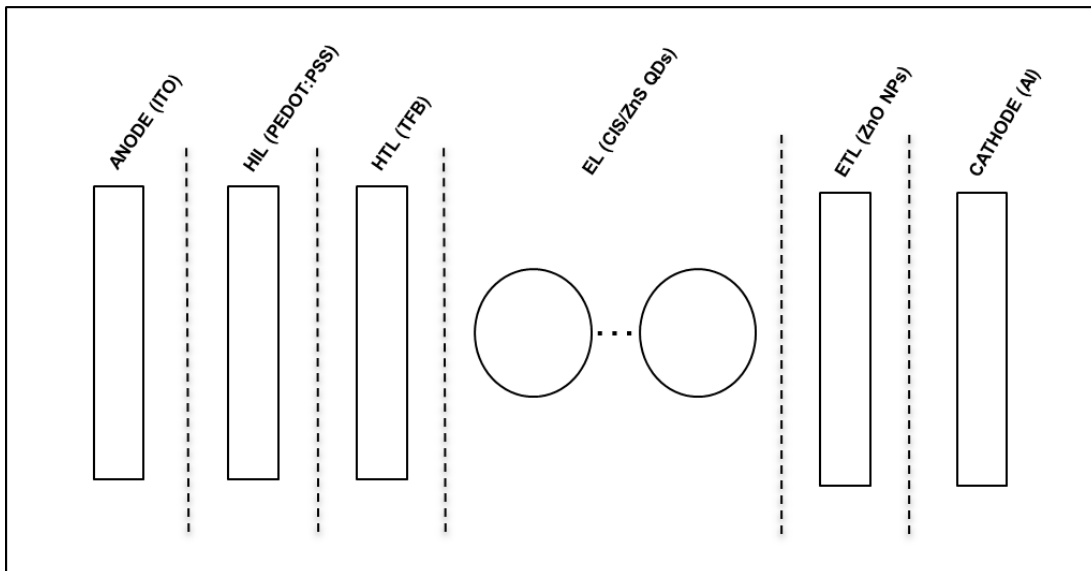


Figure 87: Structure of the QLED device proposed with all layers depicted (ITO as anode, PEDOT:PSS as hole injection layer (HIL), TFB as hole transport layer (HTL), $\text{CuInS}_2/\text{ZnS}$ QDs as active or emission layer, ZnO NPs as electron transport layer (ETL) and Al layer as cathode. Designed for this work.

Therefore, the novelty of the simulator developed and the main differences that affects simulations approaches between the work presented by Illera *et al.* and our QLED model are summarized below:

→ Targeting devices:

- QLED in our work
- MOS and solar cells in Illera *et al.* work

→ Device architecture used:

- QDs core/shell + Transport Layers + electrodes in our work
- Bare QDs + insulation + electrodes in Illera *et al.* work

→ Materials and structure used for QDs

- CuInS₂/ZnS in our work
- Si + SiO₂ in Illera *et al.* work

→ Fabrication processes:

- Thin-film deposition techniques using colloidal quantum dots in our work
- Epitaxial QDs growth in Illera *et al.* work.

Particularly, the main differences raised from quantum dots and new transport layers are introduced and defined in sections 4.3.1.1.1 and 4.3.1.1.2.

4.3.1.1.1 QUANTUM DOTS

Thereby, as core/shell structure has been particularly selected for quantum dots due to their stability as colloidal solutions, the strategy followed in this work is to use the core as quantum dot nucleus and the shell as dielectric layer, in an adapted way as used by Illera *et al.* for Si quantum dots embedded in SiO₂ matrix.

Si + SiO₂ (Illera *et al.* work) → CuInS₂/ZnS (*present work*)

4.3.1.1.2 TRANSPORT LAYER

Moreover, in order to adapt the particular QLED system developed in this work to the theoretical approach made by Illera *et al.* Transfer Hamiltonian (4.3.1) approach has been followed taking into account all layers and not only the quantum dot ones. Thus, transport layers and QD layers have been processed as individual subsystems associating a NCRE equation to each one. That equation will describe the relationship between the charge inside the layers as explained above. Furthermore, the interactions between all layers are introduced by transition rates and capacitive couplings taking into account the density of states (DOS) of each subsystem [109]. Finally, to solve the multielectron problem, the effects of the local potential are computed within the self-consistent field (SCF) regime in the same way proposed [100]. The QLED to be modelled in this work is depicted in Figure 88.

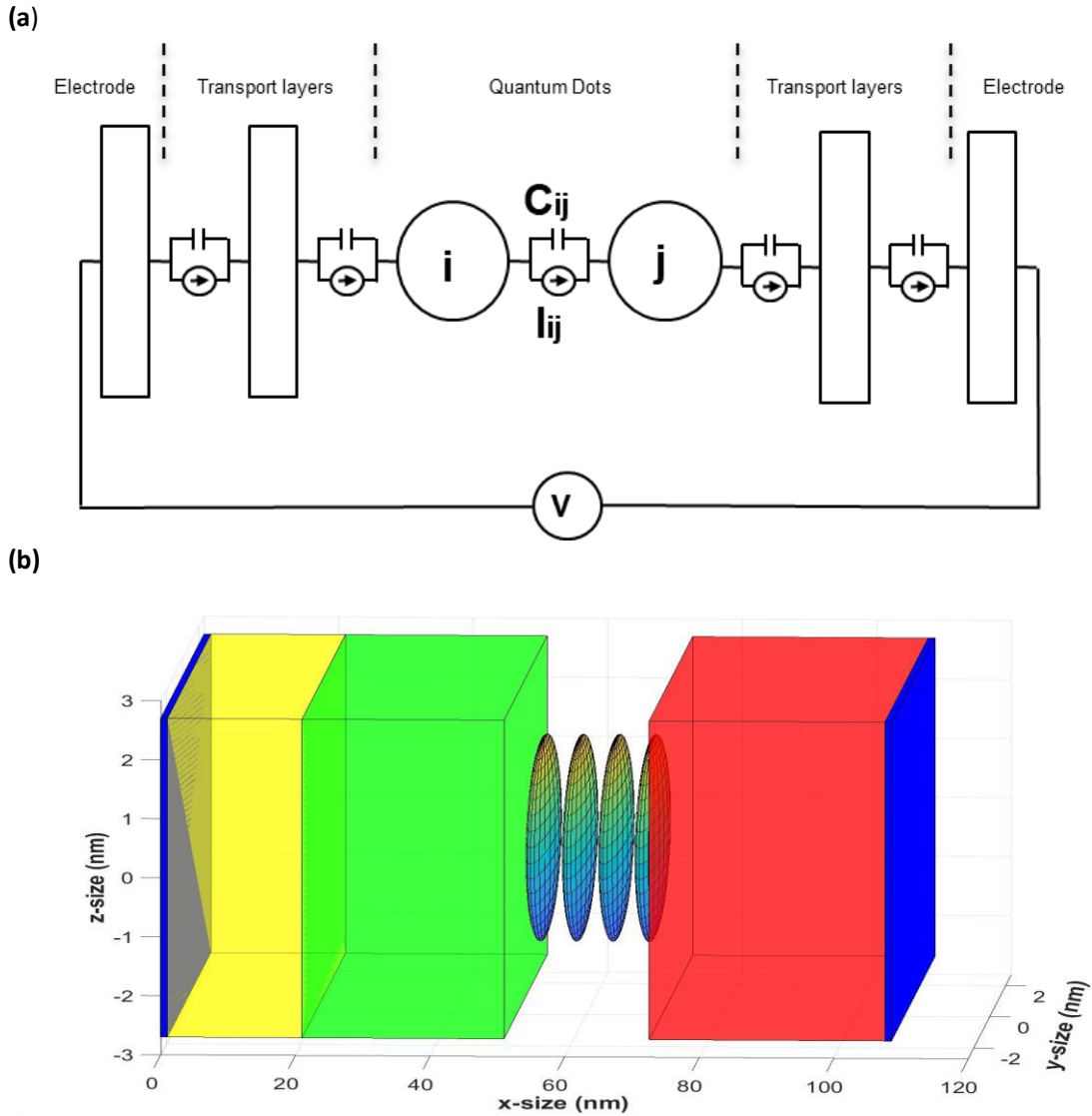


Figure 88: (a) QLED model proposed. (b) 3D view for QLED model with all transport layer of the experimental device introduced i.e. Anode/HIL/HTL/QDs/ETL/Cathode. NB: The quantum dots represented in the figure are spherical. Different scales were used in each direction for the sake of clarity. Designed for this work.

4.3.1.2 Total charge

As it was stated from Transfer Hamiltonian formalism in Eq.4, it is possible to define the current flowing between two parts (i,j), where $f_i(E)$ $f_j(E)$ are the non-equilibrium energy distribution functions in each side of the barrier.

These unknown distribution functions [100] take into account how the energy levels are filled f_j or emptied $(1 - f_j)$, as it is expected the electron transport only occurs if the initial state is filled and the final state is empty. Nevertheless, it is assumed that the distribution functions from the electrodes i.e. anode and cathode depicted in Figure 88 are well defined by the equilibrium Fermi Dirac statistics [100], [109] since it is possible to modify electrochemical potential (μ_L and μ_R) by applying a bias voltage to the electrodes. For the sake of clarity anode will be referred as LEFT (L) and cathode as RIGHT (R) following the same strategy proposed by Illera *et al* [100].

Therefore as well described in [105], and in equilibrium state, the electrochemical potential is the same throughout the whole system, being the current between any two parts of the system equal to zero.

$$I_{ij} = 0 \quad (5)$$

Now, if an external bias voltage (V) is applied at the electrodes, the whole system is driving out of equilibrium [105], creating carrier currents due to the different population in each electrode [106]. Thereby, the electrochemical potential of the electrodes will become as follows

$$\mu_L - \mu_R = qV \quad (6)$$

Additionally, it can be calculated the total charge inside each QLED layer (i) following the usual definition

$$N_i = \int \rho_i(E) n_i(E) dE \quad (7)$$

where both $\rho_i(E)$ and $n_i(E)$ are the density of states (DOS) and the distribution functions (unknown) for each layer (i) respectively [100].

NB: For the sake of clarity and following Illera et al. work, the distribution function for each layer (i) from the QLED will be defined as $n_i(E)$ while $f_L(E)$ and $f_R(E)$ will be reserved for the distribution function of the left and right electrodes.

4.3.1.3 Distribution functions

Following 4.3.1.2, the only distribution functions known are the ones related to the electrodes i.e. $f_L(E)$ and $f_R(E)$. However when the system is out of equilibrium, the distribution function for each layer (i) inside the QLED is unknown.

Therefore, in this chapter it is intended to derive the calculus of each distribution function associated with each layer (transport layers + QDs). To do so it is possible to write the evolution of the charge over time as follows [105],

$$N_i(t) = \sum_j \int I_{ij} dt \quad (8)$$

where the subscript i refers to the i th layer and j runs over the other components of the system. Thus taking into account the definition of the current between two parts (i - j) of the system defined by the Transfer Hamiltonian approach in Eq.4, it is possible to obtain a set of integro-differential equations for the charge evolution in time as shown in next Eq.9 [105].

$$\frac{dN_i}{dt} = \frac{4\pi q}{\hbar} \left(\int T_{Li} \rho_L \rho_i (f_L - n_i) dE + \int T_{Ri} \rho_R \rho_i (f_R - n_i) dE + \sum_{j \neq i}^{(N-1)} \int T_{ji} \rho_j \rho_i (n_j - n_i) dE \right) \quad (9)$$

$\forall i=1 \dots N$

Eq.9 shows all the current terms contributions i.e. contributions from the electrodes (first and second term) and the contribution of all neighbor layers (j) with the layer under study (i) (last term) [105], [109].

As stated previously, it is assumed that the functions of the electrodes (f_L, f_R) follow the Fermi-Dirac distributions using different electrochemical potentials (μ_L, μ_R). Thus, considering no inelastic scattering [105], [109], it is possible to obtain the unknown distribution functions for each layer (transport and QDs) by evolving Eq.9 to the steady state. Then for each energy step, a system of equations as extracted from Illera *et al.* work [105] is set.

$$\begin{pmatrix} -T_{L1}\rho_L - T_{R1}\rho_R - \sum_{j \neq 1}^{(N-1)} T_{1j}\rho_j & \dots & T_{1N}\rho_N \\ \vdots & \ddots & \vdots \\ T_{1N}\rho_1 & \dots & -T_{LN}\rho_L - T_{RN}\rho_R - \sum_{j \neq N}^{(N-1)} T_{Nj}\rho_j \end{pmatrix} \begin{pmatrix} n_1 \\ \vdots \\ n_N \end{pmatrix} = \begin{pmatrix} -T_{L1}\rho_L f_L - T_{R1}\rho_R f_R \\ \vdots \\ -T_{LN}\rho_L f_L - T_{RN}\rho_R f_R \end{pmatrix} \quad (10)$$

Eventually, it is possible to reach a solution for the unknown distribution function n_i by solving the system of equations above for each energy step as stated previously.

4.3.1.3.1 Electron and holes

Hitherto, a general carrier current contribution has been taken into account. However, since semiconductor materials are considered and approximating the organic ones to them (see 3.4.2), it is necessary to distinguish between two different type of bands i.e. conduction band and valence band. Therefore, two kinds of current carrier contribution have to be borne in mind: electrons and holes. In this way, Eq.9 and thus the system of equations described in 4.3.1.3 have to take into consideration both electron and holes contributions for each conduction and valence band. However, before presenting how this contribution will be realized in the equations, the transmission coefficients used will be deployed in next chapter 4.3.1.4.

4.3.1.4 *Transmission coefficients*

In bulk semiconductor theory, conduction band and valence band are well defined [109]. However, in quantum dots and in 2D layers there are discrete energy states and it is needed to discuss about electron and hole energy states [109]. Therefore, it is convenient to take into account transport tunneling processes as carrier electrical current mechanism.

The three main tunneling processes in semiconductor materials [109] that will be used in our modelling system and will be introduced in the rate equations from 4.3.1.3 are the following [100], [109],

- ECB: electron tunneling from conduction band to conduction band.
- EVB: hole tunneling from valence band to conduction band (since the transmission coefficients are symmetric, the EVB process also involves the inverse case: tunneling from conduction band to valence band).
- HVB: hole tunneling from valence band to valence band.

As well described by Illera *et al.* the following Figure 89 shows the three mechanisms considered

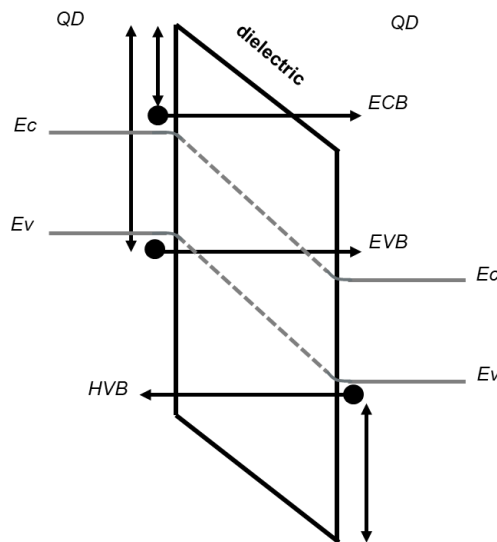


Figure 89: Different tunneling processes identified for our QLED system. Adapted from [100].

Then, once tunneling processes have been identified in our system, it becomes necessary to describe the transmission coefficients used in the application. As per definition, transmission coefficients from Eq.9 are the tunnel probability of the carriers to pass through the dielectric media depicted in Figure 89 [100], and at every particular energy, that probability should be analyzed.

Following Illera *et al.* work, semiclassical and one-dimensional Wentzel-Kramers-Brillouin (WKB) approximation will be used to calculate the transmission coefficients since it allows the analytical extraction of those coefficients in a simple way [109].

4.3.1.4.1 Wentzel-Kramers-Brillouin (WKB) approximation

The WKB approximation is an approach often used in semiclassical calculation in quantum mechanics to find approximate solutions to linear partial differential equations. This approximation allows us to obtain solutions to the time-independent Schrödinger equation in one dimension, being a method extensively used to calculate tunneling probabilities [109].

Out of equilibrium, it is considered that the tunneling barrier is bended when a potential difference between its sides is applied [109]. An electric field across the barrier is generated by this potential difference and assuming a linear dependence of the barrier on the applied electric field [109], the modified potential $\Phi_0(x)$ can be expressed as

$$\Phi_0(x) = \Phi_1 - qE_{diel}x = \Phi_1 - qV_{12} \quad (11)$$

where $E_{diel} = \frac{V_{12}}{d}$ and d is the overall tunneling thickness distance [109].

Furthermore, it is possible to depict the relationship between the different tunneling processes explained at the beginning of chapter 4.3.1.4 and the incident carrier energy. This is shown in Figure 90.

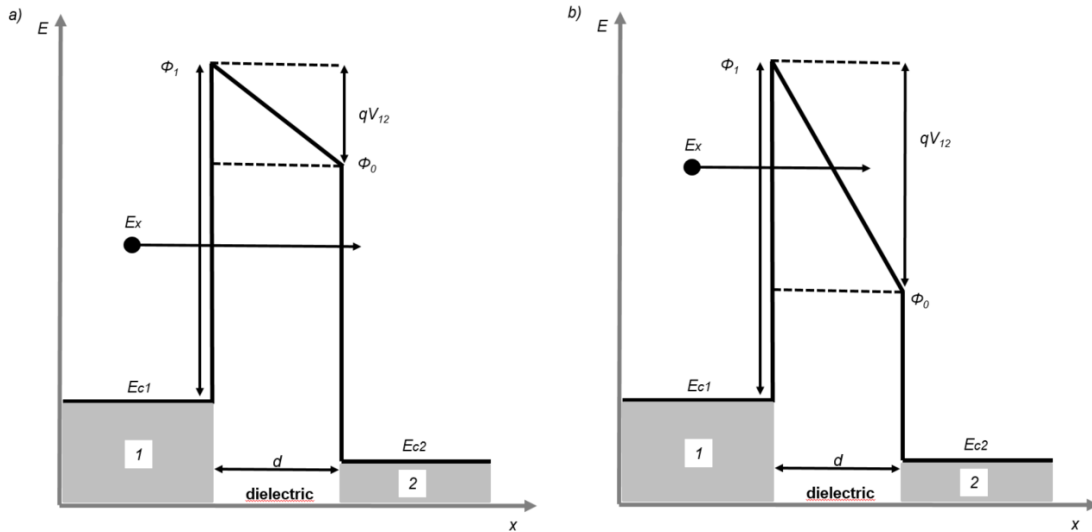


Figure 90: Energy band diagram for a) direct tunnel and b) Fowler-Nordheim process (trapezoidal). Adapted from [100], [109].

From Figure 90 above, extracted from Illera *et al.* work, it can be concluded that if the incident carrier energy (E) is less than the modified energy barrier ($q\Phi_0$) a direct tunnel expression will be used [109]. On the other hand, if the incident carrier energy (E) is greater than the modified energy barrier ($q\Phi_0$), Fowler-Nordheim expression will be taken into account [100], [109]. These expressions depend on the incident electron energy but also depend on the polarization voltage and are shown in Eq.12.

$$T(E) = \begin{cases} \exp \left\{ -4 \frac{\sqrt{2m_{diel}^*}}{3\hbar q E_{diel}} \left((\Phi_1 - E)^{3/2} - (\Phi_0 - E)^{3/2} \right) \right\} & \text{for } \Phi_0 \geq E \\ \exp \left\{ -4 \frac{\sqrt{2m_{diel}^*}}{3\hbar q E_{diel}} (\Phi_1 - E)^{3/2} \right\} & \text{for } \Phi_1 \geq E \geq \Phi_0 \\ 1 & \text{for } E \geq \Phi_1 \end{cases} \quad (12)$$

where Φ_1 is the potential barrier height, Φ_0 is the modified potential barrier height and m_{diel}^* is the electron effective mass in the dielectric [100], [109]. The transmission coefficients for the holes can be extracted in a similar manner, as the potential barrier is the difference between the valence bands of the layers and the dielectric [100], [109].

4.3.1.4.2 Final Equations

Finally, the rate equations defined in Eq.9 for each layer inside the QLED system will take the following form (taking into account both electron and holes carrier contributions and the different tunneling processing through the transmission coefficients i.e. ECB, EVB, HVB).

$$\begin{aligned} \frac{dN_i}{dt} = & \frac{4\pi q}{\hbar} \left(\int_{-\infty}^{+\infty} T_{ECB} \rho_L \rho_i^{CB} (f_L - n_i) dE + \int_{-\infty}^{+\infty} T_{HVB} \rho_L \rho_i^{VB} (f_L - n_i) dE \right) + \\ & \frac{4\pi q}{\hbar} \left(\int_{-\infty}^{+\infty} T_{ECB} \rho_R \rho_i^{CB} (f_R - n_i) dE + \int_{-\infty}^{+\infty} T_{HVB} \rho_R \rho_i^{VB} (f_R - n_i) dE \right) + \\ & \left\{ + \frac{4\pi q}{\hbar} \sum_{j,j \neq i}^N \left\{ \int_{-\infty}^{+\infty} T_{ECB} \rho_i^{CB} \rho_j^{CB} (n_j - n_i) dE + \int_{-\infty}^{+\infty} T_{HVB} \rho_i^{VB} \rho_j^{VB} (n_j - n_i) dE \right\} \right. \\ & \left. + \frac{4\pi q}{\hbar} \sum_{j,j \neq i}^N \left\{ \int_{-\infty}^{+\infty} T_{EVB} \rho_i^{CB} \rho_j^{VB} (n_j - n_i) dE + \int_{-\infty}^{+\infty} T_{EVB} \rho_j^{CB} \rho_i^{VB} (n_j - n_i) dE \right\} \right\} \end{aligned} \quad (13)$$

$\forall i=1...N$ (number of layers i the QLED)

As well defined in Illera *et al.* work [100], the first and second pair terms are related to the electrodes (left and right respectively), the electron and the hole contributions. For simplicity, it is assumed infinite metallic leads thus only the continuum DOS of the electrodes are written (ρ_L, ρ_R) meanwhile in the other layers (QDs + transport), DOS are defined in separately terms, conduction band (ρ_i^{CB}) and valence (ρ_i^{VB}) band [100]. In these two contributions, the Fermi-Dirac distribution function is used to describe the electrodes with $\mu_L - \mu_R = qV$ electrochemical potentials. In each current term, the appropriate transmission coefficients are used. The last two pairs of current terms represent the current from the neighbor layers (QDs + transport) [100]. The subscript j runs over all the layers except the layer under consideration. Likewise, the different processes, tunneling from the conduction band (CB) to conduction band (CB) and tunneling from valence band (VB) to valence band

(VB) are taken into account. Moreover, tunneling that combines the bands (EVB processes) is considered twofold, from CB to VB and from VB to CB [100], [109].

Eventually, that set of equations, Eq.13 can be solved to the steady state. Considering that there is no inelastic scattering, the system can be written in a matrix form and solved for each energy step to obtain the non-equilibrium distribution function for each layer (n_i) [100].

4.3.1.5 Density of States (DOS)

4.3.1.5.1 Quantum Dots

It is well assumed that quantum dots are nanostructures in which electrons and holes are confined in a small region. Thus, the wave function of the QDs confined carriers allows us to determine its electrical and optical properties. Furthermore, literature offers different methods to describe those electronic properties of the QDs. Therefore and following again Illera *et al.* work [109], a simplified model to represent the discrete energy levels in the QDs, based on finite spherical potential well approach has been used (applied for the conduction band (CB) and valence band (VB)) [100]. In that approach, some assumptions used in the QD framework description has been put in place as follows [109]:

- Finite spherical potential well within the Effective Mass Approximation (EMA) has been implemented i.e. the bulk effective masses are used to describe the electron and holes.
- Each QD is considered independent from the other. Thus, electrical properties of each QD are independent from the surroundings. This assumption is valid for weak tunnel coupling between the QDs, being the electrons localized in the individual QDs.
- Spherical shape is considered for QDs due to experimental part developed.
- The energy level spectra are obtained in the independent particle framework. The discrete states appear as a solution of the Schrödinger equation assuming an effective finite potential barrier outside the QD. Due to spherical symmetry, solution is restricted to $l=0$ case [110].
- Electron-electron interaction is included in the self-consistent field (SCF) and in the Poisson equation due to injected charge.
- Electronic properties of QDs are independent of the applied electric field. This electric field only shifts the energy levels, as a solution of the Poisson equation.

4.3.1.5.1.1 Energy levels

Following the approach described above, each quantum dot will be treated as a finite spherical potential well within the EMA [100], [107], [109]. The height of the well is the difference between the conduction band energy level of the QD shell and the QD core based on the experimental development presented for the synthesized quantum dots (core/shell). Thereby, the electron confinement potentials inside and outside of a QD of radius R can be written as follows [109].

$$V_e(r) = \begin{cases} 0 & \text{for } r < R \\ V_e & \text{for } r > R \end{cases} \quad (14)$$

NB: Hole confinement is also described with Eq.14 but with a different potential V_h .

These potentials arise from the band offset between the material of the core and the material of the shell. In this way, it is necessary to include the break of the effective masses between both materials for also both electrons and holes i.e. $m_{core}^{e/h}$ and $m_{shell}^{e/h}$ [109].

Then, using the symmetry of the system [109], [110], the electron Hamiltonian (calculus is similar for holes) can be expressed in spherical coordinates

$$\left\{ -\frac{\hbar^2}{2m_e} \left[\frac{\partial^2}{\partial^2 r} + \frac{2}{r} \frac{\partial}{\partial r} \right] + \frac{l(l+1)\hbar^2}{2m_e r^2} + V_e(r) \right\} R_l(r) = E_l R_l(r) \quad (15)$$

where the angular solution of the wave function is given by the spherical harmonics $Y_l^m(\theta, \Phi)$ [109]. The energy does not depend on the quantum number m [110]. The solution of lowest energy is spherically symmetric, with $l=m=0$, and in this case the widely-known one-dimensional problem for $R_l(r)$ is obtained [110]. Thus, solving the spherical Schrödinger equation inside the well for $l=0$, typical binding states are extracted [109], [110].

Eventually, the number of binding states and their energetically position depend on the height of the well V_0 , the radius R of the QD and the electron effective masses (in the core $[m_{core}^{e/h}]$ and in the shell $[m_{shell}^{e/h}]$). Imposing continuity of the wavefunction and its first derivative in $r=R$ the transcendental equation that determines the binding states is the following one [109], [110].

$$\cot(x) = -\frac{m_{shell}^*}{m_{core}^*} \sqrt{\left(\frac{\sigma_0}{x}\right)^2 - 1} \quad (16)$$

where

$$\sigma_0 = \sqrt{\frac{2m_{core}^* V_0}{\hbar^2}} R^2 \quad \text{and} \quad x = \sqrt{\frac{2m_{core}^*}{\hbar^2}} R^2 \epsilon_i$$

This Eq.16 does not have an analytical solution and numerical methods need to be used to solve it [109], [110]. The solutions of the latter equation contain the discrete binding energy levels (ϵ_i) of the QD.

It is worth saying that the energy level solutions above need to be shifted [109]. Particularly, since the Schrödinger equation gives the zero energy origin located at the bottom of the well, it becomes essential to shift the energy ϵ_i proportional to the bulk band gap E_g so as to have a common Fermi level as shown in next Eq.17

$$\epsilon'_i = \epsilon_i + E_{shift} \quad (17)$$

where E_{shift} is proportional to bulk band gap E_g .

4.3.1.5.1.2 DOS

Once the discrete energy levels of the QDs have been calculated and following the definition of the DOS for these kinds of nanostructures, it is possible to define the DOS for quantum dots as presented in Eq.18.

$$\rho(E) = \sum_i^n \delta(E - \epsilon'_i) \quad (18)$$

where n is the total number of binding states (valid for holes and electrons).

From the above definition, it is considered that QDs are independent parts [109] of the whole QLED system. However, the reality is different since QDs are coupled between them and the other transport layers. Therefore, the use of a Lorentzian shape to introduce the broadening of the discrete energy levels is a well-known procedure [100], [106], [109] to generate the latter coupling between the parts of the system.

$$\delta(E - \epsilon'_i) \rightarrow \frac{\frac{\gamma}{2\pi}}{(E - \epsilon'_i)^2 + \left(\frac{\gamma}{2\pi}\right)^2} \quad (19)$$

Where γ is the broadening of the level and it is related to the tunnel probabilities [100], [109]. In this way, the total density of states (DOS) for each QD is the total sum of energy levels taking into account both conduction (CB) and valence band (VB) as shown below in Eq.20.

$$\rho(E) = \sum_i^n \frac{\frac{\gamma}{2\pi}}{(E - \epsilon'_i)^2 + \left(\frac{\gamma}{2\pi}\right)^2} \quad (20)$$

As it can be extracted from Eq.20, DOS calculated for each QD is a simplified modelling of the reality. To obtain more accurate results, other approaches like *ab initio* methods (DFT) should be challenged.

4.3.1.5.2 Transport layers

Once QDs have been analyzed in terms of energy levels and DOS, it is necessary to make the same study for the transport layer to conform the whole QLED system. Transport layers could be considered as different structures than QDs. Taking into account the experimental results from BL3, where the thickness of the layers deposited after spin coating methods are on the nanometric range, it is sensible to think on these transport layers as two-dimensional materials (2D nanostructures).

Moreover, in the transport layer modelling, some assumptions made for QDs in 4.3.1.5.1 will be also applied

- Each transport layer is considered independent from the other. Thus, electrical properties of each layer is independent of the surroundings. This assumption is valid for weak tunnel coupling between the layers, being the electrons localized in the individual transport layers.
- Electron-electron interaction due to injected charge is included in the self-consistent field (SCF) and in the Poisson equation
- Electronic properties of the transport layers are independent of the applied electric field. This electric field only shifts the energy levels, as a solution of the Poisson equation.

Besides, other considerations will be taken into account

- Infinite potential well within EMA approach will be considered to calculate the energy level spectra. As it will be discussed in chapter 4.5, this first simple approach could be upgraded to a more realistic one (potential barrier seen depending on the electric field applied).
- As stated at the beginning, two-dimensional materials (2D nanostructures) based on experimental results are considered to calculate the DOS.
- Finally, as described in the experimental implementation, the QLED transport layers have two types of materials. Particularly, for ETL, inorganic materials from ZnO nanoparticles are used. However, HIL (PEDOT:PSS) and HTL (TFB) are organic materials. For inorganic semiconductors, it is clear that conduction-valence band diagram definition can be applied. Furthermore, for organic materials, similar band diagram approach made in QDs will be used taking into account the similarity HOMO-LUMO to conduction-valence band diagrams.

4.3.1.5.2.1 Energy levels

As described above, infinite potential well within EMA approach will be considered to calculate the energy level spectra. This first approach is the simplest example of quantum well [110]. Therefore, it is considered that barriers present an infinitely high potential energy outside the well. Thus, for a quantum well of width a , the energy levels associated are the following ones

$$\epsilon_i = \frac{\hbar^2 \pi^2 i^2}{2m^* a^2} \quad (21)$$

where the integer $i \in \mathbb{N}$, is the quantum number that labels the states [110].

NB: Again, as it will be discussed in chapter 4.5, this first simple approach could be upgraded to a more realistic one (potential barrier seen depending on the electric field applied).

4.3.1.5.2.2 DOS

In the same way as done for QDs, once the discrete energy levels of the transport layers have been calculated and following the definition of the DOS for these kinds of 2D dimensional nanostructures [111], it is possible to define the density of states as in Eq.22.

$$\rho(E)^{2D} = \frac{m^*}{\pi \hbar^2} \sum_{i=1}^n \theta(E - \epsilon_i) \quad (22)$$

where ϵ_i are the energy quantized states and $\theta(E - \epsilon_i)$ is the step function [111].

4.3.1.6 Potential energy

As it can be extracted from Figure 88, each QLED junction has been modelled as a current tunnel junction in parallel with a capacitor. These capacities represent the electrostatic influence between the different parts of the system as described in [100]. Thus, each specific layer has a local potential V_i due to the applied bias voltage.

Following Illera *et al.* work [100], [105]–[109] and generalizing the same strategy relating to electron-electron interaction, not only for QDs but for the transport layers of the QLED device, it is possible to evaluate the change in the local potential V_i for all layers (QDs and transport).

Therefore, as described in 4.3.1.5.1, electron-electron interaction due to injected charge is included directly by the solution of the Poisson equation [109] below.

$$\vec{\nabla} \cdot (\epsilon_r \vec{\nabla} V_i) = -\frac{q \Delta N_i}{\Omega} \quad (23)$$

where ϵ_r is the relative permittivity of the dielectric media and Ω is the layer volume. ΔN_i is the change in the number of electrons, calculated with respect to the number of electrons N_0 initially in the i_{th} layer [100], [109], [112]. Then, the general solution of the Poisson equation for the local potential energy i.e. $U_i = -qV_i$ of each layer can be written as shown in Eq.24 [100], [109], [112].

$$U_i = \sum_{j \neq i} \frac{C_{ij}}{C_{tot,i}} (-qV_j) + U_{0i} \Delta N_i \quad (24)$$

$$C_{tot,i} = \sum_{j, j \neq i} C_{ij}$$

$$U_{0i} = \frac{q^2}{C_{tot,i}}$$

where the subscript j runs over all the components of the system, C_{ij} is the capacitive coupling between the i_{th} and j_{th} component and $C_{tot,i}$ is the total capacitive coupling of i_{th} layer. Moreover, the charge energy constant U_{0i} is the potential increase as a consequence of the injection of one electron into the layer (QD or transport layer) [100], [109], [112].

Therefore, Eq.24 can be divided into two terms. The second one is associated to the potential increase due to the injection of electrons into each layer. On the other hand, the first term is the Laplace term U_i^L and it is divided into the electrostatic influence of the electrodes or leads in which the bias voltage is applied and the electrostatic coupling with the neighboring layers [100], [109], [112]. In this way, the Laplace term described previously can be extended as follows

$$\begin{pmatrix} U_1^L \\ \vdots \\ U_N^L \end{pmatrix} = \begin{pmatrix} 1/C_{tot,1} & \cdots & 0 \\ \vdots & \ddots & \vdots \\ 0 & \cdots & C_{tot,N} \end{pmatrix} \times \left[\begin{pmatrix} C_1^{electrode} \\ \vdots \\ C_N^{electrode} \end{pmatrix} (-qV_{bias}) - \begin{pmatrix} 0 & \cdots & C_{1,N} \\ \vdots & \ddots & \vdots \\ C_{N,1} & \cdots & 0 \end{pmatrix} \begin{pmatrix} qV_1 \\ \vdots \\ qV_N \end{pmatrix} \right] \quad (25)$$

As it can be seen, the neighbors' capacitive matrix is defined as $N \times N$ symmetric matrix with zero in the diagonal terms. Both terms are multiplied by the inverse of the total layer capacity [100], [112].

4.3.1.7 Capacitive elements

Finally, capacitive elements shown in Eq.24 as solution of Poisson equation are analyzed. As seen, that local potential in each layer can be divided into two terms [109], [112]:

$$\begin{aligned} \text{➤ } \text{Laplace term: } & \frac{C_{ij}}{C_{tot,i}} (-qV_j) & \text{➤ } \text{Charge term: } & U_{0i} \Delta N_i \end{aligned}$$

Particularly and concerning to the Laplace term, the solution is given as function of the capacitive couplings between the different QLED layers with the rest of the system [109]. Furthermore, those capacitive couplings are quite important to the final device current calculation since they have a

direct influence in the energy levels shift inside each layer. Moreover, electrons need available states in order to have transport and DOS of each layer depends on the local potential [100].

Therefore, a good modelling of those capacitive coupling will be essential to obtain a realistic I-V characteristic curve. Adapting Illera *et al.* work [109], the following capacitive calculations for the real devices have been taken into account

1) Sphere to conducting plane capacitance: $C_{ij}^{QD-Layer}$

Since sphere shape has been considered for QDs, the objective is to model the capacitance between the layers (transport and electrodes) and the QDs as follows

$$C_{ij}^{QD-Layer} = 4\pi\epsilon_0\epsilon_r\sqrt{r^2 - R^2} \sum_{n=1}^{\infty} \frac{1}{\sinh\left(n \operatorname{arccosh}\left(\frac{r}{R}\right)\right)} \quad (26)$$

where ϵ_0 is the permittivity in vacuum, ϵ_r is the permittivity of the dielectric media, R is the QD radius and r is the distance between the plane and the center of the QD.

2) Interdot capacitances: C_{ij}^{QD-QD}

For QDs case, (interdot capacitances C_{ij}^{QD-QD}) there is no analytical expression for the capacitance. Thus, numerical method of image charges to calculate interdot capacitance between QDs has been used and implemented [100].

Nevertheless, after analyzing the QLED device, it is necessary to introduce another coupling capacitive mechanisms calculation not used by Illera *et al.* i.e. the coupling between different layers and junction coupling between electrodes and the layers.

3) Layer to layer capacitances: $C_{ij}^{Layer-Layer}$

In this case, capacitance between parallel planes is used to model the capacitance between different layers following the well known equation

$$C_{ij}^{Layer-Layer} = \epsilon_0\epsilon_r \frac{S}{d} \quad (27)$$

where ϵ_0 is the permittivity in vacuum, ϵ_r is the permittivity of the dielectric media, S is the layer surface and d is the distance between both planes.

4) Interface layer capacitances: $C_{ij}^{Layer \text{ interfaces}}$

At this point, the junction capacitance due to the contact between the electrodes and the next layers and the interfaces between layers have been estimated and used as a fitting parameter to achieve the final results. A way about how to calculate this capacitance has been proposed in chapter 4.5.6.

4.3.1.8 Self-consistent solution

Once this point has been reached, all elements that take part in the whole transport mechanism through the Transfer Hamiltonian approach have been analyzed. However, as it can be deduced from the equations exposed, there are dependencies among them. It means that it is necessary to enter a self-consistent field in order to obtain a final solution value.

As explained by Illera *et al.* and extended for the whole QLED device in this work, the effects of the local potential on each layer has to be computed in the QD and transport layer DOS $\rho_i(E) \rightarrow \rho_i(E - U_i)$ shifting the position of the energy levels. In the same way, this fact modifies the different layers' charge and the currents. In addition, from Eq.24 it is observed that the local potential depends on the increasing charge density but at the same time the charge depends on the DOS that is modified by the local potential. Eventually, these considerations impose a self-consistent solution of the following group of equations Eq.28 for the charge, DOS and the local potential [100] as shown in Figure 91.

$$\begin{aligned}
 N_i &= \int \rho_i(E) n_i(E) dE \\
 \rho(E) &= \sum_i^n \frac{\frac{\gamma}{2\pi}}{(E - \epsilon'_i)^2 + \left(\frac{\gamma}{2\pi}\right)^2} \\
 \rho(E)^{2D} &= \frac{m^*}{\pi \hbar^2} \sum_{i=1}^n \sigma(E - \epsilon_i) \\
 U_i &= \sum_{j \neq i} \frac{C_{ij}}{C_{tot,i}} (-qV_j) + U_{0i} \Delta N_i
 \end{aligned} \tag{28}$$

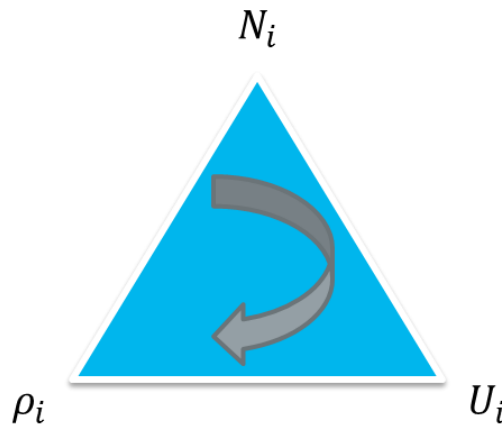


Figure 91: self-consistent field in order to achieve a final solution value convergence. Designed for this work.

4.3.2 Computational algorithm proposal: QLEDsim

As analyzed in 4.3.1.8 there is no possible analytical solution and a self-consistent field is required to finally achieve a convergence result. In this chapter the flowchart and algorithm implemented, and adapted from Illera *et al.* to the final QLEDsim is depicted in Figure 92.

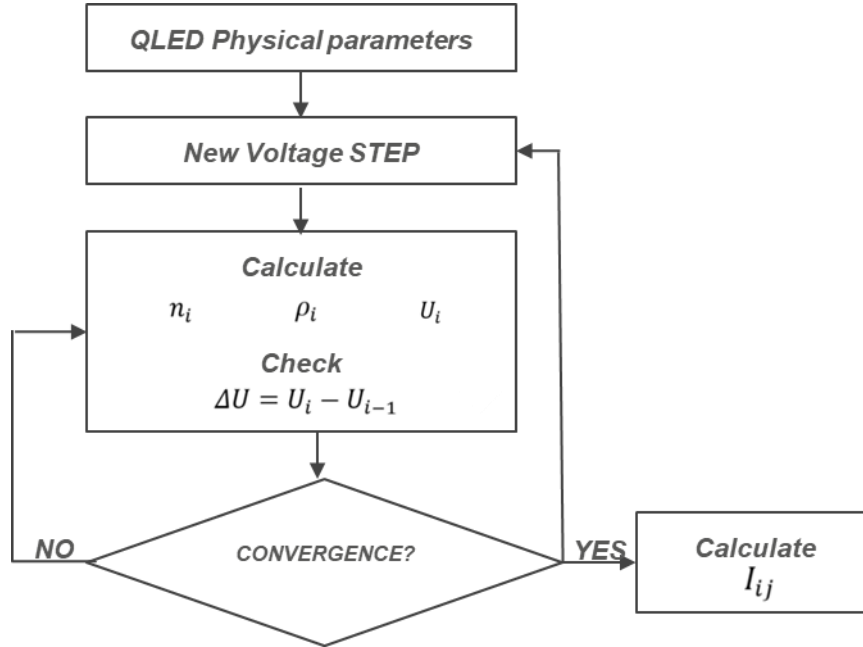


Figure 92: self-consistent field algorithm implemented. Designed for this work.

As it can be extracted from [100], [109] and generalizing for the whole QLED system, a description of the QLED device with all physical and geometrical parameters is firstly introduced. After this first step, a bias voltage is set to the electrodes. Then, the local potential is calculated for the Laplace potential term U_i^L and the transmission coefficients are assessed. In addition, the QDs and transport layers density of states (DOS) are shifted and the set of non-coherent equations (NCE) are solved for this local potential.

Finally, the charge in each QD and transport layer is computed N_i and the total solution of the Poisson equation, U_i , is obtained. Eventually, the convergence for the local potential is assessed and, if the desired objective is achieved, the current and other output values are calculated to proceed to the next voltage step in order to repeat the whole loop until the total bias voltage range applied to the electrodes is complete.

4.3.2.1 MATLAB® implementation

The algorithm proposal has been implemented and codified using matrix-oriented syntax of MATLAB®.

4.4 SIMULATION RESULTS

Once the theoretical background behind the QLED modelling has been established and the algorithm proposed to implement the latter has been codified in the software, the current density, the total QLED current, the electronic charge density evolution and the band diagram of the device are extracted from the QLED simulator (*QLEDsim*).

Thereby, Figure 93 shows the physical implementation carried out for the QLED device. In this case all geometrical parameters, extracted from the experimental part in BL3, have been taken into account.

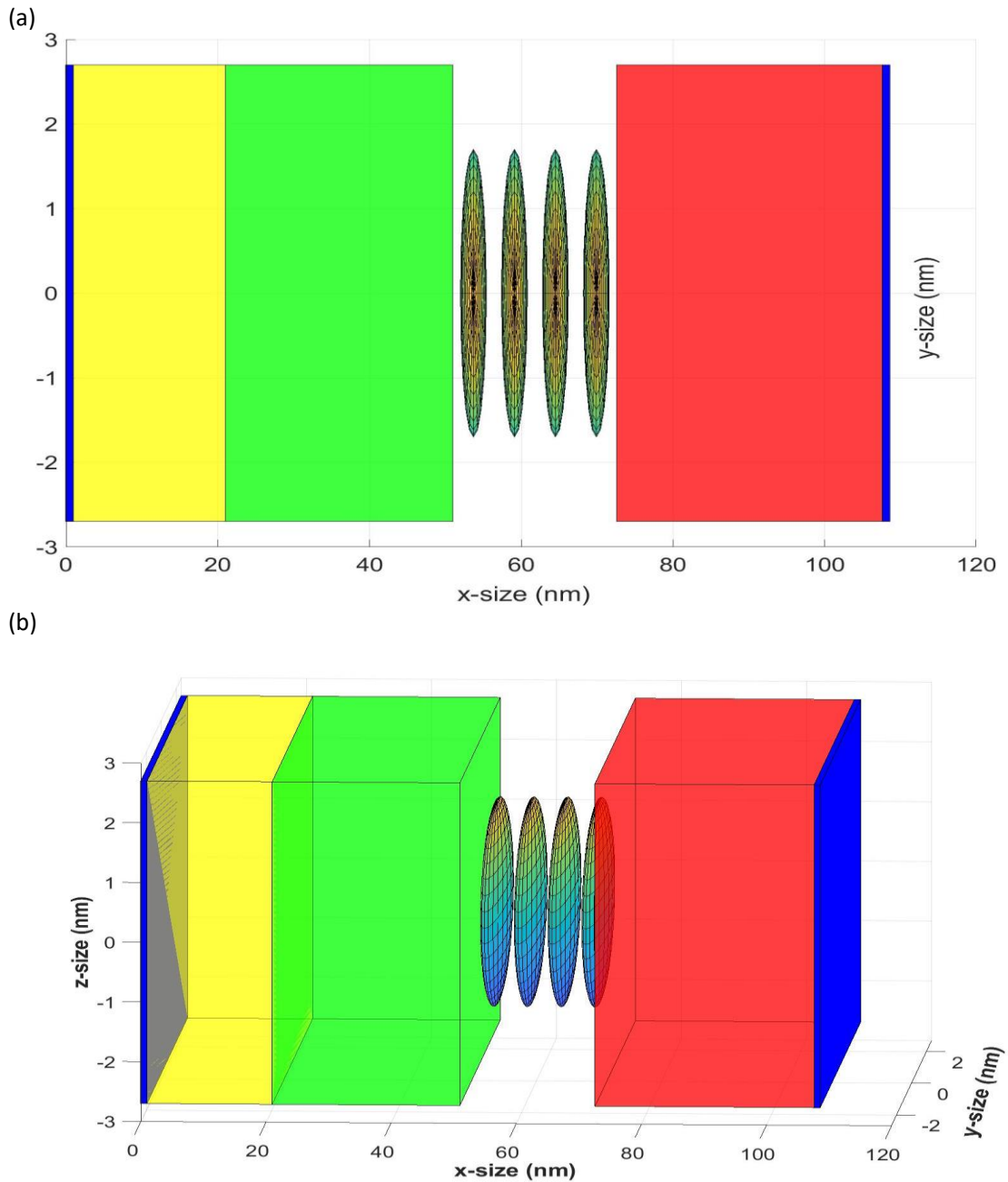


Figure 93: (a) TOP view of QLED device modelling. (b) 3D view for QLED model with all transport layers of the experimental device introduced i.e. anode/HIL/HTL/QDs/ETL/cathode. NB: The quantum dots represented in the figure are spherical. Different scales were used in each direction for the sake of clarity. Designed for this work.

4.4.1 Current density J

Once the *QLEDsim* simulator has been created, the first step to take is to draw the current density curve versus the bias voltage applied to the device presented in Figure 94. QLED device area of QD diameter (core/shell) simulated has been considered.

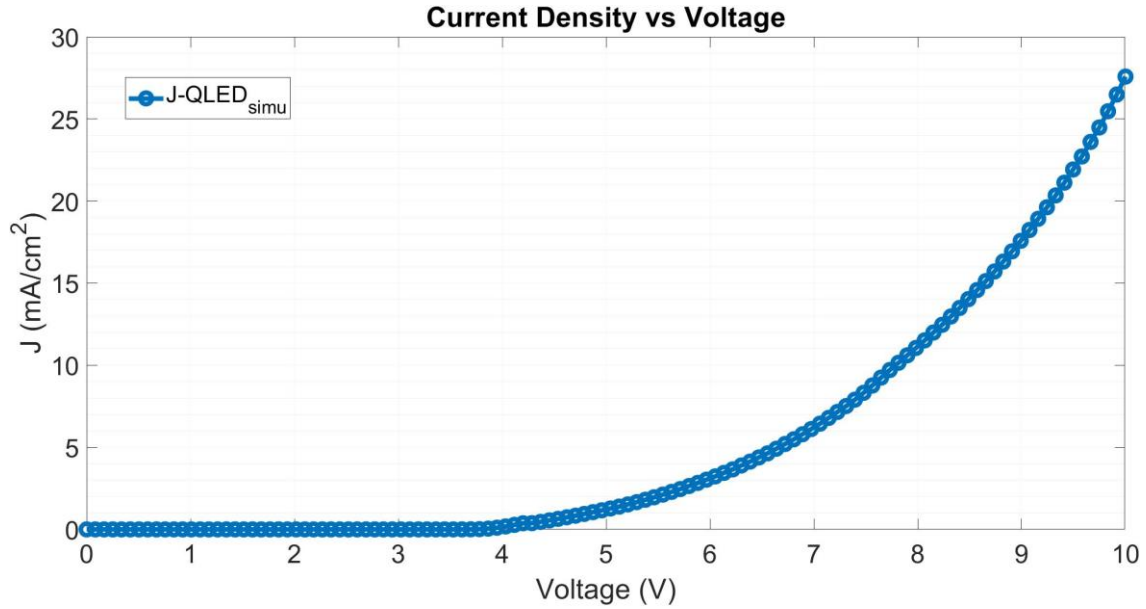


Figure 94: Simulated current density J (mA/cm²) curve for the QLED modelling device extracted from QLEDsim simulator

4.4.2 Approximation to 3D device (I - V curve)

After obtaining the current density for the QLED modelling, it is possible to make the approximation to the real 3D device as shown in Figure 95. The way followed as a first approach is to multiply the current density by the area given in individual pixels from QLED manufactured experimentally in BL3. This pixel area was set to 4.5mm².

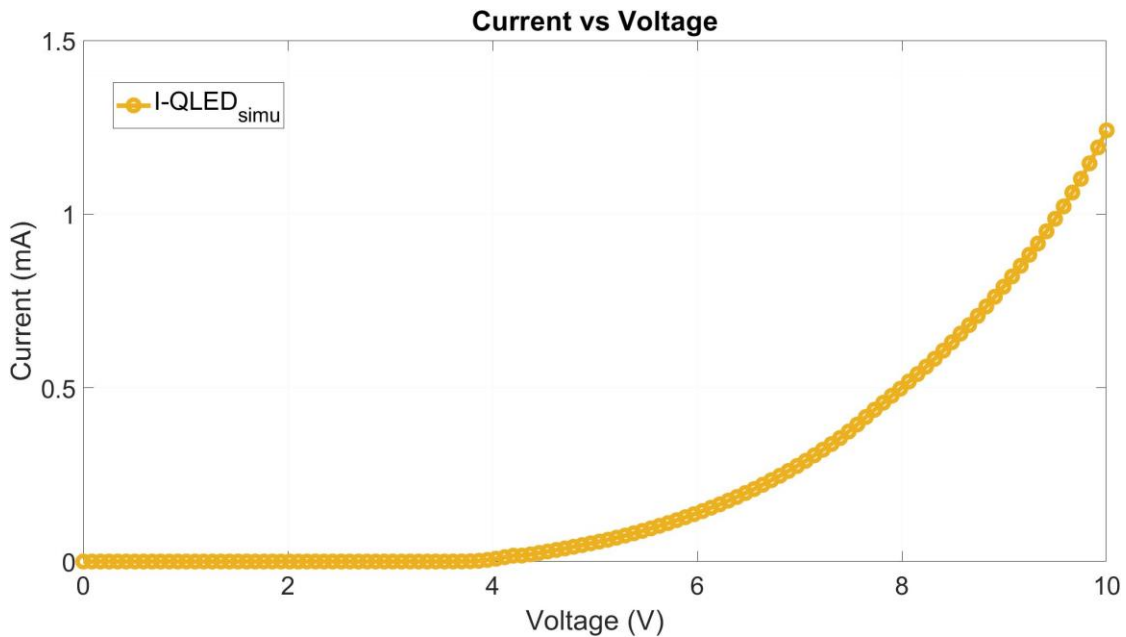


Figure 95: Simulated curve for the QLED modelling device extracted from QLEDsim simulator.

This approximation is based on ballistic transport. It means that carriers move directly from anode to cathode without interacting with other QDs located in different positions in 3D space. However, more realistic approaches can be made if those QDs interactions are taken into account. In addition, device border effects could be modelled to introduce second order effects. Anyway, all of these *QLEDsim* simulator improvements will be discussed in chapter 4.5.

4.4.3 *Theoretical vs Experimental*

Eventually, it is possible to compare now both experimental and theoretical results. To do so, Figure 96 shows this comparison in the same picture.

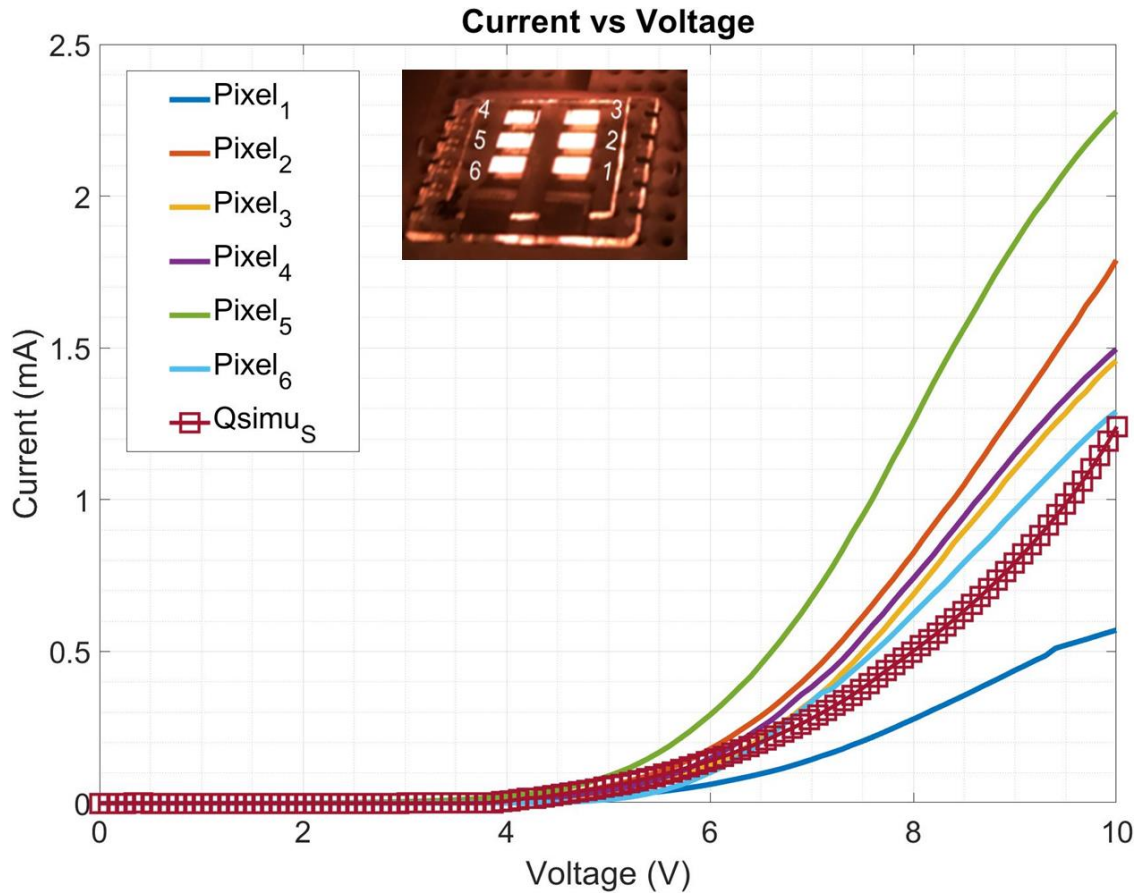


Figure 96: Experimental curve for the 6-pixel QLED device manufactured in this work compared to the simulated curve (red-square line) obtained from *QLEDsim*.

In conclusion, it can be seen that simulated I-V curve stays in the experimental range of curves measured from the 6-pixel QLED device manufactured. Therefore, I-V curve was simulated and compared with experimental results, reaching a remarkable agreement as shown in Figure 96. Furthermore, the localization and structure of the CuInS₂/ZnS QDs in the device prevents lateral charge spreading and Coulomb repulsion of charges into the QDs [113], being the carrier tunneling, the prominent mechanism for current flowing through the QLED device.

Thus, the simulator can be used to simulate real devices before going to the laboratory to perform the experimental device implementation.

4.4.4 Band Diagram

In this chapter both the energy levels from vacuum and the band diagram of the heterojunction in equilibrium depending on the applied voltage are presented.

4.4.4.1 Proposed energy levels of the multilayered device

Figure 97 shows the proposed energy levels from vacuum level independently obtained from literature [61]–[63] in BL2 and represented thanks to the *QLEDsim* simulator functionality included.

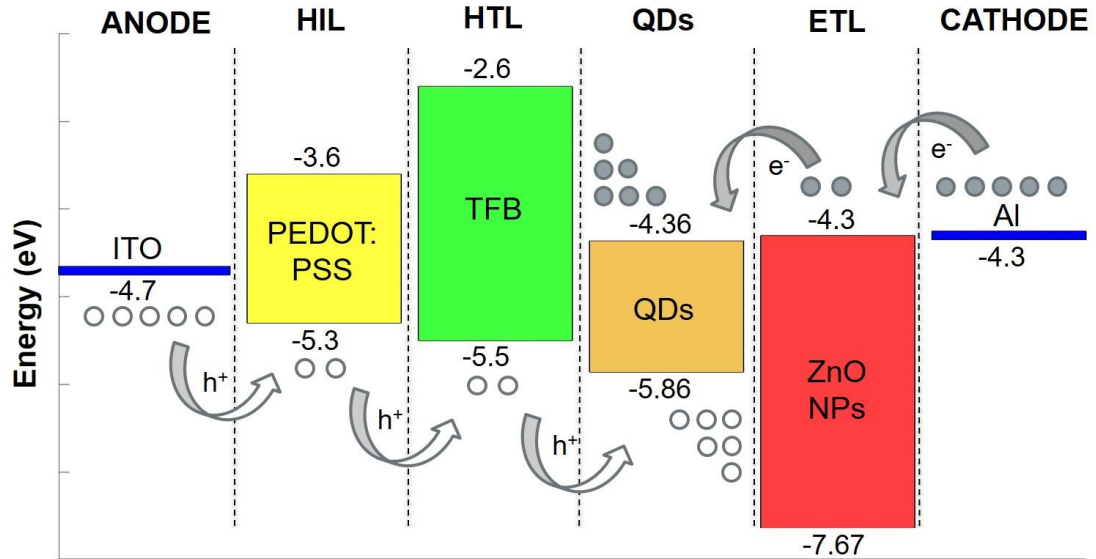


Figure 97: Energy levels proposed from vacuum reference extracted from *QLEDsim* simulator. Designed for this work.

Using the bulk material values of electron affinity and band gaps shown, it is possible to follow the “electron affinity rule” and band alignment [114] at the different material junctions to depict the heterojunction band diagram in both equilibrium and dynamic state.

4.4.4.2 Equilibrium band diagram of the heterojunction

Once the energy levels from vacuum reference in an independent layer material way are presented, the next step will be to introduce the band diagram of the heterojunction in equilibrium. That band diagram is presented for the conduction band (CB) and valence band (VB) i.e. when those materials are put in contact (with no bias voltage applied). Thus, the Fermi level reaches a flat and constant value throughout the whole device with the associated band bending in the depletion junction areas. In addition, conduction and valence band offsets [114]. have been calculated for every junction interface at the heterojunction. Moreover, the QD layer has been deployed following the core/shell quantum dot structure and real device size (i.e. 4 QDs to be considered) in a realistic way to depict the whole heterojunction band diagram. The result is shown in Figure 98.

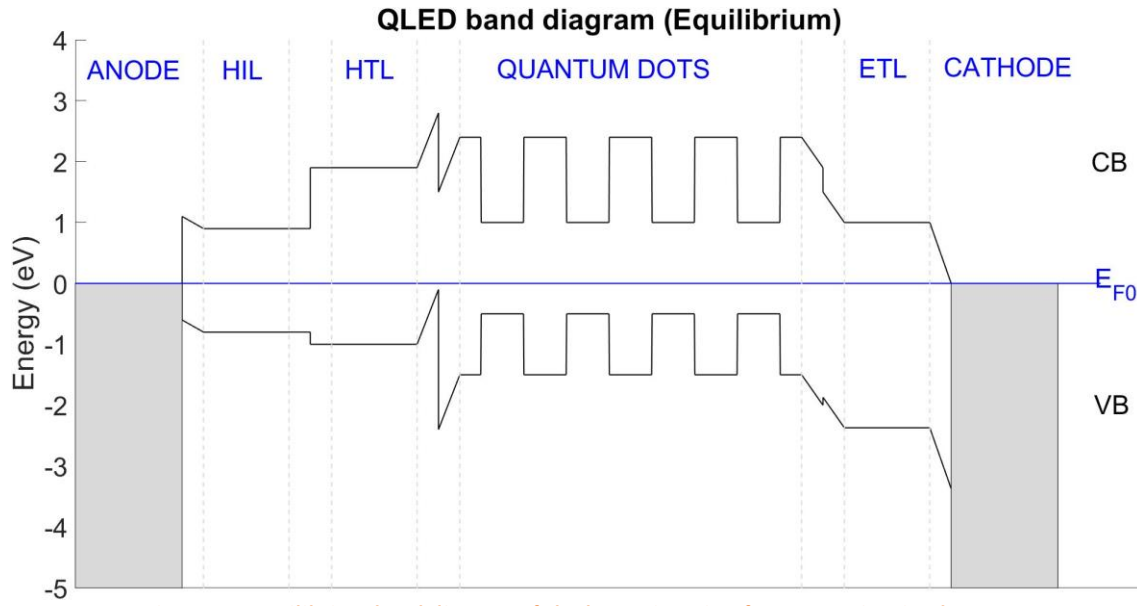


Figure 98: Equilibrium band diagram of the heterojunction from QLEDsim simulator.

NB1: Fermi level in equilibrium is taken as reference in y-axis ($E_{F0}=0$ eV).

NB2: Figure 98 (equilibrium) and Figure 99, Figure 100, Figure 101 and Figure 102 (biased) depict the conduction and valence band profiles when the potential, calculated from Eq.(24), is considered. The equation yields the potential in each device layer, the details of the potential profile within each layer are not represented. Each core/shell quantum dot layer is considered as a single-material layer, and therefore the potential profile representation within the quantum dots should not be considered as an accurate representation.

4.4.4.3 Dynamic band diagram of the heterojunction

Now forward biased QLED is considered i.e. a voltage $V_{bias} = (V_{ANODE} - V_{CATHODE}) > 0$ is applied to the electrodes. Therefore, the system will be out of the equilibrium and, as any heterojunction system, band diagram will be modified with the voltage applied. Thanks to *QLEDsim* simulator, it is possible to calculate the potential energy increase in each layer allowing us to draw Figure 99, Figure 100, Figure 101 and Figure 102 for each bias voltage step for $V=[2,5,8,10]$ V.

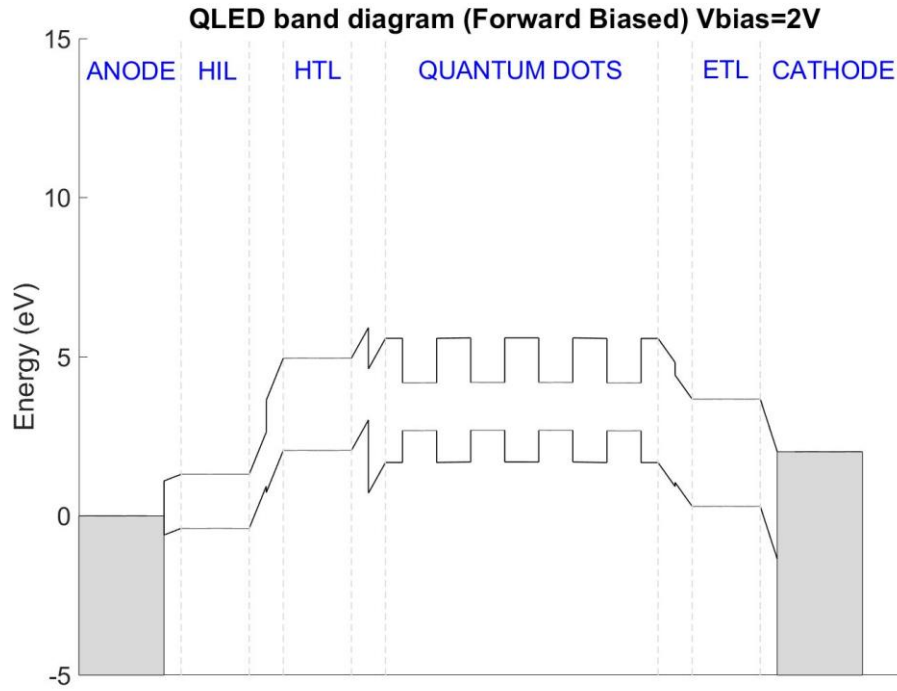


Figure 99: QLED forward biased (V=2V) band diagram of the heterojunction from QLEDsim simulator.

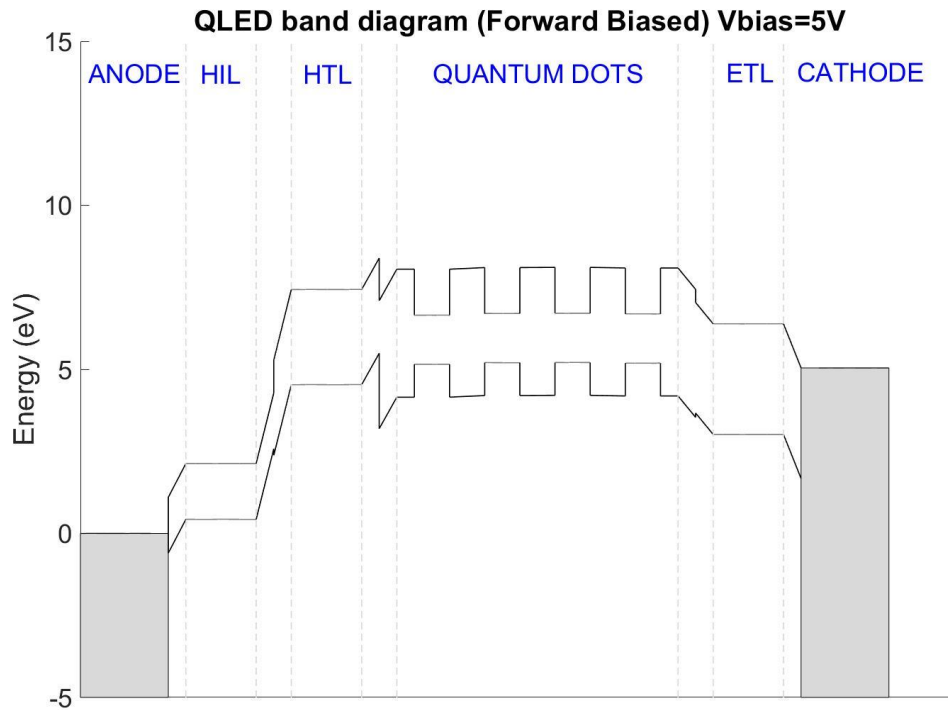


Figure 100: QLED forward biased (V=5V) band diagram of the heterojunction from QLEDsim simulator.

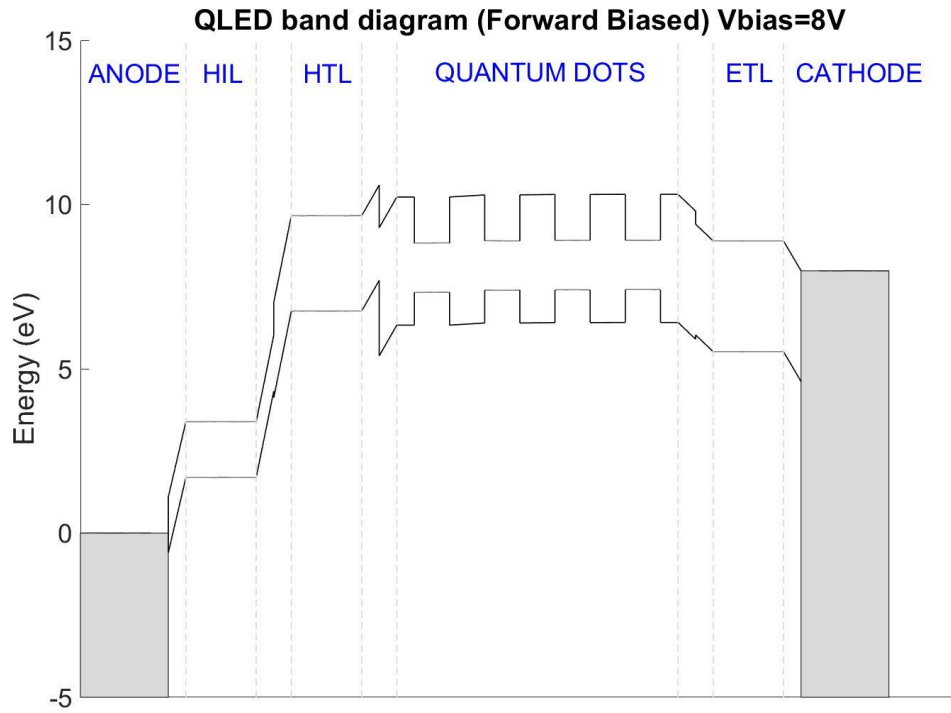


Figure 101: QLED forward biased (V=8V) band diagram of the heterojunction from QLEDsim simulator.

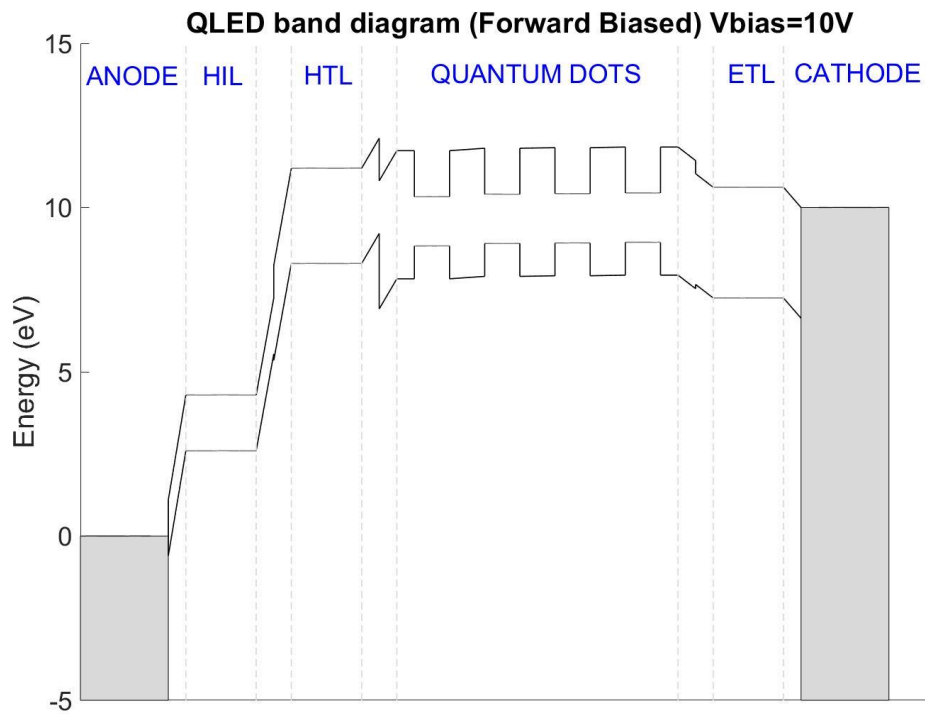


Figure 102: QLED forward biased (V=10V) band diagram of the heterojunction from QLEDsim simulator.

4.4.5 Accumulated charge distribution

Once the QLED is out of equilibrium and the band diagram has been described, the accumulated charge distribution in each layer is depicted for each voltage step taken. Thereby, it is possible to calculate the variation of number of electrons ($\Delta N = N - N_0$) for each voltage step. That relationship indicates the variation of electrons (N) with respect to the initial number (N_0). That initial value of the charge is obtained at zero bias voltage in equilibrium state. Thus, as described by Illera *et al.* [100], [109], if the variation is negative, it implies that the system loses charge (hole accumulation). On the other hand, if the variation is positive, the system increases its charge (electron accumulation).

Therefore, Figure 103 describes the accumulated charge for each layer depending on the voltage step variation applied dynamically.

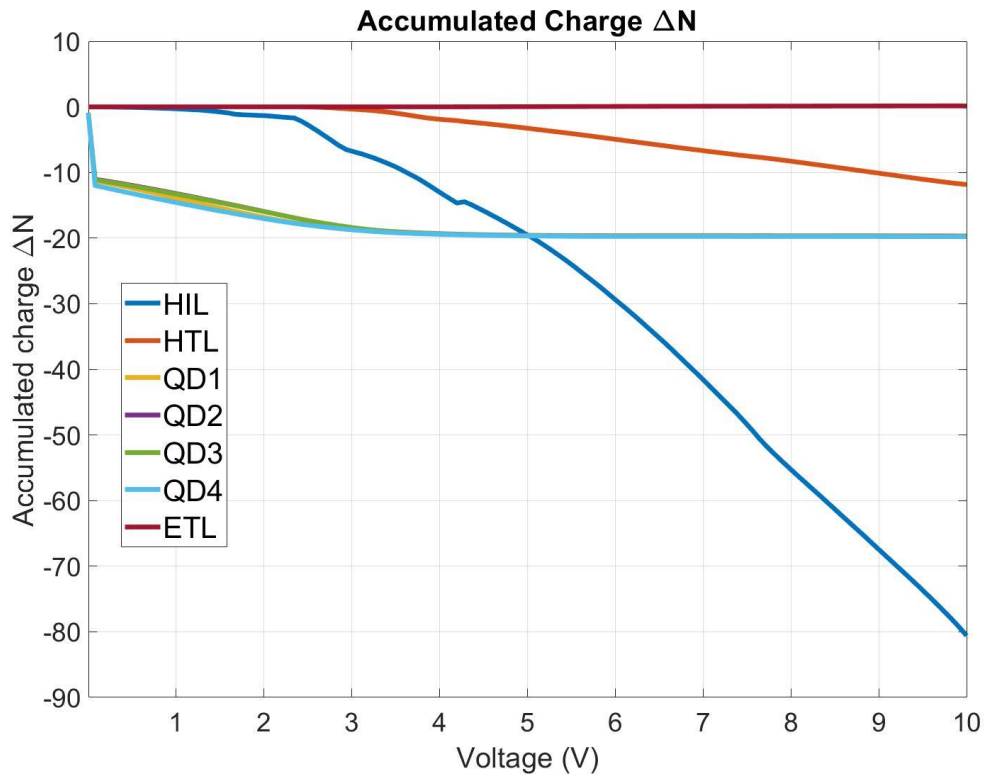


Figure 103: QLED accumulated charge for each layer extracted from QLEDsim simulator.

Furthermore, Figure 104 represents that accumulated charge for each layer out of the equilibrium in a graphical colormap description.

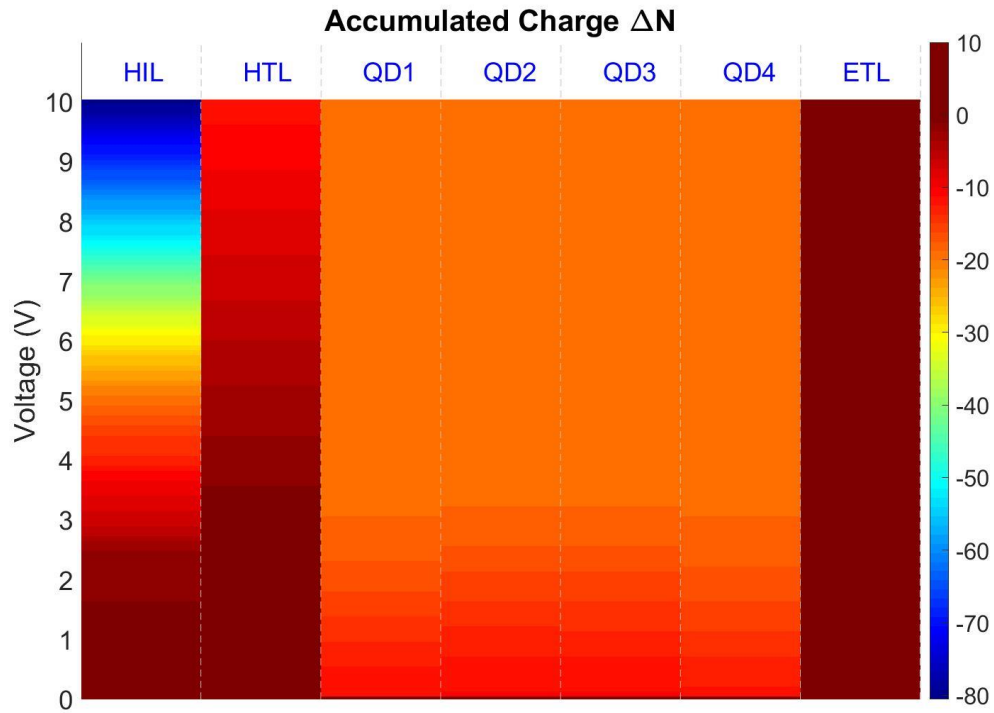


Figure 104: QLED graphical color mapping of accumulated charge for each layer extracted from *QLEDsim*.

As it can be extracted from the figures above, the QLED system behaves as expected. Injection hole layer (HIL) and hole transport layer (HTL) tend to accumulate holes whereas electron transport layer (ETL) increases its electron charge to inject into QDs. On the other hand, the accumulated charge in QDs stays stable when the voltage increase is applied.

4.5 VALIDITY OF SIMULATION MODEL

As extracted from [115], simulation refers to the application of computational models to the study and prediction of physical events or the behavior of engineered systems. The accuracy of those computational models when comparing to reality is key to develop data utilized for managerial or technical decision-making [115].

Particularly, in the case at hand, a computational model has been developed to simulate the behavior of the QLED device in reality. Thus, a mathematical model has been built up based on the parameters extracted from the physical system.

Specifically, when comparing the experimental and simulated results in Figure 96, it is possible to conclude that the computational model developed fits reality accurately. However, as in any theoretical model, some strategies can be improved so as to make the model even closer to reality.

Thereby, although the numerical data are validated experimentally and are in good agreement with the experiment results, we would like to highlight some of the limitations of the present simulator developed.

4.5.1 Radiative recombination

The actual theoretical model does not deal with this topic in the present simulator version. In order to introduce the latter, a generation/recombination rate might be incorporated in Eq.9. Nevertheless, we decided to postpone this study due to the relative low visible radiative phenomena of the device and the good agreement obtained with the experimental results. Further steps about how to integrate this light term in the simulator are introduced in 4.5.7.1.

4.5.2 Density of States (DOS)

DOS is key to calculate the final I-V curve of the system. In the current computational model, some basic approaches have been used as described in 4.3.1.5. Thus, improvements in the models used to calculate DOS both for QDs and the transport layer could come up with better accurate results compared with experimental data from a real QLED device.

4.5.2.1 Quantum Dots

As explained, DOS for QD elements are calculated based on the use of a Lorentzian shape to introduce the broadening of the discrete energy levels from Eq.20 where γ is the broadening of the level and it is related to the tunnel probabilities [100], [109].

However, other techniques as *ab-initio* methods like DFT (Density Functional Theory) could give more accurate results when comparing with reality. Thus, a more realistic modelling for QD DOS might help to improve the *QLEDsim* simulator results.

4.5.2.2 Transport Layers

As explained, transport layers could be considered as different structures from QDs and they have been identified as two-dimensional materials. For these kinds of 2D dimensional nanostructures DOS was defined in Eq.22.

In this case, the improvement to be made is more related to the calculation of energy levels ϵ_n since infinite potential well within EMA approach has been considered to calculate them. This first simple approach could be upgraded to a more realistic one where a potential barrier is “seen” depending on the electric field applied. Thus, it would be possible, in principle, to introduce this calculation of energy levels dynamically with the bias potential applied. Therefore, in each voltage step, the barrier height is taken into account and the energy level is reassessed to finally obtain a more realistic curve for the density of states.

4.5.3 Thermal Dissipation

From a macroscopic point of view, heat dissipation might play an important role when designing the QLED device for real applications, particularly for automotive lighting ones. Nevertheless, thermal dissipation features were not considered in the current computational model, since the characterization of the experimental fabricated QLED was performed in a short period of time i.e. electrical characterization was made through a source meter unit (SMU) laboratory tool in a matter of seconds. Therefore, the influence of self-heating in the I-V figure was considered negligible for the objective of this work, and the good agreement between experimental and simulation results seems to support our approach.

4.5.4 Electrode Interface Capacitance

As shown in Eq.24, the solution of the Poisson equation in our model for the local potential can be divided into two terms. The first one is called the Laplace term [100], [112] and it contains the capacitive couplings between the different layers of the QLED device. These capacitive couplings have an important contribution in the final QLED current since they dominate the DOS shift, changing therefore the number of energy levels which might contribute to the transport process [100].

Furthermore, our model shows that the junction capacitance at the interface between the electrodes and the related transport layers plays an important role in the I-V performance, specifically in both the current device capability and the QLED turn-on voltage parameters. Particularly, Anode-HIL interface capacitance has a greater influence in the I-V plot shape.

Thereby, Figure 105 proves how these two parameters i.e. current capability and turn-on voltage can be modified by adjusting the interface capacitance at the anode side. Thanks to the QLED simulator developed, this task can be carried out easily by either changing the transport layers or directly estimating that impact of the capacitance value in the whole model system.

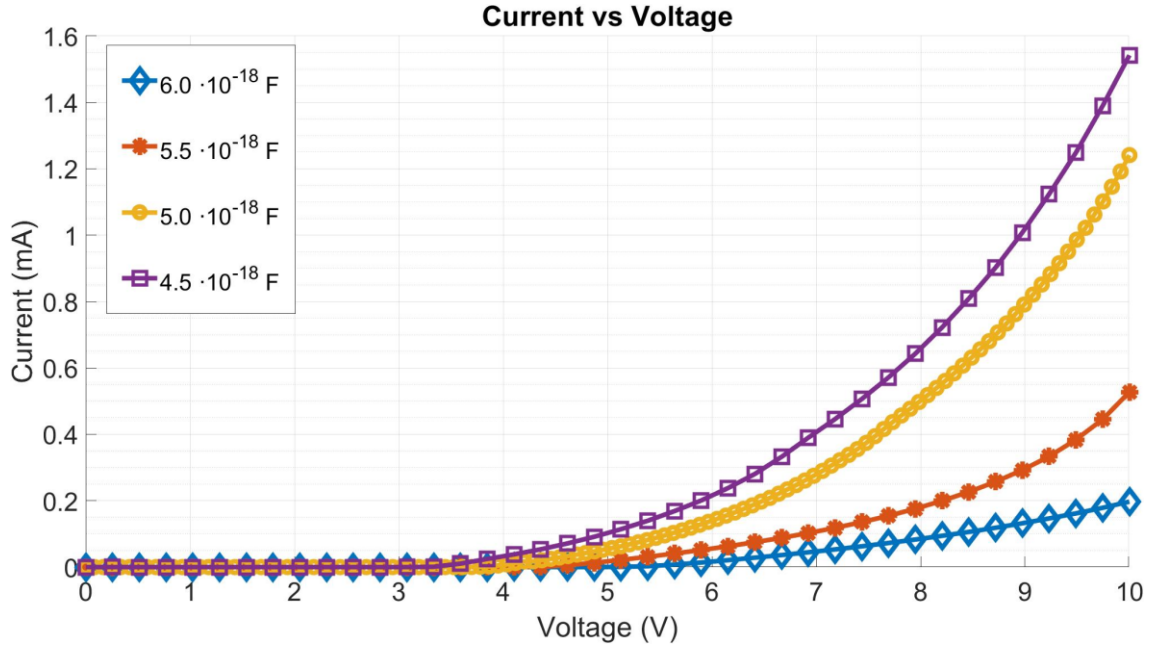


Figure 105: I-V QLED plot varying Anode-HIL interface capacitance. Simulated for this work.

It is worth saying that the values of capacitance used in our work for Anode-HIL interface are the same order of magnitude as the capacitances given by the Coulomb blockade effect in similar systems. Moreover, those values are below the maximum capacitance per unit area (C_{\max}) reported by Islam *et al.* [116], [117] and shown in Eq.(29).

$$C_{\max} = \frac{\epsilon_r \epsilon_0}{t} \quad (29)$$

where ϵ_r is the relative permittivity of the dielectric media, ϵ_0 is the free space permittivity and t is the layer thickness.

Eventually, in order to help to design a real QLED device, that Anode-HIL interface capacitance should be put under control; firstly during the manufacturing process (HIL layer deposition on the anode electrode by using accurate thin-film deposition techniques) to have uniform layers which would lead to the same I-V characteristics for all pixels built on the same substrate. And secondly, by modifying that capacitance value through some kind of the transport layers doping, which could give an optimal charge injection balance into the device.

4.5.5 Quantum Dot size

Another topic to bear in mind is the variation of current transport with the QD size. As reported in the literature, a current increase with the dot size is expected since both the DOS of QDs and the conduction gap have a strong influence in the final current. Specifically, as size increases, the available states inside the nanoparticles increase, while the QD band gap decreases due to relaxation of quantum confinement. Those effects contribute to increasing the current with the dot size [108].

4.5.6 Fitting parameters

4.5.6.1 Interface layer capacitances: $C_{ij}^{Layer\ interfaces}$

Capacitive elements used in the Poisson equation solution were analyzed in 4.3.1.7. Particularly and concerning to the Laplace term, the solution is given as a function of the capacitive couplings between the different QLED layers with the rest of the system [109]. Therefore, a good modelling of this capacitive coupling is essential to obtain a realistic I-V characteristic curve.

Specifically the interface layer capacitances have not been calculated with an explicit formula but estimated and used as fitting parameters for the *QLEDsim* simulator. A possible more accurate calculation would consist in using the junction capacitance for a depletion region when two semiconductor materials are in contact. This formula is proposed below [118] in Eq.30 where W is the width of the depletion area.

$$C_{ij}^{Layer\ interfaces} = A \frac{\epsilon_0 \epsilon_r}{W} \quad (30)$$

This junction capacitance expression has the same expression as the junction capacitance between parallel planes but using the distance between planes taking W as the width of the depletion area. Thus, if abrupt union is considered:

$$W = \sqrt{\frac{2\epsilon_0 \epsilon_r}{q} \left(\frac{N_A + N_D}{N_A N_D} \right) (V_{bi} - V)} \quad (31)$$

As it can be extracted from the above Eq.31, W is voltage dependent on V_{bi} (electrostatic contact potential). In this way, for each bias voltage step, it would be necessary to assess $C_{ij}^{Layer\ interfaces}$ dynamically out of equilibrium. Therefore, although the algorithm would be more complex, the final results might be closer to reality and thus similar or more accurate to experimental data obtained.

4.5.6.2 Dielectric constant for organic layers (HIL, HTL)

Due to the specific materials used for the hole injection and transport layers (HIL and HTL), it has been difficult to find particular literature to obtain values of the dielectric constant of those materials. In order to extract more accurate results it would be necessary to characterize all materials used to manufacture the QLED device as much as possible. Thus, accurate theoretical results compared to the experimental ones would be finally obtained.

4.5.7 Future research with *QLEDsim* simulator

Thanks to the *QLEDsim* simulator developed, further research can be established in the future so as to emulate new computational strategies to approach the theoretical basis to the experimental results. Thus, some possible ways to boost the capabilities of this simulator are presented below.

4.5.7.1 Light term integration

This could be an important step to further research on the *QLEDsim* simulator. Currently, the term of light (generation and/or absorption) is not included in the equations described in this BL4. Nevertheless, since an optoelectronic device is in play, particularly a light emitting diode, it might be useful to introduce this term for making an accurate current contribution for the bias voltage applied and also for the emitting light calculation.

Likewise, to have a complete QLED system description, optical transitions between electron and hole states, stimulated generation and recombination and the electrical response of the whole system under external perturbations i.e. light and bias voltage [107], [109] should be taken into account.

This research has been left for future improvements of the simulator. However, it is pointed out where this term should be included in the algorithm. Thus, the rate equations should be modified to introduce stimulated generation/recombination carrier processes to be reflected in Eq.32 below.

$$\frac{dN_i}{dt} = \frac{4\pi q}{h} \left(\int T_{Li} \rho_L \rho_i (f_L - n_i) dE + \int T_{Ri} \rho_R \rho_i (f_R - n_i) dE + \sum_{j \neq i}^{(N-1)} \int T_{ji} \rho_j \rho_i (n_j - n_i) dE \right) + X \quad (32)$$

$\forall i=1 \dots N$

The equation above shows all the current terms contributions i.e. contributions from the electrodes (first and second term) and the contribution of all neighbor layers [105], [109]. Thus, it is necessary to introduce a new light term contribution X in the rate equations.

4.5.7.2 QLED configurations

Eventually, other QLED physical structures can be studied by easily introducing the correct parameters in the *QLEDsim* simulator. In this work, CuInS₂/ZnS nanostructures combined with different organic/inorganic layers have been studied. However, other kinds of configuration based on InP/ZnS, identified in the first literature research BL1, along with different transport layers for both hole and electron carriers could be further investigated.

4.6 CONCLUSIONS

Thanks to the previous research made on both QD and QLED device, a model to describe the electrical behavior of the experimentally manufactured lighting system was presented. That model was based on the Transfer Hamiltonian approach and it was upgraded from the work made by Illera *et al.* and adapted to our specific QLED device. Thus, I-V curve was simulated and compared with experimental results, concluding that the theoretical background developed and implemented in the *QLEDsim* simulator was in good agreement with the experimental outcome due to the convergence of the results obtained. It allowed us to understand the different QLED electrical behaviors and to propose some improvements in the QLED design and fabrication process. Therefore, it is possible to state that the simulator can be used to electrically model QLED devices before going to the laboratory to perform the experimental implementation.

5 BL5 – AUTOMOTIVE INTEGRATION

5.1 SCOPE

The last part of this research is based on the work developed in the previous blocks. Thereby, once the physical mechanisms behind quantum dots, i.e. electroluminescence and photoluminescence, have been deeply studied, the next leap to take is to integrate those nanoparticles in a real automotive application. As already highlighted along this manuscript, and to the best of our knowledge, this is the first study made to introduce this nanotechnology in automotive lighting products, particularly in exterior lighting systems.

As it has been deployed during the whole research, this work spins around lighting systems in the automotive field. Therefore, this final block BL5 deals with the different possibilities of using quantum dots and QLEDs in a particular automotive lighting application.

In order to complete this eventual step successfully, the automotive multinational company VALEO has actively participated in the final lighting product integration. In this way, this BL5 has been developed in close collaboration with VALEO VISION located in Paris, France. Therefore, the rules and requirements from an automotive lighting point of view will be thoroughly analyzed, allowing us to compare the current LED/OLED technology with a QLED device demonstrator designed and fabricated by creating some important figures of merit for the automotive field accordingly.

5.1.1 Research Plan

Having a look into the research plan defined at the beginning of the PhD project, it is possible to depict graphically the location level of this block BL5 inside the bottom-up methodology presented.

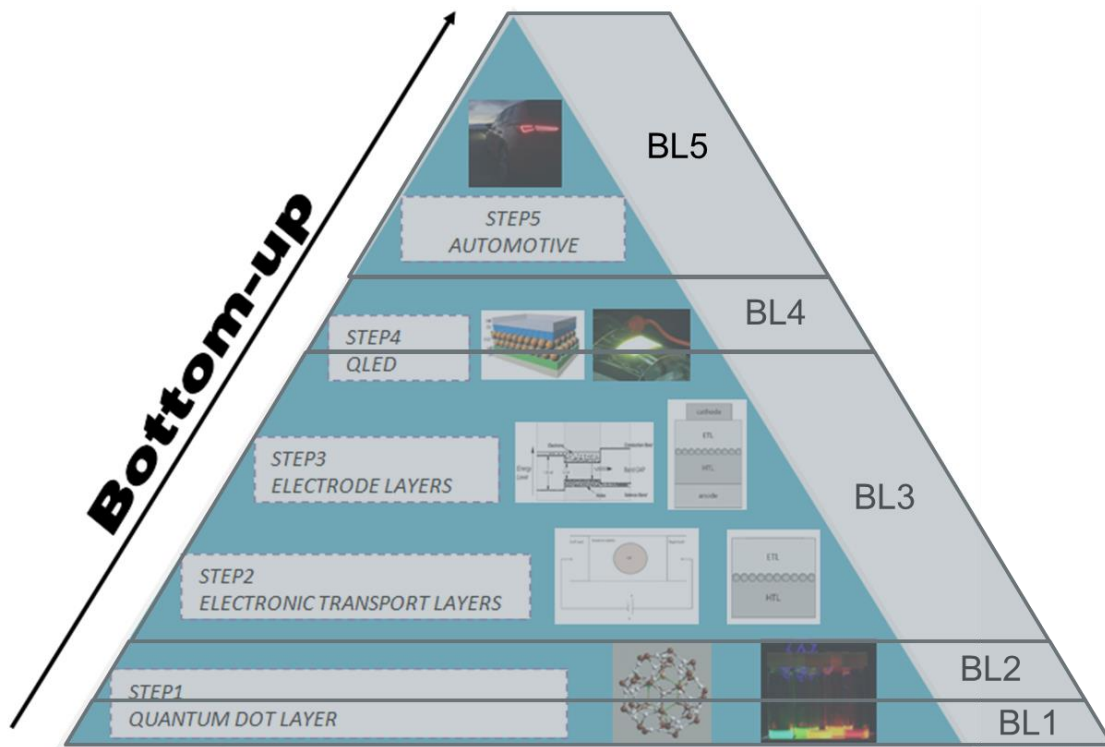


Figure 106: Block BL5. BOTTOM-UP methodology.

5.2 VALEO - SMART TECHNOLOGY FOR SMARTER MOBILITY



Figure 107: Valeo logo. Reproduced from [119].

This industrial PhD work has been carried out under the collaboration frame of Valeo multinational company. Valeo is an automotive supplier and partner to automakers worldwide. As a technology company, Valeo designs innovative solutions for smart mobility, with a particular focus on intuitive driving and reducing CO₂ emissions. Valeo Group also provides and distributes spare parts for automakers and independent aftermarket operators [119]. Key figures are shown in Table 46.

VALEO key figures		
114,700 employees	19,244 million euros in sales	33 countries
199 production units	2,029 million euros in R&D expenditure	59 R&D centers

Table 46: VALEO 2019 key figures. Extracted from [119].

As a global automotive supplier, Valeo operates in 33 countries to design innovative technologies and systems that will make the car of tomorrow more intuitive, autonomous, connected and environmentally friendly [119].

Valeo's ambition, as a tech company, is to play a major role in tomorrow's mobility. At the heart of today's environmental and social issues, future mobility must be greener, safer and more diverse. It must also contribute to the well-being and safety of citizens and consumers. As claimed in Valeo statement of purpose [119]:

We will achieve our ambition thanks to our unique positioning and technological leadership in areas that are at the heart of the transformation of the automotive industry and sustainable mobility, across the globe. This positioning and leadership are rooted in our expertise, innovations and operational excellence. They are driven by our values and business culture, oriented towards serving our customers, employees, shareholders and the regions in which we operate.

Valeo Business Groups are responsible for global growth and operating performance for their Product Groups and Product Lines. Each of the Business Groups, described below, is structured to reinforce cooperation and stimulate growth for all of Valeo product groups worldwide [119].

- **Driving Assistance Systems** – making driving safer, more autonomous and better connected through perception systems and artificial intelligence. Providing reinvented mobility solutions and human-machine interfaces. Resulting in an innovative user experience.
- **Powertrain Systems** – developing comprehensive, integrated electric powertrain solutions for all vehicles categories, from small urban cars to premium sedans, and technologies to make internal combustion engines cleaner.
- **Thermal Systems** – reducing pollutant emissions from internal combustion engines, optimizing the driving range and battery life of hybrid and electric vehicles, and improving comfort and well-being for passengers in the cabin.
- **Visibility Systems** – designing and producing innovative and efficient lighting and washing systems for safer, more comfortable manual driving and for an improved and enhanced travel experience in autonomous vehicles.

These Valeo Business Groups are depicted in Figure 108.

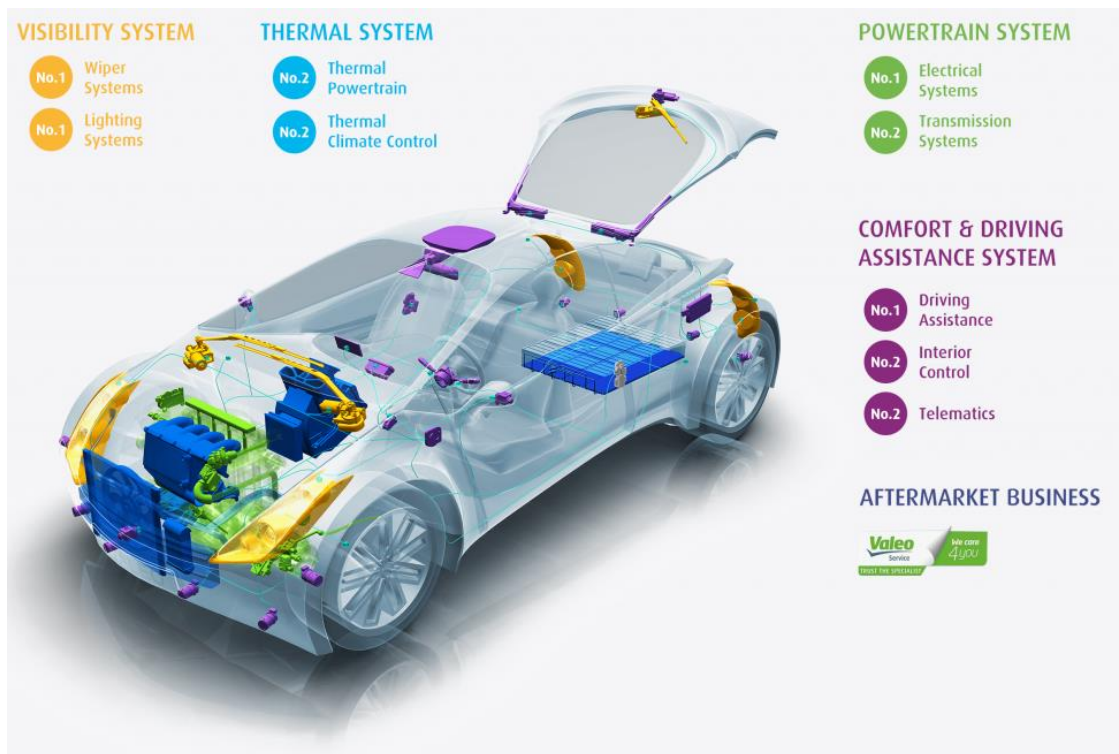


Figure 108: Valeo Business Groups. Reproduced from [119].

5.2.1 Visibility Systems

The Visibility Systems Business Group – made up of two Product Groups, Wiper Systems and Lighting Systems – designs and produces innovative technologies to ensure the best possible visibility and safety for drivers in all weather conditions, at both day and night, with optimum design and comfort [119].

5.2.1.1 Lighting Systems

Lighting products portfolio is part of Valeo's Visibility Business Group. Valeo designs interior and exterior lighting solutions tailored to meet all automaker model requirements. From the latest adaptive lighting technologies to intuitive interior lighting solutions to stylish and design-centric external lighting, Valeo constantly innovates to improve comfort and safety for drivers and passengers alike. Figure 109 shows the three product line inside lighting systems product group [119].



Figure 109: Valeo Product Lines. Reproduced from [119].

Thereby, from innovative interior and exterior lighting solutions (headlamps and lights), to LED lights and non-blinding “road” beams, each solution addresses the needs and market trends of cars, while ensuring clear visibility and the safety of drivers [119].

5.3 LIGHTING SYSTEMS DEFINITIONS

Valeo launched a brand new technical handbook under its Valeoscope program covering all lighting systems in the automotive industry. For the sake of clarity, the following technical information and definitions for this chapter 5.3 have been extracted from that Valeo technical handbook [120].

5.3.1 *The human eye*

The eye is able to sense only a small portion of all electromagnetic radiations. Thus, visible light is composed of a range of wavelengths from 380nm “blue light” to 750nm “red light”. In fact, some colors are better perceived than others due to the structure of the human eye, and the sensitivity of the human eye to wavelengths outside that range drops dramatically as depicted in Figure 110 [120].

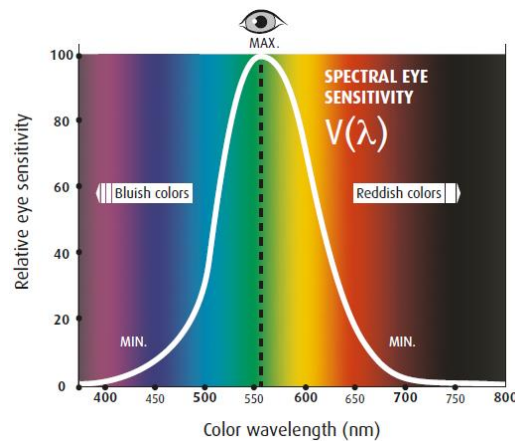


Figure 110: Relative eye sensitivity. Reproduced from [120].

Human eyes behave differently at night compared to daylight. The sensitivity of the human eye to colors strongly depends on whether it is light or dark. In dark conditions, a whiter light (bluer in the spectrum) improves visibility [120]. It is shown in Figure 111.

Day and night-time eye sensitivity

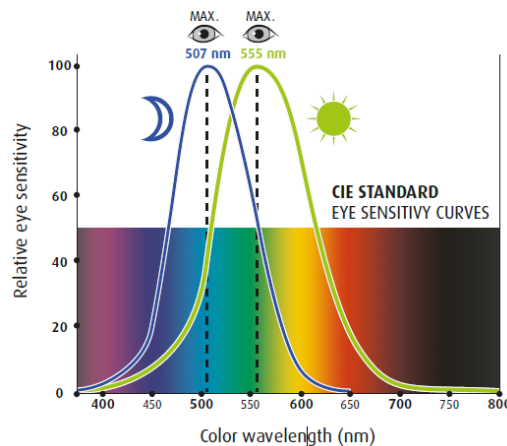


Figure 111: Day and night-time eye sensitivity. Reproduced from [120].

In this way, automotive lighting systems are designed according to the visual perception of the human eye and are developed to compensate the visual weaknesses in some driving situations. The lighting systems on vehicles have evolved enormously in the last few generations to ensure road users comfort, safety and security [120].

5.3.2 *Light color*

5.3.2.1 *The colorimetric graph: CIE grid*

The International Commission on Illumination also known as the CIE, is an international standardization body devoted to worldwide cooperation for lighting, color and vision purposes. The CIE has defined a standard grid that permits us to specify light sources colors. This CIE grid depicted in Figure 112, represents all of the colors that are visible to the average person [120].

- The edges of this diagram corresponds to the so-called monochromatic lights. Monochromatic colors are specified by their unique or preponderant colors and wavelengths in nanometers (nm).
- Chromatic lights are located in the interior of this diagram. Chromatic colors are specified with the so-called X and Y coordinates.
- White colors are located in the center of this global chromaticity diagram. As “whites” are at the border of several chromatic colors, there is a large pallet of white colors.

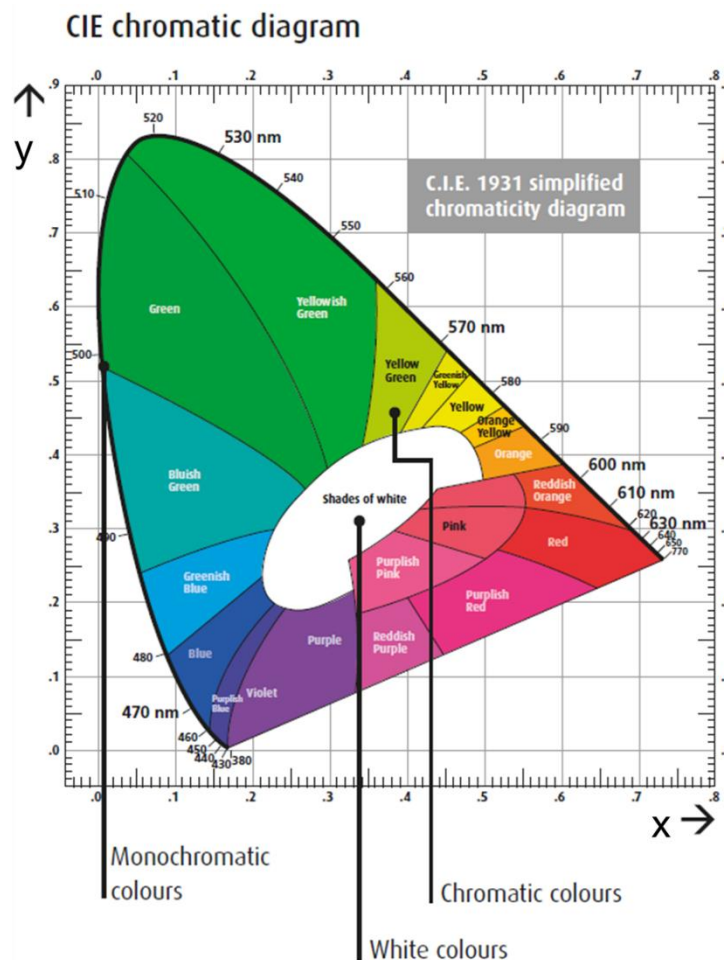


Figure 112: CIE chromatic diagram. Reproduced from [120].

5.3.2.2 *White colors*

White colors are defined in the CIE grid, either by their “color coordinates” or their so-called “color temperatures” [120].

- Colour coordinates x, y are defined on the CIE chromaticity diagram.
- Colour temperature (in Kelvin: K) is another way to characterize white illuminants.

Colour temperatures over 5000K are called cold colors (bluish white), lower color temperatures (2700-3000)K are called warm colors (yellowish white through red). Some color temperatures depending on the lighting source are presented below [120]:

- Day light temperature $\sim 6500\text{K}$
- LEDs $> 4500\text{K}$
- Xenon lamps $\sim 4300\text{K}$
- Halogen lamp $\sim 2800\text{K}$
- Candle flame $\sim 1850\text{K}$

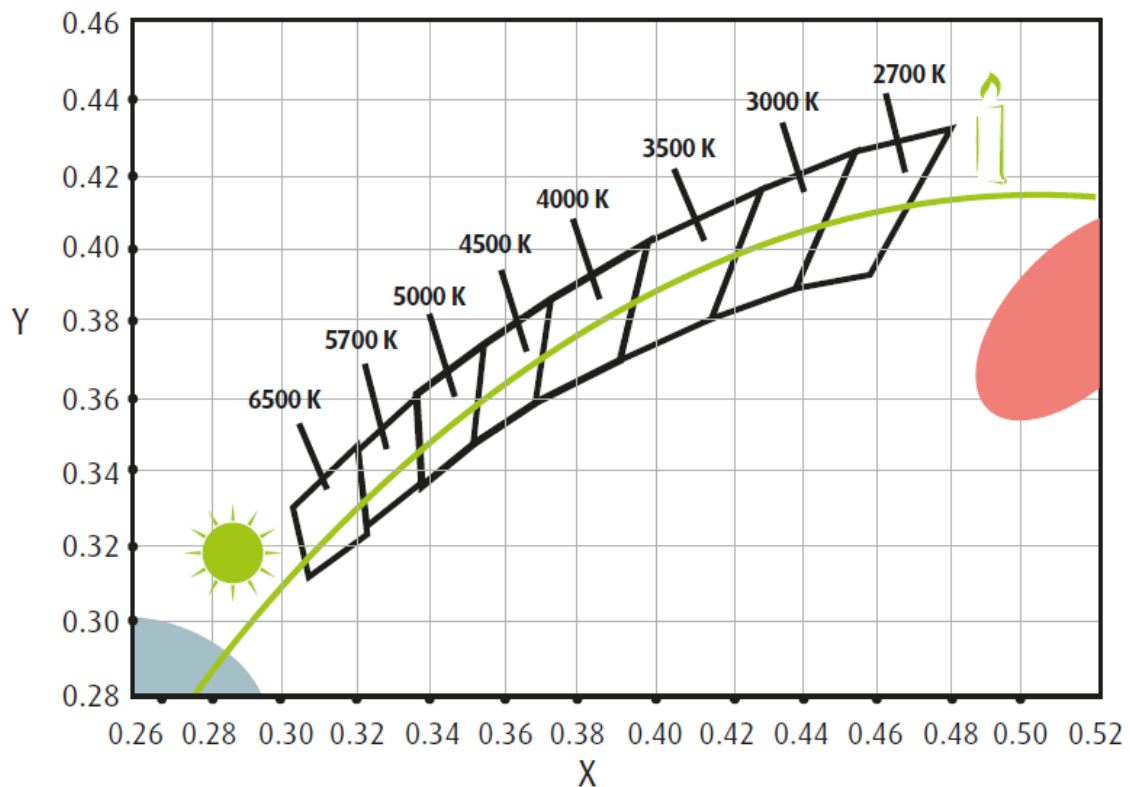


Figure 113: CIE x, y chromaticity diagram. Reproduced from [120].

5.3.3 Photometric basis

Photometry is the science concerned with the measuring of human visual response to light. Some definitions are introduced below [120].

5.3.3.1 Light intensity

The intensity is the luminous energy from a lighting source in a specific direction.

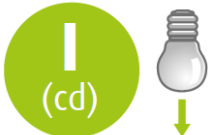
Symbol	Unit	
I	Candela (cd)	

Table 47: Light intensity symbol. Extracted from [120].

Light intensity varies depending on which direction the light source is being viewed from. This is reflected in Figure 114 where it can be seen how intensity drops from 140 cd @20° (front viewing) to 70 cd @90° (side viewing).

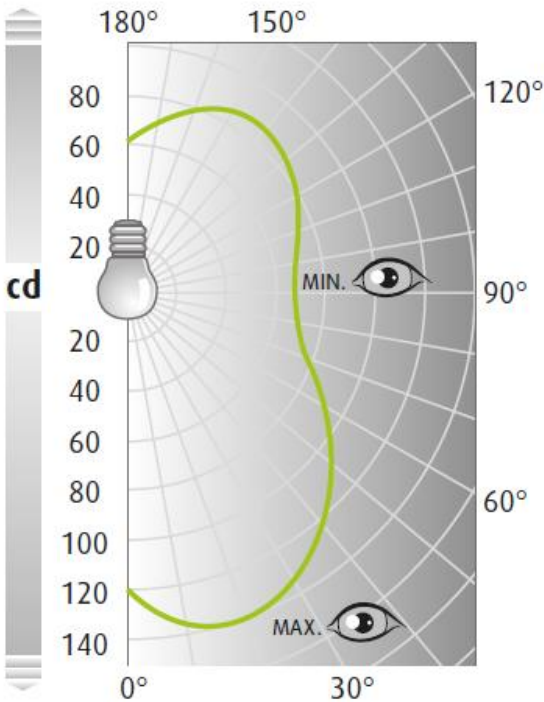


Figure 114: Light source emission profile. Intensity versus angular viewing. Reproduced from [120].

5.3.3.2 Luminous flux

The luminous flux is the complete light output radiated from a light source. Luminous flux is the measure of the perceived power of light and it is adjusted to reflect the varying sensitivity of the human eye to different wavelengths of light. The unit of luminous flux is the lumen (lm). One lumen is defined as the luminous flux of light produced by a light source that emits 1 cd of luminous intensity over a solid angle of 1 sr [120].

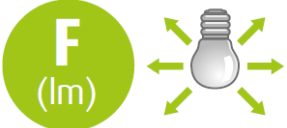
Symbol	Unit	
Φ	Lumen (lm)	

Table 48: Flux symbol. Extracted from [120].

Lumen is defined taking the human eye sensitivity curve as a basis. Figure 115 shows how the human eye perceives a light source depending on its color composition. The red curve shows the sensitivity of the human eye to color stimulus [120].

It can be seen that many color peaks in source Nr.2 are close to the red line, meaning that the peaks in source Nr.2 will be perceived by the human eye as a higher luminance source than in source Nr.1 [120].

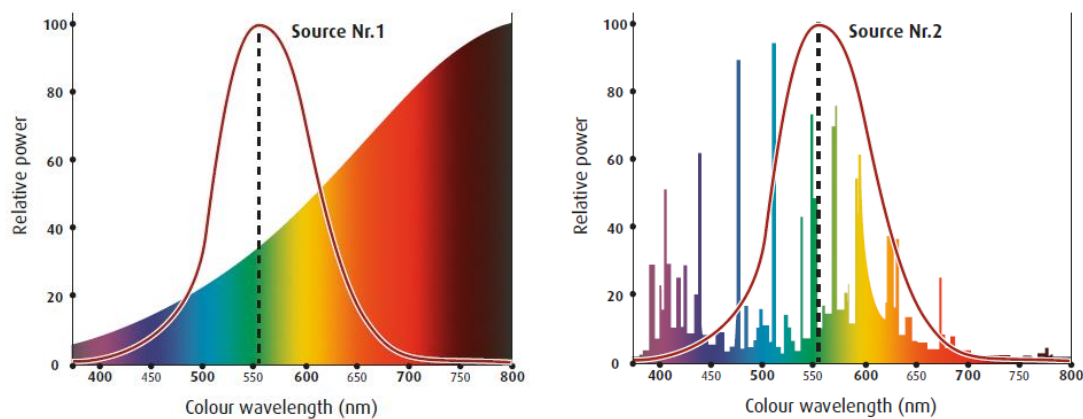


Figure 115: Light sources. The theoretical and ideal light source for a human eye would have a spectral decomposition fitting perfectly into the red line. Reproduced from [120].

5.3.3.3 Illuminance

The luminous flux from a light source (lumens) falling on a unit of surface (m^2) is called illuminance [120].

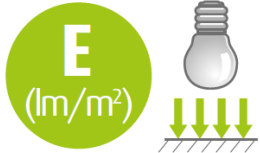
Symbol	Unit	
E	Lumen/ m^2 (Lux)	

Table 49: Illuminance symbol. Extracted from [120].

Illuminance levels on the road are specified according to automotive standards, which depend on the type of light source, such as incandescent (Halogen), gas discharge (Xenon) or LED (Light Emitting Diode) lamps. Figure 116 shows the illuminance projection of the headlamp equipped with a Xenon lamp. This curve is called an Isolux curve where lines indicate illuminance levels in steps.

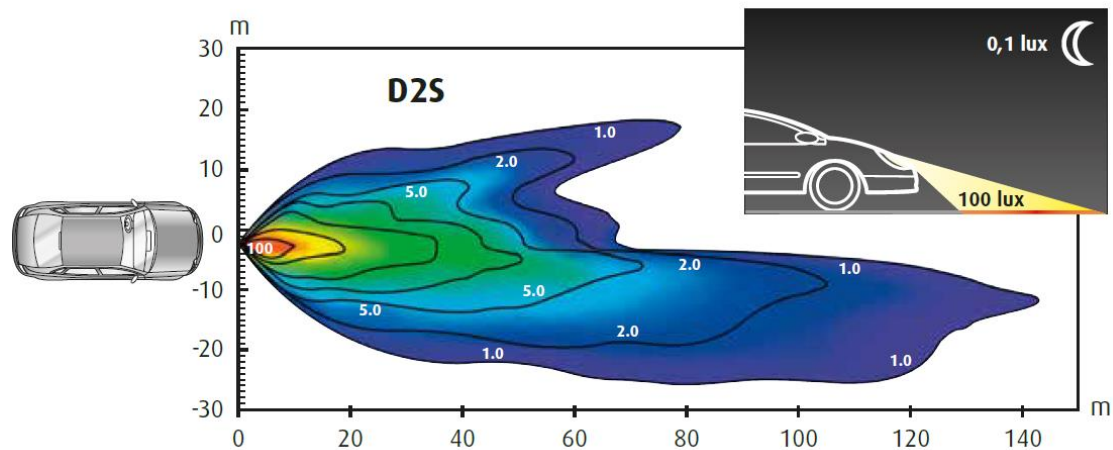


Figure 116: Diagram of the illuminance projection of a headlamp. Reproduced from [120].

In this example, the illuminance reaches a maximum at 100 lux in the front of the car and minimum of 1 lux on the outer line (1.0). The illumination level does not make allowance for the amount of light reflected off the surface. The reflected light is called the luminance (seen in the next chapter), which depends on the nature of the surface, including its color[120].

5.3.3.4 Luminance

Luminance measures the reflected light from a surface to a given direction. The surface can itself be light-emitting, transmitting or reflecting light from another source. Luminance is related to a luminous intensity emitted per unit of area from a surface in a specific direction [120].

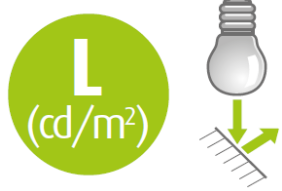
Symbol	Unit	
L	Candela/m²	

Table 50: Luminance symbol. Extracted from [120].

Luminance is the perceived brightness and it is used to categorize [120]:

- Light sources (eg. lamps).
- Lighting systems (eg. headlights).
- Any surface that is bright (eg. road signs).

5.3.3.5 *Luminous efficacy*

Luminous efficacy is a figure of merit for light sources. It is the “proportion” of visible radiations over the entire radiation emitted by this light source. The luminous efficacy is expressed in lumens per watt and it is defined as the ratio between the total luminous flux emitted (lumens) by the total amount of electrical power (watts) it consumes [120].

Symbol	Unit	
η	lm/W	

Table 51: Luminance symbol. Extracted from [120].

It is an important factor in overall efforts to improve energy consumption and reduce vehicle CO₂ emissions.

5.4 AUTOMOTIVE LIGHTING SYSTEMS: TO SEE AND TO BE SEEN

Valeo launched a brand new technical handbook under its Valeoscope program covering all lighting systems in the automotive industry. For the sake of clarity, the following technical information and definitions for this chapter 5.4 have been extracted from that Valeo technical handbook [120].

The lighting system can be divided in two subfamilies **to see and to be seen**.

- **Lighting:** to project light to better anticipate the road ahead (bends, road signs, pedestrians, trees, etc). The better you can see the safer you are.
- **Signalling:** to allow light to be seen by other drivers and pedestrians: being seen allows others to better detect and anticipate your movements.

Both lighting and signaling functions, depicted in Figure 117, are specified and designed according to regulations.

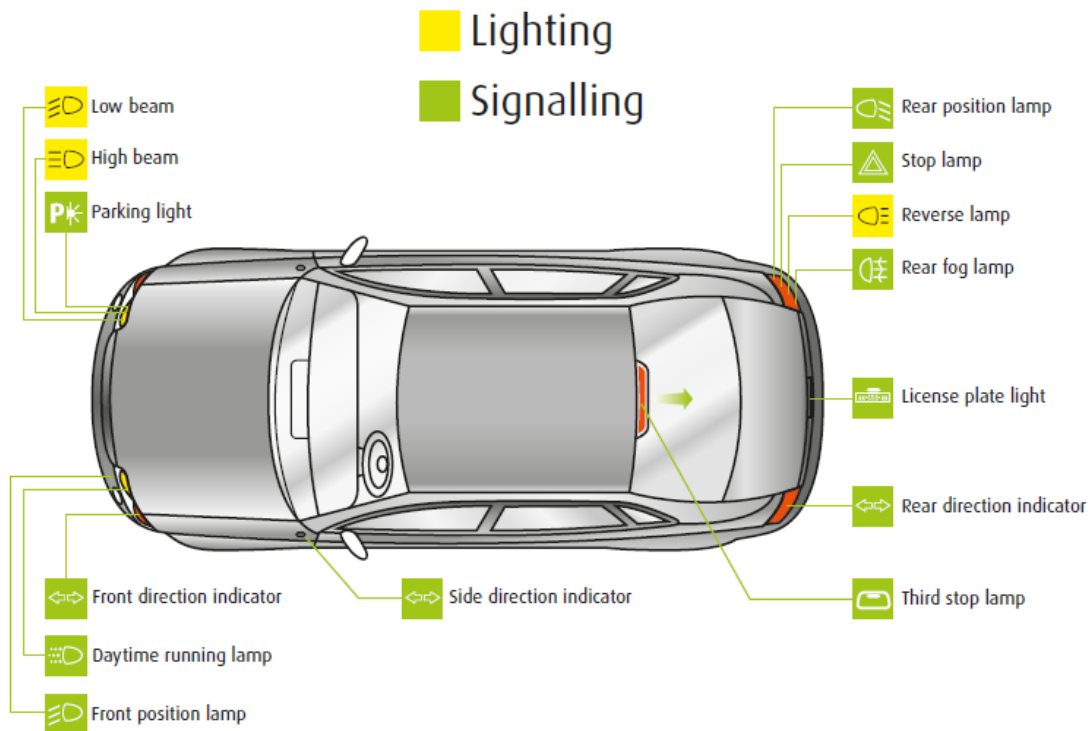


Figure 117: Lighting and signaling functions in automotive. Reproduced from [120].

5.4.1 *Front Lighting Functions – HEADLAMPS Beams*

A good front lighting function provides maximum visibility with minimum inconvenience for other road users. Headlight beams are standard patterns that set the light projection levels and limits on the road [120]. Several beams are defined and depicted in Figure 118:

- Low beam also called passing or dipped beam.
- High beam also called main-beam or full-beam.
- Fog beam

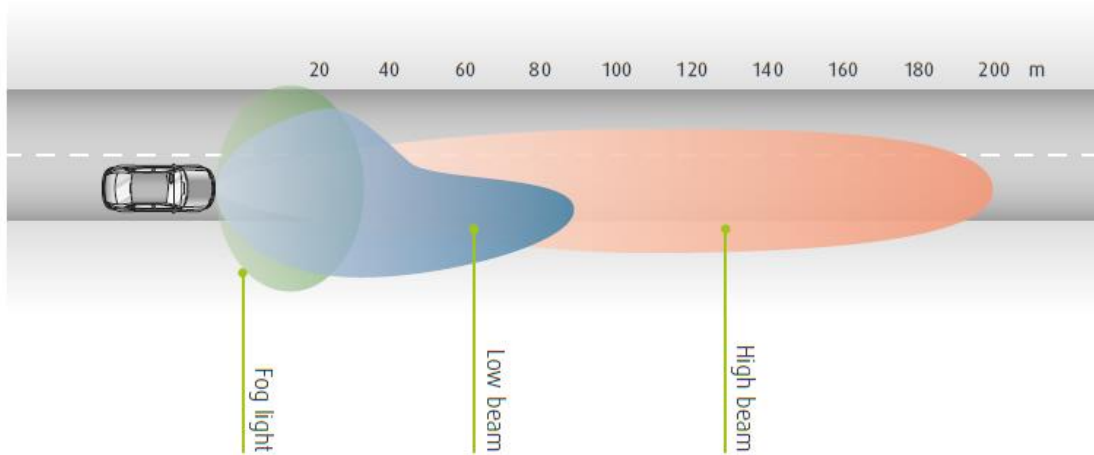


Figure 118: Lighting headlamps beams. Reproduced from [120].

5.4.2 *Signaling Functions – REAR and HEADLAMPS*

The signaling has a major function to vehicle safety, it permits distance communication to other vehicles by indicating presence and direction changes. From rearlamps, to fender-lamps, trunk-lamps and bumper-lamps, the signaling product line offers a wide diversity of designs [120].

Similarly to the lighting function, the signaling function evolved a lot from historical products to the most sophisticated laser etched and lightguide designs. The main signaling functions are named below [120].

- STOP function
- TAIL function
- TURN INDICATOR function
- REAR FOG function
- REVERSING function
- DAYTIME RUNNING LIGHT (DRL) function (headlamps)

5.4.3 *Photometry in signaling functions*

5.4.3.1 *Photometric Charts*

In order to simplify control lighting systems specification, photometric charts have been standardized for each type of light source and have been updated according to systems evolution and complexity. Photometric charts are a 2D representation of light projection on a flat vertical screen. The illumination mapping is defined via vertical (V) and horizontal (H) coordinates on a photometric chart as shown in Figure 119 [120].

Points or zones are associated to intensity value limits (min or max) in candela. This flat image reflects the real illumination on the road as shown in Figure 119, where the areas to be illuminated or not in front of the vehicle and their respective intensity levels are the basis of photometric charts, for the following areas [120]:

- 1-Eye fixation
- 2-Rear view mirror
- 3-Posted panels (50 m)
- 4-Posted panels (100 m)
- 5-Opposers eyes (50 m)
- 6-Road signs (50 m)
- 7-Road signs (50 m)
- 8-Pedestrians (50 m)
- 9-Crash barriers (50 m)

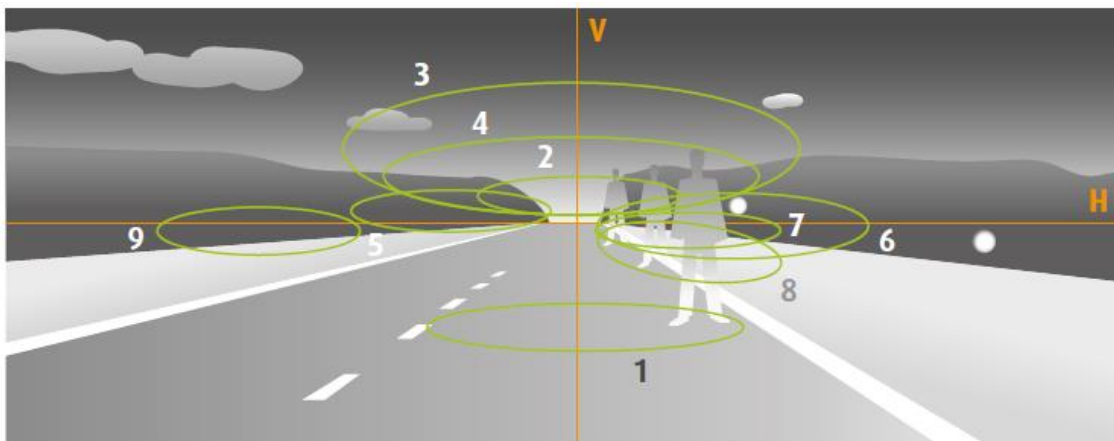


Figure 119: Photometric charts with vertical (V) and horizontal (H) coordinates in front of the vehicle. Reproduced from [120].

5.4.3.2 *Luminous Intensity and Flux values in automotive*

Luminous intensity $I_v(\text{cd})$ is a measure of the quantity of visible light that is emitted in unit time per unit solid angle, based on the luminosity function, a standardized model of the sensitivity of the human eye. The unit of luminous intensity in the International System of Units is the candela (cd) [120].

As for lighting, the signaling devices have to comply with photometric specifications. European Commission standard (ECE) set photometric limits and all measurements conditions. Minimum and maximum luminous intensity values are defined in various directions of measurements, the minimum intensities are defined as a percentage of the minimum required in the axis for each lamp (100% in the direction $H=0^\circ$ and $V=0^\circ$). In order to achieve those photometric intensity values, it is needed to achieve a minimum luminous flux $\Phi_v(\text{lm})$, which depends on the optical system designed.

Therefore, as explained previously, the design of the optical system to achieve the luminous intensity required for automotive homologation at each different function is essential. Thus, depending on that optical system a different magnitude of the luminous flux is demanded on every single signaling function. In Table 52, the minimum flux requirement by lighting source, assuming a perfect optical system, and the main photometric features are shown for ECE regulation [120].

<i>Signaling Function</i>	<i>Color</i>	<i>Max I_v [H,V] (cd)</i>	<i>Min I_v [H,V] (cd)</i>	<i>Min Φ_v (lm)</i>
STOP	<i>Red</i>	260	60	5.5
TAIL	<i>Red</i>	17	4	0.41
TURN INDICATOR	<i>Amber</i>	500	50	4.7
FOG	<i>Red</i>	300	150	12.4
REVERSE	<i>White</i>	300	80	15.2
DRL	<i>White</i>	1200	400	37.8

Table 52: Minimum luminous intensity and flux requirements based on ECE automotive regulations. Extracted from [121] and [122].

5.4.4 Materials used in automotive lighting systems

Automotive lighting systems are formed by different parts. Particularly, headlamps and rearlamps incorporate bezels, reflectors, lens, light sources, electronics, mechanical parts etc. Among others, common plastic materials used for lighting systems are Polypropylene (PP), Acrylonitrile butadiene styrene (ABS), Polycarbonate (PC) or Poly(methyl methacrylate) (PMMA) [123].

The main reasons to use those materials as automotive plastics are based on: [123]

-Elasticity.

-Weight.

-Corrosion and impact resistance.

-Processability (molding)

Particularly, the materials identified above are briefly described in the following lines: [123]

→ PC

PC is widely used in headlights modules due to its good impact performance and transparency along with the mechanical and electrical insulation properties it offers.

→ PP

PP is used for both head and rearlight housing. It gives good electrical insulation and chemical corrosion resistance at a low cost price.

→ ABS

ABS and a mixture with PC material are often applied in taillight housing.

→ PMMA

PMMA, also known as acrylic or plexiglass, offers a good transparent performance used for optical transparent products, taillight lens and interior optical systems.

5.5 ELECTROLUMINESCENCE OR PHOTOLUMINISCENCE

QLEDs were manufactured following both physical phenomena i.e. photoluminescence and electroluminescence in block BL3. Particularly in chapters 3.2, 3.3 and 3.4 the latter was thoroughly analyzed. Moreover, when comparing with data from the first state-of-the-art research carried out in BL1 (chapter 1.7 and 1.8) it is possible to conclude that higher photometrical values can be achieved nowadays by using a photoluminescence phenomenon instead of an electroluminescent one.

Thereby, after analyzing the photometrical values required by the different signaling functions shown in Table 52, it can be stated that photoluminescent QLED devices could take over in a short-term timing. However, in the medium/long term it will be necessary to wait for more development time to introduce electroluminescent QLED devices in the automotive field.

We would like to introduce Figure 120 as our own estimation of the introduction of quantum dots in the automotive field, taking into account the different phenomena versus the integration time.

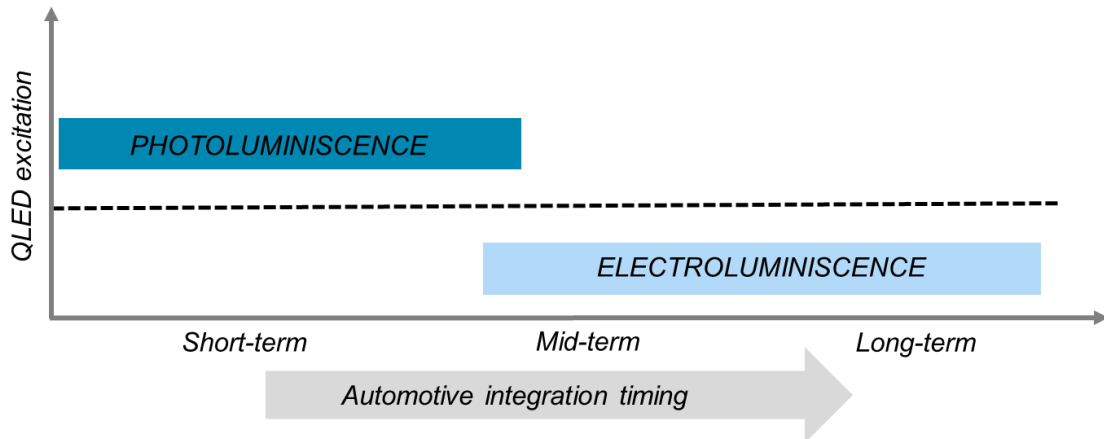


Figure 120: Estimation of quantum dot technology integration in automotive lighting systems applications in terms of physical excitation phenomena. Designed for this work.

Therefore, in order to complete the final objective of QLED device integration in an automotive product, photoluminescence phenomenon will be targeted due to its higher technological advance in the market.

To do so, quantum dot film sheets, including quantum dots as main nanoparticles to be excited by a higher energy radiation, will be used as a main part of the QLED automotive integration demonstrators which will be built up in the following chapters.

5.6 DEMONSTRATORS

5.6.1 *Quantum Dot Demonstrator*

Following chapter 5.5 and using the photoluminescence phenomenon, a **quantum dot dynamic demonstrator** was built up (Figure 121). The objective of this demonstrator is to show the great features of quantum dots as energy down conversion nanoparticles when they are excited with a higher energy radiation. In this case, the excitation source consists in blue LEDs (~ 450 nm peak) that hit different quantum dots nanostructures tuned to specific output wavelengths.



Figure 121: Dynamic quantum dot demonstrator. Designed for this work.

These colloidal solutions are contained in 5 ml of toluene solvent and were identified from the material selection carried out in BL1 during the literature research:

- Samples1: $\text{ZnSe/ZnS} \rightarrow$ Blue output color
- Samples2: $\text{CuS}_2/\text{ZnS} \rightarrow$ Red, Yellow and Green colors
- Samples3: $\text{InP/ZnS} \rightarrow$ Red, Yellow and Green colors

Then, once the quantum dots are excited through blue light, a wavelength conversion happens in the different quantum dots, obtaining the red, yellow, green and blue colors as output, as shown in the following snapshot in Figure 122.



Figure 122: Different colloidal quantum dots excited with 450nm wavelength. Designed for this work.

5.6.2 *QLED Automotive Lighting Application*

Using again the photoluminescence phenomenon, a **QLED dynamic demonstrator** was built up (Figure 123). The objective of this second demonstrator is to create a specific mockup, which could be integrated, in a real automotive product.



Figure 123: Dynamic photoluminescence QLED application for automotive lighting systems. Designed for this work.

Particularly, a 60-triangular-pixel dynamic mockup was designed and physically implemented. Thus, a mechanical, optical and electronics design was carried out to integrate the QDF sheets in a specific QLED automotive lighting application.

5.6.2.1 *Quantum Dot Film*

The whole design spins around the QDF sheets (Figure 124) acquired commercially from Nanjing Bready Electronics® [124]. Here, the main technical features of the QDF used are presented.



Figure 124: Commercial QDF from Nanjing Bready Electronics®. Reproduced from [124].

As it can be found in the QDF datasheet, these quantum dot films absorb the blue light in the backlight and red and green wavelengths, which are eventually mixed with part of the blue light to form the final white light, are emitted [124].

<i>Optical Specifications</i>	<i>Value</i>	<i>Unit</i>
<i>Transmittance</i>	≥ 50	%
<i>Haze</i>	≥ 80	%
<i>Luminance Uniformity</i>	≥ 70	%
<i>Red peak wavelength</i>	624	nm
<i>FWHM red</i>	≤ 25	nm
<i>Green peak wavelength</i>	531	nm
<i>FWHM green</i>	≤ 30	nm

Table 53: Optical specifications of QDF used from Nanjing Bready Electronics®. Extracted from [124].

Considering the haze parameter from Table 53, it is possible to anticipate a good light scattering, created by the quantum dots incorporated, which will lead to great surface light homogeneity.

Therefore, thanks to these QDF, it is possible to generate white light spectrally composed by blue, green and red wavelengths. This white light could be used to make automotive lighting functions like DRL/PL or it can be just color-filtered afterwards to perform TAIL or STOP ones as shown in Figure 125.

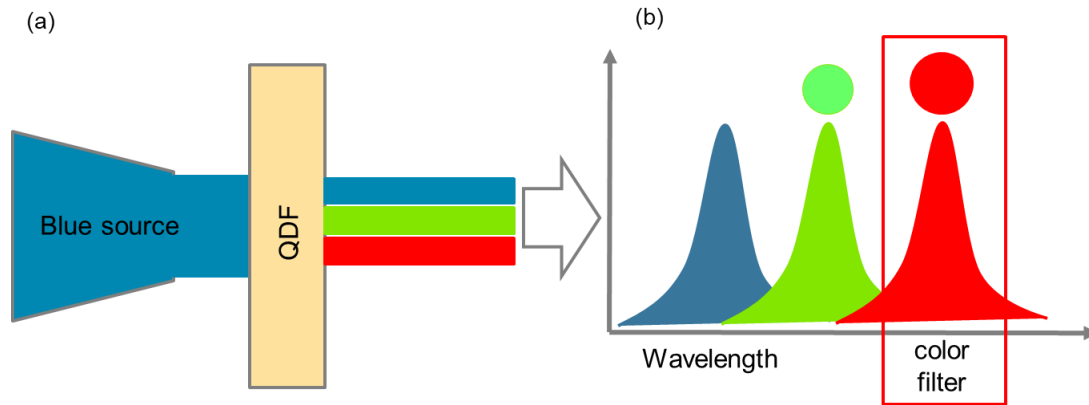


Figure 125: Automotive lighting functions possibilities from a QDF incorporating green and red QDs. (a) Physical implementation. (b) Output optical spectrum achieved. Designed for this work.

Although some experimental measurements will be made on QDF just after the color conversion, i.e. on the white color surface, this work will be focused on the red color to compare the performance with automotive TAIL lighting function versus the current LED/OLED technology.

5.6.2.2 Mechanical-Optical design

To begin with, GPL free computer-aided design (CAD) software *Blender*® has been used to build up the mechanical-optical implementation.



Figure 126: CAD software Blender®.

Thanks to this software, the QLED demonstrator was designed. Thus, different mechanical parts were drawn to integrate the 60 triangular-shape pixels, as shown in Figure 127.

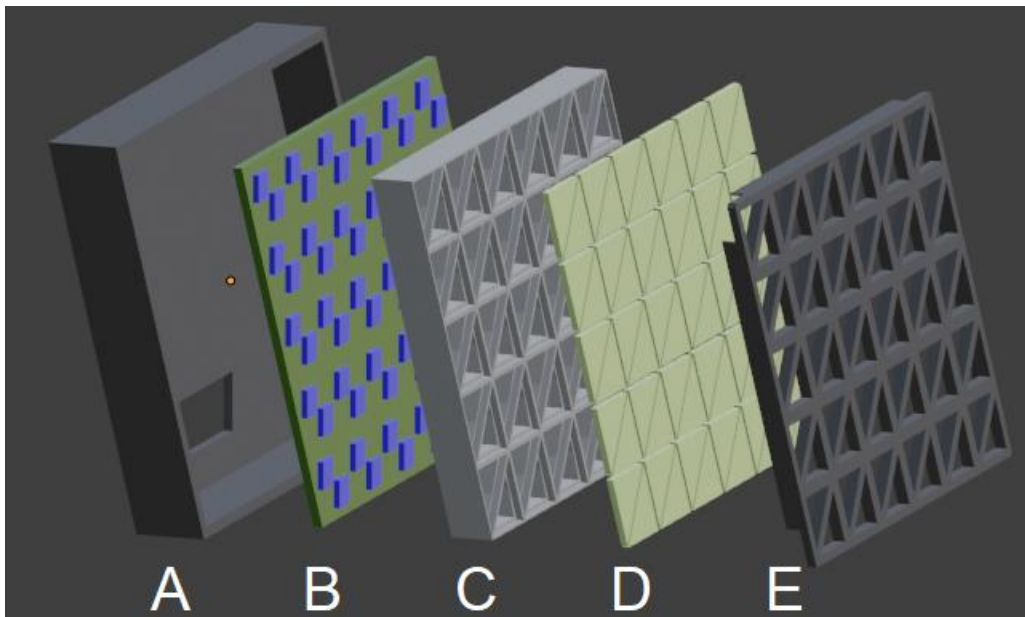


Figure 127: Exploded view of the experimental QLED device assembled. A) Case, B) Blue LEDs, C) Optical system, D) QDF, E) Light cover. Designed for this work.

As it can be seen from Figure 127, a first mechanical case, which will support the whole QLED device, contains the electronics printed circuit board (PCB) in first place. That PCB incorporates the centered-positioned blue LEDs to act as main source to excite the red and green quantum dots included in the QDF layer. To optically guide the blue light to the specific pixels formed in the QDF, a system formed by optical cavities is located in between. Finally, a light cover to adjust the output light from the QDF photoluminescence layer is placed on the top of the QLED device. Optionally, a color filter can be positioned after the light cover part to filter red wavelength as shown in Figure 125.

Moreover, in order to physically support the QLED device and to integrate all the electronics to control the individual blue LEDs, a mechanical base was designed as depicted in Figure 128.

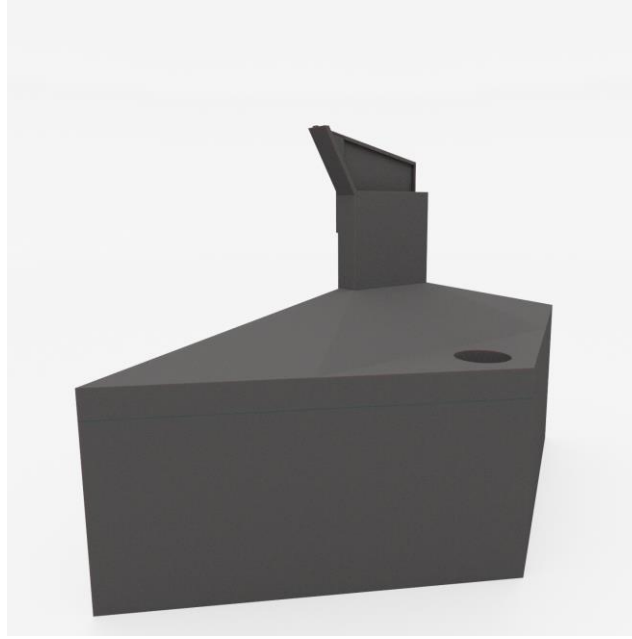


Figure 128: Demonstrator mechanical base. Designed for this work.

Eventually, mechanical and optical parts were 3D printed, post processed and assembled to fit the QLED device and the electronics presented in chapter 5.6.2.3.

5.6.2.3 *Electronics design*

The electronics part is the core of the dynamic motion of the QLED demonstrator introduced in chapter 5.6.2.4. It is composed of two different related developments i.e. hardware (HW) and software (SW). These two implementations are briefly described below.

5.6.2.3.1 Hardware (HW)

Figure 129 shows the HW block diagram of the electronics design.

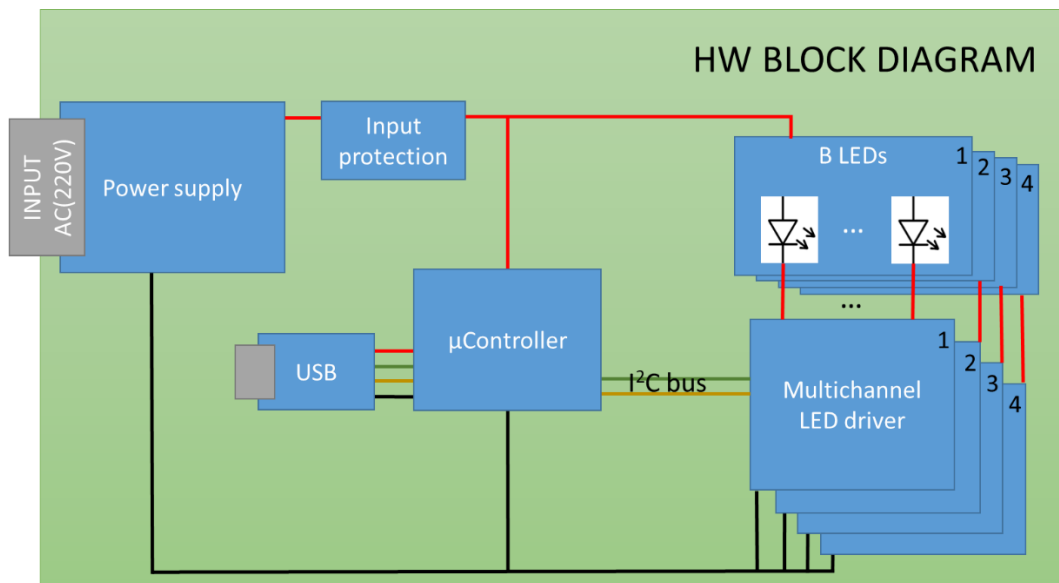


Figure 129: HW block diagram. Designed for this work.

Thus an AC/DC conversion is placed firstly to regulate the voltage input around 6 V. This voltage supplies the linear multichannel driver topology controlled by a microcontroller, which is in charge to activate the individual driver channels throughout I²C bus communication to set a specific current to the blue LEDs. The system is also prepared to be programmed by USB interface. Finally, the mechatronics integration of the electronics in the mechanical base is shown in Figure 130.

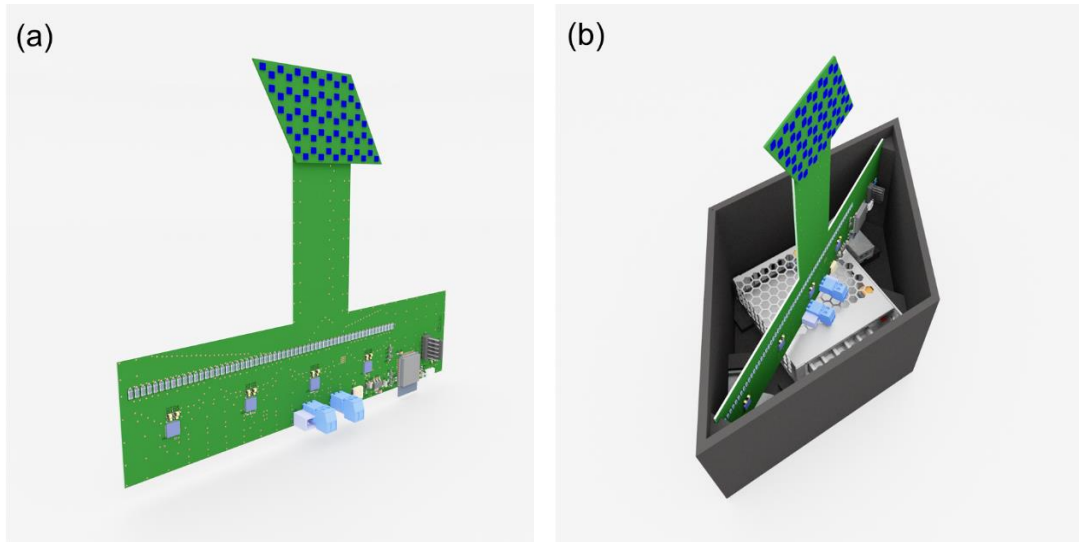


Figure 130: Mechatronics integration. (a) Electronics + PCB. (b) Mechanical base with power supply. Designed for this work.

5.6.2.3.2 Software (SW)

The SW is uploaded to the microcontroller device throughout over-the-air programming (OTA) thanks to the capability of the microcontroller to set a WIFI link. Thus, using a .csv file (generated by Matlab[®] code), the dynamic scenarios to individually control the 60 pixels in the QLED device can be set. In addition, an HTML coded application was created as QLED device interface. In this application, both the current passing through the LED and the duty cycle of the latter can be accurately set. Besides, the dynamic motion or preset animations can be selected as well (once the .csv file is uploaded into the microcontroller memory).

5.6.2.4 *AUTOMOTIVE Lighting Functions*

As claimed by Kruppa *et al.* [7], [8], personalization and Car-to-X communication (real-time information exchange between the vehicle and its surroundings) is a desirable feature in rearlamp lighting systems since digital information can be shared with the vehicle surroundings, which is vital for the final autonomous vehicle implementation. Specifically, the use of a high number of lighting segments (>50) or pixels, as named in this work, for particular taillighting functions to customize and create an endless number of combinations might become a revolution since digital information can be projected.

Currently, the most promising optoelectronics technology to make it real is based on OLED devices [7], [8]. Thereby, some carmakers like AUDI® and OLED suppliers like OLEDworks® are modifying the OLED devices into a highly segmented display [125]. Thus, individually addressable segmentation OLEDs demonstrators [125] were presented at ISAL 2019 by AUDI® as shown in Figure 131.



Figure 131: Digital OLED demonstrator by Audi®, ISAL 2019.

Following that digital lighting trend, we decided to design the dynamic photoluminescence QLED demonstrator in a similar segmentation shape than the one shown in Figure 131. Thus, some examples of digital animations, which can be created with the QLED device designed are shown in Figure 132.

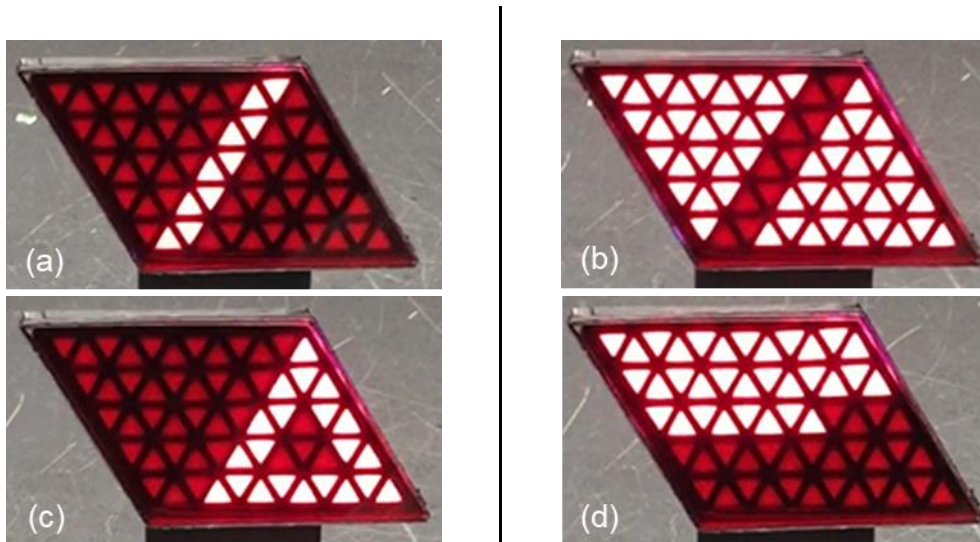


Figure 132: Digital QLED device dynamic lighting scenario examples in this work. Car-to-X communication in rearlamps. (a) Coming home scenario 1. (b) Coming home scenario 2. (c) Warning mode scenario. (d) Leaving home scenario. Designed for this work.

Furthermore, it is worth saying that, although the QLED device offers the possibility to perform other different automotive functions like DRL/PL, TI or STOP, this work will be focused on the TAIL to compare the performance with the automotive OLED technology introduced above.

5.7 QLED AUTOMOTIVE APPLICATION CHARACTERIZATION

Once the QLED automotive application has been built up in chapter 5.6.2 using the QDF described throughout photoluminescence phenomenon to excite the quantum dots, the performance of the final device is assessed. That evaluation is based on the automotive photometric values highlighted in chapter 5.4.3.2 and particularly specified by signaling automotive function in Table 52.

Therefore, the general objective is to make a comparison between the boundary photometric conditions around automotive applications and the performance that photoluminescence-based QLED can offer to the field.

5.7.1 Goals

By performing this experiment, the following physical quantities are pursued:

- a) Emission spectrum (λ)
- b) Luminous flux (Φ)
- c) Light intensity (I)
- d) Luminance (L)
- e) Luminous efficacy (η)

This experiment was carried out at VALEO LIGHTING SYSTEMS facilities.

5.7.2 Experimental Units

The experimental unit used in this characterization is the QLED device manufactured and integrated in the automotive application built up in chapter 5.6.2.

5.7.3 Laboratory Instrumentation

The specific laboratory techniques and instrumentation used for QLED device characterization are described below.

- Emission spectrum → Optical spectrometer
- Luminous flux → Optical spectrometer
- Light intensity → Photometer
- Luminance → Photometer
- Luminous efficacy → Source meter

5.7.3.1 OPTICAL SPECTROMETER

An optical spectrometer is designed to measure spectral radiance or irradiance across various spectral ranges. It measures light from approximately 380 nm to 780 nm. Due to its high accuracy, it is often used as a reference instrument in research and development laboratories [126].



Figure 133: Feasa LED Spectrometer. Reproduced from FEASA® website.

SCOPE: The use of the optical spectrometer will allow us to perform a photometric analysis to extract emission spectrum data.

5.7.3.2 PHOTOMETER

A photometer is an instrument that measures different photometrical quantities like illuminance, luminous intensity, luminous flux and luminance (cd/m^2).



Figure 134: LMK imaging photometer used. Reproduced from TechnoTeam® website.

SCOPE: The use of the photometer will allow us to extract light intensity and luminance.

5.7.3.3 SOURCE METER

See chapter 3.6.3.1 for definition details about this laboratory instrumentation.

Table 54 makes a short summary of the techniques and tools used for the QLED device photometric characterization.

QLED	Value	Tool	Site
Photometric	Emission spectrum Luminous flux	Optical spectrometer	VALEO
	Light intensity Luminance	Photometer	VALEO
	Luminous efficacy	Sourcimeter	VALEO

Table 54: Summary of instrumentation used for QLED device characterization.

5.7.4 Experimental Design 5: QLED demonstrator characterization

Once the dynamic photoluminescent QLED device has been built up, the next step to take is its characterization. As described in 5.7.1, the optical and electrical performance of the device will be the objectives to focus on. Thus, the different parameters to be measured at each device layer will be analyzed in the following sections.

5.7.4.1 Blue Light Source

To begin with, the blue light source used to excite the quantum dots is characterized. The commercial LED used as blue main source is the NE2B757GT part number (MPN) from Nichia® optoelectronics supplier. The main parameters of that LED shown in Table 55 are extracted from the technical datasheet [127].

Blue LED (DATASHEET)	Symbol	Forward Current(mA)	Typ	Unit
Forward Voltage	V_F	$I_F=100\text{mA}$	2.9	V
Luminous Flux	Φ_V		8.7	lm
Chromaticity Coordinate	x		0.133	-
	y		0.075	-
Thermal Resistance	$R_{\Phi JS}$	-	20	°C/W

Table 55: Blue LED electrical/optical characteristics from datasheet. Extracted from [127].

In order to experimentally characterize the blue LED used, different currents at room temperature (25 °C) are set through it to extract the data in Table 56 by using the Feasa® optical spectrometer.

<i>Blue LED (EXPERIMENTAL)</i>	<i>Symbol</i>	<i>Forward Current(mA)</i>	<i>Value</i>	<i>Unit</i>
<i>Radiant Power</i>	Φ_E	5	4.2	mW
		10	10.6	
		25	29.1	
		52	63.9	
		75	90.6	
		90	106.6	
		100	114.5	
<i>Luminous Flux</i>	Φ_V	5	0.28	lm
		10	0.76	
		25	1.99	
		52	4.35	
		75	5.98	
		90	6.98	
		100	7.35	
<i>Chromaticity Coordinate</i>	(x,y)	5	(0.129,0.059)	-
		10	(0.135,0.066)	
		25	(0.135,0.061)	
		52	(0.137,0.062)	
		75	(0.136,0.059)	
		90	(0.136,0.058)	
		100	(0.135,0.057)	
<i>Dominant wavelength</i>	λ_d	5	469.1	nm
		10	469.1	
		25	468.4	
		52	467.9	
		75	467.7	
		90	467.6	
		100	467.5	
<i>Peak wavelength</i>	λ_p	5	466.2	nm
		10	465.9	
		25	465.2	
		52	464.8	
		75	464.4	
		90	464.3	
		100	464.1	

Table 56: Experimentally characterization of blue LED used as main source.

Moreover, both the optical spectrum and the chromaticity diagram are shown in Figure 135 and Figure 136 at a forward current of 100 mA.

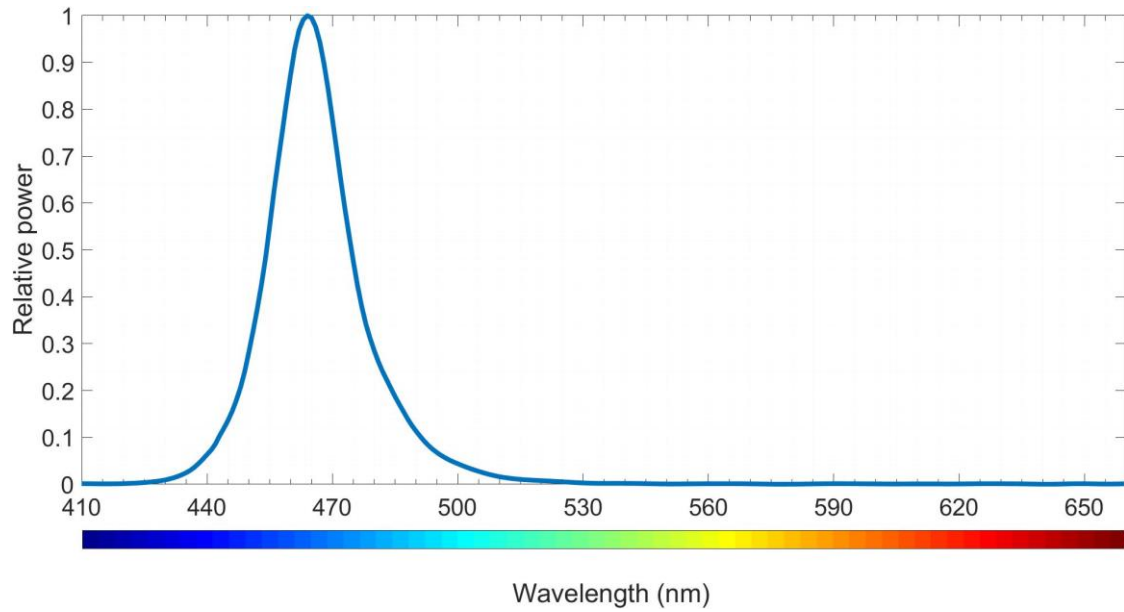


Figure 135: Blue LED optical spectrum @ $I_f=100\text{mA}$ measured in this work.

As it can be seen, the values obtained experimentally are in line with the ones extracted from the datasheet of the blue LED.

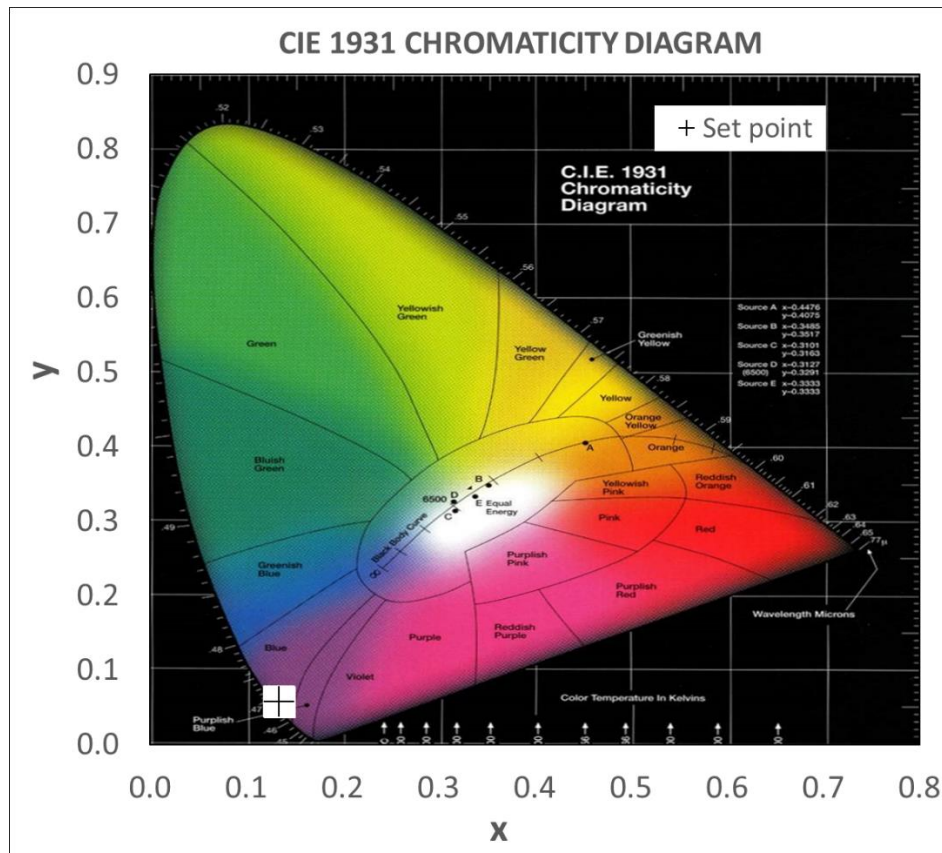


Figure 136: CIE diagram created @ $I_f=100\text{ mA}$. The cross-shaped set-point shows the color from the blue LED source.

5.7.4.2 QDF

Once the blue LED source has been analyzed, the quantum dot layer or QDF will be characterized. Thus, following the same previous strategy, different currents at room temperature (25°C) are set through the blue LEDs to extract the data in Table 57 from the spectrometer instrument, just after the QDF layer.

QDF (EXPERIMENTAL)	Symbol	Forward Current(mA)	Value	Unit
Radiant Power	Φ_E	25	2.9	mW
		52	6.6	
		75	9.7	
		90	11.6	
		100	12.8	
Luminous Flux	Φ_V	25	0.58	lm
		52	1.29	
		75	1.92	
		90	2.29	
		100	2.54	
Chromaticity Coordinate	(x,y)	25	(0.206,0.199)	-
		52	(0.205,0.200)	
		75	(0.207,0.202)	
		90	(0.208,0.202)	
		100	(0.208,0.202)	
Dominant wavelength	λ_d	25	476.4	nm
		52	476.1	
		75	476.0	
		90	475.9	
		100	475.9	
Peak wavelength	λ_p	25	465.9	nm
		52	465.4	
		75	465.2	
		90	465.1	
		100	464.9	

Table 57: Experimentally characterization of QDF layer.

Moreover, both the optical spectrum and the chromaticity diagram are shown in Figure 137 and Figure 138 at a forward current of 100 mA.

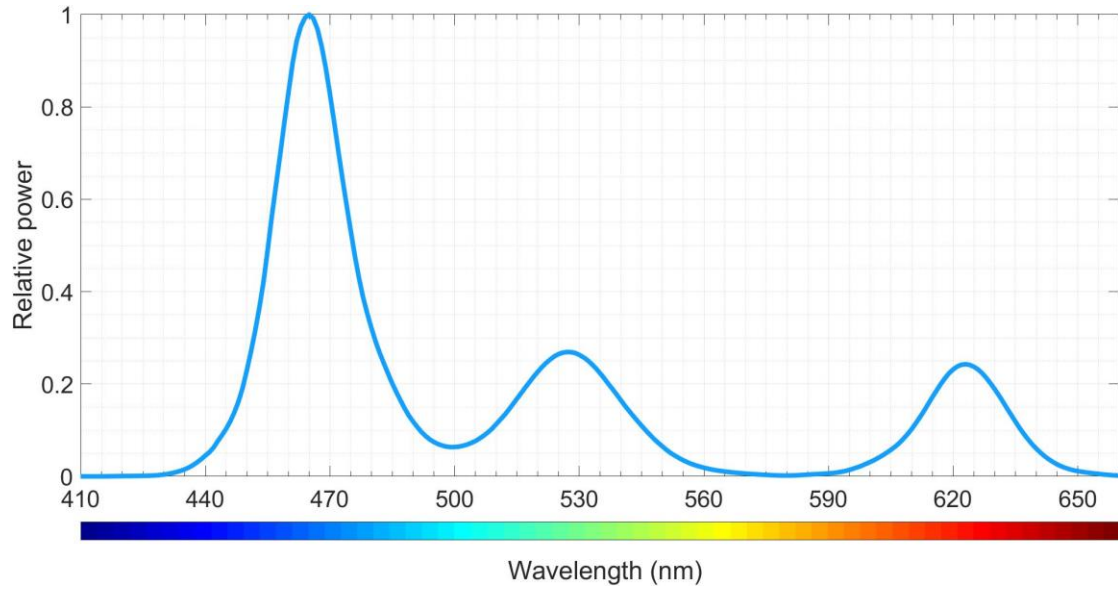


Figure 137: QDF optical spectrum measured @ $I_f=100$ mA.

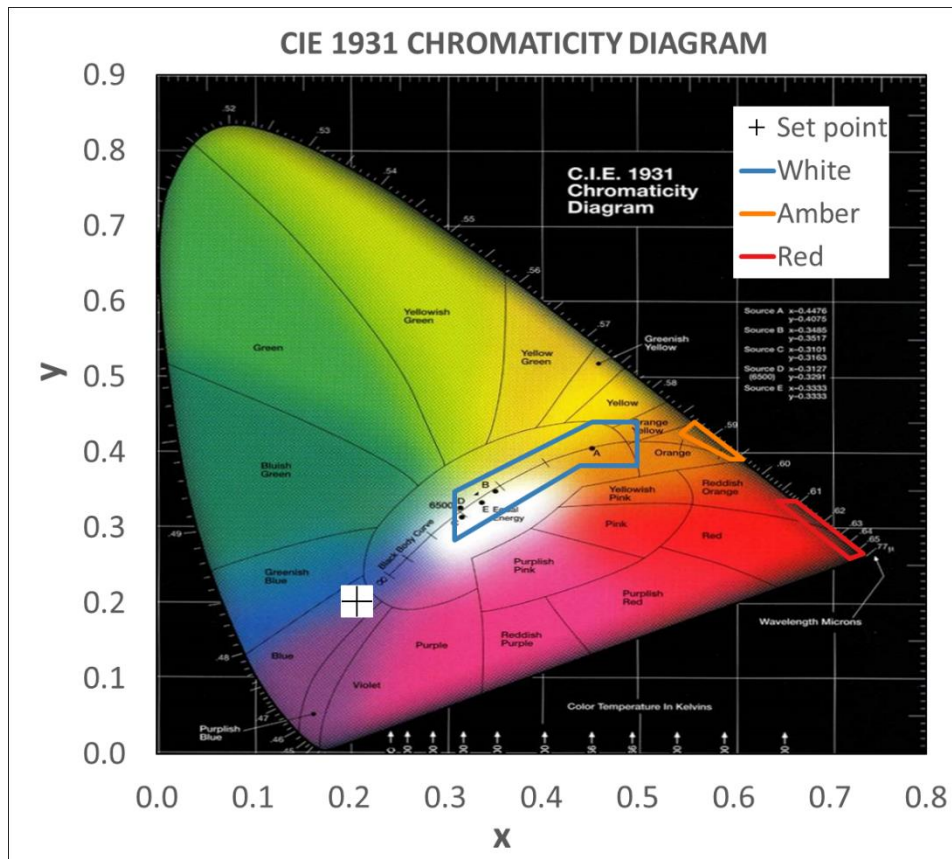


Figure 138: QDF CIE diagram created @ $I_f=100$ mA. Set point is out of automotive white area. Blue, orange and red highlighted polygons indicate the allowed automotive points for white, amber and red colors from a legal aspect. The cross-shaped set-point shows the output color of the QDF, which is out of automotive white area [10].

As expected, two new spectral components appear i.e. green and red contributions, due to the quantum dots incorporated in the QDF. Those results are in line with the QDF datasheet specifications from Table 53, where the green peak wavelength is found at 531 nm and the red peak one is positioned at 624 nm.

However, as the QDF is a commercially layer and it has not been specifically designed for our automotive purpose, it can be observed that the blue contribution to the whole spectrum is much larger than the green and red ones. Thus, the output color after the QDF is not automotive-white strictly speaking but bluish instead.

In fact, if we focus now on the output chromaticity coordinates and particularly on the color automotive homologation areas defined in the CIE space and represented in Figure 138, it is possible to conclude that some actions have to be put in place to consider the QDF as an automotive wavelength conversion layer.

Therefore, our proposal to obtain a white color inside the homologation area for the automotive field is twofold. Firstly, by increasing the density and QY of green and red quantum dots in the QDF, the spectral contribution of green and red could be increased. And secondly, by adding some specific blue-color-blocking layer we can compensate the contribution of blue color to the final output spectrum.

Besides, and going on with the automotive homologation photometrical values, the luminous intensity (I_v) was also measured, taking into account the whole QLED device segments, as shown in Table 58. In addition, those intensity values were compared with the automotive regulation data from Table 52 for some current configuration at $[H=0^\circ, V=0^\circ]$ points, i.e. the horizontal and vertical coordinates associated with the luminous intensity value limits of the photometric chart.

<i>QDF (EXPERIMENTAL)</i>	<i>Symbol</i>	<i>Forward Current(mA)</i>	<i>Value</i>	<i>Unit</i>
<i>Luminous Intensity</i>	I_v	25	18.7	cd
		50	38.6	
		75	57.7	
		100	76.4	

Table 58: Luminous intensity in cd as output from the QDF layer.

Those data are represented in Figure 139, where a linear trend may be predicted.

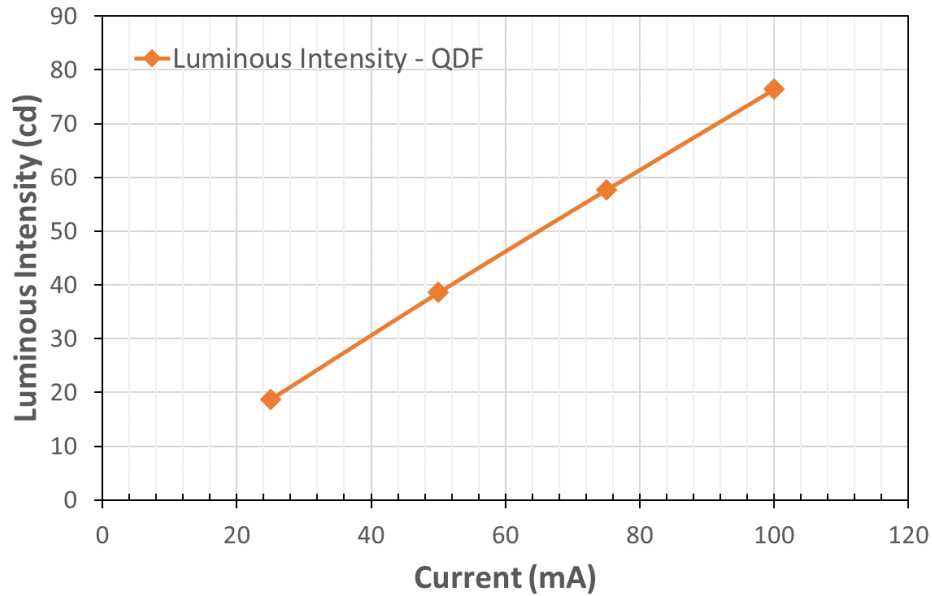


Figure 139: Luminous intensity vs Current on the QDF layer used in this work. The lines are a guide for the eye.

In this way, without taking into account the color points and just the luminous intensity values from Table 58, we could imagine different automotive lighting scenarios. Thus, lighting functions like STOP_ $([H,V]_{\min}=60\text{cd})$, TAIL_ $([H,V]_{\min}=4\text{cd})$, TURN INDICATOR_ $([H,V]_{\min}=50\text{cd})$ or even REVERSE_ $([H,V]_{\min}=80\text{cd})$ would fit the performance given by the QDF and could be theoretically implemented in an automotive environment. However, other lighting functions like DRL_ $([H,V]_{\min}=400\text{cd})$ or FOG_ $([H,V]_{\min}=150\text{cd})$ are far from the actual QDF performance. Although again, by designing a specific automotive QDF, the whole efficiency system could be increased and higher values of luminous intensity might be targeted.

On the other hand, it is possible to define some performance indicators like the luminous efficacy (lm/W) and the current efficiency (cd/A). Thus, using the first blue LED layer as electroluminescent layer (to try to compare our photoluminescence device with an electroluminescent one), the latter indicators are shown in Table 59 and represented in Figure 140.

QDF (EXPERIMENTAL)	Symbol	Forward Current(mA)	Value	Unit
Luminous efficacy	η_P	25	8.0	lm/W
		52	8.6	
		75	8.8	
		100	8.8	
Current efficiency	η_L	25	12.5	cd/A
		50	12.9	
		75	12.8	
		100	12.7	

Table 59: QDF layer performance indicators.

NB: Luminous efficacy and current efficiency were measured at individual or segment level of the QLED device. Moreover, for luminous efficacy, the typical $V_f = 2.9\text{ V}$ from Table 55 is used in all cases as approximation to calculate the electrical power in the blue source.

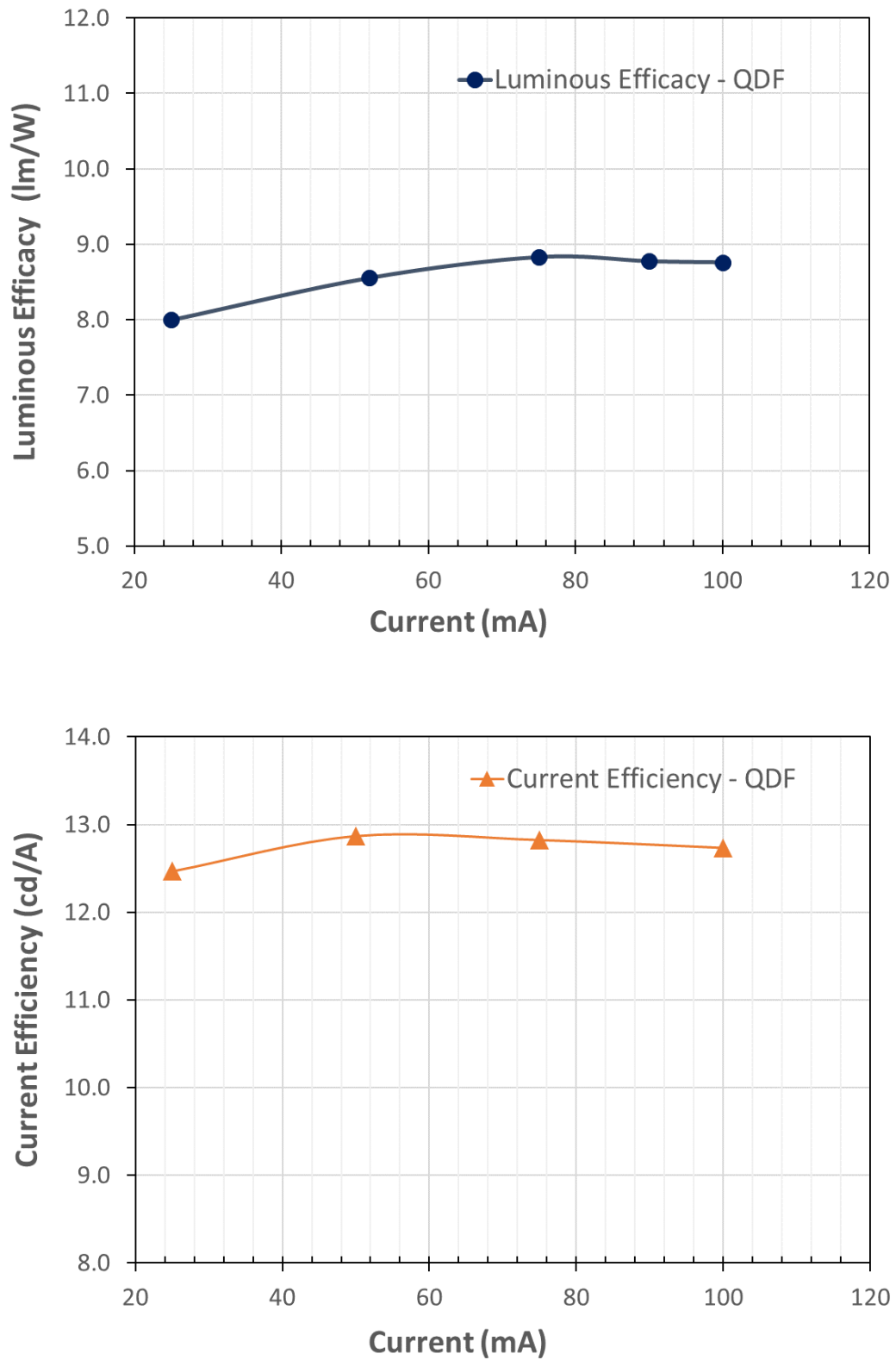


Figure 140: QDF performance indicators calculated for this work.

These QDF indicators values, specifically the luminous efficacy, could be higher in reality due to two main factors. Firstly, the light leakage due to the QLED device built up process. Since it has been a proof-of-concept mockup, several mechanical improvements could be made to avoid any leakage of light. And secondly, the instrumentation used i.e. the optical spectrometer and particularly the integrated sphere incorporated to collect the optical radiation cannot take all the output light from the QDF surface accurately.

Furthermore, although it is not specified in the QDF datasheet, an increase in the quantum yield of the quantum dots used could result in a global efficiency increase as well. To do so, both the materials and the synthesization process should be analyzed thoroughly.

Moreover, it seems that there is a saturation in the blue LED used as main source when it is driven at high current (maximum $I_F=140$ mA from datasheet) as extracted from Figure 140 from the luminous efficacy indicator. Thus, it is possible to state that the optimal driven current in our application is around 80 mA. Therefore, depending on the lighting application pursued, a specific blue LED should be careful chosen to comply with the automotive lighting values required.

Besides, the current efficiency indicator increases at low current injection levels and stays flat from 50 mA to around 80 mA. After that point, the efficiency is slightly reduced until the 100 mA. Thus, as previously said, it is really important to select the correct blue LED source for the specific lighting application chosen.

Finally, the luminance given by the QDF was measured. This figure of merit is especially important in the automotive field. As highlighted in the introduction chapter, style is vital for automotive lighting systems. In fact, the homogeneity aspect of the lighting functions at rearlamp level is one of the highly desired factors that carmakers are pursuing from an aesthetic point of view. Thus, luminance in rearlamp applications for taillights [8], [125] is vital since the homogenous quality of the illuminating surface can be analyzed by calculating the uniformity (%) parameter given by Eq.(33)

$$U = 1 - \frac{(L_{max} - L_{min})}{(L_{max} + L_{min})} \quad (33)$$

where L_{max} and L_{min} are the maximum and minimum values of luminance in the specific lighting area measured.

Additionally, the luminance analysis has been performed using a specific optical SW tool by taking a 750 point-line going through 6 segments of the QLED device as shown in Figure 141. The procedure followed is explained below for the QDF layer at 25mA for the blue LED source.

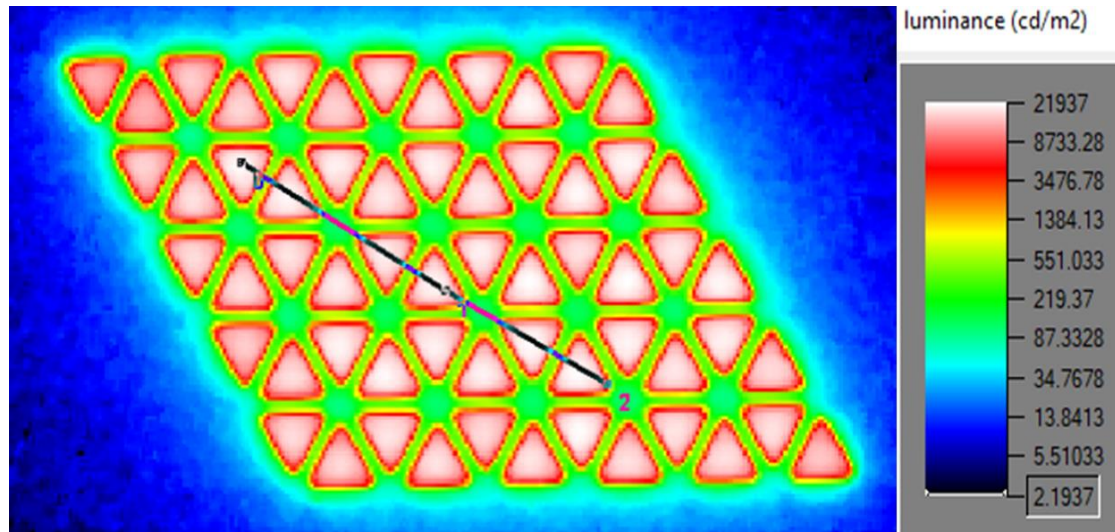


Figure 141: Luminance analysis procedure of the QLED device (QDF@25 mA) used in this work.

By observing Figure 141, it is easier to identify the maximum luminance (L_{\max}) of the device. However, the minimum luminance (L_{\min}) requires to identify a minimum lighting threshold since a bezel or light cover, as shown in Figure 127, is located above the segments under consideration in the luminance line traced. Thus, some “black” areas, corresponding to the green zones from Figure 141, are located between two segments, creating a false value of minimum luminance.

Therefore, so as to define that minimum luminance threshold procedure, a two-segment analysis was carried out in first place as shown in Figure 142 as general example. Here, the value of L_{\min} is identified in the plot, considering the transition limit of the bezel or light cover between segments once the maximum slope of the luminance value curve occurs as depicted in the graph.

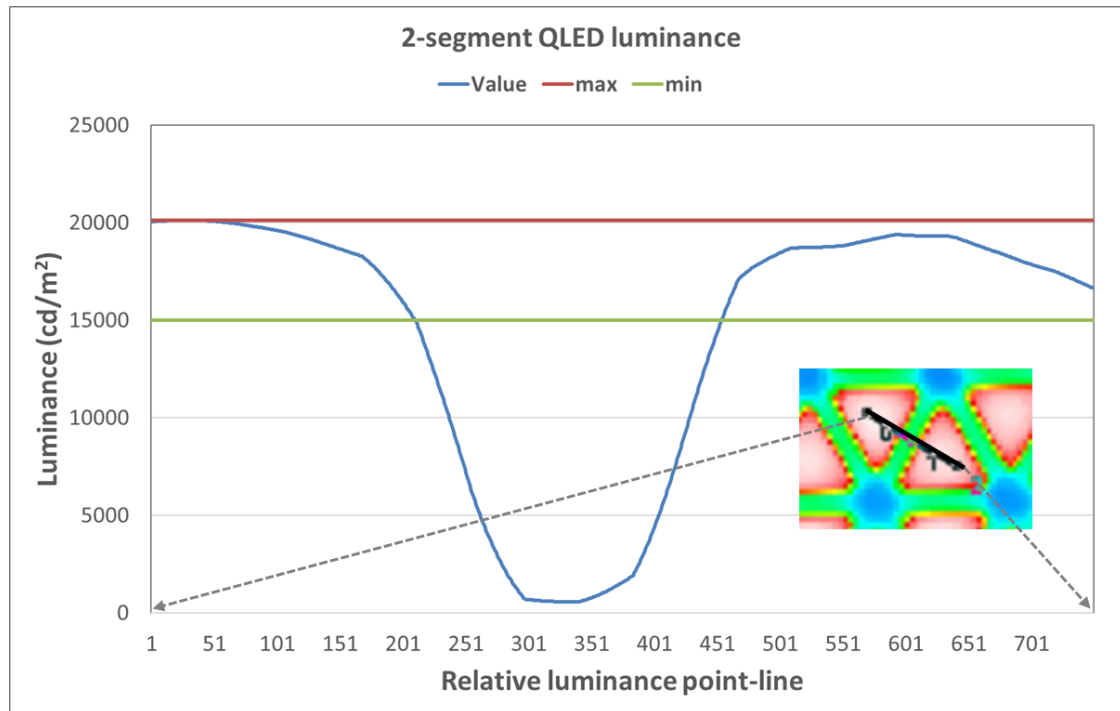


Figure 142: L_{\min} threshold analysis procedure of the QLED device (QDF@25 mA) used in this work.

Thus, once the determination of the minimum value of luminance is established, it is possible to measure both L_{\min} and L_{\max} to eventually calculate the uniformity parameter U from Figure 141 and given by Eq.(33) as shown in Figure 143.

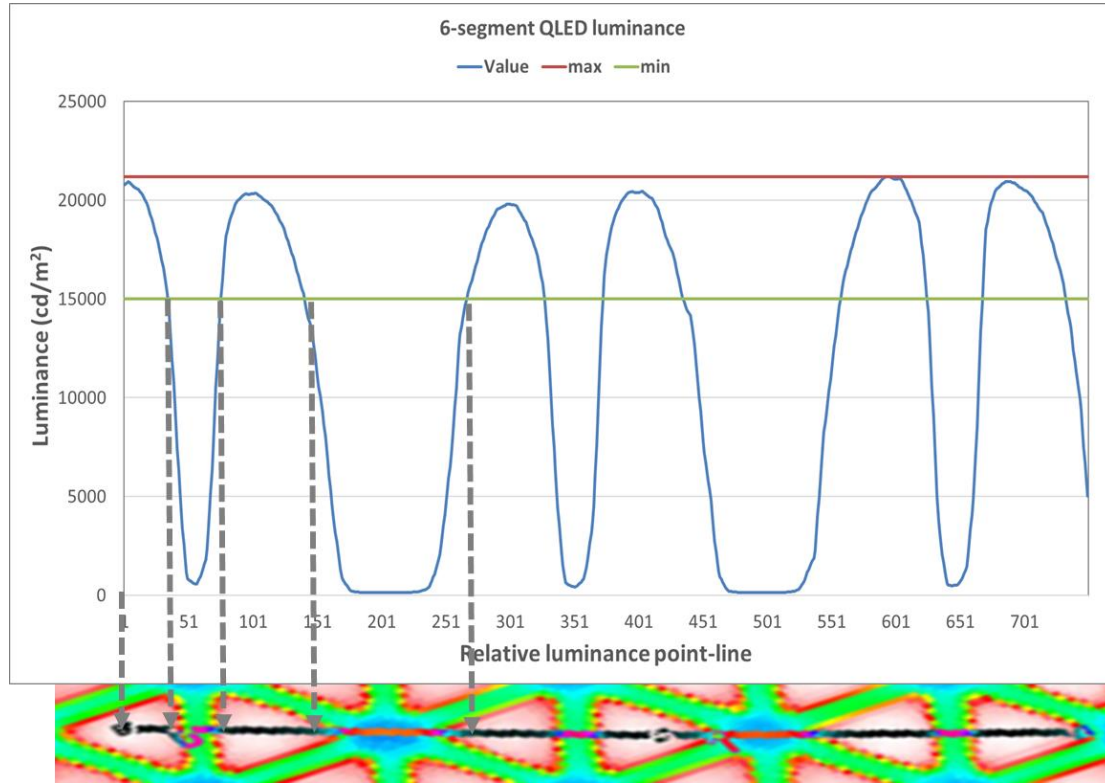


Figure 143: Example of L_{\max} and L_{\min} measurements of 6 segments of the QLED device (QDF@25 mA) used in this work.

Then, once the luminance measurement procedure is set, it is possible to calculate the uniformity U of the QDF layer for different currents applied to the blue LED source as depicted in Table 60.

QDF	Forward Current (mA)	Luminance (cd/m ²)	Uniformity (%)
<i>Luminance vs Uniformity</i>	25	17000	89.0
	50	35000	88.6
	75	50500	87.5
	100	69000	89.1

Table 60: Luminance vs uniformity calculation of the QLED device for the QDF layer used in this work.

As observed, both the luminance values and the uniformity achieved by the QLED device is quite high, getting values between 80% and 90% for the different currents applied.

5.7.4.3 PMMA red filter

As explained previously, although experimental measurements were made on the QDF to characterize it, now this work will be focused on the TAIL lighting function to compare the performance with the automotive OLED technology introduced above. To do so, and after analyzing the QDF layer proposed, it is necessary to try to convert the bluish white color into red. Thus, a red automotive filter made of Poly(methyl methacrylate) (PMMA) is added as the last layer of the QLED

device (Figure 123 and Figure 132). The goal is to create a red wavelength filter (Figure 125) and compare some figures of merit with the OLED technology.

PMMA offers a good transparent performance used for optical transparent products, taillight lens and interior optical systems [123].

In this work, a standard red-colored PMMA material with a thickness of 2.5 mm was used as red filter. Following the same procedure as the one done for the QDF layer, the output optical spectrum and chromaticity diagram are obtained using the output values of the QDF measured in the previous chapter as input data.

Since the PMMA filter used is well-known, a chromaticity analysis on the output optical spectrum was carried out in first place. Thus, using the spectrum obtained from the QDF and depicted in Figure 137 as input for the SW tool, it is possible to obtain the final output spectral curves drawn in Figure 144.

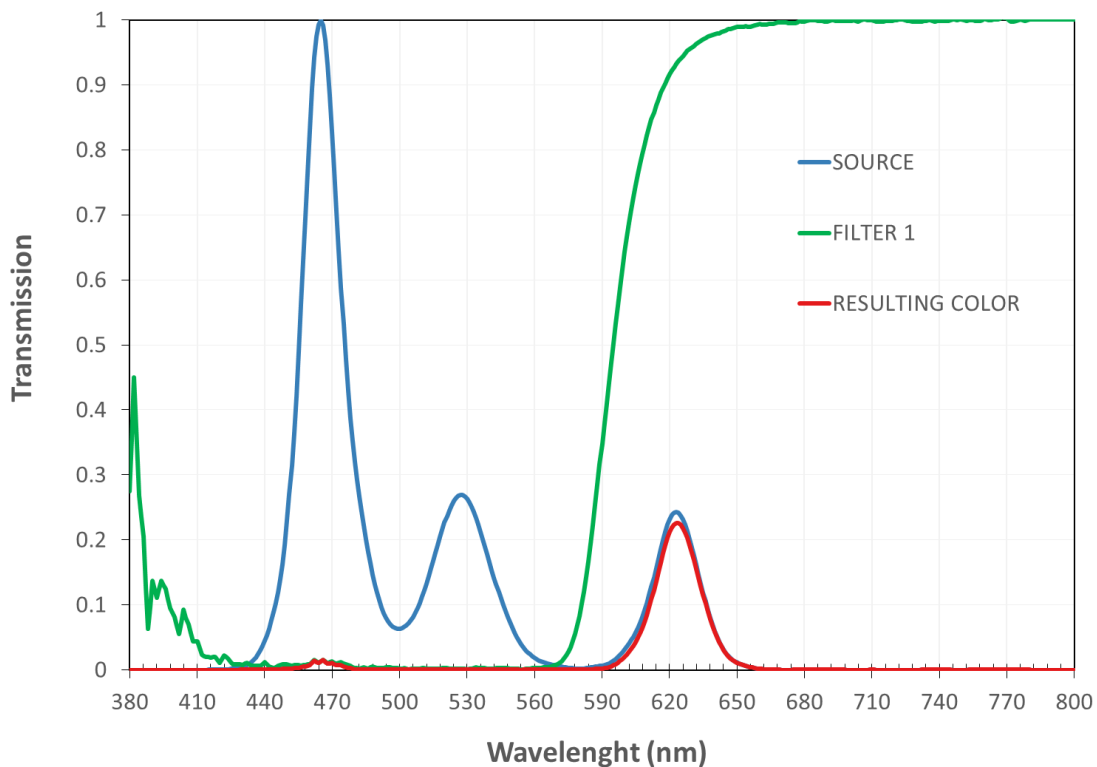


Figure 144: Normalized spectral curves before PMMA filter (SOURCE) and after it (RESULTING COLOR). The green curve (FILTER1) is the PMMA transfer function for the material used in this work.

Therefore, from Figure 144, the QDF spectrum (blue curve) is used as input. Then, taking into account the filter characteristic (green curve), the final output (red curve) is plotted. As it can be extracted from the red curve, two peaks are obtained due to the PMMA filter characteristics. The first one is centered on the input blue peak (465 nm) from the original blue LED source and the second one is positioned at the emission peak (624 nm) from the red quantum dot. It is worth saying that this red peak is also attenuated in an 8.3% due to filter response.

Moreover, CIE diagram space, with both input and output colors, is drawn in Figure 145.

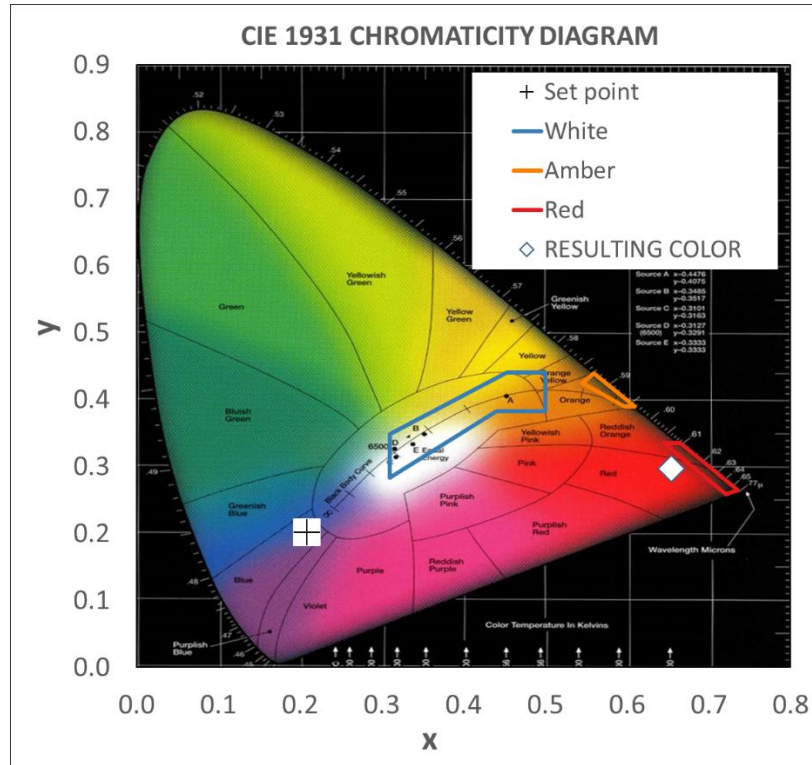


Figure 145: PMMA CIE diagram created for this work. Resulting color is out of automotive red area. Blue, orange and red highlighted polygons indicate the allowed automotive points for white, amber and red colors from a legal aspect [10]. The cross-shaped set-point shows the output color of the QDF.

Although the main objective of red color filtering has been achieved, it is possible to analyze from Figure 145 that red output color ($x=0.654$, $y=0.297$) is out of the automotive homologation area for red. This is due to PMMA filter response, which filters some blue light from the original source at 465 nm. This can be accurately assessed in Figure 146.

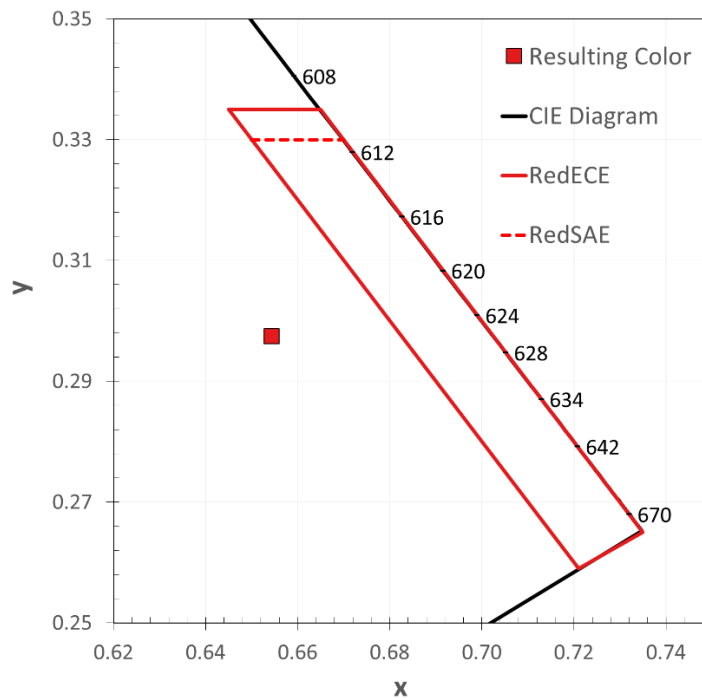


Figure 146: CIE diagram created for this work and centered on the legal automotive regulation area (red line polygon) for ECE and SAE norms. Red square: resulting output color ($x=0.654$, $y=0.297$) after PMMA filter.

On the other hand, the luminous intensity after the red color filter was measured as shown in Table 61 and depicted in Figure 147, where a linear trend is predicted.

PMMA filter (EXPERIMENTAL)	Symbol	Forward Current(mA)	Value	Unit
Luminous Intensity	I_v	25	3	cd
		50	6.3	
		75	9.5	
		100	12.5	

Table 61: Experimental values of luminous intensity in cd as output of the PMMA filter.

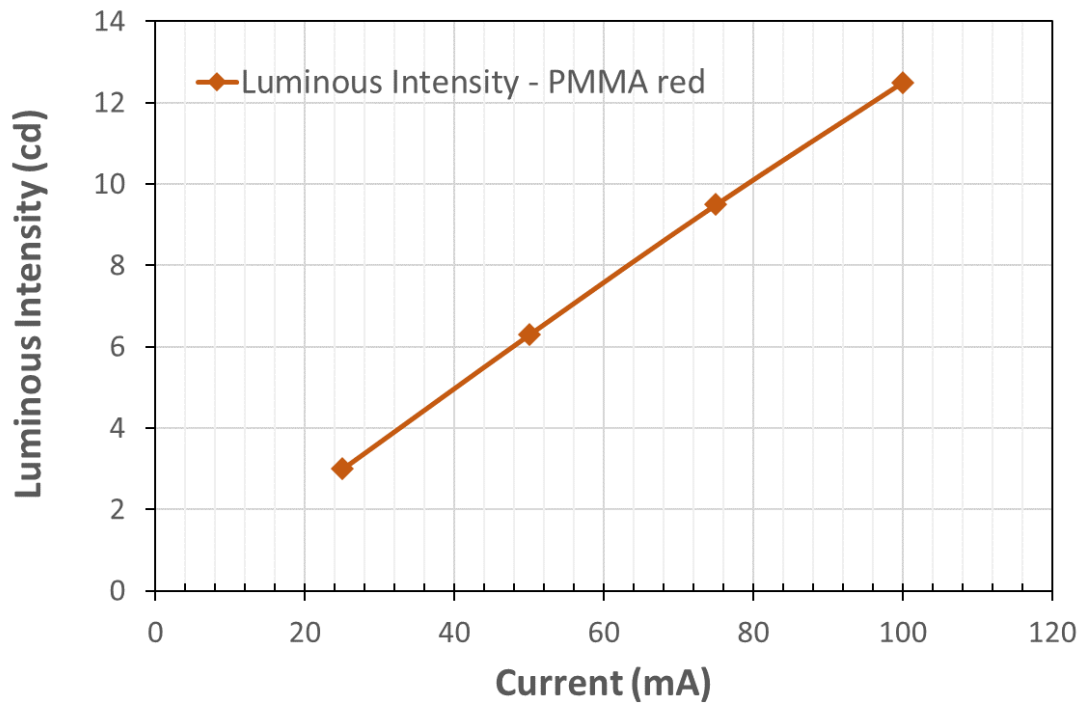


Figure 147: Luminous intensity vs Current after the red PMMA filter used in this work.

Therefore, following Table 52, which defines the minimum and maximum [H,V] luminous intensity values ([4-17] cd for TAIL lighting function) it is possible to extrapolate the values of the curve from Figure 147 in a linear way, to anticipate an optimal current range of the LED blue source. In this specific QLED system a range of current of [32 - 95] mA for each segment or pixel would be necessary to comply with an automotive taillighting function.

It is worth saying that those values could be reduced by optimizing the whole QLED system designed as it will be discussed in 5.7.5.

Eventually, the luminance and the uniformity of this PMMA layer can be assessed. Thus, following the same strategy used for the QDF layer, those values were measured and shown in Table 62.

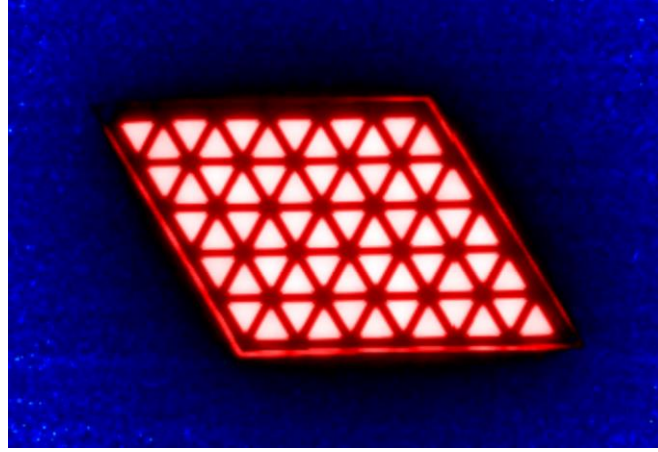


Figure 148: SW-processed QLED device with PMMA filter for luminance analysis in this work.

PMMA filter	Forward Current (mA)	Luminance (cd/m ²)	Uniformity (%)
Luminance vs Uniformity	25	2500	80.9
	50	5000	81.9
	75	7000	81.8
	100	8800	81.6

Table 62: Experimental values of mean luminance and uniformity at the output of the PMMA filter.

Finally, in order to extract some conclusions, those measurements were compared with an OLED device. To do so, the results of the work made by Kruppa *et al.* [7], [8] were used as reference for the OLED values shown in Figure 149.

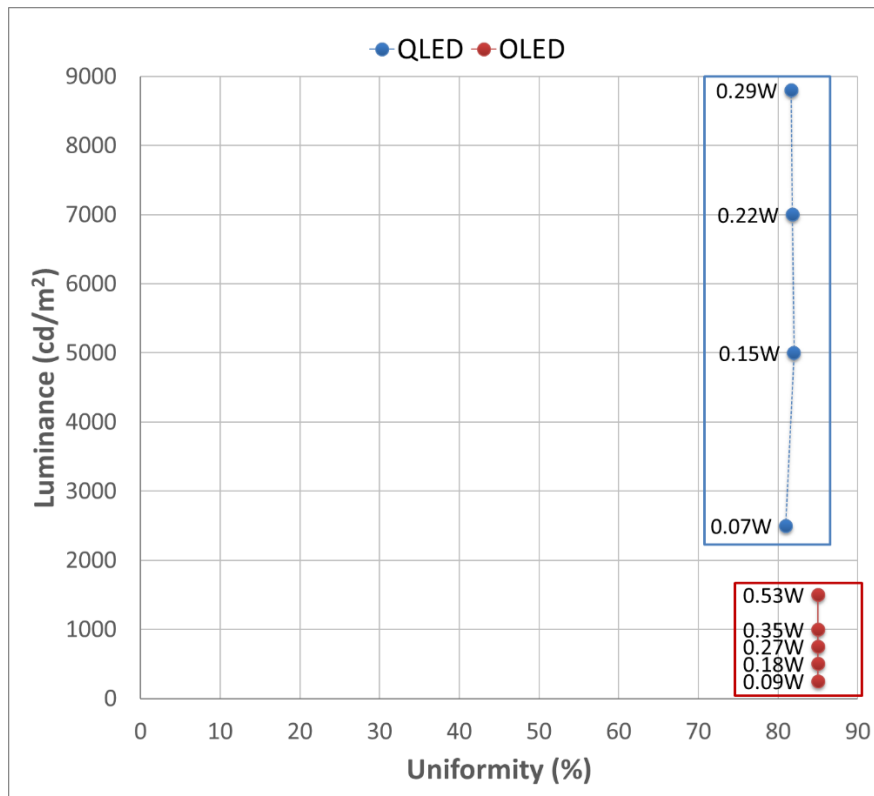


Figure 149: QLED (this work) and OLED comparison of luminance vs uniformity values. OLED values are extracted from Kruppa *et al.* work [7], [8]. Typical $V_f = 2.9$ V from Table 55 is used in all cases as approximation to calculate the power in the blue source.

As highlighted in the introduction chapter, style is a key parameter for automotive lighting systems. The current and future trend in the automotive world is to achieve even greater lighting surfaces. In fact, the homogeneity aspect of the lighting functions at rearlamp level is one of the highly desired factors that carmakers are pursuing from an aesthetic point of view.

Thus, as it can be extracted from Figure 149, uniformity values are higher for OLED device than for the photoluminescence QLED one. However the uniformity values obtained for the QLED device (>80%) offer a promising approach to obtain uniform lighting surfaces for automotive lighting applications [7], [8], [125].

On the other hand, the values of luminance achieved from the QLED are higher compared to the OLED device as shown in Figure 149. This is an interesting point since it would be possible to perform not only taillighting functions but also other like STOP by reaching a good compromise in the uniformity values, which would lead to a good homogeneity aspect of those automotive lighting functions performed.

Moreover, relating to the device power consumption, it is worth noting that OLED active areas taking from Kruppa *et al.* work [7], [8] and QLED emissive areas under comparison are not the same. Thus, the power shown in Figure 149 for each value of luminance are not utterly comparable. It means that probably more than one blue LED would be necessary to achieve the OLED areas considered by Kruppa *et al.* by keeping the same values of QLED uniformity. Then, the values of QLED power shown in Figure 149 would be higher if both emissive areas (QLED and OLED) had the same magnitude. Therefore, a more accurate study on both OLED and QLED devices should be carried out to extract a real power consumption comparison.

Following this high-homogeneous lighting surface strategy, and to achieve endless ways of designs and styles, OLEDs are the best solution in terms of uniformity (compared to QLED working under photoluminescence phenomenon). However, currently only taillighting can be performed using OLEDs due to the optical requirements, i.e. luminance, needed for the rest of automotive lighting functions (STOP, TURN INDICATOR, DRL ...). Then the other current possibility to be implemented is the use of optical diffusers to scatter the light in combination with single-color emitting LEDs (for example red LEDs for TAIL or STOP lighting functions; amber or yellow for TURN INDICATOR). Nevertheless, a dramatic system-based optical efficacy loss happens by using those optical diffusers. In this manner, in order to improve the homogeneity, it is necessary to increase the diffuser material thickness [7], [8], which leads to a low-efficiency optical systems as a whole.

Therefore, our proposal to use QDF as wavelength conversion layer could be an actual solution between the systems formed by discrete point light sources (single-color emitting LEDs) and the OLED devices in terms of homogeneity and uniformity.

This argumentation is based on the fact that our system contains QDs which act as active nanoparticles and not merely light-dispersive grains (as it is the case of some polymers used in optical diffusers). In this way, each QD becomes a light emitter after converting the wavelength from the blue source into the desired color (red in the case of TAIL or STOP). Thus, the dispersion of light in

the QDF is increased and a greater level of homogeneity is achieved through a more efficient system compared to the use of single-color emitting LEDs + passive optical diffusers.

To sum up, when using QLEDs (photoluminescence through QDF) we might have an acceptable uniformity, higher than current LEDs devices, but less than OLED technology. However, it is possible to implement other lighting functions with the QLED (not only the taillighting), achieving high levels of luminance with optical systems more efficient than the current ones.

On the other hand, other advantages can be obtained by using QLEDs (photoluminescence) in automotive lighting systems. They are based on the QD features already described in the introduction chapter. Thus, by controlling the size of the nanocrystal during the synthesis process the output wavelength and, therefore, the color can be accurately selected according to carmakers requirements. Then customized output spectra can be generated by mixing the correct density of different types of QDs on the same substrate. Moreover, narrow emission bands with small FWHM value may be achieved as well by obtaining the purest color ever seen in automotive. Furthermore, the methods of synthesis of QDs through colloidal solutions, offer new ways of depositing the QDs over optical surfaces thanks to the good intrinsic processability. Finally, the inorganic nature of QDs offers good promises relating to stability when facing the automotive environment conditions.

Besides, when using QLEDs as QDF, for example for white, the conversion of wavelength takes place outside the encapsulation of the LED source (blue) itself (in the end, a white LED used nowadays is a blue LED with a phosphor that turns yellow and mixes it with blue at the output to obtain the final white). For this reason, when using QDs, this conversion occurs in the QD layer, further for the blue LED source, and avoiding certain self-heating that must be dissipated in large aluminum radiators in current LED technology. Therefore, with this solution (QDF), more efficient and smaller thermal systems (less weight) could be anticipated, reducing the carbon footprint as well.

In conclusion, we might say that QLEDs (used as QDFs) are not going to replace OLEDs today in automotive lighting systems. However, they can be an ideal complement to that technology in order to increase the homogeneity of the optical surfaces and the efficiency of the overall optical system in relation to current optoelectronic solutions designed by discrete single-color emitting LEDs. Additionally, as previously described, the possibility of performing other types of high-homogeneous lighting functions such as the STOP, TURN INDICATOR, FOG, opens up new styling and design options that could be attractive to carmakers in the future.

5.7.5 *Summary*

Eventually, some general conclusions from this dynamic photoluminescent QLED device may be set. As it was described at the beginning of chapter 5.7, the main objective was to evaluate the suitability of QLEDs devices in the automotive industry, for which the electrical and optical parameters have been obtained to characterize the QLED layers i.e. blue LED source, the quantum dot film and the final device output when passing through a red filter.

Therefore, the blue LED source was measured and compared with the datasheet, establishing a good correlation between the theoretical and experimental data. Once the optical spectrum and the chromaticity points were totally defined for the blue source, the QDF output was measured, using the latter blue source as input excitation. Those measurements were quite interesting since it was possible to observe how the spectral plot changed and two new wavelength peaks appear. Those spectral contributions were due to the red and green quantum dots incorporated in the QDF. In the same way, the chromaticity coordinates moved to the white color. Nevertheless, since the QDF was not specifically designed, the blue contribution of the main source is very high and white coordinates are out of the automotive white color homologation. At this point, two possible actions should be taken into account if white color is pursued in future applications. Firstly, increasing the red and green spectral contribution by increasing the density and QY of quantum dots in the QDF, and secondly, by adding some specific blue-blocking layer to compensate the contribution of that color.

On the other hand, several figures of merit were extracted. Particularly, the luminous intensity was measured, reaching values comparable with different automotive lighting functions. Thus, without taking into account the color points and just the luminous intensity values, lighting functions like STOP, TAIL, TURN INDICATOR or even REVERSE would fit the performance given by the QDF for our QLED device fabricated. This is an interesting point, since by choosing the correct power blue LED source almost all automotive lighting functions could be implemented following this QDF strategy.

Moreover, performance indicators like luminous efficacy and current efficiency were calculated from the measurements. These QDF indicators values could be higher in reality due to the light leakage in the QLED device built up process (the QLED is a proof of concept mockup) and the instrumentation used. Likewise, both the quantum dot materials and the synthesization process should be revisited in order to increase the global QLED efficiency.

Furthermore, the luminance of the QDF was analyzed obtaining good values in the range of [15000 - 70000]cd/m² compared to the ones required in automotive (2000 cd/m²) applications [7], [8]. In addition, the values of luminance uniformity between 80% and 90% for the different currents applied are in good agreement with the values expected for automotive lighting systems.

Finally, a red PMMA filter was used to implement the TAIL lighting function. The objective of the filter was to remove the blue and green spectral components by keeping only the red one. Nevertheless, the characterized filter material allowed some blue spectral contribution. Thus, the final color calculated and measured was slightly out of the automotive homologation region and a different filter with distinct features would be necessary. In the same manner, the luminous intensity

was measured reaching the conclusion that a range of main blue LED current of [32-95] mA for each segment would be necessary to comply with an automotive taillighting [H,V] values.

Likewise, the final red filter layer luminance was measured and compared with an OLED automotive application. In this case, both the values of luminance [2500- 8800]cd/m² and the uniformity (>80%) achieved are inside the values required for automotive lighting applications.

Eventually, if an automotive lighting function implemented by quantum dots is desired using photoluminescence phenomena, both the blue LED source and the QDF layer have to be specifically designed. Therefore, if a red lighting function like TAIL or STOP is pursued for example, red quantum dots have to be used and a compromise between the blue excitation and the conversion to the red color has to be achieved to avoid final blue contribution. In the same way, if white color is required, the spectral contributions of the different quantum dots and the blue source must be compensated to obtain regulatory values for automotive lighting systems.

5.8 CONCLUSIONS

In this block BL5, an automotive lighting application was developed using quantum dots as down-converter nanoparticles. Thus, after introducing the main lighting functions and the quantity of the values required in the automotive field, we reached the conclusion that photoluminescence physical phenomena of quantum dots is more mature than the electroluminescence one. Therefore, different demonstrators and proofs of concept were fabricated to show the potential use of this nanotechnology in the future of mobility.

Thereby, by using a commercial QDF sheet containing quantum dots tuned to red and green wavelengths, a dynamic photoluminescence QLED device was built up following the digital lighting trend in automotive lighting applications and offering photometric values (luminance and homogeneity) that indicate the possible integration of this technology in automotive applications in the future. In general, the study carried out in this PhD may establish the foundations for future research in the sector, being one of the first as far as it is known. In addition, this research might have important social implications due to the large volume of possible devices that could be integrated into vehicles, within a key technological sector worldwide.

Besides, it can be stated that all objectives defined at the scope of the block relating to the QLED automotive integration and characterization have been achieved.

- Redesign of an automotive product using the QLED technology studied for a specific lighting function.

- Correlation of the performance of the previous final product for the same lighting function with conventional LED / OLED technology.

Thus, this mockup was totally characterized obtaining the general conclusion that quantum dots could be a potential candidate for lighting systems inside the automotive world in the future.

6 CONCLUSIONS

QLEDs are considered in the literature as a next generation display technology due to their narrow emission spectra, tunable emission peaks and low cost manufacturing. In combination with the fact that they are formed by quantum dot inorganic semiconductors, which allows them to withstand extreme temperature profiles, QLEDs may be taken into account as potential optoelectronic devices to be used in the automotive lighting systems in the close future.

Two main physical excitation mechanisms are behind QLEDs i.e. electroluminescence and photoluminescence. After a literature research carried out on the Cd-free quantum dots suitable for automotive lighting applications, we reached the conclusion that photoluminescent QLED devices could take over in a short-term timing, while it will be necessary to think of introducing electroluminescent QLED devices in the automotive field in a medium/long term.

In any case, both physical phenomena have been studied in this work. Therefore, an electroluminescence device, i.e. a 6-pixel ($4.5\text{mm}^2/\text{pixel}$) QLED system, based on characterized $\text{CuInS}_2/\text{ZnS}$ QDs was designed and fabricated with a conventional structure: ITO as anode, PEDOT:PSS (HIL), TFB (HTL), $\text{CuInS}_2/\text{ZnS}$ QDs(EL), ZnO NPs (ETL) and Al layer as cathode. In addition, each pixel was electrically characterized to obtain the electrical I-V curve, which gives some insight about how the fabrication process and layer thickness have an influence in the shape of the plot.

Furthermore, a computational model based on the Transfer Hamiltonian approach to describe the electrical behavior of the lighting system was presented. Thus, I-V curve was simulated and compared with experimental results, reaching a remarkable agreement as shown in Figure 96. The influence of critical parameters as the junction capacitance between the anode and the HIL layer was studied in the simulator to report the close relation of I-V curve with the fabrication process relating to the thickness and material type conforming the electroluminescent device. Therefore, that variability in the fabrication process has a huge influence in the device performance, specifically in the current flowing throughout the device.

Therefore, the computational model offers the possibility to model an electroluminescent QLED device by anticipating the electrical performance in a theoretical design before going to the automotive QLED manufacturing at the laboratory.

Likewise, an automotive lighting application was developed using quantum dots as wavelength converter nanoparticles. By using a commercial QDF sheet containing quantum dots tuned to red and green wavelengths, a dynamic photoluminescence QLED device was built up following the digital lighting trend in automotive lighting applications, showing the potential use of this nanotechnology in the future of mobility. Thus, this mockup was totally characterized, concluding that quantum dots could be a potential candidate for lighting systems inside the automotive world in the future.

Besides, it can be stated that all objectives defined in the research plan presented at the beginning of this PhD work have been successfully achieved.

To conclude, QLEDs might offer a great advantage in the automotive field, offering the possibility of using this technology worldwide in automotive applications such as interior and exterior lighting products. Thus, starting by the development of different experimental devices along with a good electrical simulation behavior in the electroluminescent case, the QLED models and demonstrators developed could set the basis for further research on the field of vehicle lighting systems.

6.1 FUTURE RESEARCH

The foreseen future work will be based on two different ways depending on the physical phenomenon of QDs excitation to be considered. In this manner, and as shown in Figure 120, it is possible to conclude that higher photometrical values can be achieved nowadays by using a photoluminescence phenomenon instead of an electroluminescent one. Therefore, due to the different timings in a possible implementation in the automotive field, two different strategies should be taken into account.

6.1.1 Photoluminescence

As already highlighted, this is a more mature technology to be introduced in a short/medium term in the automotive lighting products. Thus, the next steps would be to create a specific QDF designed to fulfill a particular vehicle lighting function like TAIL, STOP, TI or even DRL. To do so, specific QDs with high QY, low FWHM and spectrally tuned according to carmakers requirements should be synthesized and introduced in particular automotive qualified plastics. Moreover, a specific design of rearlamp or headlamp should be identified, to proceed the optical, environmental and electrical validation afterwards according to automotive norms. In this way, this phenomenon could be validated and be ready for the introduction and integration in actual vehicles.

6.1.2 Electroluminescence

This is a more challenging phenomenon that would require more time for the final automotive integration. Particularly, the future research on this point would be based on the QLED simulator. It would be important to continue improving the development of this useful tool, which will allow us to obtain more accurate results by introducing new features in its algorithm. In this way, the objective would be to try to cover all the limitation identified in chapter 4.5 in order to make more realistic modelling of the QLED from a computational side. This would give us great advantages to understand the physical effects of QLED devices to improve their efficiency by using different layer configurations and materials as well as taking into account secondary effects at nanoscale level.

6.1.3 Synergies

In both cases (photoluminescence and electroluminescent) common actions should be taken into account in future research. Probably the main one is relating to the QD synthesis, where ligands play an important role for both the passivation as well as carriers injection into the QD core. Thus, it is important to find QD synthesis specialists and procedures to fabricate the suitable QDs, which fit automotive requirements. In this way, collaborations with different partners at both levels i.e. academic (universities and technological centers) and industrial (carmakers) will be key to successfully integrate this nanotechnology in vehicle lighting products in the next future.

7 PUBLICATIONS

7.1 JOURNAL ARTICLES

- J J Santaella, K Critchley, S Rodríguez-Bolívar and F M Gómez-Campos, “Design and fabrication of CuInS₂/ZnS-based QLED for automotive lighting systems,” *Nanotechnology*, vol.32, no.10, p.105204, 2020. DOI: 10.1088/1361-6528/abcced.
- J J Santaella, S Rodríguez-Bolívar, L Puga-Pedregosa, A González-Rico, M Marín-González and F M Gómez-Campos, “High-luminance QLED device with digital and dynamic lighting functions for efficient automotive systems”. Submitted to: *Transportation Research Part C: Emerging Technologies*.
- J J Santaella, K Critchley, S Rodríguez-Bolívar and F M Gómez-Campos, “Electrical simulation of a QLED device based on quantum dots using the Transfer Hamiltonian approach,” Submitted to: *13th Spanish Conference on electron Devices (CDE-2021)*.
- J J Santaella, S Rodríguez-Bolívar and F M Gómez-Campos, “Light term integration for radiative recombination in QLED devices using the Transfer Hamiltonian approach,” In preparation.

7.2 PATENTS

- Patent Application, **EP3546821A1**, “LIGHTING DEVICE”, Date of publication: 02-10-2019, Applicant: Valeo Vision, INVENTORS: SANTAELLA, Juan-Jose; MARIN, Maria; MARTÍNEZ-PEREZ, Jose-Ramon; ILLAN, Antonio Domingo; LARA-CABEZA, Juan; PENA, Miguel-Angel; BARRAGAN, Mari-Angeles. Status: **PUBLISHED**.
<https://worldwide.espacenet.com/patent/search/family/062002616/publication/EP3546821A1?&q=EP3546821>
- Patent Application, **FR3099540A1**, “DISPOSITIF LUMINEUX POUR VÉHICULE AUTOMOBILE”, Date of publication: 05-02-2021, Applicant: Valeo Vision, INVENTORS: SANTAELLA, Juan-Jose; ILLAN, Antonio Domingo. Status: **PUBLISHED**.
<https://worldwide.espacenet.com/patent/search/family/069190857/publication/FR3099540A1?&q=FR3099540>
- Patent Application, **FR2101342**, “AUTOMOTIVE LUMINOUS DEVICE”, Date of filing: 12-02-2021, Applicant: Valeo Vision, INVENTORS: SANTAELLA, Juan-Jose; GONZALEZ RICO, Alberto; PUGA PEDREGOSA, Lucía; MARÍN GONZÁLEZ, Maria. Status: **FILED**.
- Patent Application, **FR2101344**, “AUTOMOTIVE LUMINOUS DEVICE”, Date of filing: 12-02-2021, Applicant: Valeo Vision, INVENTORS: SANTAELLA, Juan-Jose; ROMO PEÑA, Jesus. Status: **FILED**.

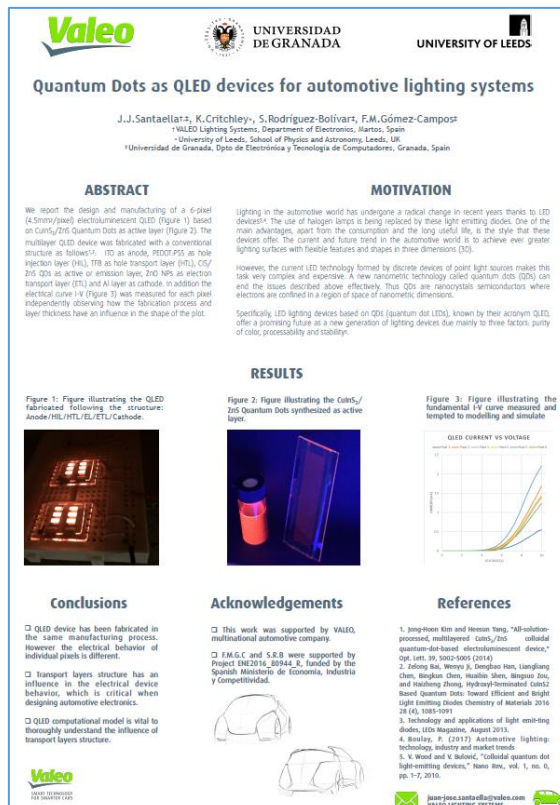
7.3 ORAL PRESENTATIONS

- **2020 Phosphors & Quantum Dots Industry Forum.** LOCATION: Portland, Oregon (USA). DATE: November 11-13, 2020. TITLE: "Quantum Dots as QLED devices for automotive lighting systems". AUTHORS: J J Santaella, K Critchley, S Rodríguez-Bolívar and F M Gómez-Campos.



7.4 POSTER PRESENTATIONS

- **5th edition of Nanotech France 2019 International Conference and Exhibition.** LOCATION: Paris, (FRANCE). DATE: June 26-28, 2019. TITLE: "Quantum Dots as QLED devices for automotive lighting systems". AUTHORS: J J Santaella, K Critchley, S Rodríguez-Bolívar and F M Gómez-Campos.



ABSTRACT

We report the design and manufacturing of a 6-pixel (4.5mm/jaw) electroluminescent QLED (Figure 1) based on CuInS₂/ZnS Quantum Dots as active layer (Figure 2). The multilayer QLED device was fabricated with a conventional structure as follows: HTL as anode, PEDOT:PSS as hole injection layer (HIL), TFB as hole transport layer (HTL), CuS/ZnS QDs as active or emission layer, ZnO NPs as electron transport layer (ETL) and Al layer as cathode. In addition the electrical curve I-V (Figure 3) was measured for each pixel independently observing how the fabrication process and layer thickness have an influence in the shape of the plot.

MOTIVATION

Lighting in the automotive world has undergone a radical change in recent years thanks to LED devices¹. The use of halogen lamps is being replaced by these light emitting diodes. One of the main advantages, apart from the consumption and the long useful life, is the style that these devices offer. The current and future trend in the automotive world is to achieve ever greater lighting surfaces with flexible features and shapes in three dimensions (3D).

However, the current LED technology formed by discrete devices of point light sources makes this task very complex and expensive. A new nanometric technology called quantum dots (QDs) can end the issues described above effectively. These QDs are nanocrystals semiconductors where electrons are confined in a region of space of nanometric dimensions.

Specifically, LED lighting devices based on QDs (quantum dot LEDs), known by their acronym QLED, offer a promising future as a new generation of lighting devices due mainly to three factors: purity of color, processability and stability.

RESULTS

Figure 1: Figure illustrating the QLED fabricated following the structure: Anode/HTL/HTL/ETL/ETL/Cathode.

Figure 2: Figure illustrating the CuInS₂/ZnS Quantum Dots synthesized as active layer.

Figure 3: Figure illustrating the fundamental I-V curve measured and attempted to modelling and simulate.

Conclusions

- QLED device has been fabricated in the same manufacturing process. However the electrical behavior of individual pixels is different.
- Transport layers structure has an influence in the electrical device behavior, which is critical when designing automotive electronics.
- QLED computational model is vital to thoroughly understand the influence of transport layers structure.

Acknowledgements

- This work was supported by VALEO, multinational automotive company.
- F.M.G.C. and S.R.B. were supported by Project EN2019_80944_R, funded by the Spanish Ministerio de Economía, Industria y Competitividad.

References

1. Jong-Hoon Kim and Heon-Teng, "All-solution-processed, multilayered CuInS₂/ZnS colloidal quantum-dot-based electroluminescent device," Opt. Lett. 39, 5002-5005 (2014).
2. Jibang Bai, Wenye J. Songbo Han, Liangliang Chen, Bingkun Chen, Huihui Shen, Qingguo Xu, and Jianfeng Zhang, "Hybrid-Perovskite QLEDs Based Quantum Dots: Toward Efficient and Bright Light Emitting Diodes," Chemistry of Materials 2016, 28 (4), 1085-1091.
3. Technology and applications of light emitting diodes, LED Magazine, August 2013.
4. Bouley, P. (2017) Automotive lighting: technology, industry and market trends.
5. V. Wood and V. Bulović, "Colloidal quantum dot light-emitting devices," Nature Rev., vol. 1, no. 5, pp. 1-7, 2010.

8 REFERENCES

- [1] J. Aschenbroich, "How Valeo is creating major change as a result of digital technology," *Le journal de l'école de Paris du management*, vol. 132, no. 4, pp. 23–29, 2018.
- [2] S. I.-N. Delhi, "Automotive Revolution & Perspective Towards 2030," *Auto Tech Review*, vol. 5, no. 4, pp. 20–25, 2016.
- [3] VALEO, "Valeo, a technology company at the epicenter of several automotive industry revolutions," in *CES LAS VEGAS*, 2018, p. 16.
- [4] VALEO, "Valeo at the heart of the 3 automotive revolutions," in *Franckfurt Motor Show*, 2017, no. October, p. 12.
- [5] M. Fachot, "Technology and applications of light emitting diodes," *LEDs Magazine*, vol. 10, p. 1, 2013.
- [6] P. Boulay, "Automotive Lighting Technology, Industry and Market Trends 2017 Report," no. October, 2017.
- [7] M. Kruppa, W. Thomas, and W. Huhn, "An OLED taillight revolution: From point light sources to segmented area light sources," *Information Display*, vol. 35, no. 4, pp. 14–18, 2019.
- [8] M. Kruppa and W. Thomas, "DIGITAL OLED for Taillighting – Most Efficient , Homogeneous , and Flexible Display Technology," in *ISAL*, 2019, pp. 525–533.
- [9] G. Konstantatos and E. H. Sargent, *Colloidal Quantum Dot Optoelectronics and Photovoltaics*, 1st ed. Cambridge: Cambridge University Press, 2013.
- [10] UNECE, "Uniform provisions concerning the approval of vehicles with regard to the installation of lighting and light-signalling devices," in *Addendum 47: Regulation No. 48*, 2014, p. 131.
- [11] M. Fox, *Optical Properties of Solids*, 2nd ed. Inc., New York: Oxford University Press, 2010.
- [12] V. Wood and V. Bulović, "Colloidal quantum dot light-emitting devices," *Nano Reviews*, vol. 1, no. 1, p. 5202, 2010.
- [13] ANFAC, "Informe anual 2019," in *Asociación Española de Fabricantes de Automóviles y Camiones*, 2019, pp. 1–55.
- [14] ANFAC, "Liderando la movilidad sostenible. Informe Ejecutivo," in *Plan de la Automoción 2020-40.*, 2020, pp. 1–56.
- [15] A. M. Brouwer, "Standards for photoluminescence quantum yield measurements in solution (IUPAC technical report)," *Pure and Applied Chemistry*, vol. 83, no. 12, pp. 2213–2228, 2011.
- [16] M. D. Tessier, D. Dupont, K. De Nolf, J. De Roo, and Z. Hens, "Economic and Size-tunable Synthesis of InP/ZnE (E = S,Se) Colloidal Quantum Dots.," *Chemistry of Materials*, vol. 27, p. 4893–4898, 2015.
- [17] Instituto Nacional de Seguridad e Higiene en el Trabajo (INSHT), *Límites de exposición profesional para agentes químicos en España*. Madrid, 2014.
- [18] GADSL, "Global Automotive Declarable Substance List (GADSL)," *gadsl.org*, 2017. [Online]. Available: <https://www.gadsl.org/>. [Accessed: 27-Jun-2017].
- [19] Imds Professional, "The GADSL: Global Automotive Declarable Substance List," *imds-professional.com*, 2017. [Online]. Available: <https://www.imds-professional.com/es/info-points/the-gadsl.html>. [Accessed: 27-Jun-2017].

- [20] G. Xu, S. Zeng, B. Zhang, M. T. Swihart, K. T. Yong, and P. N. Prasad, "New Generation Cadmium-Free Quantum Dots for Biophotonics and Nanomedicine," *Chemical Reviews*, vol. 116, no. 19, pp. 12234–12327, 2016.
- [21] C. Ippen, T. Greco, and A. Wedel, "InP/ZnSe/ZnS: A Novel Multishell System for InP Quantum Dots for Improved Luminescence Efficiency and Its application in a Light-Emitting Device," *Journal of Information Display*, vol. 13, no. 2, pp. 91–95, 2012.
- [22] L. Li, A. Pandey, D. J. Werder, B. P. Khanal, J. M. Pietryga, and V. I. Klimov, "Efficient synthesis of highly luminescent copper indium sulfide-based core/shell nanocrystals with surprisingly long-lived emission," *Journal of the American Chemical Society*, vol. 133, no. 5, pp. 1176–1179, 2011.
- [23] D. Deng *et al.*, "High-Quality CuInS₂/ZnS Quantum Dots for In vitro and In vivo Bioimaging," *Chemistry of Materials*, vol. 24, no. 15, pp. 3029–3037, 2012.
- [24] S. Liu, H. Zhang, Y. Qiao, and X. Su, "One-pot synthesis of ternary CuInS₂ quantum dots with near-infrared fluorescence in aqueous solution," *RSC Advances*, vol. 2, no. 3, pp. 819–825, 2012.
- [25] L. Li, T. J. Daou, I. Texier, T. T. Kim Chi, N. Q. Liem, and P. Reiss, "Highly Luminescent CuInS₂/ZnS Core/Shell Nanocrystals: Cadmium-Free Quantum Dots for In Vivo Imaging," *Chemistry of Materials*, vol. 21, no. 12, pp. 2422–2429, 2009.
- [26] S. Li, Y. Chen, L. Huang, and D. Pan, "Simple continuous-flow synthesis of Cu–In–Zn–S/ZnS and Ag–In–Zn–S/ZnS core/shell quantum dots," *Nanotechnology*, vol. 24, no. 39, p. 395705, 2013.
- [27] Y. Chen, S. Li, L. Huang, and D. Pan, "Green and Facile Synthesis of Water-Soluble Cu – In – S/ZnS Core/Shell Quantum Dots," *Inorganic Chemistry*, vol. 52, no. 14, pp. 7819–7821, 2013.
- [28] W. W. Xiong, G. H. Yang, X. C. Wu, and J. J. Zhu, "Aqueous synthesis of color-tunable CuInS₂/ZnS nanocrystals for the detection of human interleukin 6," *ACS Applied Materials and Interfaces*, vol. 5, no. 16, pp. 8210–8216, 2013.
- [29] J. H. Kim and H. Yang, "High-Efficiency Cu-In-S Quantum-Dot-Light-Emitting Device Exceeding 7%," *Chemistry of Materials*, vol. 28, no. 17, pp. 6329–6335, 2016.
- [30] T. Ogawa, T. Kuzuya, Y. Hamanaka, and K. Sumiyama, "Synthesis of Ag-In binary sulfide nanoparticles-structural tuning and their photoluminescence properties," *Journal of Materials Chemistry*, vol. 20, no. 11, pp. 2226–2231, 2010.
- [31] Y. Hamanaka, K. Ozawa, and T. Kuzuya, "Enhancement of Donor – Acceptor Pair Emissions in Colloidal AgInS₂ Quantum Dots with High Concentrations of Defects," *Journal of Physical Chemistry C*, vol. 118, p. 14562–14568, 2014.
- [32] B. Mao, C. Chuang, C. McCleese, J. Zhu, and C. Burda, "Near-Infrared Emitting AgInS₂/ZnS Nanocrystals," *The Journal of Physical Chemistry C*, vol. 118, no. 25, pp. 13883–13889, 2014.
- [33] T. Torimoto *et al.*, "Facile synthesis of ZnS-AgInS₂ solid solution nanoparticles for a color-adjustable luminophore.," *Journal of the American Chemical Society*, vol. 129, no. 41, pp. 12388–12389, 2007.
- [34] P. Subramaniam, S. J. Lee, S. Shah, S. Patel, V. Starovoytov, and K. B. Lee, "Generation of a library of non-toxic quantum dots for cellular imaging and siRNA delivery," *Advanced Materials*, vol. 24, no. 29, pp. 4014–4019, 2012.
- [35] D. Deng, L. Qu, J. Zhang, Y. Ma, and Y. Gu, "Quaternary Zn–Ag–In–Se Quantum Dots for Biomedical Optical Imaging of RGD-Modified Micelles," vol. 5, no. 21, pp. 10858–10865, 2013.
- [36] B. B. Srivastava *et al.*, "Highly luminescent Mn-doped ZnS nanocrystals: Gram-scale synthesis," *Journal of Physical Chemistry Letters*, vol. 1, no. 9, pp. 1454–1458, 2010.

- [37] M. H. Abib *et al.*, "Simulation-Based Optical Spectra Analyses and Synthesis of Highly Monodispersed Mn-Doped ZnSe Nanocrystal," *Nano: Brief Reports and Reviews*, vol. 11, p. 1650086, 2016.
- [38] X. Wu, F. Tian, W. Wang, J. Chen, M. Wu, and J. X. Zhao, "Fabrication of highly fluorescent graphene quantum dots using L-glutamic acid for in vitro/in vivo imaging and sensing.," *J. Mater. Chem. C*, vol. 1, no. 31, pp. 4676–4684, 2013.
- [39] H. Sugimoto, M. Fujii, Y. Fukuda, K. Imakita, and K. Akamatsu, "All-inorganic water-dispersible silicon quantum dots: highly efficient near-infrared luminescence in a wide pH range.," *Nanoscale*, vol. 6, no. 1, pp. 122–126, 2014.
- [40] S. Ozdemir, Y. E. Suyolcu, S. Turan, and B. Aslan, "Influence of the growth conditions on the optical and structural properties of self-assembled InAs/GaAs quantum dots for low As/In ratio," *Applied Surface Science*, vol. 392, pp. 817–825, 2017.
- [41] Q. H. Vo, K. Watanabe, T. Kageyama, S. Iwamoto, and Y. Arakawa, "Self-assembled formation of GaAsP nano-apertures above InAs/GaAs quantum dots by the thermal diffusion of phosphorus," *Phys. Status Solidi b*, vol. 253, no. 4, pp. 659–663, 2016.
- [42] V. Grigel, D. Dupont, K. De Nolf, Z. Hens, and M. D. Tessier, "InAs Colloidal Quantum Dots Synthesis via Aminonictogen Precursor Chemistry," *Journal of the American Chemical Society*, vol. 138, no. 41, pp. 13485–13488, 2016.
- [43] D. Franke *et al.*, "Continuous injection synthesis of indium arsenide quantum dots emissive in the short-wavelength infrared," *Nature Communications*, vol. 7, p. 12749, 2016.
- [44] R. Khafajeh, M. Molaei, and M. Karimipour, "Synthesis of ZnSe and ZnSe: Cu quantum dots by a room temperature photochemical (UV-assisted) approach using Na₂SeO₃ as Se source and investigating optical properties," *Luminescence*, vol. 32, no. 4, pp. 581–587, 2016.
- [45] M. Herrera, M. F. Chisholm, M. A. Kamarudin, Q. D. Zhuang, M. Hayne, and S. I. Molina, "Effect of an in-situ thermal annealing on the structural properties of self-assembled GaSb / GaAs quantum dots," *Applied Surface Science*, vol. 395, pp. 136–139, 2016.
- [46] S. Xu, J. Ziegler, and T. Nann, "Rapid synthesis of highly luminescent InP and InP/ZnS nanocrystals," *Journal of Materials Chemistry*, vol. 18, no. 23, pp. 2653–2656, 2008.
- [47] X. Yang *et al.*, "A bright cadmium-free, hybrid organic/quantum dot white light-emitting diode," *Applied Physics Letters*, vol. 101, no. 23, 2012.
- [48] J. Lim *et al.*, "Highly efficient cadmium-free quantum dot light-emitting diodes enabled by the direct formation of excitons within InP@ZnSeS quantum dots," *ACS Nano*, vol. 7, no. 10, pp. 9019–9026, 2013.
- [49] H. C. Wang *et al.*, "Cadmium-Free InP/ZnSeS/ZnS Heterostructure-Based Quantum Dot Light-Emitting Diodes with a ZnMgO Electron Transport Layer and a Brightness of Over 10 000 cd m⁻²," *Small*, vol. 13, no. 13, pp. 1–7, 2017.
- [50] J.-H. Jo *et al.*, "High-efficiency red electroluminescent device based on multishelled InP quantum dots," *Optics Letters*, vol. 41, no. 17, pp. 3984–3987, 2016.
- [51] V. V. Romanov, P. A. Dement'ev, and K. D. Moiseev, "Effect of multicomponent InAsSbP matrix surface on formation of InSb quantum dots at MOVPE growth," *Semiconductors*, vol. 50, no. 7, pp. 910–914, 2016.
- [52] I. Karomi, P. M. Smowton, S. Shutts, A. B. Krysa, and R. Beanland, "InAsP quantum dot lasers grown by MOVPE," *Optics Express*, vol. 23, no. 21, pp. 27282–27291, 2015.
- [53] H. Lee, C.-R. Lee, H.-K. Ahn, J. S. Kim, and M.-Y. Ryu, "Emission characteristics of shape-engineered InAs/InAlGaAs quantum dots subjected to thermal treatments," *Journal of the Korean Physical Society*, vol. 69, no. 1, pp. 85–90, 2016.

- [54] I. Jang *et al.*, "Inverted InP quantum dot light-emitting diodes using low-temperature solution-processed metal-oxide as an electron transport layer," *Japanese Journal of Applied Physics*, vol. 54, no. 2S, p. 02BC01, 2015.
- [55] I. Jang *et al.*, "Study of ethanolamine surface treatment on the metal-oxide electron transport layer in inverted InP quantum dot light-emitting diodes," *Electronic Materials Letters*, vol. 11, no. 6, pp. 1066–1071, 2015.
- [56] C. Ippen *et al.*, "Color tuning of indium phosphide quantum dots for cadmium-free quantum dot light-emitting devices with high efficiency and color saturation," *Journal of the Society for Information Display*, vol. 23, no. 7, pp. 285–293, 2015.
- [57] Y. Kim, T. Greco, C. Ippen, A. Wedel, and J. Kim, "Indium phosphide (InP) colloidal quantum dot based light-emitting diodes designed on Flexible PEN substrate," in *IEEE 5th International Nanoelectronics Conference (INEC)*, 2013, pp. 425–427.
- [58] H. Y. Kim *et al.*, "Transparent InP Quantum Dot Light-Emitting Diodes with ZrO₂ Electron Transport Layer and Indium Zinc Oxide Top Electrode," *Advanced Functional Materials*, vol. 26, no. 20, pp. 3454–3461, 2016.
- [59] Y. Kim *et al.*, "Increased shell thickness in indium phosphide multishell quantum dots leading to efficiency and stability enhancement in light-emitting diodes," *Optical Materials Express*, vol. 4, no. 7, pp. 1436–1443, 2014.
- [60] Y. Kim, C. Ippen, B. Fischer, A. Lange, and A. Wedel, "Efficiency enhancement of InP-based inverted QD-LEDs by incorporation of a polyethylenimine modified Al:ZnO layer," *Journal of the Society for Information Display*, vol. 23, no. 8, pp. 377–383, 2015.
- [61] Z. Bai *et al.*, "Hydroxyl-Terminated CuInS₂ Based Quantum Dots: Toward Efficient and Bright Light Emitting Diodes," *Chemistry of Materials*, vol. 28, no. 4, pp. 1085–1091, 2016.
- [62] J.-H. Kim and H. Yang, "All-solution-processed, multilayered CuInS₂/ZnS colloidal quantum-dot-based electroluminescent device," *Optics Letters*, vol. 39, no. 17, pp. 5002–5005, 2014.
- [63] Z. Liu *et al.*, "Solution-processed high-efficiency cadmium-free Cu-Zn-In-S-based quantum-dot light-emitting diodes with low turn-on voltage," *Organic Electronics*, vol. 36, pp. 97–102, 2016.
- [64] E. A. Margulies, P. L. T. Boudreaux, V. I. Adamovich, B. D. Alleyne, M. S. Weaver, and J. J. Brown, "Narrow spectrum deep red emitters for OLED lighting and display," *Digest of Technical Papers - SID International Symposium*, vol. 50, no. 1, pp. 911–913, 2019.
- [65] W. Monch, "On the physics of metal-semiconductor interfaces," *Reports on Progress in Physics*, vol. 53, pp. 221–278, 1990.
- [66] Toutestquantique, "Transmission Electron Microscope (TEM)," *toutestquantique.fr*, 2017. [Online]. Available: <http://toutestquantique.fr/en/microscopy>. [Accessed: 15-Oct-2017].
- [67] H. Borchert *et al.*, "Determination of nanocrystal sizes: A comparison of TEM, SAXS, and XRD studies of highly monodisperse CoPt 3 particles," *Langmuir*, vol. 21, no. 5, pp. 1931–1936, 2005.
- [68] L. D. S. Yadav, "Ultraviolet (UV) and Visible Spectroscopy," in *Organic Spectroscopy*, Springer Netherlands, 2005.
- [69] T. H. Gfroerer, "Photoluminescence in Analysis of Surfaces and Interfaces," in *Encyclopedia of Analytical Chemistry*, J. W. and Sons, Ed. American Cancer Society, 2000.
- [70] NIOSH, "General Safe Practices for Working with Engineered Nanomaterials in Research Laboratories," pp. 1–60, 2012.
- [71] D. E. Clark, "Safety and the laboratory centrifuge," *Chemical Health and Safety*, vol. 8, no. 6, pp. 7–13, 2001.

- [72] M. Booth, A. P. Brown, S. D. Evans, and K. Critchley, "Determining the concentration of CuInS₂ quantum dots from the size-dependent molar extinction coefficient," *Chemistry of Materials*, vol. 24, no. 11, pp. 2064–2070, 2012.
- [73] A. J. Harvie *et al.*, "Observation of compositional domains within individual copper indium sulfide quantum dots," *Nanoscale*, vol. 8, no. 36, pp. 16157–16161, 2016.
- [74] H. Kim *et al.*, "Electrical, optical, and structural properties of indium-tin-oxide thin films for organic light-emitting devices," *Journal of Applied Physics*, vol. 86, no. 11, pp. 6451–6461, 1999.
- [75] P. R. Huang, Y. He, C. Cao, and Z. H. Lu, "The origin of the high work function of chlorinated indium tin oxide," *NPG Asia Materials*, vol. 5, no. e57, pp. 1–5, 2013.
- [76] Ossila, "OPV and OLED Fabrication Guide," *ossila.com*, 2017. [Online]. Available: <https://www.ossila.com/pages/organic-photovoltaic-opv-and-organic-light-emitting-diode-oled-fabrication-manual>. [Accessed: 20-Nov-2017].
- [77] H. Bednarski *et al.*, "The influence of PEDOT to PSS ratio on the optical properties of PEDOT: PSS thin solid films - Insight from spectroscopic ellipsometry," *Acta Physica Polonica A*, vol. 130, no. 5, pp. 1242–1244, 2016.
- [78] E. S. Muckley *et al.*, "New Insights on Electro-Optical Response of Poly(3,4-ethylenedioxythiophene):Poly(styrenesulfonate) Film to Humidity," *ACS Applied Materials and Interfaces*, vol. 9, no. 18, pp. 15880–15886, 2017.
- [79] J. Chen *et al.*, "All solution-processed stable white quantum dot light-emitting diodes with hybrid ZnO@TiO₂ as blue emitters," *Scientific Reports*, vol. 4, pp. 1–6, 2014.
- [80] Q. Zheng, J. Sun, S. Cheng, Y. Lai, H. Zhou, and J. Yu, "Power conversion efficiency enhancement of polymer solar cells using MoO₃/TFB as hole transport layer," *Applied Physics A*, vol. 120, pp. 857–861, 2015.
- [81] D. A. Ahn, S. Lee, J. Chung, Y. Park, and M. C. Suh, "Impact of Interface Mixing on the Performance of Solution Processed Organic Light Emitting Diodes - Impedance and Ultraviolet Photoelectron Spectroscopy Study," *ACS Applied Materials and Interfaces*, vol. 9, no. 27, pp. 22748–22756, 2017.
- [82] A. Shabaev, M. J. Mehl, and A. L. Efros, "Energy band structure of CuInS₂ and optical spectra of CuInS₂ nanocrystals," *Physical Review B*, vol. 92, no. 3, p. 035431, 2015.
- [83] D. C. Look and J. C. Manthuruthil, "Electron and hole conductivity in CuInS₂," *Journal of Physics and Chemistry of Solids*, vol. 37, no. 2, pp. 173–180, 1976.
- [84] J. Krustok, J. Raudoja, and H. Collan, "Photoluminescence and the tetragonal distortion in CuInS₂," *Thin Solid Films*, vol. 387, no. 1–2, pp. 195–197, 2001.
- [85] M. Oda, T. Miyaoka, S. Yamada, and T. Tani, "Synthesis, Characterization and its Photoluminescence Properties of Group I-III-VI₂ CuInS₂ nanocrystals," *Physics Procedia*, vol. 29, pp. 18–24, 2012.
- [86] J. K. Larsen *et al.*, "Sulfurization of Co-Evaporated Cu(In,Ga)Se₂ as a Postdeposition Treatment," *IEEE Journal of Photovoltaics*, vol. 8, no. 2, pp. 604–610, 2018.
- [87] H. Ramli, S. K. Abdul Rahim, T. Abd Rahim, and M. Muhaimin Aminuddin, "Optimization of zinc sulfide (ZnS) electron affinity in copper indium sulfide (CIS) based photovoltaic cell," *Chalcogenide Letters*, vol. 10, no. 6, pp. 189–195, 2013.
- [88] N. Uzar and M. C. Arikan, "Synthesis and investigation of optical properties of ZnS nanostructures," *Bulletin of Materials Science*, vol. 34, no. 2, pp. 287–292, 2011.
- [89] G.-M. Malgorzata, "Synthesis of stable and non-cadmium containing quantum dots conjugated with folic acid for imaging of cancer cells," 2011.

- [90] S. Sabir, M. Arshad, and S. K. Chaudhari, "Zinc oxide nanoparticles for revolutionizing agriculture: Synthesis and applications," *Scientific World Journal*, vol. 2014, p. 8, 2014.
- [91] M. Properties, "Zinc Oxide (ZnO) Semiconductors," *AZO Materials*, 2013. [Online]. Available: <https://www.azom.com/article.aspx?ArticleID=8417>. [Accessed: 15-Jun-2018].
- [92] T. Tharsika, A. S. M. A. Haseeb, S. A. Akbar, M. F. Mohd Sabri, and W. Y. Hoong, "Enhanced ethanol gas sensing properties of SnO₂-core/ZnO-shell nanostructures," *Sensors*, vol. 14, no. 8, pp. 14586–14600, 2014.
- [93] M. Oshikiri, Y. Imanaka, F. Aryasetiawan, and G. Kido, "Comparison of the electron effective mass of the n-type ZnO in the wurtzite structure measured by cyclotron resonance and calculated from first principle theory," *Physica B: Condensed Matter*, vol. 298, no. 1–4, pp. 472–476, 2001.
- [94] S. Sharma and C. Periasamy, "Simulation study and performance analysis of n-ZnO/p-Si heterojunction photodetector," *Journal of Electron Devices*, vol. 19, pp. 1633–1636, 2014.
- [95] J. X. J. Zhang and K. Hoshino, "Chapter 2 - Fundamentals of nano/microfabrication and scale effect," in *Molecular Sensors and Nanodevices (Second Edition)*, Second Edition., J. X. J. Zhang and K. Hoshino, Eds. Academic Press, 2019, pp. 43–111.
- [96] Ossila, "Spin Coating: Complete Guide to Theory and Techniques," *ossila.com*, 2017. [Online]. Available: <https://www.ossila.com/pages/spin-coating>. [Accessed: 20-Nov-2017].
- [97] R. Luttge, "Chapter 2 - Basic Technologies for Microsystems," in *Microfabrication for Industrial Applications*, R. Luttge, Ed. Boston: William Andrew Publishing, 2011, pp. 13–54.
- [98] T. J. Mason, "Ultrasonic cleaning: An historical perspective," *Ultrasonics Sonochemistry*, vol. 29, pp. 519–523, 2016.
- [99] D. Vasileska, S. M. Goodnick, and G. Klimeck, *Computational Electronics. Semiclassical and Quantum Device Modeling and Simulation*. 2010.
- [100] S. Illera, J. D. Prades, A. Cirera, and A. Cornet, "A transfer Hamiltonian model for devices based on quantum dot arrays," *Scientific World Journal*, vol. 2015, pp. 1–20, 2015.
- [101] M. Passoni and C. E. Bottani, "Transfer Hamiltonian analytical theory of scanning tunneling spectroscopy," *Physical Review B*, vol. 76, no. 11, p. 115404, 2007.
- [102] J. Bardeen, "Tunneling from a many-particle point of view," *Physical Review Letters*, vol. 6, no. 2, pp. 57–59, 1961.
- [103] C. Noguera, "Validity of the transfer Hamiltonian approach : application to the STM spectroscopic mode," *Journal de Physique*, vol. 50, no. 18, pp. 2587–2599, 1989.
- [104] M. C. Payne, "Transfer hamiltonian description of resonant tunnelling," *Journal of Physics C: Solid State Physics*, vol. 19, no. 8, pp. 1145–1155, 1986.
- [105] S. Illera, N. Garcia-Castello, J. D. Prades, and A. Cirera, "A transfer Hamiltonian approach for an arbitrary quantum dot array in the self-consistent field regime," *Journal of Applied Physics*, vol. 112, p. 093701, 2012.
- [106] S. Illera, J. D. Prades, A. Cirera, and A. Cornet, "Transport in quantum dot stacks using the transfer Hamiltonian method in self-consistent field regime," *Europhysics Letters Association*, vol. 98, no. 1, p. 17003, 2012.
- [107] S. Illera, J. D. Prades, and A. Cirera, "A compact theoretical model for opto-electronic devices based on quantum dot arrays," *arXiv:1305.3612 [cond-mat.mes-hall]*, pp. 1–14, 2013.
- [108] N. Garcia-Castello, S. Illera, R. Guerra, J. D. Prades, S. Ossicini, and A. Cirera, "Silicon quantum dots embedded in a SiO₂ matrix: From structural study to carrier transport properties," *Physical Review B*, vol. 88, no. 7, p. 075322, 2013.

- [109] S. I. Robles, "Electron transport in low-dimensional systems : optoelectronic device simulations," Ph.D. dissertation, Universitat de Barcelona, 2015.
- [110] J. H. Davies, *The Physics of Low- Dimensional Semiconductors: An Introduction*. Cambridge University Press, 1998.
- [111] P. C. Deliyannis, "Density of states," *Journal of Mathematical Physics*, vol. 12, no. 5, p. 860, 1971.
- [112] S. Datta, "Electrical resistance: An atomistic view," *Nanotechnology*, vol. 15, no. 7, p. S433, 2004.
- [113] S. M. Islam, P. Biswas, P. Banerji, and S. Chakraborty, "InAs quantum dots as charge storing elements for applications in flash memory devices," *Materials Science and Engineering B*, vol. 198, pp. 102–107, 2015.
- [114] F. Rana, "Chapter 2: Semiconductor Heterostructures," in *Semiconductor Optoelectronics*, NY, Ed. Cornell University, 2011, pp. 1–29.
- [115] N. S. Foundation, "Simulation-based engineering science," in *National Science Foundation*, 2006, no. May, pp. 1–66.
- [116] S. M. Islam and P. Banerji, "Size effect of InAs quantum dots grown by metal organic chemical vapor deposition technique in storing electrical charges for memory applications," *RSC Advances*, vol. 5, no. 9, pp. 6906–6911, 2015.
- [117] S. M. Islam, K. Sarkar, P. Banerji, K. J. Sarkar, and B. Pal, "Leakage current characteristics in MOCVD grown InAs quantum dot embedded GaAs metal-oxide-semiconductor capacitor," *RSC Advances*, vol. 5, no. 102, pp. 83837–83842, 2015.
- [118] C. Poole and I. Darwazeh, "Chapter 11 - Microwave semiconductor materials and diodes," in *Microwave Active Circuit Analysis and Design*, C. Poole and I. Darwazeh, Eds. Oxford: Academic Press, 2016, pp. 355–393.
- [119] VALEO, "Smart technology for smarter mobility," *valeo.com*, 2021. [Online]. Available: <https://www.valeo.com>. [Accessed: 02-Feb-2021].
- [120] VALEO Lighting Systems, "From light to advanced vision technologies," in *Technical handbook - valeoscope*, 2016, pp. 219–264.
- [121] W. Falicoff, "Optical Design Considerations for Automotive Lighting with LEDs," in *Strategies In Light Workshop*, no. February, 2003, pp. 1–22.
- [122] LUMILEDS, "Using Superflux LEDs in Automotive signal lamps," in *Application Note AB20-1*, 2004.
- [123] J. MAXWELL, "1 - Materials for cars," in *Plastics in the Automotive Industry*, J. MAXWELL, Ed. Woodhead Publishing, 1994, pp. 1–12.
- [124] BREADY, "Quantum Dot Film Product Specification," in *Nanjing Bready Electronics Datasheet BQ150*, 2020, p. 12.
- [125] M. Kondakova and K. Vaeth, "OLED Lighting for automotive solutions," in *OLEDWorks*, 2021, pp. 1–10.
- [126] A. Wego, "Accuracy simulation of an LED based spectrophotometer," *Optik*, vol. 124, no. 7, pp. 644–649, 2013.
- [127] NICHIA, "LED Product Specification," in *Nichia Corporation Datasheet NE2B757GT*, 2020, p. 18.